

**Mechanisms and Strategies for Fetal
Membrane Weakening and Repair after
Trauma**

Submitted in partial fulfilment of the requirements of the
Degree of Doctor of Philosophy
(Queen Mary University of London)

Presented by

DAVID WILLIAM BARRETT

Statement of originality

I, David William Barrett, confirm that the research included within this thesis is my own work or that where it has been carried out in collaboration with, or supported by others, that this is duly acknowledged below, and my contribution indicated. Previously published material is also acknowledged below.

I attest that I have exercised reasonable care to ensure that the work is original and does not to the best of my knowledge break any UK law, infringe any third party's copyright or other Intellectual Property Right, or contain any confidential material.

I accept that the College has the right to use plagiarism detection software to check the electronic version of the thesis.

I confirm that this thesis has not been previously submitted for the award of a degree by this or any other university.

The copyright of this thesis rests with the author and no quotation from it or information derived from it may be published without the prior written consent of the author.

Signature:

A handwritten signature in black ink, appearing to read 'D.W. Barrett', written over a light blue horizontal line.

Date: 21/01/2018

Abstract

Preterm premature rupture of membranes (PPROM) is the rupture of fetal membranes prior to 37 weeks gestation, and before the onset of labour. PPRM complicates 40% of preterm births, which can result in lifelong disabilities such as respiratory, cardiac and neurological disorders. The causes of PPRM are multifactorial and not well understood. Iatrogenic PPRM is a major complication after invasive fetal interventions and occurs in 6-45% of cases. The high prevalence of iatrogenic PPRM after fetal surgery, due to the absent healing capacity of fetal membranes, reduces the effectiveness of interventions to treat fetal abnormalities demonstrating a need to design therapies with clinical potential.

The present study demonstrates that connexin 43 (Cx43) is overexpressed in amniotic membrane (AM) after fetoscopic surgery and artificial *in vitro* trauma. Cx43 was preferentially distributed in mesenchymal cells compared to epithelial cells, with significant expression in the fibroblast layer compared to the epithelial layer. Polarisation of mesenchymal cell nuclei and collagen fibres at the wound edge is also reported. To investigate mechanotransduction AM weakening mechanisms we used an *ex-vivo* bioreactor system to study the effect of cyclic tensile strain. Changes in matrix composition (collagen, elastin and GAG), and pro-inflammatory factors (MMPs and PGE₂) after 24 hours were studied. Cyclic tensile strain significantly increased GAG synthesis and release of MMPs and PGE₂, with an associated reduction of collagen and elastin content, compared to unstrained AM. Furthermore, we demonstrate the reversal of these biochemical changes induced by cyclic tensile strain after AM exposure to pharmacological agents that target the broad group of PI3-kinases and selectively inhibit AKT-1/2 activity. Interestingly, addition of Cx43 and COX-2 inhibiting agents also reversed the biochemical response after cyclic tensile strain. It is suggested that alterations in the ECM composition affects AM integrity and leads to fetal membrane weakening following cyclic tensile strain. Finally, a novel sealing approach based on peptide amphiphile self-assembling gels in the presence of amniotic fluid is developed. By using peptide amphiphiles we were able to seal fetal membrane defects *in vitro*. This innovative approach provides a new avenue for a tissue engineering approach to prevent PPRM.

The results obtained in this study contributes to our understanding on: (1) AM wound healing and repair capacity, the (2) mechanotransduction mechanisms behind AM weakening, and (3) a novel tissue engineering approach to seal fetal membrane defects using self-assembly of peptide amphiphiles for iatrogenic PPRM prevention.

Acknowledgements

Special mention goes to my supervisors, Dr. Tina Chowdhury, Prof. Anna David, and Prof. Alvaro Mata for their continued enthusiasm and support throughout this exciting project. I would like to thank Prof. Jan Deprest and Dr. Alexander Engels for their input on the project and giving me the opportunity to visit their facilities at KU Leuven. I thank Alex for generously hosting me in Belgium. My sincere thanks go to the Fetal Medicine Unit staff at UCLH who assisted in the collection of placentas. I have many remarkable memories being able to observe fetoscopy at UCLH, and open fetal surgery (KU Leuven), all being powerful reminders for the importance of this research. I thank the technical staff at Queen Mary, including Chris Mole, Shafir Iqbal, and Dong Sheng, for providing me with fantastic lab training. I would also like to thank Dr. Alex Virasami and Prof. Neil Sebire for their help with histology. I extend my thanks to Dr. Chris Thrasivoulou, for his training on confocal and multiphoton microscopy, and for sharing his expertise on Cx43. Thanks must be given to Rosetrees Trust medical research charity, the prenatal therapy charity (UCLH), and the Institute of Bioengineering (QMUL) for funding this project. I would like to thank my family for their relentless encouragement and support. Finally, I would like to thank Sarah for supporting me throughout writing this thesis, and life in general.

Table of Contents

Statement of originality	I
Abstract	II
Acknowledgements	III
List of figures	IX
List of abbreviations	XIX
Chapter 1: General Introduction	2
1.1 Fetal membrane embryonic origin and structure.....	2
1.1.1 Embryonic development of the fetal membranes	2
1.1.2 Fetal membrane structure	6
1.2 The zone of altered morphology.....	11
1.2.1 Structural differences in the ZAM	11
1.2.2 Differences in biochemistry of the ZAM	13
1.3 Tissue biomechanics of the fetal membrane	15
1.3.1 Tensile properties of the fetal membrane	15
1.3.2 Amniotic membrane mechanics.....	17
Chapter 2: Physiological and pathological membrane rupture	21
2.1 Normal physiological events of parturition.....	21
2.2 Preterm premature rupture of membranes.....	23
2.2.1 Risk factors of PPRM.....	24
2.2.2 Pathological mechanisms	26
2.3 Iatrogenic preterm premature rupture of the membranes.....	27
2.3.1 Types of fetal surgery.....	27
2.3.2 Fetal surgery effects on the fetal membrane.....	30
2.4 Healing properties of the amniotic membrane	32
2.4 Aims and Objectives	35
Chapter 3: Materials and methods	39
3.1 Patient recruitment and tissue procurement	39
3.1.1 Ethical approval	39
3.1.2 Collection of term fetal membranes after Caesarean section	39
3.1.3 Collection of fetal membranes after fetal surgery	40

3.1.4 Amniotic fluid collection.....	41
3.2 Biochemical analysis of fetal membranes.....	41
3.2.1 Fetal membrane digestion	41
3.2.2 Determining DNA levels.....	41
3.2.3 Determining sulphated glycosaminoglycan content	42
3.2.4 Quantification of collagen levels	43
3.2.5 Determining elastin content.....	45
3.2.6 Determining prostaglandin E ₂ release.....	47
3.2.7 Determining total MMP activity.....	48
3.2.8 Western blotting.....	49
3.2.9 List of antibodies used in this thesis	52
3.3 Measuring gene expression	53
3.3.1 RNA extraction.....	53
3.3.2 RNA isolation and purification.....	53
3.3.3 First strand cDNA synthesis by Reverse Transcription	55
3.3.4 Quantitative real-time PCR	55
3.3.5 Quantitative PCR assay optimisation and data analysis	56
3.4 Determining cell viability	63
3.5 Immunofluorescence confocal microscopy.....	64
3.6 Second-harmonic generation imaging microscopy	67
3.7 Image analysis	67
3.7.1 Immunofluorescence data analysis	67
3.8 Scanning electron microscopy.....	72
3.9 Histological analysis	72
3.9.1 Chemical fixation.....	72
3.9.2 Tissue processing	73
3.9.3 Tissue staining	73
3.10 Statistics	74

Chapter 4: Cx43 is overexpressed in human amniotic membrane defects after fetal surgery and artificial <i>in vitro</i> trauma	77
4.1 Introduction	77
4.1.1 Gap junction structure and function.....	77
4.1.2 Cx43 activation and plaque formation	78

4.1.3 Cx43 activation regulates healing in wounded skin	80
4.1.4 Cx43 and chronic wound healing	81
4.2 Methods.....	83
4.2.1 Fetal membrane used for fetal surgery study.....	83
4.2.2 Fetal membranes used for the <i>in vitro</i> artificial fetoscopic trauma model....	86
4.2.3 Development of artificial <i>in vitro</i> fetal membrane trauma model	87
4.3 Results: Investigation of AM trauma after fetoscopic surgery	89
4.3.1 Scanning electron microscopy of wounded fetal membranes after fetoscopic surgery.....	89
4.3.2 Cell morphological changes in wounded AM after fetoscopic surgery.....	91
4.3.3 Quantification of mesenchymal cell polarisation in the wounded AM after fetoscopic surgery.....	93
4.3.4 Changes in Cx43 and COX-2 gene expression in AM wounds after fetoscopy	94
4.3.5 Changes in Cx43 protein expression in wounded AM after fetoscopic surgery	95
4.3.6 Collagen alignment and intensity in wound edge vs. control regions	98
4.4 Results summary.....	101
4.5 Results: Investigation of AM wounds after <i>in vitro</i> artificial trauma.....	103
4.5.1 Cell morphological and Cx43 changes in AM after trauma.....	103
4.5.2 Collagen alignment in wound edge and control AM after <i>in vitro</i> artificial trauma	106
4.6 Results summary.....	108
4.7 Discussion	110

Chapter 5: Molecular self-assembly of peptide amphiphile membrane macrostructures triggered by amniotic fluid for sealing human fetal membrane defects	116
5.1 Introduction	116
5.1.1 Previous approaches for sealing fetal membrane defects.....	116
5.1.2 Potential peptide amphiphiles for sealing defects in the fetal membranes ..	130
5.1.3 Molecular self-assembly.....	132
5.1.4 Liquid-liquid interfacial systems for a tissue engineering approach	132
5.2 Methods.....	136

5.2.1 Amniotic fluid collection.....	136
5.2.2 Fetal membrane collection	136
5.2.3 PDMS fluidic device fabrication	138
5.2.4 Self-assembly of PA-AF macrostructures.....	139
5.2.5 PA synthesis and purification.....	141
5.2.6 PA subtypes and properties	142
5.2.7 Fluorescently labelled peptide amphiphile self-assembly.....	143
5.2.8 ζ -potential measurement (ζ) for amniotic fluid charge	143
5.3 Results.....	144
5.3.1 Peptide amphiphile – amniotic fluid (PA-AF) systems	145
5.3.2 PAK3-AF self-assembling system: membrane microstructure	150
5.3.3 Self-assembled PAK3-AF membranes for sealing artificial fetal membrane wounds	154
5.3.4 Histological analysis of sealed fetal membrane defects.....	156
5.4 Results summary.....	162
5.5 Discussion	164

Chapter 6: Mechanotransduction mechanisms that induce fetal membrane weakening and tissue damage169

6.1 Introduction	169
6.1.1 Factors associated with fetal membrane weakening.....	169
6.1.2 Mechanotransduction mechanisms in fetal membranes.....	171
6.2 Methods.....	174
6.2.1 Patient recruitment.....	174
6.2.2 Uniaxial cyclic tensile strain loading using the ex-vivo bioreactor system.....	174
6.3 Results.....	182
6.3.1 Understanding fetal membrane weakening mechanisms	182
6.3.2 Targeting pro-inflammatory pathways reduces fetal membrane weakening factors.....	195
6.4 Results summary.....	199
6.5 Discussion	205

Chapter 7: Final Discussion and Future Prospects213

7.1 Cx43 is overexpressed in AM after fetoscopic surgery and artificial in vitro trauma and delays cell migration and repair	213
--	-----

7.2 Development of a new PA-based sealing strategy for human AM repair	214
7.3 Mechanotransduction mechanisms that induce AM weakening and production of inflammatory mediators leading to ECM damage	215
7.4 Implications and future research.....	217
7.4.1 Identification of targets for mechanotransduction and FM weakening	217
7.4.2 Pharmacological strategies for the induction of healing mechanisms and repair of FM defects.....	219
7.4.3 Strategies for sealing the AM using tissue engineering models.....	221
List of publications	222
National and international conference contributions.....	223
List of Awards	225
References.....	228

List of figures

Figure 1.1:	Early fetal membrane development in the first month of gestation after fertilization.	4
Figure 1.2:	Later development of the fetal membrane and fusion of key components including fusion of the separate amnion and chorion layers to form the amniochorion at 12 weeks gestation leading to fusion of the amniochorion with the decidua parietalis lining of the uterine cavity to form the fetal membrane at 15-24 weeks gestation.	5
Figure 1.3:	Schematic representation of the human fetal membrane.	7
Figure 1.4:	Electron micrograph showing the apical side of cuboidal epithelial cells (EC) separated by intercellular canals (ICC) taken from full term amniotic membrane.	8
Figure 1.5:	Hematoxylin and eosin (H&E) staining of term human fetal membrane taken away from the close to the placental disc and from the zone of altered morphology.	12
Figure 1.6:	Comparison of mechanical data obtained from term fetal membranes for failure stress and failure tension following different mechanical testing devices including biaxial inflation, biaxial puncture and uniaxial tension.	17
Figure 1.7:	Variations in collagen fibre organisation in amniotic membrane samples of term fetal membranes imaged using second harmonic generation imaging.	19
Figure 2.1:	Gestational age ranges for preterm and term deliveries.	23
Figure 2.2:	List of major maternal, uteroplacental and fetal PPROM risk factors.	25
Figure 2.3:	Typical 10.0 FR trocar used during fetoscopic surgery.	28

Figure 3.1:	Typical DNA assay standard curve showing the relationship of fluorescence intensity (460 nm) and the fluorimetric dye, Hoechst 33258.	43
Figure 3.2:	Typical DMMB assay standard curve showing the linear relationship of absorbance at 595 nm and the chondroitin sulfate standards.	44
Figure 3.3:	Typical hydroxyproline assay standard curve showing the linear relationship between absorbance (570 nm) and trans-4-Hydroxy-L-proline dye.	46
Figure 3.4:	Typical elastin assay standard curve showing the linear relationship between absorbance (513 nm) and elastin standard.	48
Figure 3.5:	Typical prostaglandin E ₂ assay standard curve showing the relationship between absorbance (450 nm) and PGE ₂ standard based on a forward sequential competitive binding technique.	49
Figure 3.6:	Typical BSA standard curve showing the relationship between absorbance (562 nm) and BSA standard.	51
Figure 3.7:	Amplification plots showing typical before and after amplifications for Cx43 and GAPDH PCR assays following several steps that improved RNA purification, DNA contamination removal prior to first strand cDNA synthesis, and optimisation of primers during the final PCR assay.	59
Figure 3.8:	Standard curve using 100 nM Cx43 primers showing initial copy number of template vs. threshold cycle (Ct).	60
Figure 3.9:	Standard curve using 300 nM COL1A1 primers showing initial copy number of template vs. threshold cycle (Ct).	61
Figure 3.10:	Standard curve using 300 nM GAPDH primers showing initial copy number of template vs. threshold cycle (Ct).	61
Figure 3.11:	Standard curve using 200 nM COX-2 primers showing initial copy number of template vs. threshold cycle (Ct).	62
Figure 3.12:	Melting curve analysis before and after key optimisation steps taken in the design of the PCR protocol.	63

Figure 3.13:	Connexin 43 antibody specificity was determined by staining cervical term amniotic membrane tissue in incubations of primary antibody only secondary antibody only and positive control primary and secondary antibody.	67
Figure 3.14:	Optimal AM imaging parameters for confocal laser scanning immunofluorescence and second harmonic generation microscopy.	69
Figure 3.15:	Key steps in image processing for nuclei count within epithelial and fibroblast layer of the amniotic membrane using ImageJ software.	71
Figure 3.16:	Key steps in image processing for Cx43 plaque count within epithelial and fibroblast layer of the amniotic membrane using ImageJ software.	72
Figure 4.1:	Schematic of gap junctional plaque and connexin structure.	80
Figure 4.2:	Reasons for fetoscopic surgery shown as a percentage.	86
Figure 4.3:	Indication for caesarean section shown as a percentage.	88
Figure 4.4:	Electron micrograph of the fetal membrane wound following fetoscopic surgery.	92
Figure 4.5:	Immunofluorescence confocal laser scanning microscopy of human amniotic membrane fetoscopic defects and representative control region with nuclear staining using DAPI.	94
Figure 4.6:	Quantification of mesenchymal cell nuclei morphology at the wound edge (<100 μ m from wound margin) and control (>5 cm from wound edge) in amniotic membrane following fetoscopic surgery.	95
Figure 4.7:	Gene expression fold change for Cx43 (GJA1), COX-2, and COL1A1 with y-axis presented as logarithmic scale.	96
Figure 4.8:	Human amniotic membrane fetoscopy patient Cx43 staining at wound edge (WE) and control regions.	98
Figure 4.9:	Cx43 protein quantification per area and per cell nuclei.	99

Figure 4.10:	Second harmonic generation signal intensity in wound edge and control specimens across full thickness samples approximately 425 μm^2 and mean SHG intensities.	101
Figure 4.11:	Second harmonic generation imaging analysis of collagen density SHG signal intensity in wound edge amniotic membrane compared to control.	102
Figure 4.12:	Immunofluorescence confocal laser scanning microscopy of nuclei morphology and Cx43 protein expression.	106
Figure 4.13:	Cx43 protein quantification per area (0.5 mm^2) and per nuclei following in vitro trauma of human amniotic membrane.	107
Figure 4.14:	Second harmonic generation imaging analysis of collagen alignment in wound edge amniotic membrane compared to control following in vitro trauma.	109
Figure 5.1:	Peptide amphiphiles are composed of three key regions including the hydrophobic alkyl tail, the β -sheet forming peptide domain, and the charged amino acid group domain.	132
Figure 5.2:	Peptide amphiphile gels and biomedical applications.	137
Figure 5.3:	Indication for caesarean section shown as a percentage.	138
Figure 5.4:	Fabrication of PDMS channels for investigating formation of self-assembling membranes between amniotic fluid and peptide amphiphile solutions.	139
Figure 5.5:	Methods used to test the self-assembly of macrostructures at the amniotic fluid and peptide amphiphile interface.	140
Figure 5.6:	Confirmation of negatively charged amniotic fluid suspensions and presence of highly negatively charged long unbranched polysaccharide glycosaminoglycans.	145
Figure 5.7:	Peptide amphiphile and amniotic fluid macrostructure self-assembly.	147

Figure 5.8: Formation of self-assembling membranes at the PAK3-AF interface using PDMS channels as a fluidic device. 148

Figure 5.9:	Direction of PA-AF system membrane self-assembly and stages of gel formation.	150
Figure 5.10:	Electron micrographs of PAK3-AF system following injection of PAK3 aqueous solution into AF.	152
Figure 5.11:	Electron micrographs of PAK3-AF system formed within the PDMS fluidic device.	153
Figure 5.12:	Sealing of fetal membrane defects using the PAK3-AF system in the artificial fetal membrane trauma model.	154
Figure 5.13:	Electron micrographs of fetal membrane defects sealed using the PAK3-AF system using the artificial fetal membrane trauma model.	155
Figure 5.14:	Cross-sectional histological H&E staining of the human fetal membrane showing clearly the amniotic membrane (AM) and chorionic membrane (CM) layers, and the non-healing nature of the fetal membrane wound.	156
Figure 5.15:	Histological analysis of fetal membrane explants and PAK3-AF plug.	158
Figure 5.16:	Fetal membrane cytotoxicity testing of peptide amphiphile subtypes.	160
Figure 6.1:	List of reported fetal membrane weakening factors	169
Figure 6.2:	Types of in vitro mechanical testing devices used for studying biomechanics and fetal membrane weakening pathways.	172
Figure 6.3:	Cell viability analysis performed for mechanotransduction studies in both CAM and PAM tissue regions.	174
Figure 6.4:	Method of fetal membrane dissection.	175

Figure 6.5:	Second harmonic generation imaging microscopy of CAM and PAM specimens.	176
Figure 6.6:	Equipment used to assemble individual BOSE chambers and assembly of BOSE chamber containing amniotic membrane clamped between the movable upper grip and stationary bottom grip.	179
Figure 6.7:	Bose chamber system with individual chambers containing dissected AM tissue undergoing cyclic tensile strain.	180
Figure 6.8:	The effect cyclic tensile strain (CTS) on cervical (CAM) and placental (PAM) amniotic membrane sulfated glycosaminoglycan content.	182
Figure 6.9:	The effect cyclic tensile strain on cervical (CAM) and placental (PAM) amniotic membrane hydroxyproline (collagen) content.	183
Figure 6.10:	The effect cyclic tensile strain on cervical (CAM) and placental (PAM) amniotic membrane elastin content.	184
Figure 6.11:	The effect cyclic tensile strain on cervical (CAM) and placental (PAM) amniotic membrane prostaglandin E ₂ release.	185
Figure 6.12:	The effect cyclic tensile strain on cervical (CAM) and placental (PAM) amniotic membrane total MMP activity (RFU).	186
Figure 6.13:	Activation and inhibition and AKT-1/2/3 protein expression.	187
Figure 6.14:	Activation and inhibition and Cx43 protein expression.	188
Figure 6.15:	The effect cyclic tensile strain and inhibition of AKT on cervical (CAM) and placental (PAM) amniotic membrane GAG, collagen, and elastin production; and release of PGE ₂ and total MMP.	191
Figure 6.16:	The effect cyclic tensile strain and inhibition of Cx43 on cervical (CAM) and placental (PAM) amniotic membrane GAG, collagen, and elastin production; and release of PGE ₂ and total MMP.	192

Figure 6.17:	The effect cyclic tensile strain and inhibition of PI3-kinase on cervical (CAM) and placental (PAM) amniotic membrane GAG, collagen, and elastin production; and release of PGE ₂ and total MMP.	195
Figure 6.18:	The effect cyclic tensile strain and inhibition of cyclooxygenase-2 on cervical (CAM) and placental (PAM) amniotic membrane GAG, collagen, and elastin production; and release of PGE ₂ and total MMP.	196
Figure 6.19:	Putative flow of major events that could lead to fetal membrane rupture in response to stretch and activation of stretch-activated proteins (SAPs).	206
Figure 6.20:	Synergy of events that lead to fetal membrane rupture following activation of stretch-activated inflammatory pathways.	209

List of Tables

Table 1.1:	Thickness of fetal membrane layers reported in literature.	12
Table 1.2:	Key changes reported that lead to alterations in the biochemistry of the zone of altered morphology in preparation for parturition.	14
Table 2.1:	Fetal complications and respective fetal surgery procedures.	29
Table 2.2:	Key in vivo studies on fetal membrane healing in different species.	33
Table 3.1:	Details of primary and secondary antibodies used in this study.	53
Table 3.2:	Thermocycling conditions for quantitative polymerase chain reaction.	57
Table 3.3:	Forward and reverse gene sequences with optimal concentrations and correlating reaction efficiency values.	58
Table 4.1:	Clinical information for patients undergoing laser ablation therapy.	87
Table 5.1:	Fibrin-based strategies for sealing fetal membrane defects (chronologically arranged).	121-122
Table 5.2:	Gelatin and collagen based PPRM sealing strategies.	124

Table 5.3:	Collagen and gelatin plug strategies for prevention of iPPROM.	126-127
Table 5.4:	Other strategies for sealing fetal membrane defects for prevention of iPPROM.	128
Table 5.5:	Bioinspired tissue adhesive strategies for sealing fetal membrane defects.	130
Table 5.6:	The molecular details of the peptide amphiphiles used in this thesis.	143-144
Table 6.1:	Overall response to repetitive cyclic tensile strain of the human amniotic membrane given as a percentage change for GAG, collagen, elastin, PGE ₂ and total MMP activity.	198
Table 6.2:	Overall summary for AKTi treated human amniotic membrane tissue with patient-matched controls following cyclic tensile strain.	199
Table 6.3:	Overall summary for Cx43asODN treated human amniotic membrane tissue with patient-matched controls following cyclic tensile strain.	200
Table 6.4:	Overall summary for wortmannin treated human amniotic membrane tissue with patient-matched controls following cyclic tensile strain.	201
Table 6.5:	Overall summary for NS-398 treated human amniotic membrane tissue with patient-matched controls following cyclic tensile strain.	202

List of abbreviations

AF – Amniotic fluid
AKT – Protein kinase B
AM – Amniotic membrane/amnion
CAM – cervical amniotic membrane
CM – Chorionic membrane/chorion
COX-2 – Cyclooxygenase-2
CTS – cyclic tensile strain
Cx43 – Connexin 43
Cx43asODNs – Cx43 antisense oligodeoxynucleotides
dH₂O – Distilled water
DMEM – Dulbecco's Modified Eagles Medium
DMSO – Dimethyl Sulfoxide
DNA – Deoxyribonucleic Acid
DNase - Deoxyribonuclease
dNTP – Deoxynucleotide Triphosphates
ECM – extracellular matrix
FBS – Fetal bovine serum
FITC – Fluorescien Isothiocyanate
FM – Fetal membrane
GAG - glycosaminoglycan
HCl – Hydrogen Chloride
IMF – Immunofluorescence
iPPROM – iatrogenic PPROM
kDa – Kilodalton
MMP – Matrix metalloproteinase
mRNA – Messenger ribonucleic acid
PAGE – Polyacrylamide gel electrophoresis
PA – Peptide amphiphile
PAE – PA with glutamic acid residue
PAK – PA with lysine residue
PAM – placental amniotic membrane
PBS – Phosphate-buffered saline

PCR – Polymerase chain reaction
PFA – Paraformaldehyde
PGE₂ – Prostaglandin E₂
PI3K – Phosphoinositide 3-kinase
PKB – Protein Kinase B
PROM – Premature rupture of membranes
PPROM – Preterm premature rupture of membranes
RNA – Ribonucleic Acid
ROM – Rupture of membranes
RT – Reverse transcription
SDS – Sodium dodecyl sulphate
sGAG – sulfated glycosaminoglycan
SHG – Second harmonic generation
sPPROM – Spontaneous PPRM
siRNA – Small interfering ribonucleic acid
TTTS – Twin-to-twin transfusion syndrome
UPW – Ultrapure water
WTM - Wortmannin
ZAM – Zone of altered morphology

Chapter 1

General Introduction

Chapter 1: General Introduction

Preterm birth incidence is increasing regardless of advances in prenatal care, management, and diagnostics. The UK has one of the highest preterm birth rates with 8% of births occurring before 37 weeks, amounting to 60,000 preterm deliveries annually; and remains the leading cause of death for infants under 5. Globally, there are 15 million cases of preterm deliveries, equating to 1 in 10 births, with an estimated 1 million being stillborn every year. Preterm premature rupture of membranes (PPROM) complicates 40% of preterm births, which often result in lifelong disabilities involving respiratory, cardiac and neurological disorders. PPRM can result from uterine infection, distension of the uterus and fetal membrane, and vaginal bleeding. However, the cause is unclear and the pathological mechanisms leading to membrane rupture are not well understood. Furthermore, Iatrogenic PPRM is a major complication after invasive fetal interventions and occurs in 6-45% of cases. Previous research has shown that the human fetal membranes do not heal after spontaneous or iatrogenic rupture. The high prevalence of iatrogenic PPRM after fetal surgery reduces the effectiveness of interventions to treat fetal abnormalities demonstrating a need to design therapies with clinical potential.

1.1 Fetal membrane embryonic origin and structure

The amniochorion consists of the amniotic and chorionic membranes, which completely fuse at approximately 15-17 weeks gestation and loosely attach to the decidua parietalis of the uterine cavity. Following delivery, the tissues are collectively termed the fetal membranes. To understand the complex structure of the fetal membranes, it is important to first understand their embryonic development.

1.1.1 Embryonic development of the fetal membranes

The placenta and fetal membrane tissues are crucial for normal embryonic development. The fetal membranes form a membranous sac that contains amniotic fluid and protects the fetus from infection during fetal development. The placenta is a feto-maternal organ, having a maternal (Decidua basalis) portion formed from the tissue of the uterine wall and uterine circulation, and a fetal (Chorion frondosum) portion that develops from the

blastocyst during early embryogenesis. The placenta is responsible for transporting nutrients and oxygen to the fetus and removing waste products through the maternal blood supply, whilst also secreting amongst other proteins human chorionic gonadotropin, progesterone and oestrogen hormones to maintain a healthy pregnancy.

The amnion and chorion loosely fuse to form the amniochorion at approximately 15-17 weeks gestation when sufficient fluid accumulation in the amniotic cavity causes its expansion. After fertilisation (day 1), typically in the upper region of the oviduct, cleavage occurs (day 2) as the zygote travels to the uterus. This involves continued mitotic divisions to form a morula of 16-32 cells (day 3-4). Differentiation of inner cells leads to the formation of a blastula, which comprises a surface layer of trophoblast cells surrounding a blastocoele (fluid-filled sac) and an inner-cell mass at day 5-7 (**Figure 1.1**). Implantation typically occurs at day 7 when the blastocyst adheres to the endometrium that lines the uterus and trophoblast cells begin to invade the maternal tissue. Continued differentiation leads to the inner cell mass of the blastocyst assembling to form the bilaminar disc, containing the epiblast and hypoblast cell layers (**Figure 1.1**). The epiblast layer, which forms shortly after implantation, helps form the inner surface of the amniotic cavity lined with amniotic ectodermal cells.

Typically, towards the end of the third week, gastrulation occurs which is the process by which the bilaminar disc is converted into the trilaminar disc, which comprises three germ layers: the ectoderm, mesoderm, and endoderm (day 12, **Figure 1.1**). During the gastrulation period, which involves mesoderm spreading (day 18) and enlargement of the amniotic sac (day 23), the primitive streak, notochord and prechordal plate all begin formation and are responsible for the development of the embryo (**Figure 1.1**). The mesoderm, which is derived from the hypoblast layer of the bilaminar disc, is responsible for formation of the amniotic fibroblast layer at approximately day 12 of gestation (**Figure 1.1**). The trophoblast and extraembryonic mesoderm (**Figure 1.2a**) are responsible for the formation of the chorionic sac and chorionic villi, and the chorion that later completely adheres to the amnion to form the amniochorion at approximately 15-17 weeks is derived from the somatic mesoderm and is termed the smooth chorion (chorion laeve). Microvilli initially cover the entirety of the chorionic sac, which develops into the chorionic frondosum (**Figure 1.2b**). However, after the early stages of development at

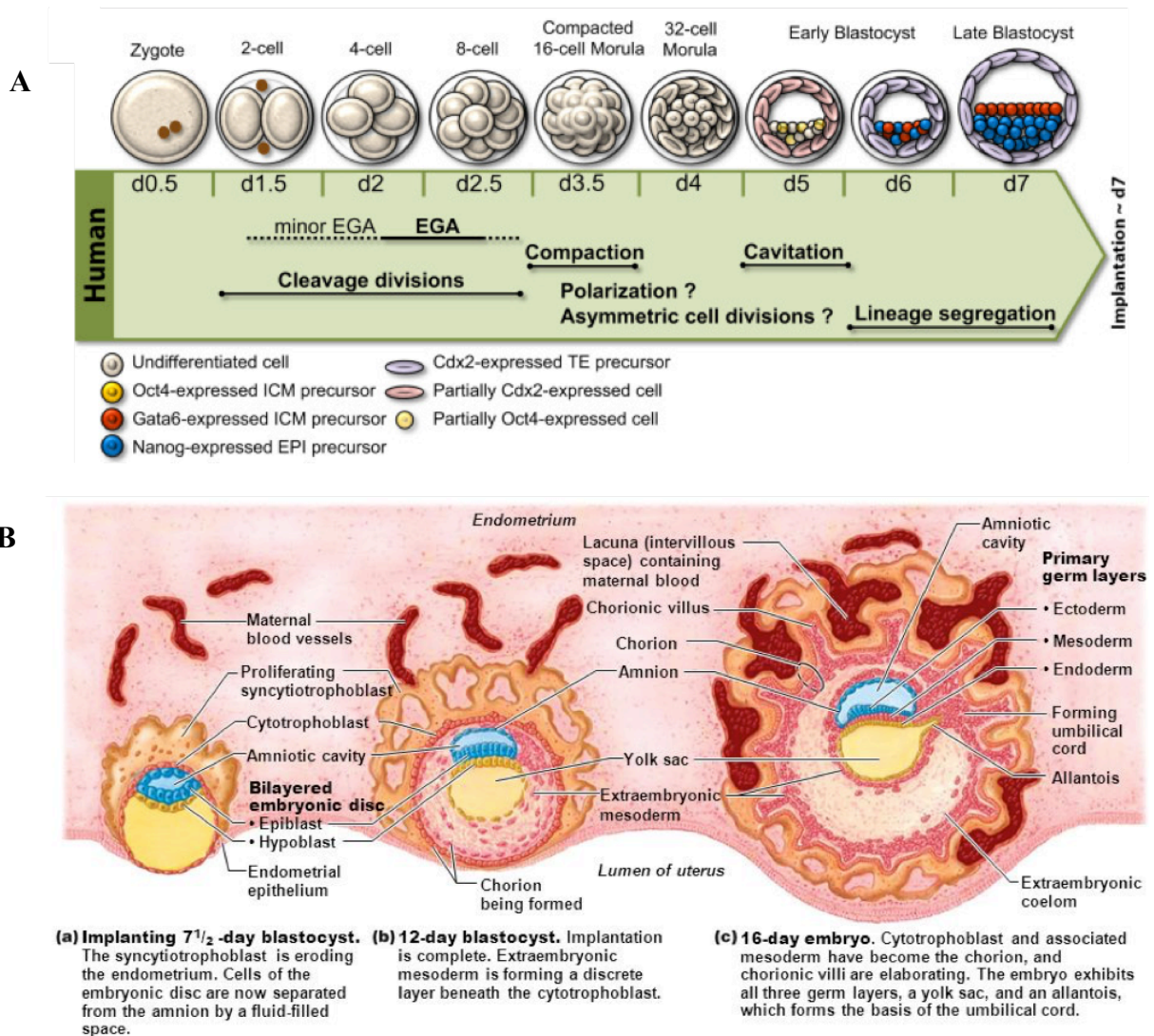


Figure 1.1: Early fetal membrane development in the first month of gestation after fertilization. The ectoderm layer of the trilaminar disc is responsible for the formation of the amniotic epithelial layer, which is in contact with the amniotic fluid throughout gestation. The mesoderm derived from the hypoblast layer of the trilaminar disc is responsible for the fibroblast layer of the amniotic membrane. Adapted from Sozen et al., (2014)²; Marieb & Hoehn (2013)⁷.

approximately 8 weeks the microvilli in close proximity to the decidua capsularis begin to regress forming the chorion laeve that later forms the outer layer of the amniochorion (smooth chorion, **Figure 1.2b**). The remaining section of the chorionic sac which contains microvilli (villous chorion, **Figure 1.2b-c**) will form an integral part of the placenta. Between approximately 15-24 weeks the amniotic cavity expands due to an increasing volume of amniotic fluid which leads to the fusing of the amniochorion and decidua

Stages of fetal membrane fusion

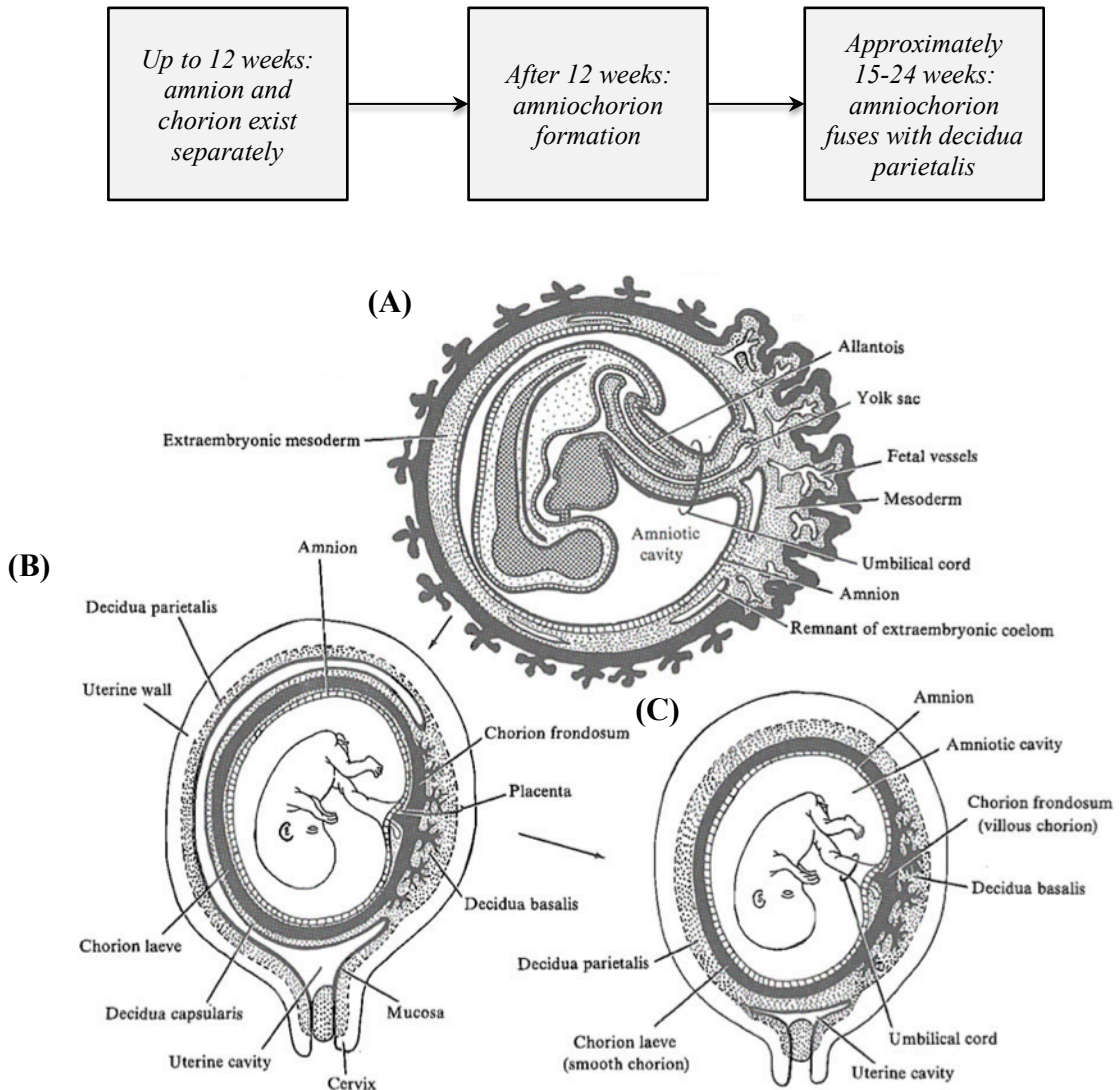


Figure 1.2: Later development of the fetal membrane and fusion of key components including fusion of the separate amnion and chorion layers to form the amniochorion at 12 weeks gestation leading to fusion of the amniochorion with the decidua parietalis lining of the uterine cavity to form the fetal membrane at 15-24 weeks gestation. Adapted from Pansky (1982)⁶.

parietalis (**Figure 1.2c**). The fetal membranes expelled after delivery of the fetus will be comprised of the amniochorion adhered to a layer of decidua parietalis.

1.1.2 Fetal membrane structure

The fetal membrane is divided into two key membranes: the (1) innermost amniotic membrane (amnion) that is in contact with the amniotic fluid, and the (2) outermost chorionic membrane (chorion) that adheres to the amnion and the underlying decidua (**Figure 1.3**). The nomenclature of the fetal membranes has remained mostly consistent since the first detailed reviews between 1960 and 1966¹⁹⁻²¹. Herein, it was clear that the amniotic membrane consisted of five layers: (1) epithelial layer, (2) basement membrane, (3) compact layer, (4) fibroblast layer, and (5) spongy layer. More recently, the spongy layer has been used interchangeably with intermediate layer^{3,22-25}. The spongy layer connects the amniotic membrane to the chorionic membrane, which has four distinct layers: (1) the cellular layer, (2) reticular layer, (3) pseudo-basement membrane, and (4) trophoblast layer.

It is important to note that the thickness of fetal membranes can change depending on species, region and gestational age. Total thickness is reported to vary between 0.5 – 1.5 mm, and thickness reported to decrease to approximately 0.5 mm in term fetal membrane compared to preterm²⁶⁻²⁸. In term tissue, the amnion is shown to swell whilst the chorion and decidua reduce in thickness, most prominently in the region overlying the cervix, termed the para-cervical weak zone, or more recently referred to as the zone of altered morphology (ZAM, see **section 1.2**: The zone of altered morphology)²⁹⁻³³. When compared to fetal membrane examined closer to the placental disc, the ZAM displays the most notable gestational-dependent morphological differences where the connective tissue layers reduce in thickness towards term gestation in order to prepare for parturition^{30,34,35}.

Importantly, the decrease in fetal membrane thickness over gestation can concomitantly reduce stiffness from approximately 8.84 MPa at 15 weeks to 2.29 MPa at 40 weeks³⁶. Indeed, researchers are examining whether fetal membrane thickness can be used to predict preterm premature rupture of membranes^{27,37}. Therefore, it is necessary to consider this variation in fetal membrane morphology when examining the overall structure.

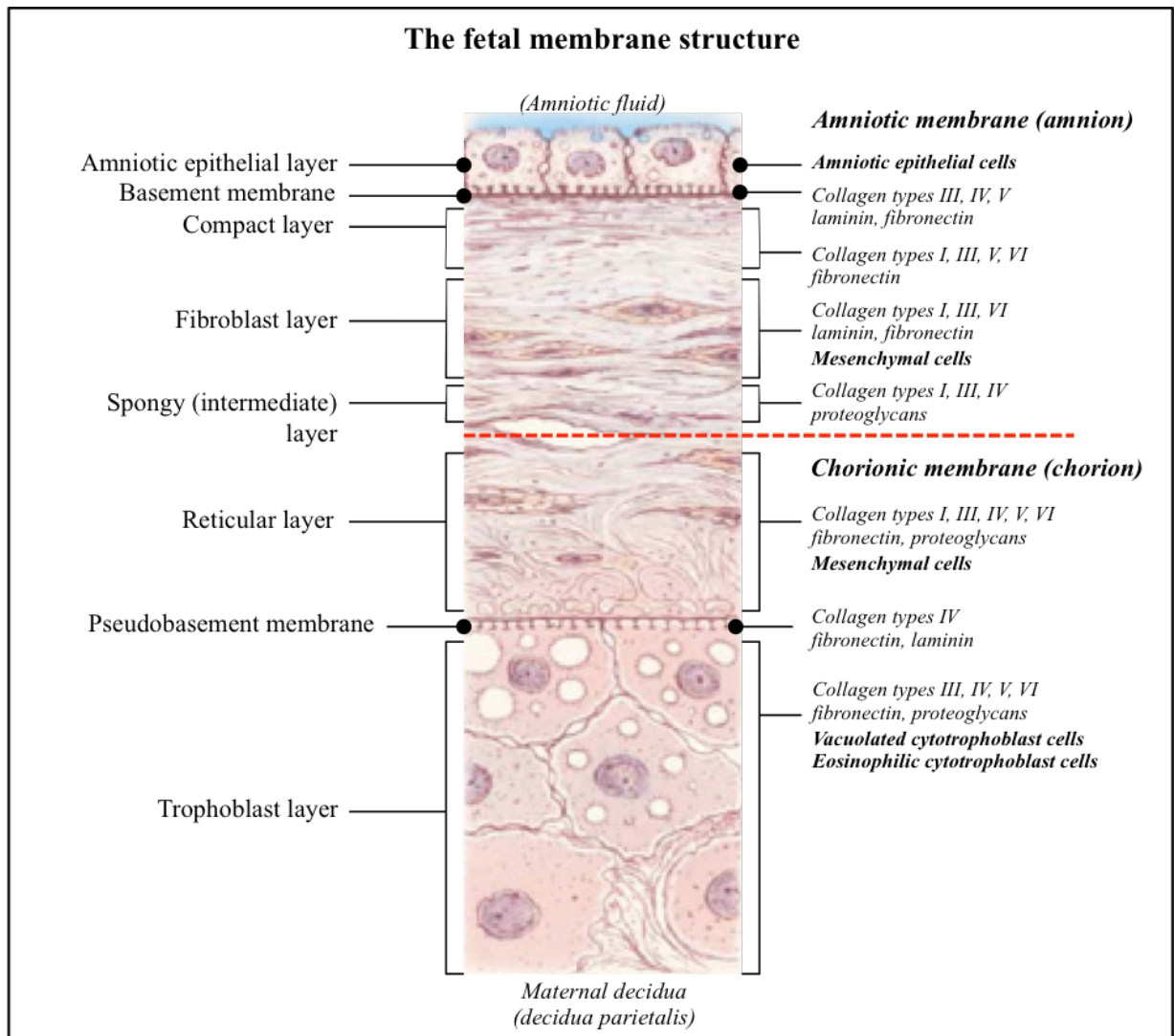


Figure 1.3: Schematic representation of the human fetal membrane. The key layers of the amnion are the epithelial layer, basement membrane, compact layer, fibroblast layer, and spongy (intermediate) layer. The key layers of the chorion are the reticular layer, pseudobasement membrane, and trophoblast layer. The innermost layer is the amniotic epithelial layer of the amnion that is in contact with the amniotic fluid throughout pregnancy and the outermost layer is the trophoblast layer of the chorion that adheres to the maternal decidua. The main extracellular matrix components and cell populations of each layer are indicated on the right. The red line indicates the separation between the amnion and chorion. Adapted from Parry & Strauss (1998)¹².

The amniotic epithelial layer

The amniotic epithelial layer mainly contains a single layer of cuboidal epithelial cells and a small amount of columnar cells that have been identified in the amniotic epithelial layer overlying the placenta²⁰. The cuboidal cells are covered in microvilli that protrude on the apical and lateral surface into the amniotic fluid forming a brush border membrane (**Figure 1.4**). They are tightly connected via intercellular desmosomes with intercellular canals (ICC) found between adjacent cells. The basal part of these cells forms basal processes that associate with the underlying basement membrane.

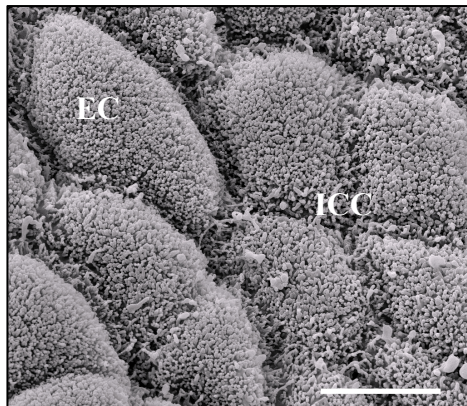


Figure 1.4: Electron micrograph showing the apical side of cuboidal epithelial cells (EC) separated by intercellular canals (ICC) taken from full term amniotic membrane. The microvilli that protrude from the epithelial cells into the amniotic fluid can be seen clearly. The photo was taken using a scanning electron microscope. Unpublished image taken by David Barrett. Scale bar: 10 μm .

The basement membrane

The amniotic basement membrane is a thin layer composed of collagen types III, IV and V. The apical surface of the basement membrane shares complex interactions with the basal surface of the amniotic epithelial cells via similar interlinking processes. Other extracellular matrix proteins in the basement membrane found in high abundance include laminin, which interacts with collagen type IV via nidogen and fibronectin proteins, known to influence cell differentiation, migration and adhesion.

The compact layer

This is a highly dense and acellular layer connected to the basement membrane by a fibrillar network containing mainly collagen type V. This layer provides the majority of amniotic membrane strength with stiffness values ranging from 9.14 ± 2.51 N/cm to 14.47 ± 3.38 N/cm³⁰. The compact layer contains fibronectin and a dense meshwork of collagen fibres consisting of collagen types I, III, V, and VI.

The presence of elastin has also been reported in the compact layer^{38,39}. However, there is dispute in the literature regarding these findings, with some groups unable to detect elastin levels in fetal membranes at all⁴⁰. More recently, resorcin fuchsin staining demonstrated a faint band of elastin in the compact layer of the amniotic membrane³. It is suggested that the difficulty in demonstrating elastin presence in fetal membranes could be due to the elastin diameter, reported to be $0.016 \mu\text{m}$ (0.08% dry weight), which is roughly 1% of that typically found in the aorta at a diameter of $1\text{-}2.5 \mu\text{m}$ (51.2% dry weight)^{39,41}.

The fibroblast layer

The fibroblast layer is much thicker and contains mainly collagen types I, III and VI arranged in a disorganised network. Laminin and fibronectin are also found in high abundance. This layer contains mesenchymal cells, which are morphologically fibroblastic and produce collagen in the stromal layers^{20,42}. Other fetal cell types have been reported including macrophages and dendritic cells of the immune system, which have been reported to show phagocytic activity^{20,43,44}. Elastin presence has also been detected in this layer^{39,40}.

The spongy layer

The spongy layer is used interchangeably with intermediate layer, and its organisation is highly variable throughout the fetal membrane regions and between patients. It is this layer that connects the amnion to the chorion forming a compressed tissue comprised mainly of collagen types I, III and IV. The layer is also highly concentrated in proteoglycans, which covalently bind to glycosaminoglycans (GAGs), a highly polar

polysaccharide that attracts water molecules and gives this layer its viscous texture^{20,42}. The spongy layer partly accounts for increase in amnion thickness found in patients with preterm premature rupture of membranes (PPROM)³² and the swelling identified in the amnion overlying the cervix in healthy full-term membranes compared to the mid-zone amnion region²⁹.

The cellular layer

The cellular layer is the first layer of the chorion adjacent to the spongy layer of the amnion. Studies of the cellular layer have been problematic due to it often being absent when imaged microscopically in term fetal membrane yet more recognisable in preterm tissue²⁰. This layer is reported to be a single layer thick of trophoblast cells²³.

The reticular layer

This is the thickest of the chorion layers and contains collagen types I, III, IV, V, and VI. It has also been reported to contain fibronectin and proteoglycans⁴⁵. The cells in the reticular layer have been described classically as fibroblasts, although more recently mesenchymal cells have been the preferred terminology with several studies showing the successful isolation of mesenchymal cells from the chorionic reticular layer^{46,47}. A high abundance of macrophages has also been reported^{20,42}.

Pseudo-basement membrane

This is the basement membrane of the trophoblast layer and contains mainly collagen type IV, fibronectin, and laminin^{42,45}.

Trophoblast layer

This is the final layer of the chorionic membrane, which adheres to the maternal decidua. It is often referred to as the cytotrophoblast layer and reported to be 2-10 trophoblast cells deep²⁰. It is also considered the epithelial layer of the chorion. There are two separate cell populations, the vacuolated cells adjacent to the pseudo-basement membrane and the eosinophilic cytotrophoblast cells, adjacent to the maternal decidua. The cells close to the

apical side of this layer, the eosinophilic cytotrophoblast cells, are said to be interwoven with collagen types III, IV, V, and VI^{20,48}. After delivery, the trophoblast layer often adheres to a thin layer of the decidua parietalis (maternal decidua), which contains blood vessels, decidual cells, and macrophages^{28,44,49}.

1.2 The zone of altered morphology

The human fetal membrane is programmed to rupture at term between 37 and 42 weeks. In preparation for parturition, the extracellular matrix (ECM) undergoes a remodelling process that results in morphological changes at the membrane adjacent to the cervix, termed the para-cervical weak zone or more commonly the zone of altered morphology (ZAM)^{29,30,32,34,50-54}.

1.2.1 Structural differences in the ZAM

Fetal membrane layer thickness can vary depending on region (**Table 1.1**). In term fetal membrane, at the ZAM region, the amnion is reported to swell whilst the choriodecidua reduces in thickness; compared to membrane studied adjacent to the placental disc, away from the cervical region^{29,30}. At delivery, the decidual layer overlying the cervix has been measured at $56.6 \pm 44.4 \mu\text{m}$ compared to thicker decidual layer measurements closer to the placental disc of approximately $121.7 \pm 29.8 \mu\text{m}$. Interestingly, the total thickness of the fetal membranes, including the amniochorion and maternal decidua, was reported to be thinner in the ZAM at $191 \pm 54 \mu\text{m}$ compared to $233 \pm 54 \mu\text{m}$ in regions away from the ZAM. However, when considering the amniochorion alone, the thickness was greater in the ZAM at $136 \pm 23 \mu\text{m}$, compared to regions away from the ZAM, due to the swelling that is observed in the amnion towards term, likely to be a result of the amnion preparing to rupture prior to parturition³⁰.

The swelling of the amnion has been reported to occur in the spongy (intermediate) layer that connects the amnion with the chorion, whilst there is a reduced thickness in the cellular layers, specifically in the trophoblast layer of the chorion^{29,32,46}. More recently, second harmonic imaging microscopy of collagen fibres demonstrated that the connective tissue layers are thicker in the ZAM ($367 \pm 100 \mu\text{m}$) compared to regions of membrane

measured away from the ZAM ($249 \pm 81 \mu\text{m}$), later confirmed following histological studies (**Figure 1.5**)³.

Table 1.1: Thickness of fetal membrane layers reported in literature. There are inconsistencies between research groups, although it is clear that the fetal membrane (amnion and chorion) reduces in total thickness towards the ZAM. Whilst the amnion layer may swell at the ZAM, this is negated by the dramatic decrease in the cell-dense chorion layer.

Layer	ZAM (cervical)	Away from ZAM (placental)
Decidual layer	$56.6 \pm 44.4 \mu\text{m}$	$121.7 \pm 29.8 \mu\text{m}$
Total fetal membrane	$191 \pm 54 \mu\text{m}$	$233 \pm 54 \mu\text{m}$
Amniochorion	$367 \pm 100 \mu\text{m}$	$249 \pm 81 \mu\text{m}$

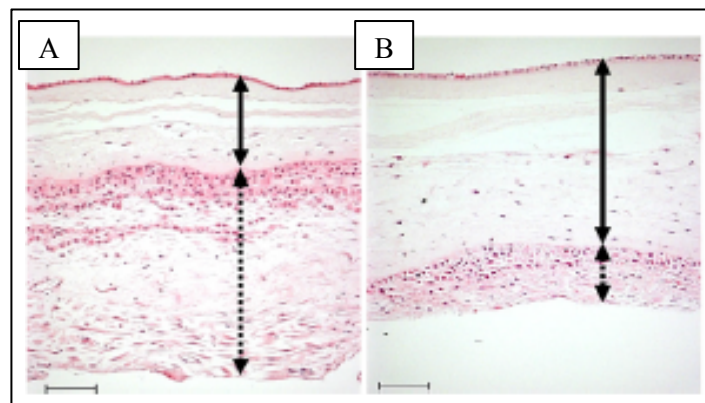


Figure 1.5: Hematoxylin and eosine (H&E) staining of term human fetal membrane taken away from the placental disc (A, away from the zone of altered morphology) and from the zone of altered morphology (B). Continuous arrows show the increase in stromal layers of the fetal membrane in ZAM due to swelling, and the dotted arrows show the decrease in cellular layer thickness in the ZAM, likely associated with increased apoptotic activity. Scale bar: $100 \mu\text{m}$. Adapted from Mauri et al., (2013)³.

1.2.2 Differences in biochemistry of the ZAM

The morphological changes observed in the ZAM have been linked to changes in biochemical factors that influence connective tissue integrity and cell viability (**Table 1.2**)³². Enzymes involved in extracellular matrix degradation include matrix metalloproteases (MMPs) and elastases, which degrade collagen and elastin. In several reports, MMP-9 is shown to increase with labour, whilst MMP inhibitor-3 (TIMP-3) is found in lower concentrations in the ZAM of term fetal membrane^{52,53,55}. Increased Poly (ADP-ribose) polymerase (PARP) cleavage has also been reported in the ZAM, indicating an increase in apoptotic activity, compared to regions away from the ZAM^{30,53,56}. Furthermore, in animal models it has also been reported that structural weakening of the fetal membrane occurs over the cervical region due to breakdown of collagen and remodelling of the connective tissue layers, and apoptosis⁵⁷⁻⁵⁹.

Changes in proteoglycan concentration have also been reported⁶⁰. Specifically, biglycan concentration in the amnion of the ZAM region was 40% lower compared to mid-zone amnion prior to labour. However, at delivery the ZAM amnion biglycan content increased 2-fold along with a 50% reduction in decorin concentration⁶⁰. Biglycan is known to disrupt collagen organisation, whereas decorin acts to stabilise collagen.

Previous studies in ZAM show increased translocation of NFκB, which enhances production of pro-inflammatory gene expression⁶¹⁻⁶³. Mitogen-activated protein kinases (MAPKs) are well known serine/threonine protein kinases that induce catabolic signalling in ZAM associated with the pro-inflammatory and apoptotic cascades⁶⁴. Other transcription factor proteins associated with induction of apoptosis have been reported and include FOXO1, FOXO3, FOXO4, and AP-1, known to trigger apoptosis through activation of BIM (Bcl-2-like protein 11) and PUMA (p53 upregulated modulator of apoptosis) proteins⁶⁵⁻⁶⁸. Increases in oxidative stress in the ZAM have also been reported⁶⁹.

Table 1.2: Key changes reported to increase tissue weakening in the zone of altered morphology in preparation for parturition.

Factor	Key findings	Study
MMP-9 TIMP-3	Increased extracellular matrix degradation leading to reduction in collagen content.	McLaren <i>et al.</i> , (2000) ⁵⁵ McLaren <i>et al.</i> , (2000) ⁵³ McParland <i>et al.</i> , (2003) ⁵²
Biglycan Decorin	Corresponded with a 30% decrease in collagen in the cervical amnion compared to mid-zone amnion after delivery.	Meinert <i>et al.</i> , (2007) ⁶⁰
NFκB	Increased NFκB expression corresponded with increase transcriptional cofactor proteins (CBP) and p300, suggested to lead to increased apoptosis and MMP synthesis associated with the ZAM.	Reti <i>et al.</i> , (2007) ⁶¹ Lappas <i>et al.</i> , (2002) ⁶² Lappas <i>et al.</i> , (2008) ⁶³
FOXO1 FOXO3 FOXO4	Increase in these transcription factors trigger apoptosis via Bcl-2-like protein 11 and p53 upregulated modulator of apoptosis proteins.	Lappas <i>et al.</i> , (2009) ⁶⁷ Lappas <i>et al.</i> , (2010) ⁶⁸
PARP	Associated with increased cellular apoptosis.	McLaren <i>et al.</i> , (1999) ⁵⁶
MAPK AP-1	Increase associated with activation of pro-inflammatory cytokines and induction of apoptosis	Lappas <i>et al.</i> , (2011) ⁶⁴
Oxidative stress	Oxidative stress augmented IL-1B induction of MMP-9 expression.	Chai <i>et al.</i> , (2012) ⁶⁹

1.3 Tissue biomechanics of the fetal membrane

Understanding etiology and developing future treatment and preventatives for PPRM requires an understanding of how the structure of fetal membrane tissue relates to the tissue mechanical properties. Simple clinical observation of the fetal membrane at delivery, and during separation of the amnion from the chorion, gives the impression that the amnion is the strongest of the layers compared to the chorion. Indeed, uniaxial mechanical tests demonstrate the amnion to be the stronger of the two layers⁷⁰. However, more recently, groups have moved towards the use of biaxial loading conditions, which better mimics the *in vivo* conditions when exposed to the pressure exerted from the amniotic fluid^{16,71-75}.

1.3.1 Tensile properties of the fetal membrane

The fetal membrane can withstand high pressure; and the amnion, even though much thinner than the chorion, has been shown to have the greater tensile strength, likely owing to the organisation of collagen and elastin fibres of the compact and fibroblast layers⁷⁶. Average thickness of the amnion is 44 μm compared to the chorion at 188 μm ³⁶. In order to test the mechanical behaviour, methods were developed in the 1960s to test whole membranes, and also more recently to test the amnion alone^{16,77-80}. Interestingly, the amnion alone was discovered to have sufficient tensile strength required for a successful pregnancy⁷⁶. Furthermore, the tensile strength can vary and has been shown to decrease with gestation²⁸. Following preterm premature rupture of membranes, the amnion has greater tensile strength compared to term tissue⁸¹. Overall, fetal membrane stiffness was reported to be 8.84 MPa at 15 weeks gestation, reducing to 2.29 MPa at 40 weeks of gestation³⁶.

The tensile strength of the fetal membrane over gestation (17-41 weeks) has also been compared with commercially available products⁷⁴. The data suggest an increase in tensile strength occurring between 17-20 weeks, after which it is maintained until decreasing at approximately 38-39 weeks. The reduction in tensile strength was also independent of labour, suggesting an important relationship between the biochemical composition and tensile properties of the fetal membrane. Tensile strength was measured using a probe

that exposed the fetal membrane at a specific point, demonstrating tensile strength as grams to burst and deflection at rupture. From 20-38 weeks, peak force to burst averaged 3.8 N, and reduced to 2.5 N between 39-42 weeks gestation. Deflection at rupture also reduced from 5.7 mm to 4.4 mm with the use of a 3 mm probe applying force at a speed of 50 mm/minute through a 1.3 cm diameter port. Indeed, collagen remodelling of the amnion in preparation for parturition has been well documented within the zone of altered morphology after vaginal delivery and non-labouring caesarean section deliveries⁸².

Many groups have performed biaxial testing using a puncture/probe set-up to assess mechanical properties of fetal membranes, whilst others have adopted a burst pressure test by introducing air or fluid^{71,83}. However, the latter offers a less controlled system due to the possibility of failure randomly throughout the sample. Using biaxial loading systems, other leading groups including Oyen *et al.* have well characterised the mechanical failure of human fetal membrane tissue^{16,84}. Importantly, Oyen *et al.* have considered that the integrity of the fetal membrane should be examined, and data presented, on an individual layer basis; regarding the amnion and chorion as separate layers. They demonstrate comparable data with other groups using biaxial loading systems, showing a peak force of 4.3 N in chorioamnion of non-labouring term tissue¹⁶. They further demonstrate that amnion alone, taken distally from the placenta, has a peak of 3.2 N, much lower than amnion obtained overlying the placenta, which has a peak force of 5.62 N. The chorion alone is reported to have the lowest peak force of 1.8 N. Importantly, there is a consistency in values of failure strength (0.9 MPa) and failure tension of the amniochorion throughout the literature and with the use of varying mechanical testing devices including biaxial inflation, biaxial puncture and uniaxial tension (**Figure 1.6**)⁸⁵.

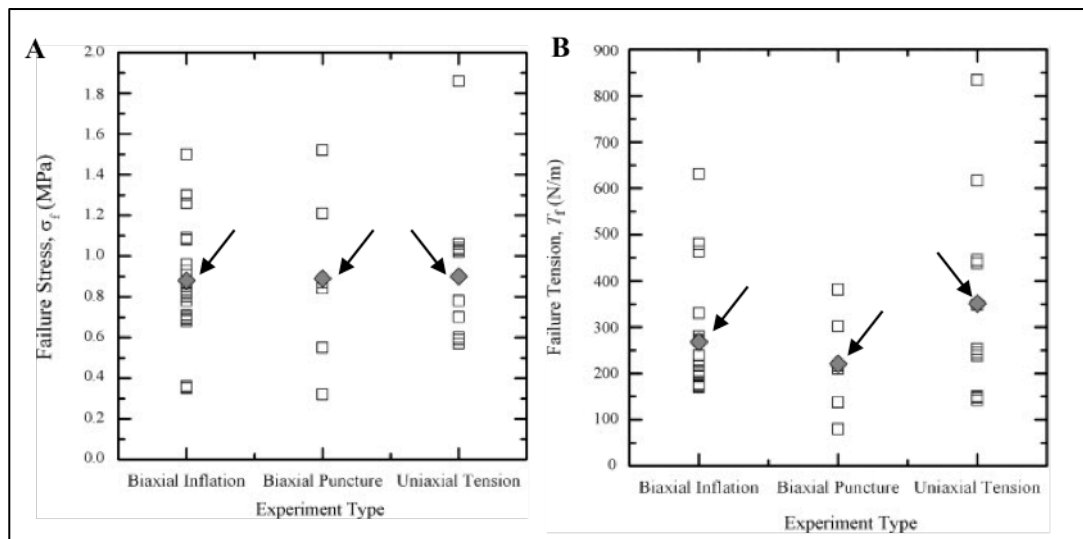


Figure 1.6: Comparison of mechanical data obtained from term fetal membranes for failure stress (A) and failure tension (B) following different mechanical testing devices including biaxial inflation, biaxial puncture and uniaxial tension. Reassuringly, this data shows consistency throughout, with little variation between experiment types. Arrows indicate the average values (grey diamonds). Adapted from Chua & Oyen (2009)⁸⁵.

1.3.2 Amniotic membrane mechanics

It has been demonstrated that the amnion dominates the outcome of the overall chorioamnion failure properties, indicating a determining layer in premature rupture. Research is now being done to characterise the effect of membrane location (relative to rupture site and cervix), the effect of pre-loading the tissue, and the effect of ECM degradation on mechanical properties. The mechanical strength of the chorion does not appear to change over gestation, or whether non-laboured or laboured delivery occurred⁸⁴. Furthermore, the puncture force required for failure of the chorion is approximately half that of the amnion.

Our group has recently demonstrated that collagen fibre organisation can influence mechanical properties of the human term amniotic membrane⁸⁶. Using second harmonic generation imaging to visualise collagen fibres the orientation could be determined to a high resolution (**Figure 1.7**). Samples were taken either parallel or perpendicular to the placental disc and cervical region, identified by placing sterile Babcock forceps onto the lower part of the membrane closest to the cervical region following delivery by elective

caesarean section. When force was applied in parallel to collagen fibre orientation, tangent modulus was higher for both cervical amniotic membrane and placental amniotic membrane specimens compared to when force was applied perpendicular, to fibre direction. Tangent modulus for placental specimens with force applied in parallel with collagen fibres was 7.5 MPa, significantly higher than when compared to cervical amniotic membrane (4.9 MPa). We further demonstrated ultimate tensile strength to be highest in placental amniotic membrane (4.52 MPa) when force was applied in parallel to fibres compared to perpendicular (1.51 MPa). Ultimate tensile strength values were also higher in cervical amniotic membrane (2.28 MPa) when force applied parallel to fibres compared to perpendicular and more disorganised fibre orientation (0.91 MPa, **Figure 1.7**). Interestingly, values reported in the literature indicate average failure strength of 0.9 MPa for the amniochorion. Similar values have also been reported since amniochorion strength in term tissue, reporting being 2.29 MPa, very similar to our failure strength reported of 2.28 MPa when cervical amniotic membrane underwent stretch with collagen organisation parallel to the direction of strain^{36,86}. This further suggests that the amnion alone dominates the overall fetal membrane mechanical properties and is an important determinant in fetal membrane rupture.

Although the amnion makes up one third in thickness of the chorioamnion, it is evident that this is the load-bearing layer and must be considered a priority for researchers in understanding how fetal membranes rupture prematurely at both the biochemical and biomechanical level. For this reason, emphasis throughout this thesis is placed on the amnion where possible.

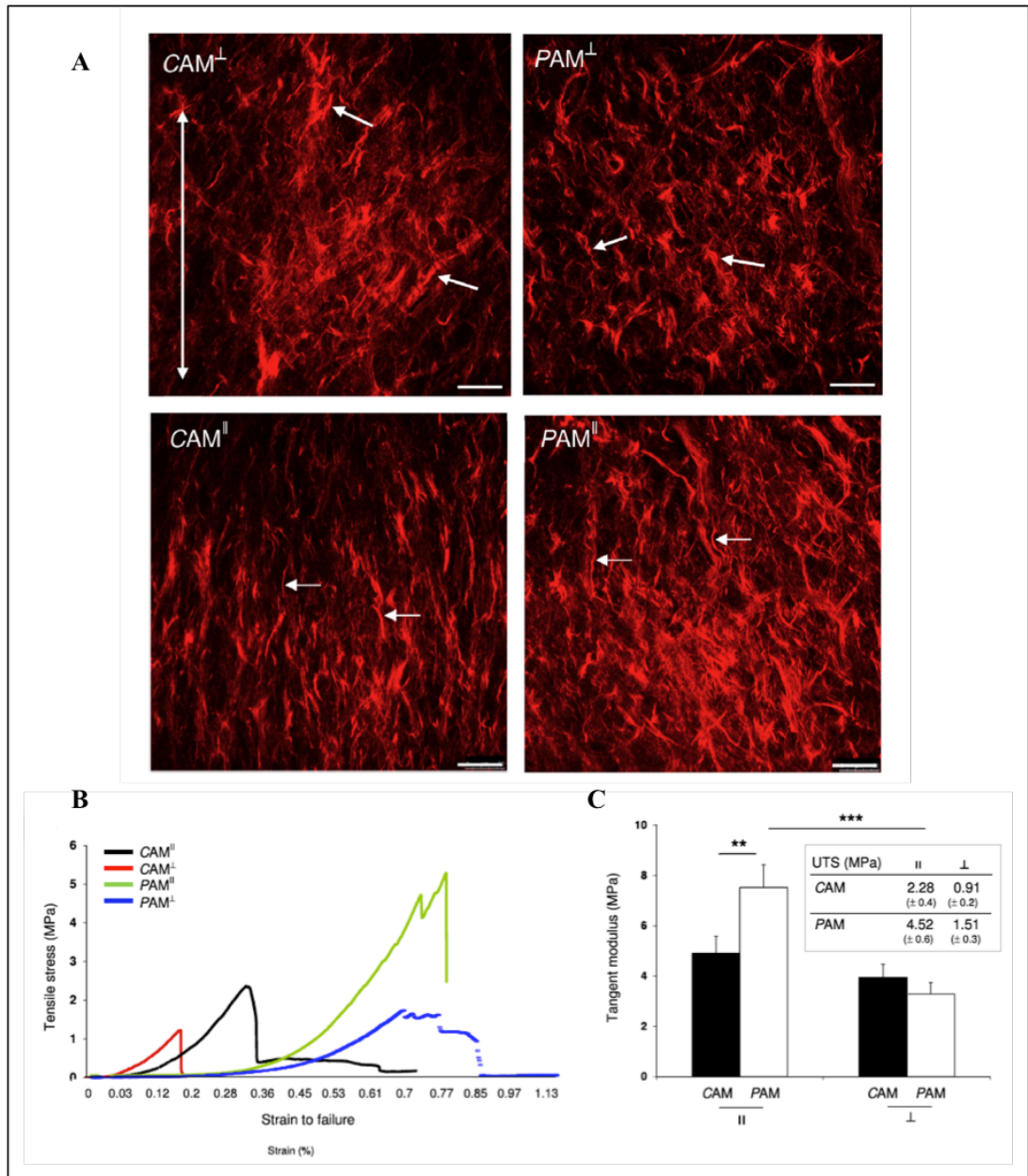


Figure 1.7: Variations in collagen fibre organisation in amniotic membrane samples of term fetal membranes imaged using second harmonic generation imaging. Samples were dissected adjacent to the cervical region or placental disc in perpendicular (top panel) or parallel (bottom panel) orientations (A). Stress strain curves shown for each condition (B) with tangent modulus values greatest in placental region specimens when force was applied in direction of the collagen fibres compares to cervical regions. Comparable results were found for ultimate tensile strength (UTS, C). Scale bars: 50 μ m. CAM: cervical amniotic membrane; PAM: placental amniotic membrane. Adapted from Chowdhury et al., (2014)⁸⁶.

Chapter 2

Physiological and pathological membrane rupture

Chapter 2: Physiological and pathological membrane rupture

Clinical motivations: Worldwide, there are 14.9 million preterm births with direct complications accounting for one million deaths⁸⁷. 1 in 10 babies are born prematurely which presents a growing economic burden, costing the British economy \$1 billion a year. Delaying preterm birth by just one week could save an estimated £260,000. The socio-economic cost associated with preterm birth in the United States has been estimated at \$26.2 billion annually⁸⁸. There is difficulty in researching PPRM due to its multifaceted etiology. This chapter will discuss what is known about physiological and pathological membrane rupture, leading on to the aims and objectives of this thesis.

2.1 Normal physiological events of parturition

There are 3 main mechanisms that can initiate and result in fetal membrane weakening and rupture: (1) myometrial contractions, (2) cervical remodelling, and (3) decidual/membrane activation. While these mechanisms are physiologically activated at term in a normal pregnancy, it is also becoming clear that they can be activated under pathological conditions during preterm pregnancy, contributing to PPRM.

Myometrial contractions

There are 3 phases of labour that occur within the myometrium: (1) proliferation phase, (2) synthetic phase, and (3) the contraction phase. Animal studies have shown that during uterine contraction the expression of cyclooxygenase-2 (COX-2), connexin 43 (Cx43), and the oxytocin receptor increases in the myometrium of term and preterm pregnancies⁸⁹⁻⁹¹. Stretch of human myometrial cells has also been shown to increase interleukin-8 (IL-8) expression⁹². Furthermore, uterine contraction has also been linked with increased numbers of myocytes and a higher expression of the anti-apoptotic proteins Bcl-2 and Bcl-211 during the initial proliferation phase of labour⁹³. Secondly, during the synthetic phase it has been shown that myocytes undergo hypertrophy, which correlates with increased secretion of the ECM proteins collagen type I and III. The final contraction phase within the myometrium has been linked with a decrease in interstitial matrix proteins and an increase in the basement membrane proteins, laminin and collagen IV. It

is important to note that these observations could be stimulated by infection, blood, distension of the uterus, polyhydramnios (excessive amniotic fluid production), and twin pregnancies, which have all been linked with myometrium contraction⁹⁴⁻⁹⁷.

Cervical remodelling

The cervical remodelling mechanisms regulate changes in the cervix including softening, ripening, dilation, and repair (after delivery). Regarding PPRM, changes in the cervix can be crucial and cervical remodelling that leads to shortening of the cervix has been shown to occur immediately before vigorous uterine contractions. This remodelling process involves the regulation of ECM proteins. Importantly, during cervical ripening collagen content decreases and fibrils become more dispersed, which could be explained by an increase in glycosaminoglycan (e.g. decorin and hyaluronan) content observed⁹⁸. Dilation of the cervix occurs due to an inflammatory phenomenon that involves an influx of macrophages and neutrophils, and matrix degradation. Chemokines then attract inflammatory cells such as macrophages that secrete pro-inflammatory cytokines interleukin-1 β (IL-1 β) and tumour necrosis factor- α (TNF- α). These factors then activate nuclear factor- $\kappa\beta$ (NF- $\kappa\beta$), which blocks progesterone receptor-mediated actions. Animal studies have shown the result is enhanced structural remodelling of the cervix, which is similar in preterm birth and in the cervix at term⁹⁹.

Decidual/membrane activation

Normal rupture of the fetal membranes involves a complex anatomical and biochemical set of events that have yet to be fully understood. In humans the fetal membranes fuse with the decidua during pregnancy and at term they separate at the lower uterine segment, where spontaneous rupture of the membranes follows. The zone of altered morphology (ZAM) overlies the cervix and is the region of the fetal membrane that is first to undergo morphological changes in preparation for delivery³. Changes in the amniotic membrane involve basement membrane degradation, swelling of the stromal layers, and a decrease in thickness^{29,33}. It has been suggested that immediately before term and preterm parturition a heavily glycosylated form of cellular fetal fibronectin (fFN) that is present at the chorionic-decidual interface is degraded causing its release into cervical and vaginal secretions¹⁰⁰. This can initiate matrix metalloproteases (MMPs) and COX-2, which

contributes to membrane softening. More extensive disruption occurs at the ZAM, which has been shown to decrease in collagen I, III, and V content. Interestingly, the levels of MMP-1, MMP-8, MMP-9, and neutrophil elastase are higher in women with PPROM compared to those in preterm labour with intact membranes¹⁰¹.

2.2 Preterm premature rupture of membranes

Preterm premature rupture of membranes (PPROM) is defined as the rupture of fetal membranes at less than 37 weeks gestation and prior to the onset of labour. Preterm birth can be divided into previable premature rupture of membranes occurring before 23 weeks gestation (generally accepted to be the limit of viability) and preterm premature rupture of membranes occurring from 23 to 37 weeks gestation (**Figure 2.1**). PPROM is further subdivided according to proximity to term, with 23 to 32 weeks gestation being remote from term PPROM and 32 to 37 weeks being near term PPROM. It is important to note that risk of perinatal morbidity and neonatal mortality decreases with increased gestational age and latency period (time of rupture to delivery). Chance of survival at delivery less than 23 weeks (previable PPROM) is close to 0%, at 23 weeks 15%, at 24 weeks rises to 55%, and at 25 weeks rises to 80%.

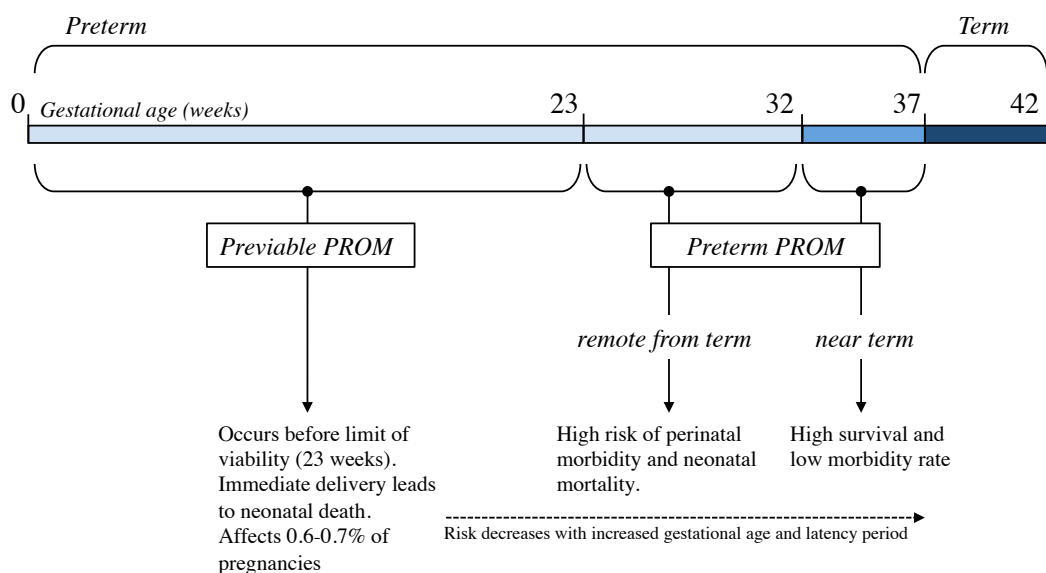


Figure 2.1: Gestational age ranges for preterm and term deliveries. Preterm birth can be sub-divided in to previable premature rupture of membranes before 23 weeks gestation and preterm premature rupture of membranes occurring between 23 and 37 weeks gestation.

Although preterm birth does not always lead to neonatal mortality, over 50% results in long-term morbidity with severe life-long complications including respiratory distress syndrome, polymicrobial intramniotic infection, intraventricular haemorrhage, fetal pulmonary hypoplasia, skeletal deformities, cerebral palsy, and other neurodevelopmental impairments. Previably PPRM (<23 weeks) is also complicated if there is severe oligohydramnios or anhydramnios as this is a critical time period for fetal lung development. The fetus breathes fluid into the lungs, closing off the epiglottis to increase airway pressure, which is vital for normal fetal lung development. Pulmonary hypoplasia can occur if there is insufficient amniotic fluid in the gestation sac before 23 weeks. This can lead to neonatal death even if the fetus is born many weeks or months after PPRM occurs.

PPROM is a major cause of preterm birth and complicates 40% of preterm deliveries¹⁰². Overall, 3-5% of pregnancies are complicated by PPRM with 50-75% of patients delivering within 1 week, even with the aid of antibiotic therapy. Every year 60,000 babies are born prematurely (1 in 9 babies in the U.K). Globally, 1 in 10 pregnancies will end in preterm birth. Preterm delivery rates are increasing irrespective of maternal and fetal medical research advances, with most recent data showing 9.63% of deliveries in the U.S. and 5-9% of deliveries in Europe being preterm. PPRM is therefore a major clinical problem and represents a growing economic burden worldwide. There is a clear shortage of research regarding preterm birth, specifically the pathology behind PPRM and the development of therapeutic interventions, which is likely due to its multifaceted etiology.

2.2.1 Risk factors of PPRM

Many maternal risk factors have been reported to increase the incidence of PPRM, such as a previous PPRM history, preterm labour, cigarette smoking, alcohol and drug consumption, anaemia, low socioeconomic status, maternal age, maternal weight (BMI < 19.8 kg/m²), and antepartum vaginal bleeding (**Figure 2.2**)¹⁰³⁻¹¹². Prior history of PPRM is associated with a recurrence rate of 16-32%. Some reports suggest a more pronounced

link between PPROM and tobacco use, compared to women who delivered preterm due to spontaneous onset of labour¹⁰³. A maternal age of less than 16 years has been linked with a 2-fold increase in preterm delivery when compared to women who were 18 – 29 years of age¹⁰⁸. In addition, a maternal age of 35 and over was also linked with increased preterm delivery rates¹¹⁰.

Uterus, placental and fetal factors linked to increased incidence of PPROM include placental abruption reported to account for 15% of PPROM and uterine overdistension caused by polyhydramnios and multiple pregnancy. Interestingly, uterine overdistension has been linked with initiation of preterm labour by inducing inflammatory pathways¹¹¹. PPROM is also estimated to complicate up to 10% of twin pregnancies. Furthermore, infection and inflammation is said to be a key risk factor in PPROM. One study showed infection diagnosed as chorioamnionitis occurred in 55% of preterm delivery patients¹¹³. Chorioamnionitis is likely to stimulate inflammatory processes and increase fetal membrane weakening factors (**Figure 2.2**). Other studies estimate chorioamnionitis is four times more prevalent in patients with PPROM than without PPROM¹¹³. Furthermore, disruption to the fetal membrane due to minimally invasive intrauterine fetal surgery can lead to iatrogenic PPROM in 30% of cases. Other procedures including amniocentesis,

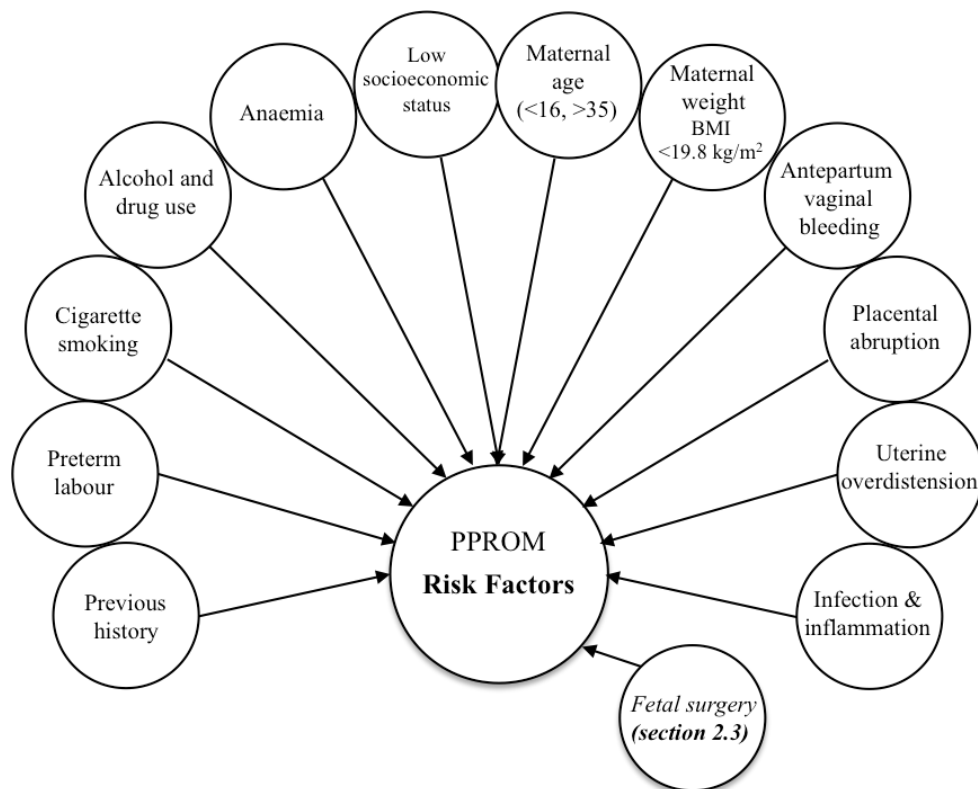


Figure 2.2: List of major maternal, uteroplacental and fetal PPROM risk factors

chorionic villus sampling and cervical cerclage can damage the fetal membrane, resulting in amniotic fluid leakage and increased incidence of PPRM.

2.2.2 Pathological mechanisms

The primary signals which initiate the inflammatory process and lead to AM weakening are unclear. **Chapter 4** discusses in more detail the implication of the gap junction protein connexin 43 (Cx43) in absent AM healing. **Chapter 6** discusses the implication of Cx43 in AM weakening mechanotransduction mechanisms. In summary, previous studies in animal models have shown that tensile stretch increased myometrial expression of cyclooxygenase-2 (COX-2), the oxytocin receptor and Cx43⁸⁹⁻⁹¹. In human amniotic cells, application of 11 % static stretch activates NF- κ B and induced expression of COX-2 and prostaglandin E₂ (PGE₂) production¹¹⁴. Cytokines such as interleukin-1 β (IL-1 β) activate NF- κ B and increase production of matrix metalloproteinase-9 (MMP-9) and PGE₂ in human amniochorion^{62,115-118}. The enhanced PGE₂ reduced collagen levels and increased tissue softening mediated by increased proteoglycans in human AM^{55,119,120}. The changes in the matrix network are characterised by abnormal weakening of AM due to loss in tensile strength and mechanical resistance leading to PPRM^{84,121,122}. Taken together, these findings highlight the complex nature of factors that control inflammation in fetal tissues. In addition, the mechanisms which initiate the repair of clinical PPRM are poorly understood making it difficult to identify targets and develop therapies which prevent PPRM following fetal therapy or promote AM healing after spontaneous PPRM. The proposed work in this thesis will investigate the role of Cx43 in AM tissue remodelling and healing. We speculate that a combination of inflammatory and mechanical factors disrupt AM biomechanics mediated by abnormal signalling via Cx43. Targeted knockdown of Cx43 in skin wounds improves healing and may be a potential therapeutic to promote AM healing and treat PPRM.

Furthermore, Cx43 expression is downregulated in normal healing wounds. In human diabetic wounds and venous leg ulcers, healing is poor due to upregulation of Cx43 expression^{123,124}. This gap junction protein is additionally enhanced in several inflammatory conditions such as hepatic cirrhosis, acute-on-chronic liver failure and astrocytic death after ischaemia-reperfusion injury^{125,126}. Previous studies report that topical application of a Cx43-specific antisense containing gel to acute wounds in rodent

models significantly accelerates the healing process whilst reducing inflammation and scar size^{123,126,127}. Furthermore, in non-healing wound edge biopsies from human venous leg ulcers, knockdown of Cx43 with antisense technology resulted in accelerated cell migration whilst reducing adhesion, proliferation and led to profound effects on fibroblast cytoskeletal dynamics¹²⁸.

2.3 Iatrogenic preterm premature rupture of the membranes

Intrauterine surgery for perinatal conditions (**Table 2.1**) has been performed for over two decades with precedence given to those conditions that carry the most severe complications. Fetal surgery is used when there is evidence that intervention before birth can improve the neonatal and adult outcomes in fetuses with structural anomalies, genetic or placental complications. The past decade has seen a dramatic increase in diagnostics, treatment, and fetal surgery physician expertise, and with that there has been an increase in the number of centres willing to offer surgical intervention for fetal abnormalities. Iatrogenic PPRM occurs in up to 35% of intra-uterine surgical cases, which undermines the success achieved by fetal surgeons¹²⁹⁻¹³¹. There is also an increased risk of maternal infection due to the leakage of amniotic fluid and ascending bacterial infection increasing the risk to mother.

2.3.1 Types of fetal surgery

Fetoscopic procedures are the most common form of intra-uterine fetal surgery. Ultrasound guidance is used to assist the surgeon on inserting a trocar (**Figure 2.3**) into the uterus, piercing the maternal abdominal wall, the myometrium and ultimately the fetal membranes. The diameter of the instrument used varies between 1.3 – 3.3 mm, and can often lead to PPRM¹³²⁻¹³⁷. Fetoscopic laser ablation for the treatment of twin-to-twin transfusion syndrome (TTTS) improves outcome after TTTS but still a third of patients lose one or both babies, with most hospitals recording a 60-65% double survival rate¹³⁸. Other common procedures are detailed in **Table 2.1**.

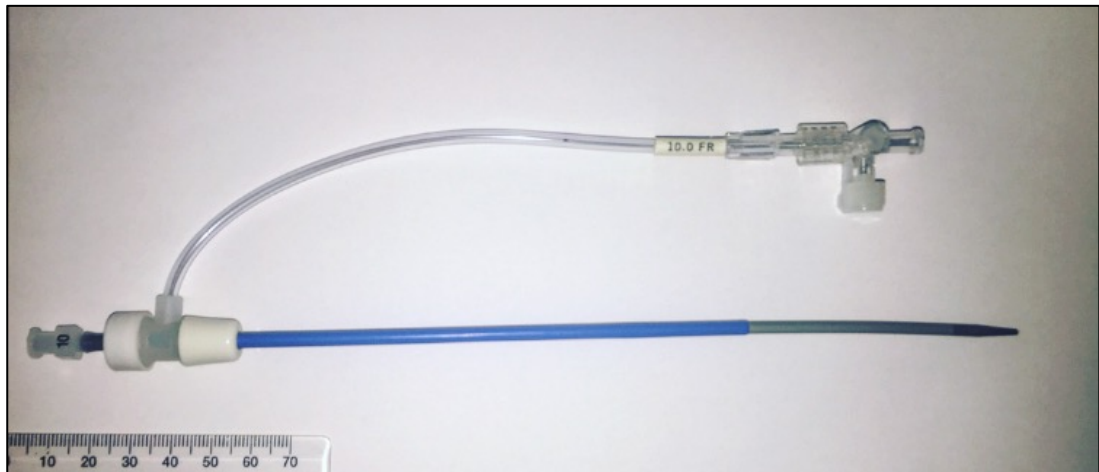


Figure 2.3: Typical 10.0 FR trocar used during fetoscopic surgery. A needle is placed within the trocar to assist insertion into the uterus and fetal membranes. The inner shaft of the trocar is then removed leaving the blue tube within the uterus and fetal membranes.

Table 2.1: fetal complications and respective fetal surgery procedures.

Complication	Surgical procedure	Details and outcome
Twin-to-twin transfusion syndrome (TTTS)	Fetoscopic laser photocoagulation.	Mortality without treatment when diagnosed in mid-trimester is >80% ¹³⁹ . Occurs in 15% of monochorionic twins. 57% survival rate post-surgery associated with high preterm birth rates ¹⁴⁰ . PPROM incidence after treatment reported in 39% of cases at mean gestational age of 29±4.5 weeks ¹⁴¹ .
Congenital diaphragmatic hernia (CDH)	Fetoscopic endoluminal tracheal occlusion.	1 in 2,000 – 5,000 births. ~75% survival rate post-surgery ¹⁴² . ~30% stillborn. PPROM incidence after treatment reported in 16.7% at 28 weeks and 33.3% at 32 weeks gestation ¹⁴³ .
Twin reversed arterial perfusion sequence (TRAPS)	Selective bipolar cord coagulation and radiofrequency ablation.	Severe variant of TTTS. Occurs in 1% monochorionic twins. 50% stillbirth of the healthy twin if left untreated. PPROM incidence after treatment reported in 22-57% of cases ^{144,145} .
Obstructive uropathy/ lower urinary tract obstruction (LUTO)	Performed using a percutaneously placed vesicoamniotic shunt.	Incidence of LUTO is ~2.2 in 10,000 births ¹⁴⁶ . Fetal mortality rate of 43% if left untreated ^{147,148} . One study has shown in selected cases 91% survival rate in first year (mean gestation at delivery was 34.6 weeks) ¹⁴⁹ . PPROM rates not well investigated. One study reports 1/7 cases resulted in PPRM ¹⁵⁰ .
Congenital cystic adenomatoid malformation (CCAM)	Open fetal surgical resection of the lung mass involving maternal hysterotomy.	Fetuses with large lung lesions often become hydropic and die in utero. One study showed in selected cases 60% survival rate following surgery ¹⁵¹ . PPROM incidence after treatment reported in 16% of cases ¹⁵¹⁻¹⁵³ .
Sacroccygeal teratoma	Open fetal surgery involving maternal hysterotomy.	Fetuses with large lesions given precedence due to high mortality risk. Perinatal mortality of 25-37% ¹⁵⁴ . Most common congenital tumour occurring in 1-2 per 20,000 pregnancies ¹⁵⁵ . PPROM rates not well investigated.

Table 2.1 continued.

Complication	Surgical procedure	Details and outcome
Spina bifida (myelomeningocele)	Open fetal surgery.	Occurs in ~1500 infants born each year ¹⁵⁶ . 15-35% do not survive beyond 5 years ¹⁵⁷ . PPROM rate of 46% following prenatal surgery ^{158,159} . Likely to move to a fetoscopic procedure in the future to reduce maternal morbidity.
Congenital heart disease	Balloon aortic valvuloplasty.	Performed for severe mid-gestation aortic stenosis leading to hypoplastic left heart syndrome. A few studies have shown in selected cases 75% survival rate over 5 years post-surgery. ^{160,161} . PPROM rate not well investigated.

The growing demands to perform prenatal surgery for fetal abnormalities will likely lead to the increased incidence of iatrogenic PPROM. Taken into account with a rise in the number of pregnancies means it is ever more important for medical research advances to be made regarding PPROM prevention with preterm birth rates likely to increase further over the next decade.

2.3.2 Fetal surgery effects on the fetal membrane

Following spontaneous PPROM and fetal surgery procedures, the fetal membrane has a lack of healing ability. This often leads to devastating complications associated with preterm birth and can even mean the difference between life and death for the fetus. This absent healing exposes the fetus to ascending bacterial infection and disturbs amniotic fluid homeostasis. Numerous attempts have been made to seal fetal membrane defects (see **section 5.1** fetal membrane sealing strategies) with limited success and no current clinically viable option. To date, there are limited studies on the effects of fetal surgery on the fetal membrane. Whilst many efforts have been made to prolong the latency period and prevent iatrogenic PPROM following fetal surgery, there is a gap in knowledge regarding fetal membrane healing. In order to improve the outcome of iPPROM preventative strategies it is important to understand why the fetal membrane fails to heal.

The human fetal membrane is not innervated and is largely avascular, although the decidual surface of the chorion is occasionally found to contain blood vessels. Therefore, it is unreasonable to suggest the occurrence of a typical wound healing response involving the sequence of hemostasis, inflammation, proliferation, and remodelling. Gratacos, *et al* reported no spontaneous fetal membrane healing following fetoscopic procedures (n=19)¹⁶². Further findings suggest sliding of the amnion and chorion layers could be the reason for absent amniotic fluid leakage after many fetal surgeries. In addition, membrane attachment to the decidua may also prevent amniotic fluid leakage in minimal cases¹²⁹. Frequently there is membrane separation seen after fetoscopic and open fetal surgical procedures where fluid is seen in the interface between the myometrium and the fetal membranes. Reports have found this condition to be associated with the formation of amniotic bands, umbilical cord strangulation, and fetal demise¹⁶³. The amnion defects (14.4 mm²) are generally found to be bigger than the chorion defects (11.1 mm²) likely due to the increased distensible properties of the amnion. Absent cell proliferation has been detected in the fetal membranes following trauma⁵⁶. Defect size has not been found to change over the elapsed time from surgical intervention to delivery (3-122 days)¹⁶². In a patient who underwent a repeat fetoscopy procedure, the initial fetal membrane defect was examined and exhibited no signs of healing¹²⁹. There was no sliding of the amnion and chorion at the wound site, which was 5-6 mm in diameter. Papanna *et al.*, demonstrated an absence of amniotic fluid leakage was most likely due to the membrane-decidual adherence¹²⁹. Interestingly, the inner muscular layer of the uterine wall showed no evidence of healing; a novel finding that shares similarity with patients that present with limited healing following previous caesarean section.

Further studies reveal absent fetal membrane healing at the trocar site following fetoscopic laser surgery for twin-to-twin transfusion syndrome (n=31)¹⁶⁴. Histological analysis showed thickened rounded edges and absent epithelialisation over the wound. Myofibroblasts, involved in normal contraction of wounds were also absent in the fetal membranes. Limited inflammation was also reported, and apoptosis levels appeared to be higher in amniotic epithelial cells compared to mesenchymal cells of the fibroblast layer. Currently there is no clinically successful means to plug iatrogenic defects post-surgery. This is probably due to poor understanding behind the pathophysiological mechanisms that lead to iatrogenic PPRM. Numerous approaches are being developed to prevent

PPROM following fetal surgery (see **Chapter 5**). Therefore, it is imperative to first understand why the fetal membranes fail to heal in order to improve the design and ultimately the clinical success of these strategies.

2.4 Healing properties of the amniotic membrane

In humans, histological analysis has reported that limited or no healing occurs following focal destruction of the membrane after fetoscopic surgery or after larger destruction of the membranes following open fetal surgery^{162,165}. In some circumstances sealing has been reported when associated with cessation of amniotic fluid leakage after fetal surgery. However, it is now known that sliding of the two fetal membrane layers or adherence of the fetal membrane to the underlining decidua is likely to have caused the cessation of amniotic fluid leakage as opposed to healing mechanisms^{129,162}. The mechanisms behind fetal membrane healing, or lack of, are not well understood. Spontaneous healing of the fetal membrane has been investigated in several species (**Table 2.2**). Limited or absent spontaneous healing has been reported in humans, non-human primates (rhesus monkey), sheep, rat, and rabbit fetal membrane^{130,162,164-171}. Interestingly, this is not always the case, as some studies report spontaneous healing of the fetal membrane in swine and mouse species^{172,173}. A fetoscopic access port site in a rhesus monkey remained open 6 weeks after surgery, showing no evidence of wound healing¹³⁰. Observation of the fetoscopic defect revealed thickened wound edges. Similarly, sheep fetal membrane wounds do not heal¹⁶⁶. Healing of the rabbit fetal membrane has been difficult to examine due to the short gestational period of 31 days. Therefore, time from fetal surgery to harvesting is limited to 7 days. When using a 14-gauge (2.1 mm diameter) needle during fetoscopy, the resulting histological analysis of wounds 7 days after surgery revealed no evidence of healing¹⁶⁸. Furthermore, the first animal model to be studied was the rat, which were examined histologically¹⁷¹. Following injury the fetal membrane did not fully restore and no tissue proliferation was reported, although thickened wound edges were documented.

In contrast, swine and mouse models have shown spontaneous healing properties and therefore are not suitable models for the study of fetal membrane sealants that could be potentially developed in humans^{172,173}. In swine fetal membrane, defects of up to 4 mm in diameter showed spontaneous healing following harvesting of the fetal membrane after

approximately 44 days post-laparotomy¹⁷². Furthermore, in mouse fetal membrane defects of 0.47 mm in diameter, spontaneous healing was reported following 3 days post-injury¹⁷³. However, slightly larger wounds (0.91 mm in diameter) showed healing rates of only 40%. Furthermore, healing rates of the chorion were poor and incomplete compared to the amnion. Interestingly, this study shows macrophage recruitment occurs from the amniotic fluid in order to enhance tissue repair. The limited healing response of larger defects were attributed to compromised migration of mesenchymal cells and ECM deposition. Increased vasculature to the swine and mouse fetal membrane could also promote tissue repair. In species that show limited or no healing of the fetal membrane, it could be hypothesised that this is an evolutionary trait acting to prevent repair of the fetal membranes to avoid sealing of potential infection within the amniotic cavity.

Table 2.2: Key *in vivo* studies on fetal membrane healing in different species

Species	Details	Reference
Human	Reported no evidence of spontaneous healing when fetal membranes (N=19) were focally destroyed during intra-uterine fetoscopy. Delivery occurred between 3-112 days after fetoscopy. Proliferation indices were very low in chorion (range: 0-7%) and absent in amnion (0%).	Gratacos <i>et al.</i> , (2006) ¹⁶²
	Reported no evidence of spontaneous healing when fetal membranes (N=31) were focally destroyed during intra-uterine fetoscopy. Only evidence of tissue remodelling included thickened edges at the wound margin. No evidence of myofibroblasts presence in the fibroblast layer of the amnion, indicating the contraction phase of wound healing mechanisms is absent.	Papanna <i>et al.</i> , (2015) ¹⁶⁴
	Reported no evidence of fetal membrane restoration. Histological analysis revealed increased collagen staining in fetal membranes at suture sites (13.22±2.84%) compared to non-sutured sites (6.16±1.09%) in patients that underwent open fetal surgery for myelomeningocele (N=10). Suture sites show loss of amniotic epithelium compared to non-sutured sites.	Carvalho <i>et al.</i> , (2017) ¹⁶⁵
Rhesus monkey	Reported no evidence of spontaneous healing after fetoscopy (N=1). Following 6 weeks from fetal membrane damage to harvesting, the defect remained open.	Devlieger <i>et al.</i> , (2006) ¹³⁰

Sheep	Limited ability to heal reported. Sheep underwent fetoscopic balloon occlusion of the trachea for experimental treatment of congenital diaphragmatic hernia between 88-99 days of gestation. At 145 days, histology of membrane defects did not show restoration (N=8).	Devlieger <i>et al.</i> , (2002) ¹⁶⁶
Rabbit	Limited ability to heal reported. Rabbits underwent fetoscopy at 23 days and samples were harvested at 32 days. It is reported that 40% of rabbits showed membrane restoration after 1 week. Interestingly MMP-2 and MMP-9, and MMP inhibitors all increased in amniotic fluid after surgery.	Devlieger <i>et al.</i> , (2000) ¹⁶⁷
	Limited ability to heal reported. Rabbits underwent fetoscopy at 23 days and samples were harvested at 30 days. Membrane integrity was maintained in 25% following injury with 14-gauge needle (2.1 mm defect diameter) when histologically assessed 7 days post-injury. However, complete restoration was not reported.	Mallik <i>et al.</i> , (2007) ¹⁶⁸
Swine	Yucatan miniature pigs were used to undergo laparotomy with a 12 Fr trocar (4 mm defect diameter) at 70 days gestation (term: 114 days). After histological examination, spontaneous healing of swine fetal membranes was reported following iatrogenic injury (N=14).	Papanna <i>et al.</i> , (2015) ¹⁷²
Rat	First known publication to study the response of animal fetal membrane to injury. Rats were subjected to laparotomy using 21-gauge needle (0.8 mm defect diameter). Following 1, 2, and 5 days, the fetal membranes were harvested. At day 1, no sealing was evident and thickening of the wound edge was most profound in the amnion. By day 5, wound size had reduced but complete closure did not occur. Reduction in wound size was speculated to occur due to prolonged contraction of the uterine muscle.	Sopher (1972) ¹⁷¹
Mouse	0.47 mm diameter wounds showed spontaneous healing 3 days post-injury in a mouse model. However, larger wounds (0.91 mm in diameter) showed healing rates of only 40%. Healing rates of the chorion were poor and incomplete compared to the amnion. Macrophage recruitment from the amniotic fluid reported to occur to enhance tissue repair.	Mogami <i>et al.</i> , (2017) ¹⁷³

2.5 Aims and Objectives

Aim 1: We examined whether surgically induced membrane defects elevate Cx43 expression in the wound edge of the AM and drives structural changes in collagen that affects healing after fetoscopic surgery.

HYPOTHESIS: Connexin 43 is overexpressed in human fetal membrane defects after fetoscopic surgery.

OBJECTIVES: We examined cell morphology and collagen microstructure by scanning electron microscopy and second harmonic imaging microscopy in fetal membranes taken from women who underwent fetal surgery. Immunofluorescence and real-time qPCR was used to examine Cx43 expression in control and wound edge AM.

PROJECT OUTCOMES: Overexpression of Cx43 in the AM after fetal surgery induces morphological and structural changes in the collagenous matrix that may interfere with normal healing mechanisms.

Aim 2: We investigated whether trauma induces Cx43 overexpression in human fetal membrane defects after artificial surgery.

HYPOTHESIS: Cx43 is overexpressed in human amniotic membrane after *in vitro* trauma within our artificial fetoscopic trauma model.

OBJECTIVES: Term human FM were traumatised *in vitro* using an artificial trauma model that mimics fetoscopic surgery. Cell morphology and Cx43 were examined in the wound edge AM by immunofluorescence confocal microscopy and compared to control AM. Collagen microstructure was examined by second harmonic generation imaging. Cell viability was assessed with calcein and ethidium staining.

PROJECT OUTCOMES: We showed that Cx43 is overexpressed in wounded fetal membranes after trauma and drives structural changes in collagen that slows down cell migration across the FM defect.

Aim 3: We will develop effective therapeutic repair of the FM defect created after fetoscopic surgery by (1) engineering bioactive membranes with peptide amphiphile sealants that promote tissue regeneration in the FM defect triggered by human amniotic fluid.

HYPOTHESIS: PAs have the potential to co-assemble with the host macromolecules from the AF environment and form composite bioactive membranes with spatial and temporal control that effectively seal the FM defect.

OBJECTIVES: Using the artificial trauma model, we will explore self-assembly of the PAs and examine structural properties and physical characteristics by SEM, histology and IMF. Mechanical properties, permeability and sealing response will be examined after sealing.

PROJECT OUTCOMES: We were able to show potential sealing capacity of PAs in the FM defect using the artificial fetoscopic trauma model.

Aim 4: To examine the effect of repetitive cyclic tensile strain on human fetal membrane weakening mechanisms and identify potential upstream therapeutic targets for prevention of ECM degradation.

HYPOTHESIS: We hypothesise that CTS (1) increases Cx43 expression and overstimulates the PGE₂ pathway, resulting in accelerated matrix breakdown and AM mechanical failure in a tissue-dependent manner and that (2) knockdown of Cx43 will restore normal tissue remodelling and promote healing mechanisms and repair in AM tissue after trauma.

OBJECTIVES: We will perform cyclic tensile strain of human amniotic membrane samples using an *ex-vivo* bioreactor system. Analysis of strained and unstrained tissue samples will be performed to examine the production of fetal membrane sulfated glycosaminoglycan (sGAG), collagen, elastin; and release of prostaglandin E₂ (PGE₂) and total matrixmetalloprotease activity (MMP). We will examine the inhibition of Cx43, AKT, PI3-kinase and COX-2 on fetal membrane weakening mechanisms following cyclic tensile strain.

PROJECT OUTCOMES: We believe that downregulation of Cx43 with Cx43asODNs promotes AM healing and could be used to prevent AM weakening observed in PPROM patients.

Chapter 3

Materials and Methods

Chapter 3: Materials and methods

3.1 Patient recruitment and tissue procurement

3.1.1 Ethical approval

Ethical approval was granted by the Joint UCL/UCLH Committees on the Ethics of Human Research (REC: 14/LO/0863). For the transfer of human fetal membranes (FM), placenta and amniotic fluid (AF) between University College London and Queen Mary University of London, a material transfer agreement (MTA) was arranged in accordance with the Human Tissue Act 2004. Human FM (n=69) were collected with informed consent from women undergoing elective caesarean section at University College London Hospital NHS Foundation Trust. Women with placenta praevia, multiple pregnancy, antepartum haemorrhage, PPRM, fetal growth restriction, clinical chorioamnionitis, meconium stained liquor, and maternal diabetes were excluded from the study.

3.1.2 Collection of term fetal membranes after Caesarean section

Term FM were collected following Caesarean section at 37-42 weeks gestation. Following delivery of the baby but before delivery of the placenta, a sterile Babcock tissue clip was placed on the lower edge of the FM overlying the internal os of the cervix within the uterine incision to provide a landmark. The placenta was separated from the uterus by gentle cord traction and after checking for clinical purposes in a clean hood, it was sampled. FM were dissected into 30 x 30 mm specimens, washed with Earle's Balanced Salt Solution (EBSS) for 2 minutes to remove excess maternal blood and incubated in DMEM + 20% FCS (Sigma-Aldrich, UK). For experiments involving mechanotransduction studies and the use of the *ex-vivo* bioreactor, two regions were dissected from each amniotic membrane (AM):

- Cervical amniotic membrane (CAM)

The tissue was dissected within 5 cm of the region identified by the Babcock tissue clip overlying the internal os of the cervix.

- Placental amniotic membrane (*PAM*)

The tissue was dissected at least 15 cm from the site identified as cervical AM and within 3 cm of the placental disc.

3.1.3 Collection of fetal membranes after fetal surgery

FM were also collected from patients that underwent fetoscopic laser ablation for twin-to-twin transfusion syndrome (TTTS) and twin reversed arterial perfusion sequence (TRAPS); fetoscopic tracheal occlusion for fetal congenital diaphragmatic hernia (CDH), and open fetal surgery for spina bifida closure. These surgeries occurred at UCLH and University Hospitals Leuven, Belgium. Ethical approval was granted by the Ethics Committee at the KU Leuven (Ref: P008-2011) for samples obtained from Belgium. However, the procurement of these samples following patient consent was sometimes difficult, as patients would return to their booking hospital after treatment in the Fetal Medicine Units at KU Leuven or UCLH. In these cases, an effort was made to obtain a letter of access, which would allow collection of the tissue from other hospitals once delivery had occurred. This included Royal Berkshire Hospital (Reading), North Middlesex University Hospitals NHS Trust, and West Hertfordshire Hospitals NHS Trust (Watford General Hospital).

Fetal surgical procedures were performed between 15+0 and 28+1 weeks of gestation and between 1 and 145 days before birth. During the surgery, the fetoscopic entry site was created by using a 10-Fr Teflon cannula (Cook Medical, Strombeek Bever, Belgium) and pyramidal trocar device (Karl Storz, Tuttlingen, Germany). At delivery, the fetoscopic defect site was identified by careful macroscopic survey of the fetal membrane, and the tissue around the wound was carefully excised. For the open fetal surgery, the hysterotomy wound was excised as part of the routine entry into the uterus at caesarean section, and then the membranes were stripped from the overlying myometrium. A control region in the fetal membrane that was aligned in the same axis as the fetal defect and was at least 5 cm away from the wound edge was excised. FM was washed with Earle's Balanced Salt Solution (EBSS) for 2 minutes to remove excess maternal blood.

3.1.4 Amniotic fluid collection

AF was collected from women undergoing fetoscopic laser ablation of placental vascular anastomoses for twin-to-twin transfusion syndrome in mid-trimester pregnancies. Immediately after ultrasound-guided placement of the laparoscope into the amniotic cavity, AF was withdrawn using sterile syringes (50-2000 ml). AF was also collected after amniocentesis for polyhydramnios and diagnostic testing, respectively.

3.2 Biochemical analysis of fetal membranes

3.2.1 Fetal membrane digestion

To obtain dry weight of tissue, samples were freeze dried (-106°C, 0.03mbar) for 24 hours and then weighed. Freeze dried tissue was then digested by placing in 1 mL of activated papain enzyme digestion solution (100 mM Sodium Phosphate Buffer/5 mM Na₂EDTA/10 mM L-cysteine 4U/mL papain) in a sterile tube. Samples were incubated overnight at 60°C for 18 hours and then vortexed to ensure full digestion. Tubes were then stored at -80°C until biochemical assay was performed.

3.2.2 Determining DNA levels

To measure DNA content within fetal membrane digest and media samples, the DNA-specific fluorometric dye, Hoechst 33258 was used to generate a standard curve (**Figure 3.1**). Hoechst 33258 binds to adjacent adenine-thymine base pairs of DNA and emits fluorescence at a wavelength of 460 nm.

Deoxyribonucleic acid sodium salt from calf thymus (Sigma-Aldrich, D1501) was used as the standard and first diluted to 20 µg/ml using digest buffer and 2X saline sodium citrate (SCC) buffer mixed in a 1:1 ratio. Digest buffer was made by dissolving cysteine hydrochloride (0.788 g) and EDTA (0.403 g) in 0.5 L PBS, ensuring a pH of 6.0 by adjusting with 1 M NaOH if necessary. A 20X SSC buffer stock was prepared by dissolving sodium chloride (87.65 g) and trisodium citrate (44.1 g) in 0.5 L deionised

H₂O and ensuring a pH of 7.0. Samples and standards are plated (100 µL/well) using a white polystyrene 96-well Nunc™ microplate. A working concentration of Hoechst 33258 reagent is prepared by diluting 1:1000 with SSC/digest buffer (1:1). Hoechst reagent (100 µL/well) was then added to each well before measuring the fluorescence (460 nm) using the BMG FLUOstar OPTIMA microplate reader.

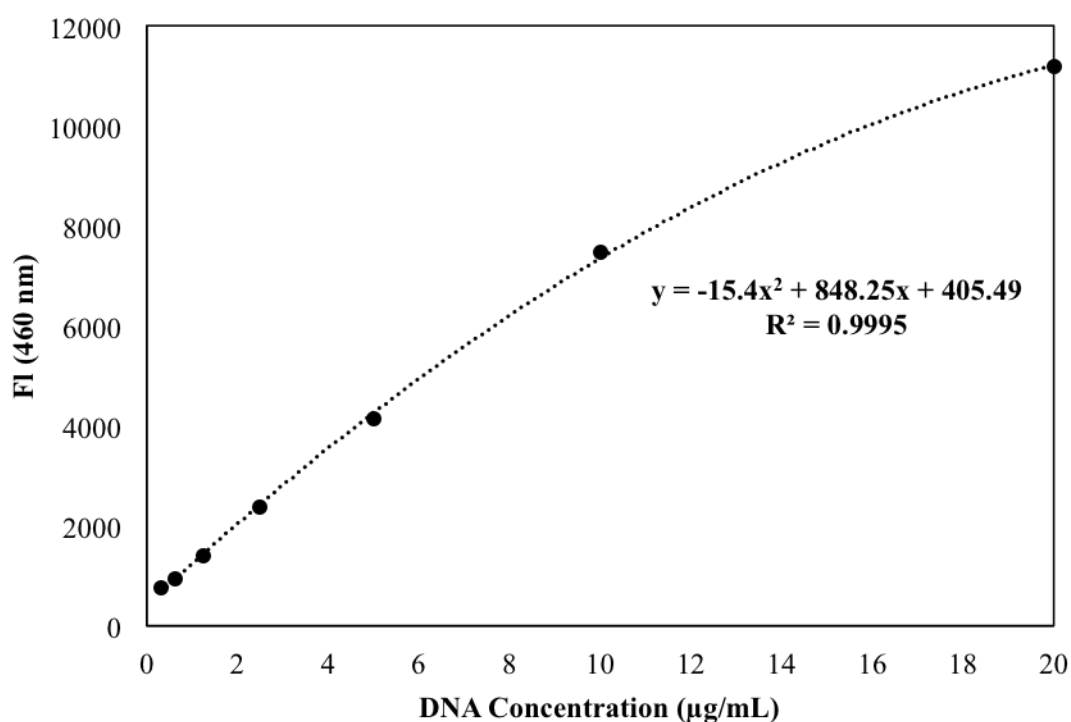


Figure 3.1: Typical DNA assay standard curve showing the relationship of fluorescence intensity (460 nm) and the fluorimetric dye, Hoechst 33258.

3.2.3 Determining sulphated glycosaminoglycan content

Dimethylmethylene blue (DMMB) reagent was prepared in a fume hood. DMMB (0.016 g) was first added to ethanol (5 mL). Sodium formate (2.0 g) was then added to deionised H₂O (850 mL). These two solutions were mixed until completely dissolved. The resulting mixture was made up to 1 L using deionised H₂O. The pH was checked using a pH meter and adjusted to pH 3.0 if necessary. The final solution is light sensitive and therefore stored in the dark.

Chondroitin sulphate was used to prepare a standard curve (**Figure 3.2**). The standard (1 mg/mL) was diluted 1:10 with digest buffer before preparing a dilution series of 0-50 µg/mL. Standard curves were checked to ensure R^2 values of above 0.98. Prior to plating all standards and samples were vortexed. Samples and standards are run in triplicate (40 µL/well) using a clear 96-well plate. A multichannel pipette was used to add DMMB reagent (250 µL/well). Plates were added to the SpectroNano Star and shaken at 360 rpm (10 seconds) prior to measuring absorbance at 595 nm.

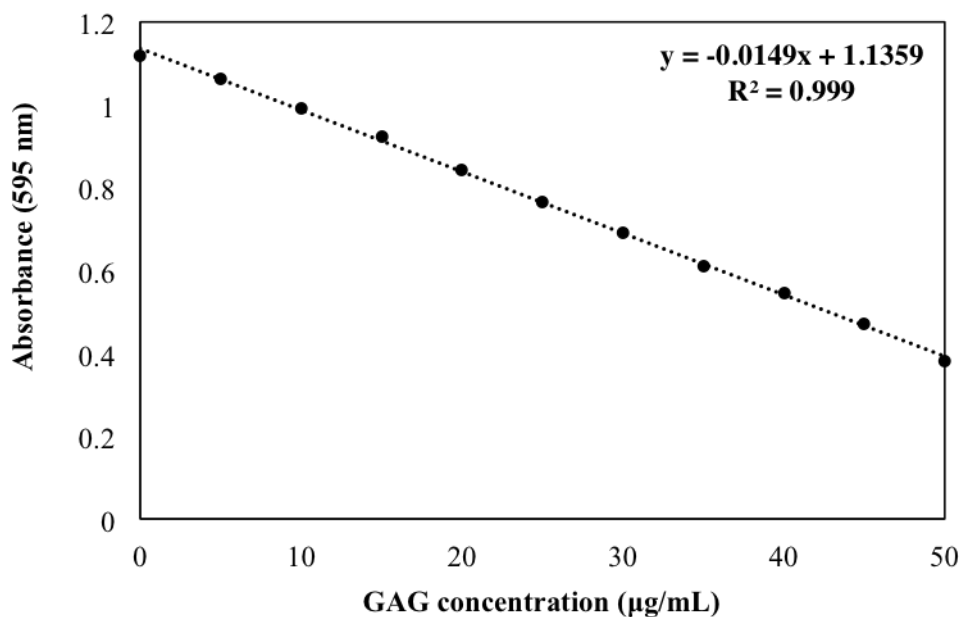


Figure 3.2: Typical DMMB assay standard curve showing the linear relationship of absorbance at 595 nm and the chondroitin sulfate standards.

3.2.4 Quantification of collagen levels

Amniotic membrane samples were digested using pepsin and acetic acid instead of papain in order to preserve the triple helix structure of collagen. Pepsin (1 mg/mL, Sigma, Poole, UK) was dissolved in 0.5 M acetic acid and added to freeze dried tissue samples for 48 hours at 4°C on a rocker. Samples were then centrifuged at 15,000 x g for 1 hour. The supernatant was discarded and 1 mL of 6 M HCl was added to each sample and vortexed. The resuspended pellet was heated to 115°C for 24 hours and then samples were stored at -80°C until the hydrolysis and neutralization procedure using concentrated HCl.

Concentrated HCl (38%) was added to each sample in a 1:1 ratio (approximately 100 µL each) and vortexed. The micro-centrifuge tubes were then placed in a heating block at

110°C for 18 hours. Samples were cooled to room temperature and centrifuged at 5000 x g for 5 minutes. Samples were dried in a fume hood for approximately 48 hours in a heating block at 50°C with the micro-centrifuge tube lids removed. 200 µL ultra-pure H₂O was then added to each sample to dissolve pellet and vortexed until complete resuspension was achieved. Samples were stored at 4°C until the hydroxyproline assay was performed.

The following solutions were prepared prior to running the hydroxyproline assay:

- Hydroxyproline stock solution – 1 mg/mL trans-4-Hydroxy-L-proline (56250 Fluka). This was stored at 4°C (maximum of 3 months).

The following solutions were prepared fresh prior to each assay:

- Citrate stock buffer – 5.04 g citric acid monohydrate (Sigma, C1909), 11.98 g sodium acetate trihydrate (Sigma S7670), 7.22 g anhydrous sodium acetate (Sigma, S2889), and 3.4 g sodium hydroxide (Sigma, 655104) was dissolved in 80 mL ultra-pure H₂O. 1.26 mL glacial acetic acid was added and pH adjust to 6.1. Ultra-pure water was added to a total volume of 100 mL and solution filtered using Whatman paper.
- Assay buffer – 1.5 mL n-propanol (Sigma, 402893) was added to 1 mL ultra-pure H₂O and made up to 7.5 mL using citrate stock buffer.
- Chloramine T Reagent – 141 mg Chloramine T (Sigma, 857319) was added to 0.5 mL ultra-pure H₂O and heated to 60°C for 10 minutes to dissolve. 0.5 mL n-propanol and 4 mL citrate stock buffer was added and the solution wrapped in tin-foil until use.
- DMBA reagent – 4.5 g 4-(Dimethylamino)benzaldehyde (Sigma, 39070) was dissolved in 6 mL n-propanol and 3 mL 70% perchloric acid (Sigma, 244252) and the solution wrapped in tin-foil until use.
- Hydroxyproline standard – 50 µg/mL hydroxyproline solution was prepared from 1 mg/mL stock in PBE and vortexed.

A standard curve was prepared in triplicate using a clear 96-well plate (**Figure 3.3**). 60 μL of samples and standards were used. To each well, 20 μL assay buffer and 40 μL Chloramine-T reagent was added and the plate was incubated for 20 minutes at room temperature in the dark to allow hydroxyproline oxidation. 80 μL DMBA reagent was added to each well ensuring solution is well mixed and clear. The plate was sealed and incubated for 20 minutes at 60°C for 20 minutes and then cooled to room temperature. The seal was removed, and absorbance read at 570 nm using the SpectroNano Star plate reader.

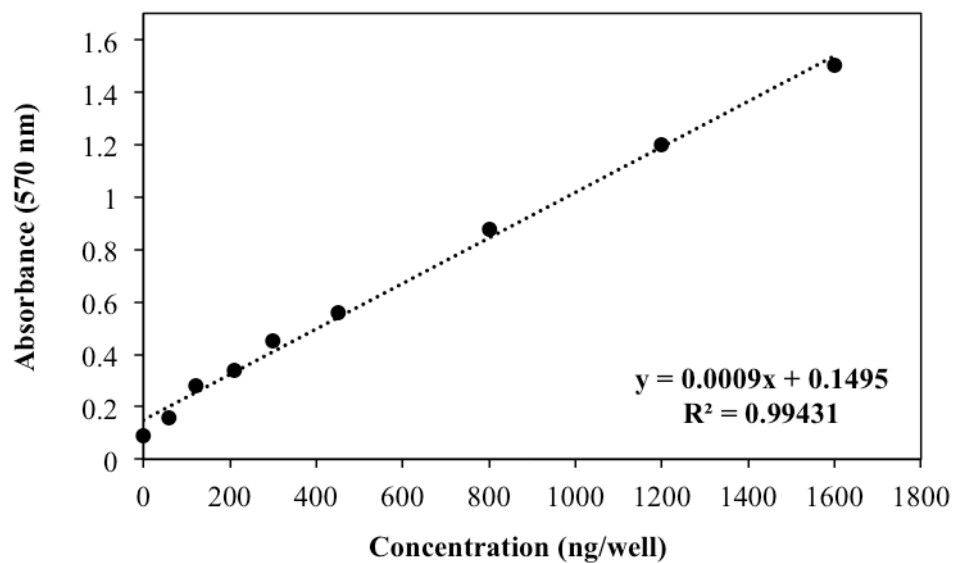


Figure 3.3: Typical hydroxyproline assay standard curve showing the linear relationship between absorbance (570 nm) and *trans*-4-Hydroxy-L-proline dye.

3.2.5 Determining elastin content

For determination of elastin content in fetal membranes, the fastin elastin quantitative dye-binding method (Biocolor) was used, which employs the dye 5, 10, 15, 20-tetraphenyl-21H,23H-porphine tetra-sulfonate (TPPS). The binding of TPPS to elastin was first discovered in 1962 and termed “The Winkelman Reaction” after James Winkelman who discovered that most tissues took up the dye but only elastin would retain TPPS overtime. The assay has the ability to measure soluble tropoelastins, lathyrogenic elastins, and insoluble elastins when solubilized to elastin polypeptide fragments (α -elastin, κ -elastin). The TPPS dye binds to non-polar and basic amino acid sequences found within mammalian elastin. It contains four sulfate groups and a synthetic

porphyrin, 5,10,15,20-tetraphenyl-21H, 23H-porphyrin, which is water soluble in the sulfonate form.

Extraction of insoluble elastin from fetal membrane

Samples were lyophilized to obtain dry weight. Hydrophobic elastin within the fetal membrane tissue was first converted to a water-soluble derivative (α -elastin) by heating to 100°C in 0.25 M oxalic acid for one hour using a metal heating block. Samples were cooled to room temperature and centrifuged at 10,000 rpm for 10 minutes. The supernatant was collected and used for analysis. The residual tissue was then treated again with 0.25 M oxalic acid for one hour at 100°C. Initially, three heat extractions were used to determine if complete solubilisation of the tissue elastin had occurred.

More than 98% tissue elastin was obtained from extraction 1. 50 μ L of test sample and α -elastin standard were prepared in duplicate aliquots. Reagent blanks were prepared using 100 μ L of test solution solvent (buffer/PBS/water/0.25 M oxalic acid).

Elastin isolation

Elastin was precipitated using elastin precipitating reagent pre-cooled to 4°C in a ratio of 1:1. Equal volumes were added to both standards and test samples. The microcentrifuge tubes were vortexed and left for 15 minutes at room temperature to complete precipitation of α -elastin. Tubes were centrifuged at 10,000 x g for 10 minutes to pack the precipitated α -elastin. The tube was then inverted and supernatant discarded. Elastin-dye complex formation was performed by adding 1 mL dye reagent to each tube. The contents were then mixed by inverting and elastin precipitate dispersed by vortexing. Tubes were then placed on a shaker at room temperature for 1.5 hours to allow sufficient reaction between α -elastin and the dye reagent. Tubes were then centrifuged at 10,000 x g for 10 minutes. Supernatant was removed by inverting and tapping the tube to ensure excess unbound dye was removed. The elastin-dye complex can be observed as a reddish-brown deposit. Dye dissociation reagent (250 μ L) was then added to each tube and vortexed. Tubes were then left at room temperature for 10 minutes before vortexing again to ensure all dye passed into solution. The contents of each tube were then transferred to a 96-well microplate (250 μ L/well) and absorbance read at 513 nm. The absorbance of elastin reference standards were plotted to determine elastin content within test samples.

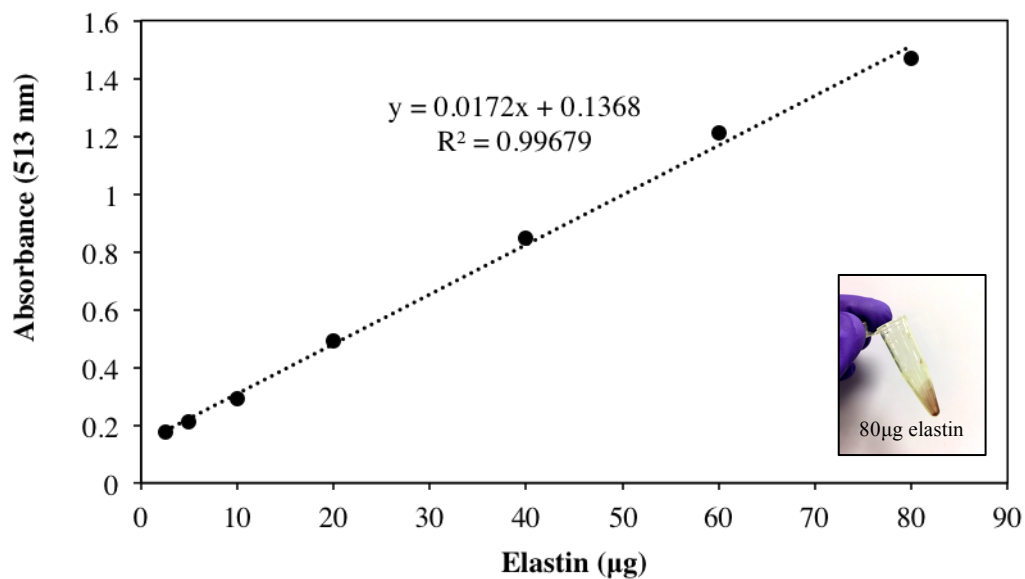


Figure 3.4: Typical elastin assay standard curve showing the linear relationship between absorbance (513 nm) and elastin standard.

3.2.6 Determining prostaglandin E₂ release

Prostaglandin E₂ concentration was determined using the Parameter PGE₂ immunoassay (R&D Systems), which is based on a forward sequential competitive binding technique. PGE₂ competes with horseradish peroxidase (HRP)-labeled PGE₂ for a limited amount of binding sites on a mouse monoclonal antibody. During the first incubation PGE₂ within the sample was allowed to bind to sites on the monoclonal antibody. During the second incubation HRP-PGE₂ binds to the remaining monoclonal antibody binding sites. After washing to remove unbound materials, enzyme activity was determined by addition of a substrate solution. The colour development was then stopped using a stop solution and the absorbance was read at 450 nm (**Figure 3.5**). Colour intensity was inversely proportional to PGE₂ sample concentration.

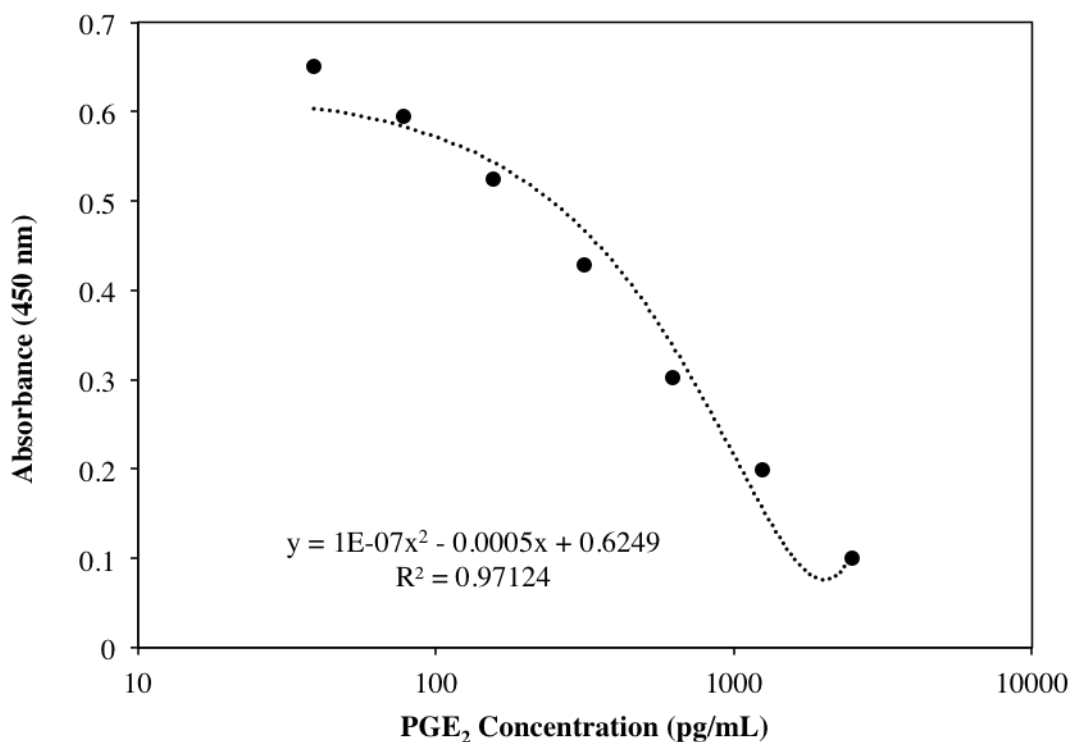


Figure 3.5: Typical prostaglandin E₂ assay standard curve showing the relationship between absorbance (450 nm) and PGE₂ standard based on a forward sequential competitive binding technique.

3.2.7 Determining total MMP activity

Protease activity was measured using the fluorogenic peptide substrate (BIOMOL Cat. P-128) with sequence: DNP-Pro-β-cyclohexyl-Ala-Gly-Cys(Me)-His-Ala-Lys(NMA)-NH₂ (DNP=2,4-dinitrophenyl; NMA=N-Me-2-aminobenzoyl). Proteases (MMP-1, MMP-3, MMP-7, MMP-8, MMP-9, MMP-11, MMP-12, MMP-13, ADAM9/MDC9) cleave the Gly-Cys(Me) peptide bond resulting in a strong fluorescence by NMA (quencher) at 440 nm, once cleavage separates it from the aromatic DNP moiety. The active protease activity can be measured by correlating with fluorescence.

The peptide substrate (MW: 1077.2) was dissolved with DMSO to 20 mM stock concentration and stored at -20°C in the dark. 10X substrate assay buffer [500 mM HEPES + 100 mM CaCl₂ + 0.5% Brij-35 (30% conc.)] was prepared and pH maintained at 7 using 1 M formic acid or 1 M NaOH. This was used to prepare 1X substrate assay

buffer A (without EDTA) and 1X substrate assay buffer B (with 500mM EDTA). 20 mM MMP substrate was added to each buffer to a concentration of 10 μ M (1:2000 dilution). EDTA stops reaction and therefore 1X substrate assay buffer B was used as a negative control. Substrate assay buffer A and B alone were also used as negative controls. 20 μ L of sample was added to a 96-well black flat-bottomed Nunc™ F96 MicroWell™ plate and 50 μ L substrate assay buffer A or B was added in triplicate. A linear regression analysis of fluorescence at 340 nm excitation from 0-120 minutes was measured using the BMG FLUOstar OPTIMA microplate reader with shaking before each cycle (cycle number = 75 seconds; flashes = 10; delays = 0.5).

3.2.8 Western blotting

Western blotting was performed to investigate protein expression of Cx43, AKT, and the housekeeping control, GAPDH in amniotic membrane samples.

Protein isolation

RIPA lysis buffer (Sigma R0278) was prepared by adding 1 Roche complete mini protease inhibitor cocktail tablet per 10 mL buffer and supplementing with 50 μ L 200 mM activated sodium orthovanadate (Na_3VO_4) phosphatase inhibitor. Briefly, 200 mM Na_3VO_4 (Sigma S6508) was prepared by dissolving 367.8 mg in 10 mL ultra pure water (UPW) and pH adjusted to 10 using 1 M NaOH or 1 M HCl. At pH 10 Na_3VO_4 appears as a yellow solution, which was then boiled until the solution turned colourless and pH readjusted to 10. Tissue samples were snap frozen in liquid nitrogen prior to homogenisation using the Mikro Dismembrator U (Sartorius) for 2 minutes at 2000 rpm. The resulting tissue powder was resuspended in 100 μ L RIPA lysis buffer. To ensure efficient homogenization, the lysate was then triturated through a 21G needle with a 1 mL syringe up to 5 times. The lysate was then centrifuged for 15 minutes at 14,000 rpm and the supernatant containing the soluble protein fraction was collected.

3.2.8.1 BCA assay

A Bicinchonic Acid (BCA) assay kit (Pierce 23227) was used to determine protein concentration. Bovine serum albumin (BSA; Sigma A2153) was used as the standard to generate a standard curve ranging from 0 – 2 mg/mL. A working reagent was prepared by adding BCA Reagent A to BCA Reagent B in a 50:1 ratio. 10 μ L of each sample and standard was added to a 96-well microplate in duplicate and 200 μ L of working reagent added to each well. The plate was mixed on a plate shaker for 30 seconds and then incubated at 37°C for 30 minutes. The SPECTROstar Nano (BMG Labtech) microplate reader was used to measure absorbance at 562 nm. A 4-parameter logistic regression curve (**Figure 3.6**) was generated using blank corrected absorbance values for each BSA standard against concentration (μ g/mL) to determine protein concentration of unknown samples.

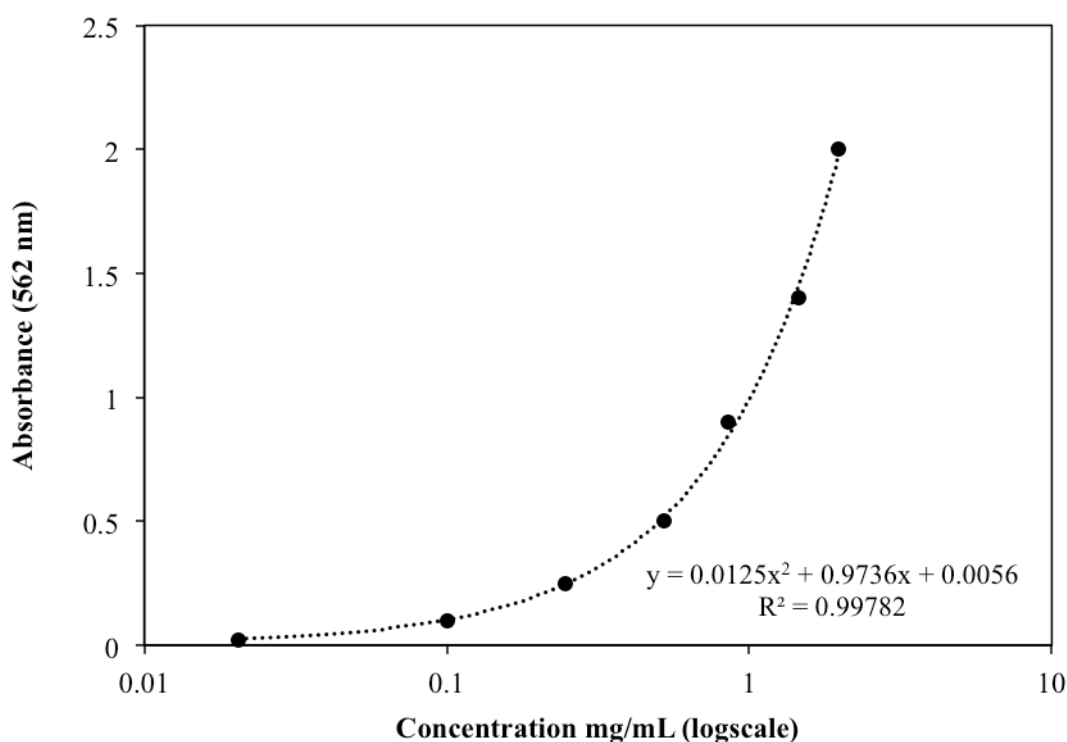


Figure 3.6: Typical BSA standard curve showing the relationship between absorbance (562 nm) and BSA standard.

3.2.8.2 SDS PAGE and protein transfer

An equal volume of the supernatant soluble protein fraction (20 µg) was mixed with Laemmli 2x (Sigma 83402) loading buffer and boiled for 5 minutes at 100°C to denature proteins. Precast gels (Bio-Rad 456-9033) were removed from packaging and rinsed with 1x running buffer prepared from 10x tris/glycine/SDS (Bio-Rad 161-0732). The kD™ Mini-PROTEAN® TGX™ precast gel was then placed in the loading bath and 1x running buffer loaded up to corresponding line depending on amount of gels being run. 30 µL of protein samples were then loaded into each well along with 5 µL of a Precision Plus Protein™ WesternC™ standard (Bio-Rad 161-0376) and the gel run at 200 mV for 30 minutes.

The gel was removed from the cassette after SDS-PAGE and placed into a Tran-Blot Turbo™ mini nitrocellulose transfer pack (Bio-Rad 170-4158). A roller was used to remove air bubbles and the protein transfer was run at 25V for 7 minutes. The nitrocellulose membrane was removed and stained in 0.1% Ponceau S (Sigma 141194) for 2 minutes to locate protein bands. The membrane was washed in PBS + 0.1% Tween for 5 minutes and placed into a 50 mL tube. 5% BSA was used to block for 1 hour on a roller at room temperature. The blocking solution was removed and primary antibody at desired concentration (**Table 3.1**) with endogenous control primary antibody added with PBS + 0.1% Tween and 5% BSA overnight at 4°C on a roller. The membrane was then washed with PBS + 0.1% Tween three times for 10 minutes at room temperature on a roller. The secondary antibody at the desired concentration (**Table 3.1**) was added with PBS + 0.1% Tween and 5% BSA for 1 hour in the dark at room temperature on a roller. The membrane was washed twice in PBS + 0.1% Tween for 10 minutes and once in PBS for 10 minutes in the dark at room temperature on a roller.

3.2.8.3 Protein blot imaging

Protein blots were scanned using the LI-COR Odyssey infrared imaging system for protein detection via infrared fluorescence. The Odyssey software was used for quantitative analysis of protein bands. Integrated intensity values were exported, and data normalized to endogenous control values.

Membrane stripping

Protein blots were stripped by incubating in restore western blot stripping buffer (Thermo Scientific) for 30 minutes at room temperature with gentle agitation. Blots were washed twice in PBS-T for 10 minutes and could then be blocked as previously described.

3.2.9 List of antibodies used in this thesis

Table 3.1: *Details of primary and secondary antibodies used in the present study.*

Antibody	Species	Predicted band size (kDa)	Company (Catalogue no.)	Dilution
Cx43	Rabbit	43	Sigma C6219	1:4000 (IFM) 1:8000 (WB)
AKT-1/2/3	Rabbit	56	Abcam 126811	1:1000 (WB)
GAPDH	Mouse	36	Abcam 8245	1:10,000 (WB)
Alexa Fluor® 488	Goat (anti-rabbit IgG)	-	Molecular probes® (Life Technologies™)	1:400
IRDye 800CW	Donkey (anti-rabbit IgG)	-	LI-COR 926-32213	1:10,000 (WB detection)
IRDye 680RD	Goat (anti-mouse IgG)	-	LI-COR 926-68070	1:10,000 (WB detection)

IFM: Immunofluorescence microscopy; WB: Western blot

3.3 Measuring gene expression

Gene expression analysis was performed for Cx43, COX-2, COL1A1, and GAPDH genes using the following steps outlined in this section.

3.3.1 RNA extraction

Total RNA was extracted from tissue samples that had been stored in liquid nitrogen or preserved in RNALater. The workbench and homogenizing apparatus were cleaned of RNase contamination using RNase Away (Sigma-Aldrich). The Mikro Dismembrator U (Sartorius) tissue homogeniser was used to grind frozen tissue samples by placing the snap frozen tissue sample in the grinding chamber at 2000 rpm for 2 minutes. The grinding chamber also contained a metal ball bearing to assist homogenization. Following the homogenization, the chamber was removed and placed in a fume hood. TRI reagent (Sigma-Aldrich) added to the chamber covering the ground tissue and allowed to thaw for 5 minutes. TRI reagent is a monophasic solution of phenol and guanidinium isothiocyanate that denatures proteins and solubilizes biological material. A micropipette was then used to mix the thawed solution and transfer to a clean RNase-free tube.

3.3.2 RNA isolation and purification

To each tube containing the solubilised tissue solution, 200 μ L of chloroform (Sigma-Aldrich) was added and tubes were vortexed. The tubes were then centrifuged for 5 minutes at 12,000 x g. Chloroform causes the solution to separate into 3 phases: (1) The aqueous phase containing RNA; (2) the middle interphase containing DNA; and (3) the organic phase containing proteins and lipids. The aqueous phase containing RNA was carefully transferred to a fresh RNase-free tube ensuring no contamination with the interphase containing DNA. Molecular biology grade isopropanol was then added to precipitate the RNA. The tube was vortexed and left for 10 minutes at room temperature to ensure full precipitation. The precipitated RNA was centrifuged for 10 minutes at 12,000 x g. The supernatant was discarded, and the RNA pellet was washed using ice cold 75% ethanol and mixed by gentle inversion. The tube was centrifuged for 5 minutes at 7,500 x g and the supernatant (ethanol) discarded. The tube was inverted and left to air

dry for 10 minutes to remove excess ethanol. The RNA pellet was resuspended using 100 μ l RNase-free water and vortexed if necessary to assist RNA rehydration.

The RNeasy mini kit (Qiagen) was used for RNA purification and all work was performed on ice. Lysis Buffer RLT and 100% ethanol was added to the sample and mixed by pipetting. The solution was transferred to an RNeasy spin column and centrifuged at 8,000 x g for 1 minute. The flow through was discarded. Wash Buffer RW1 was added to the RNeasy spin column and centrifuged at 8,000 x g for 1 minute. The flow through was discarded. This was repeated with half the volume of wash Buffer RW1 and the flow through discarded following centrifugation at 8,000 x g for 1 minute. Elution Buffer RPE was added to the RNeasy spin column and incubated for 5 minutes at room temperature. Following incubation, the RNeasy spin column was centrifuged at 8,000 x g for 1 minute, and the flow through discarded. Ice cold 75% ethanol was added to the RNeasy spin column and centrifuged at 8,000 x g for 2 minutes. The flow through was discarded and the column allowed to dry for 5 minutes to remove ethanol. The RNeasy spin column was then centrifuged again at 8,000 x g for 5 minutes to remove traces of ethanol. The inner RNeasy spin column was then transferred to a fresh collection tube and 50 μ L RNase-free water was added. To elute the RNA the RNeasy spin column was centrifuged at 10,000 x g for 1 minute. The RNA is found in the flow through and this was transferred to a fresh RNase-free tube before removing DNA contamination.

The Ambion® DNA-free™ DNase Treatment Kit was used to remove DNA contamination from the RNA preparations and then remove DNase and divalent cations (magnesium and calcium which catalyse RNA degradation when heated) from the sample. The procedure is designed to remove trace to moderate amounts of DNA (up to 50 μ g DNA/mL RNA) from RNA preparations to a level that is non-detectable during real-time RT PCR.

Treatment was performed in 0.5 mL tubes to facilitate removal of the supernatant after treatment with the DNase inactivation reagent. 10X DNase I buffer (0.1 volume) and 1 μ L rDNase I was added to the RNA and gently mixed. The solution was incubated for 30 minutes at 37°C. The DNase inactivation reagent was resuspended by vortexing and added (0.1 volume). The solution was incubated for 2 minutes at room temperature and mixed intermittently to re-disperse the DNase inactivation reagent. The tube was

centrifuged at 10,000 x g for 1.5 minutes and the supernatant (purified RNA) was transferred to a fresh tube. The Nanodrop ND-1000 spectrophotometer was used to measure yield and purity of purified RNA preparations.

3.3.3 First strand cDNA synthesis by Reverse Transcription

Reverse transcription was performed using the Enhanced Avian RT First Strand Synthesis Kit (Sigma-Aldrich) to produce high quality full-length cDNA from total RNA. Between 200 – 500 ng total RNA were transferred to a 500 μ L thin-walled PCR microcentrifuge tube and placed on ice. Nuclease-free water and 1 μ L Oligo (dT)₂₃ primer, which specifically binds the polyA tail of mRNA, was added to a total volume of 10 μ L. The tube was placed in a thermal cycler for 5 minutes at 70°C to denature RNA and then immediately placed onto ice to prevent RNA aggregation. A mastermix was prepared for each reaction using 10X buffer for eAMV-RT (1X final concentration), Enhanced avian RT enzyme (1 unit/ μ L), RNase inhibitor (1 unit/ μ L), deoxynucleotide mix (500 μ M each dNTP), and water. 10 μ L of the prepared mastermix was added to the denatured RNA to allow a total volume of 20 μ L per reaction. A minicentrifuge was briefly used to ensure all liquid had collected at the bottom of the microcentrifuge tube. Tubes were placed into the thermal cycler and heated for 1 hour at 42°C. The first strand cDNA has now been prepared and this was stored at -20°C or used immediately for the PCR amplification step.

3.3.4 Quantitative real-time PCR

Forward and reverse primer concentrations were optimized for the following genes: (1) connexin-43 (**Figure 3.8**), (2) cyclooxygenase-2 (**Figure 3.9**), (3) Collagen type I α 1 (**Figure 3.10**), and (4) GAPDH (**Figure 3.11**). Following the primer optimisation steps described below, a clear 96-well PCR plate was used to prepare each PCR reaction containing cDNA, primers and SYBR green master mix (2X) which binds to DNA. After setting up each reaction the PCR plate was briefly centrifuged to ensure all liquid was collected at the bottom of each well. The plate was placed in the Mx3000P Stratagene PCR machine. A quantitative SYBR green dye and normal 3-step PCR procedure was selected. A dissociation/melt curve was also selected to analyse the PCR specificity and

check for the formation of primer-dimers in the sample during the final analysis. The cycle parameters detailed in **Table 3.2** were used during PCR procedure.

Table 3.2: *Thermocycling conditions for quantitative polymerase chain reaction.*

1. Denaturation/RT Inactivation	95°C	3 minutes	1 cycle
2. Denaturation	95°C	30 seconds	40 cycles
3. Annealing	55°C	1 minute	
4. Extension	72°C	1 minute	
5. Final Extension	72°C	5 minutes	1 cycle
6. Hold	4°C		

3.3.5 Quantitative PCR assay optimisation and data analysis

Threshold cycle (C_T) values obtained from the Mx3000P Stratagene PCR machine were analysed using the MxPro QPCR software. Amplification plots were generated for each reaction with fluorescence (dRn) against cycle number (**Figure 3.7**). The threshold was set within the lower third of the linear phase of the amplification plot and remained constant for all experiments. Mean C_T values were normalized to GAPDH endogenous control data and the Pfaffl method used to calculate gene expression fold change as described below. Furthermore, ROX reference dye (Invitrogen) was used to normalize the fluorescent reporter signal as an internal reference to normalize for non-PCR related fluctuations in fluorescence caused by pipetting error and machine “background noise”, as well as to compensate for instrument excitation and detection variations.

Optimising the qPCR assay

Primers were optimized for use with fetal membrane cDNA samples and to ensure amplification reaction efficiencies between 95-105%. PCR primer concentrations were optimised using a dilution series of known template concentrations to establish a standard curve (**Figure 3.8-3.11**) and identify the reaction efficiencies shown in **Table 3.3**. The log starting quantity (relative, x-axis) of each known concentration in the

dilution series was plotted against the C_T value for the corresponding concentration (y-axis). A variety of information could now be deduced from this standard curve including the efficiency of the reaction and other reaction parameters that include the correlation coefficient (R^2), slope, and y-intercept. Importantly, the R^2 value is a measure of the linearity of the standard curve with <0.98 generally considered acceptable.

Table 3.3: Forward and reverse gene sequences with optimal concentrations and correlating reaction efficiency values.

Gene	Sequence	nM	Efficiency
Cx43	Forward: 5'-CTCGCCTATGTCTCCTCCTG-3', Reverse: 5'-TTGCTCACTTGCTTGCTTGT-3'	100	98%
COX-2	Forward: 5'-GGACAGGATTCTATGGAG-3', Reverse: 5'-GGATGTCAACACATAACTC-3'	200	98%
COL1A1	Forward: 5'-CCCCGAGGCTCTGAAGGT-3', Reverse: 5'-CACCAGCAATACCAGGAGCA-3'	300	101%
GAPDH	Forward: 5'-TCTCTGCTCCTCCTGTTC-3', Reverse: 5'-CGCCCAATACGACCAAAT-3'	300	97.5%

Cx43: connexin 43; COX-2: cyclooxygenase-2; COL1A1: Collagen type 1 a1; GAPDH: Glyceraldehyde 3-phosphate dehydrogenase (housekeeping gene).

Ideally, to obtain most reproducible data, the efficiency of a reaction should be close to 100% as possible, meaning the template will double after every PCR cycle during the exponential phase of the amplification. To identify the reaction efficiency, the slope of the log-linear phase from the amplification plot was used in the following equation where E = reaction efficiency:

$$E = 10^{-\left(\frac{1}{\text{slope}}\right)}$$

A number of factors can influence the efficiency of a reaction and lead to reaction efficiencies below 90% including the purity of the RNA used for cDNA synthesis, not using optimal reagent concentrations; and length, structure, and GC content of the amplicon. Furthermore, the reaction efficiency can often reach above 110% due to the presence of PCR inhibitors within the reagents. Importantly, reaction efficiency between 90% and 110% is considered acceptable which correlates to a slope of -3.58 to -3.10 and

assists towards PCR assay reproducibility. Furthermore, the specificity of primers were improved following optimisation procedures (**Figure 3.12**).

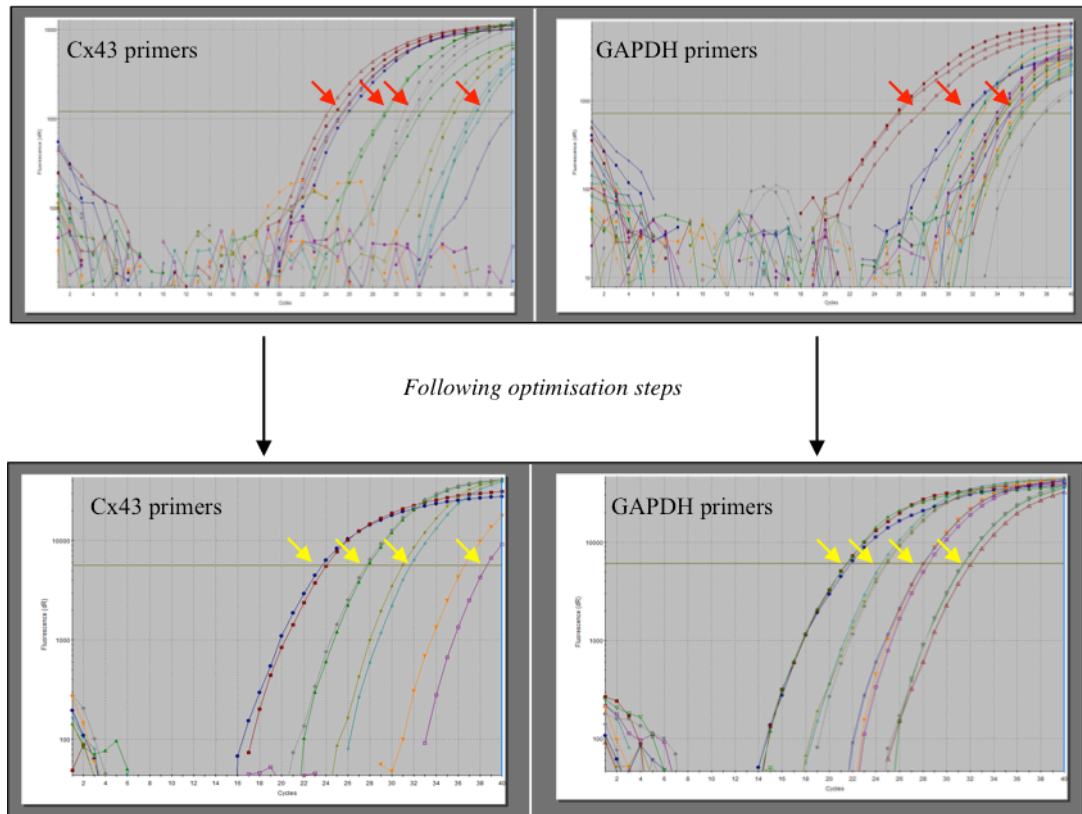


Figure 3.7: Amplification plots showing typical before and after amplifications for Cx43 and GAPDH qPCR assays following several optimisation steps that improved RNA purification, DNA contamination removal prior to first strand cDNA synthesis, and optimisation of primers during the final qPCR assay. The bottom panel shows amplification plots with negligible noise indicating removal of DNA contamination. Repeats reactions also appear reproducible compared to top panel following optimisation steps. The amplification plots show typical 10-fold dilution series for Cx43 primers (left) and GAPDH primers (right) where red arrows indicate poor repeats prior to optimisation steps and yellow arrows show improved coupling of repeats at each dilution of cDNA.

The optimal reaction efficiency obtained from standardized PCR assays were then used to help calculate gene expression fold change using the Pfaffl's method¹⁷⁴, which uses the equation below during analysis of C_T values, taking into account reaction efficiency values (*E*).

$$\text{Ratio} = \frac{(1 + E_{\text{Target}})^{\Delta C_T} (\text{MEAN}_{\text{Calibrator}} - \text{Sample})}{(1 + E_{\text{Reference}})^{\Delta C_T} (\text{MEAN}_{\text{Calibrator}} - \text{Sample})}$$

Typical standard curve analysis for Cx43, COL1A1, GAPDH, and COX-2 primers

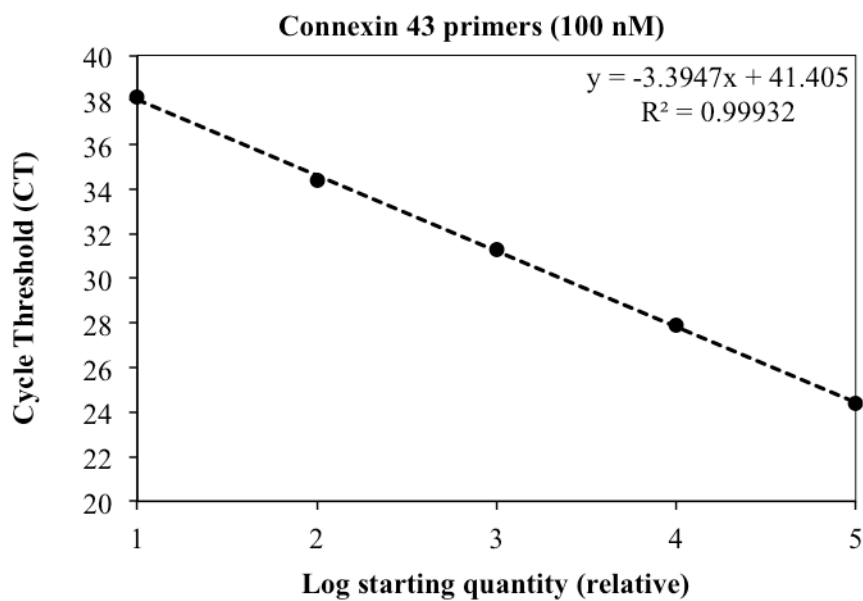


Figure 3.8: Standard curve showing initial copy number of template vs. threshold cycle (Ct). Real-time PCR of 10-fold serial dilutions of human amniotic membrane cDNA was performed using 100 nM of a Cx43 forward and reverse primer. Reactions (3 replicates per dilution) were incubated 2 minutes at 95°C, followed by 40 cycles of 95°C, 15 sec; 60°C, 1 minute; 72°C, 1 minute using an Mx3000P quantitative PCR instrument.

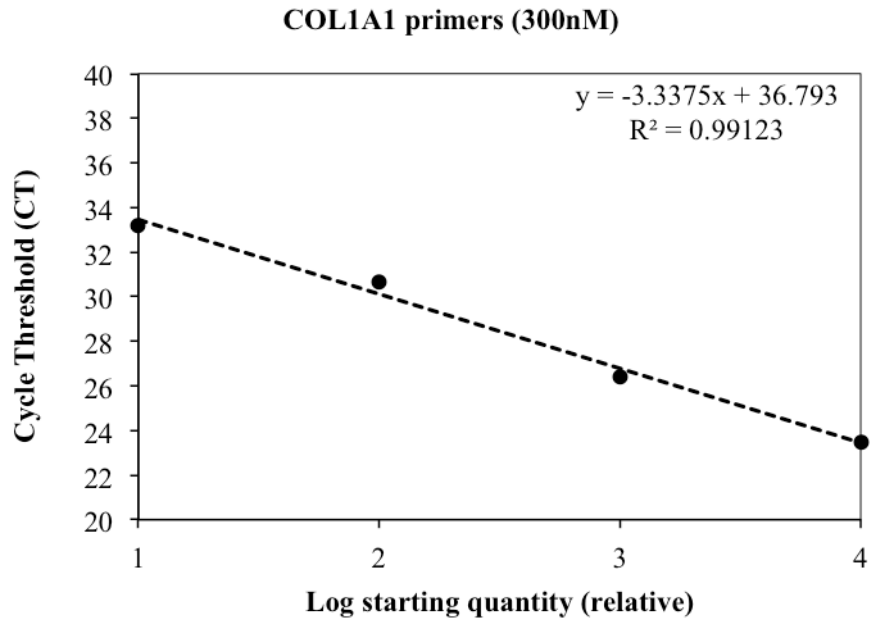


Figure 3.9: Standard curve showing initial copy number of template vs. threshold cycle (Ct). Real-time PCR of 10-fold serial dilutions of human amniotic membrane cDNA was performed using 300 nM of a COL1A1 forward and reverse primer. Reactions (3 replicates per dilution) were incubated 2 minutes at 95°C, followed by 40 cycles of 95°C, 15 sec; 60°C, 1 minute; 72°C, 1 minute using an Mx3000P quantitative PCR instrument.

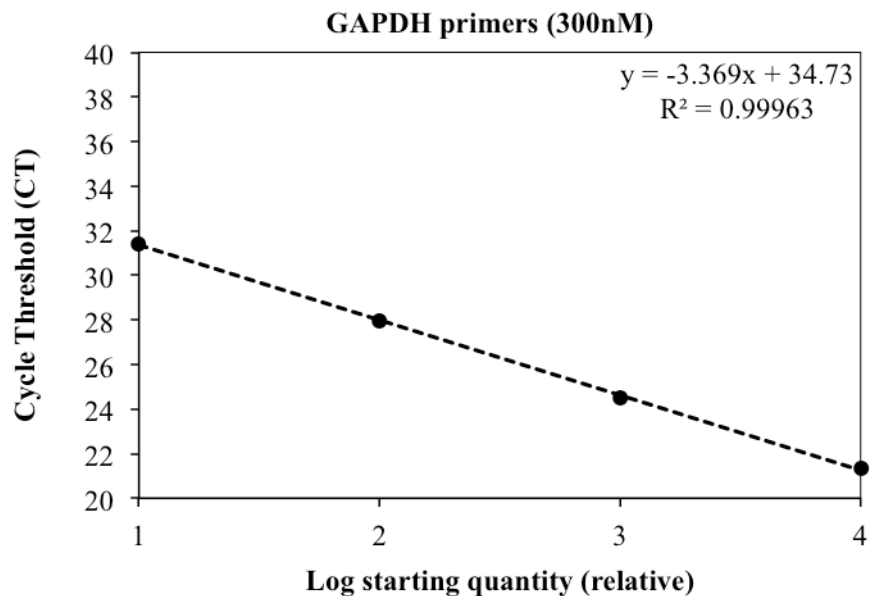


Figure 3.10: Standard curve showing initial copy number of template vs. threshold cycle (Ct). Real-time PCR of 10-fold serial dilutions of human amniotic membrane cDNA was performed using 300 nM of a GAPDH forward and reverse primer. Reactions (3 replicates per dilution) were incubated 2 minutes at 95°C, followed by 40 cycles of 95°C, 15 sec; 60°C, 1 minute; 72°C, 1 minute using an Mx3000P quantitative PCR instrument.

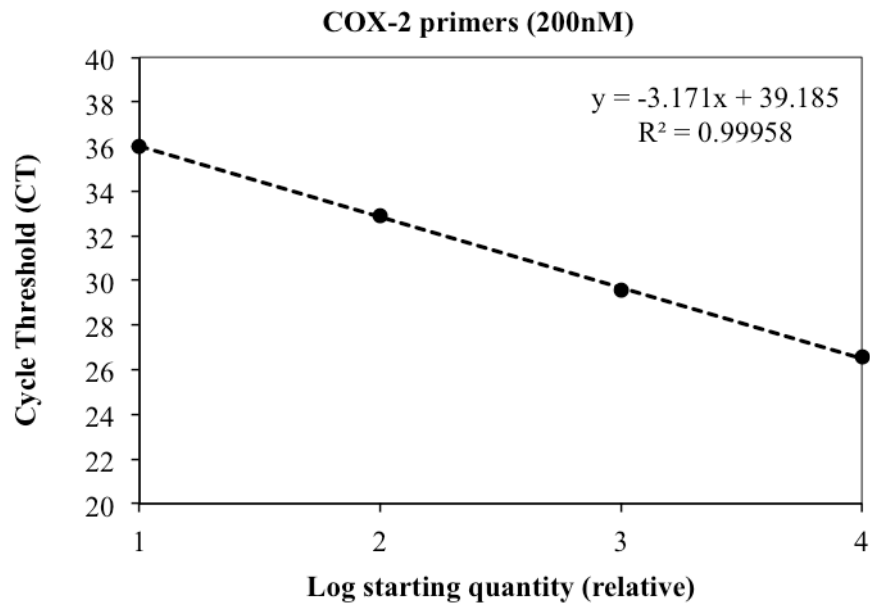


Figure 3.11: Standard curve showing initial copy number of template vs. threshold cycle (Ct). Real-time PCR of 10-fold serial dilutions of human amniotic membrane cDNA was performed using 200 nM of a COX-2 forward and reverse primer. Reactions (3 replicates per dilution) were incubated 2 minutes at 95°C, followed by 40 cycles of 95°C, 15 sec; 60°C, 1 minute; 72°C, 1 minute using an Mx3000P quantitative PCR instrument.

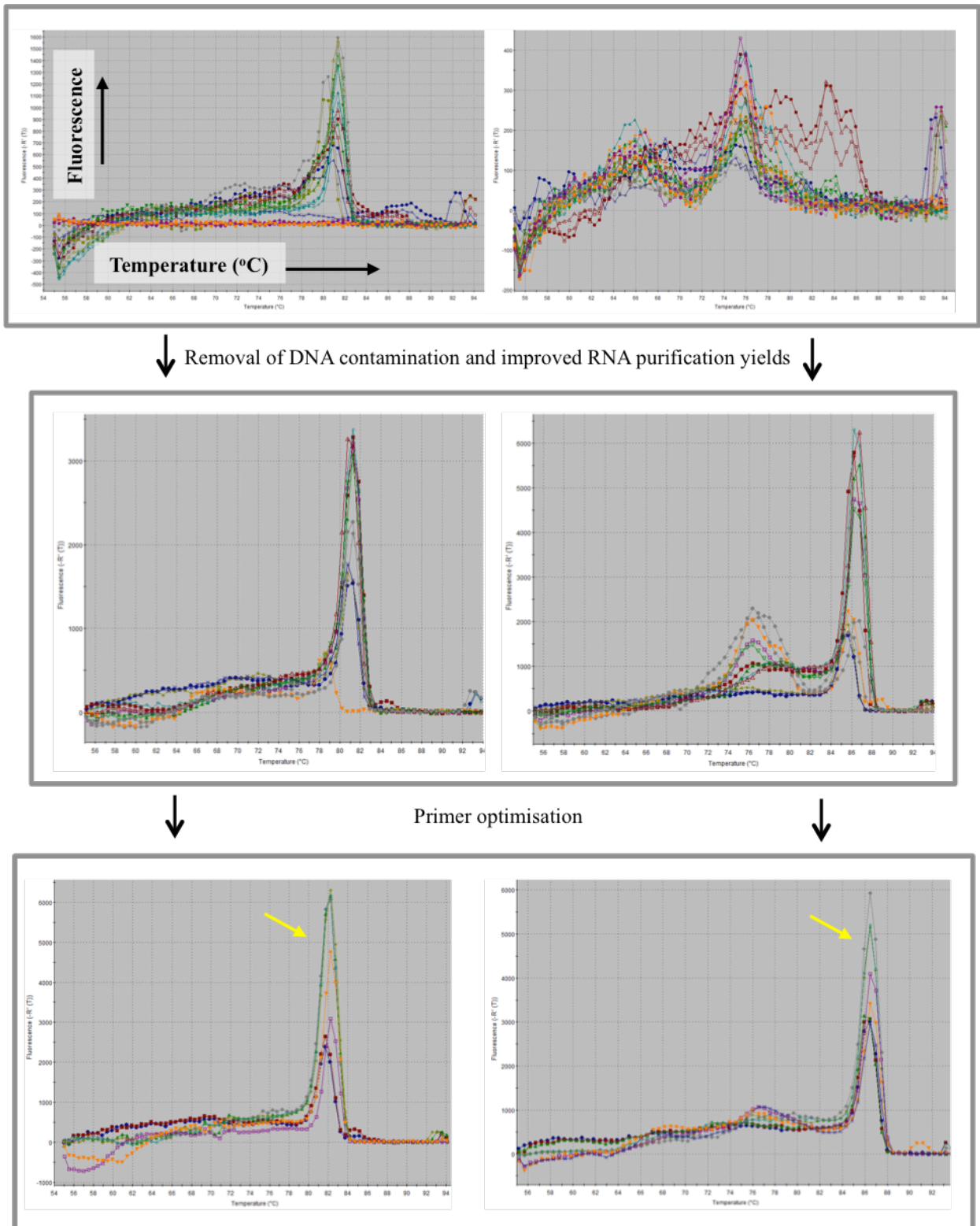


Figure 3.12: Melting curve analysis before and after key optimisation steps taken in the design of the PCR protocol. Cx43 and GAPDH primers are given here as an example. Key steps included improvement of RNA purification, DNA contamination removal prior to first strand cDNA synthesis, and primer optimisation. A rise in absorbance intensity indicates the dissociation of double-stranded DNA during heating; therefore, ideally a single peak (yellow arrow) is desirable and indicates a high standard of primer specificity without primer-dimer formation.

3.4 Determining cell viability

Live-dead staining

Cell viability was determined using a two-colour assay to stain and identify viable or non-viable cells within the tissue using Calcein-AM (Molecular Probes, Cambridge, UK) and Ethidium homodimer-1 (Calbiochem, Nottingham, UK), respectively. To assess cell viability of fetal membrane specimens, 2 mL DMEM+20%FBS containing 5 μ M Calcein-AM and 5 μ M Ethidium homodimer-1 was prepared. The tissue specimen was submerged fully in the solution for 30 minutes with gentle agitation at room temperature. The specimen was then mounted on a glass slide and a coverslip was placed on top to flatten the tissue. Calcein-AM can permeate cells and is non-fluorescent, however, upon contact with intracellular ubiquitous esterases, calcein-AM is converted to highly fluorescent polyanionic calcein which is well retained within live cells. In live cells, calcein produces an intense uniform green fluorescence (\sim 515 nm) when excited at \sim 495 nm. Ethidium homodimer-1 enters non-viable cells where the cell membrane has been perforated and non-covalently binds to nucleic acids producing a 40-fold increase in fluorescence. In non-viable cells, Ethidium homodimer-1 will bind DNA and emit a red fluorescence (635 nm) when excited with green light at 495 nm.

Data procurement and statistical analysis

To determine cell viability, fluorescence microscopy (Leica, Milton Keynes, UK) was used with a x20 objective. A typical fetal membrane sampling area was imaged with a field view of approximately 0.5 mm x 0.5 mm and the number of viable (green) and non-viable (red) cells were recorded. The percentage viability was then calculated [(viable cells/total cells)*100%] through full thickness fetal membrane containing both epithelial and fibroblast layer cell populations. The mean percentage viability was calculated from 3 replicate cell counts from different field views of approximately 0.5 mm x 0.5 mm and data presented with standard error of the mean. To determine cell viability in fetal membrane that had been treated with various peptide amphiphile solutions, the same procedure was performed however, the tissues were previously incubated with specific peptide amphiphiles in 24-well plates for 2 hours at 2% (w/v). The peptide amphiphile

solution was then replaced with DMEM+20%FBS for up to 24 hours before assessing cell viability.

3.5 Immunofluorescence confocal microscopy

Tissue preparation

Amniotic membrane samples were fixed in 4% PFA for 2 hours at room temperature and then transferred to PBS. Samples were washed twice in PBS for 5 minutes on a shaker. After the second wash, samples were transferred to PBS +Triton X-100 (0.1%) + lysine (0.1%) to permeabilise intact cell membranes in order for primary and secondary antibodies to enter the subcellular structure and bind target antigens. Tissue samples were then blocked to reduce non-specific binding using 1% serum from the secondary antibody host (rabbit) with PBS + Triton X-100 (0.1%) and placed on a shaker at room temperature for 1 hour.

The primary antibody for Cx43 (anti-rabbit; Sigma-Aldrich C6219) was then used to stain blocked tissue samples at 1:4000 dilution in PBS + Triton X-100 (0.1%). Primary antibody stain was placed in cold room (4°C) overnight on a shaker (16 hour incubation). The tissue was washed in PBS 3 times on a shaker for 5 minutes each. Alexa Fluor 488 anti-rabbit (Life Technologies) was used as a secondary antibody at a dilution of 1:400 in PBS + Triton X-100 (0.1%). Tissue samples were incubated for 1.5 hours on a shaker at room temperature and then washed in PBS 3 times on a shaker at room temperature for 10 minutes each. DAPI was then used to stain DNA by diluting to 1:1000 and incubating in PBS +Triton X-100 (0.1%) for 15 minutes at room temperature on a shaker. Samples were then washed 3 times in PBS for 5 minutes on a shaker at room temperature.

Tissue samples were carefully placed onto Superfrost/Plus microscope slides (Fisher 12-550-15) and folds removed carefully using tweezers with minimal manipulation of the tissue. Three drops of viscous CitiFluor (anti-fade mountant) were added to the tissue and coverslips (22x30-1.5, Fisher 12-544-D) carefully lowered onto the solution to reduce the chance of air bubbles. Clear varnish was used to seal the coverslip and slides were stored at 4°C in the dark until imaging.

Antibody control staining was performed to identify the specificity of the Cx43 antibody. Primary and secondary antibody incubations alone reveal no punctate staining (**Figure 3.13 a, b**). However, positive control staining of mesenchymal cells within the fibroblast layer of the amniotic membrane reveal punctate staining expected from Cx43 plaques (**Figure 3.13 c**, green channel) of around 0.1 – 1 μm . Increasing the intensity of the green channel reveals autofluorescence of mesenchymal cells in all conditions (**Figure 3.13 a-c**, dark green).

Amniotic membrane samples were imaged using a Leica TCS SP8 acousto-optic beamsplitter (AOBS) multi-photon laser scanning confocal microscope (Leica, Milton Keynes, UK) with a Coherent Chameleon Ultra, Ti Sapphire mode-locked IR laser (Coherent UK Ltd, Cambridge, UK). Samples were imaged using a 25x/0.95 NA water-immersion objective. The Cx43 signal (920 nm excitation) was collected with the non-descanned external HyD detector through a FITC emission filter (500 – 550 nm barrier filter). The DAPI signal was collected sequentially with 405 nm excitation to avoid bleed through of the nuclear signal into the Cx43 signal and emission signal via the confocal pin-hole to the de-scanned HyD detector between 400 and 490 nm.

Microscope slides were placed into the slide holder on the mechanical stage and could be manipulated using the IPC2U microscope controls in X, Y and Z directions. Before imaging the Leica STP6000 monitor was switched on and the optical parameter oscillator (OPO) and remote was connected. Prior to imaging, the condenser was always reset to ensure the light was focused at the correct distance from the sample.

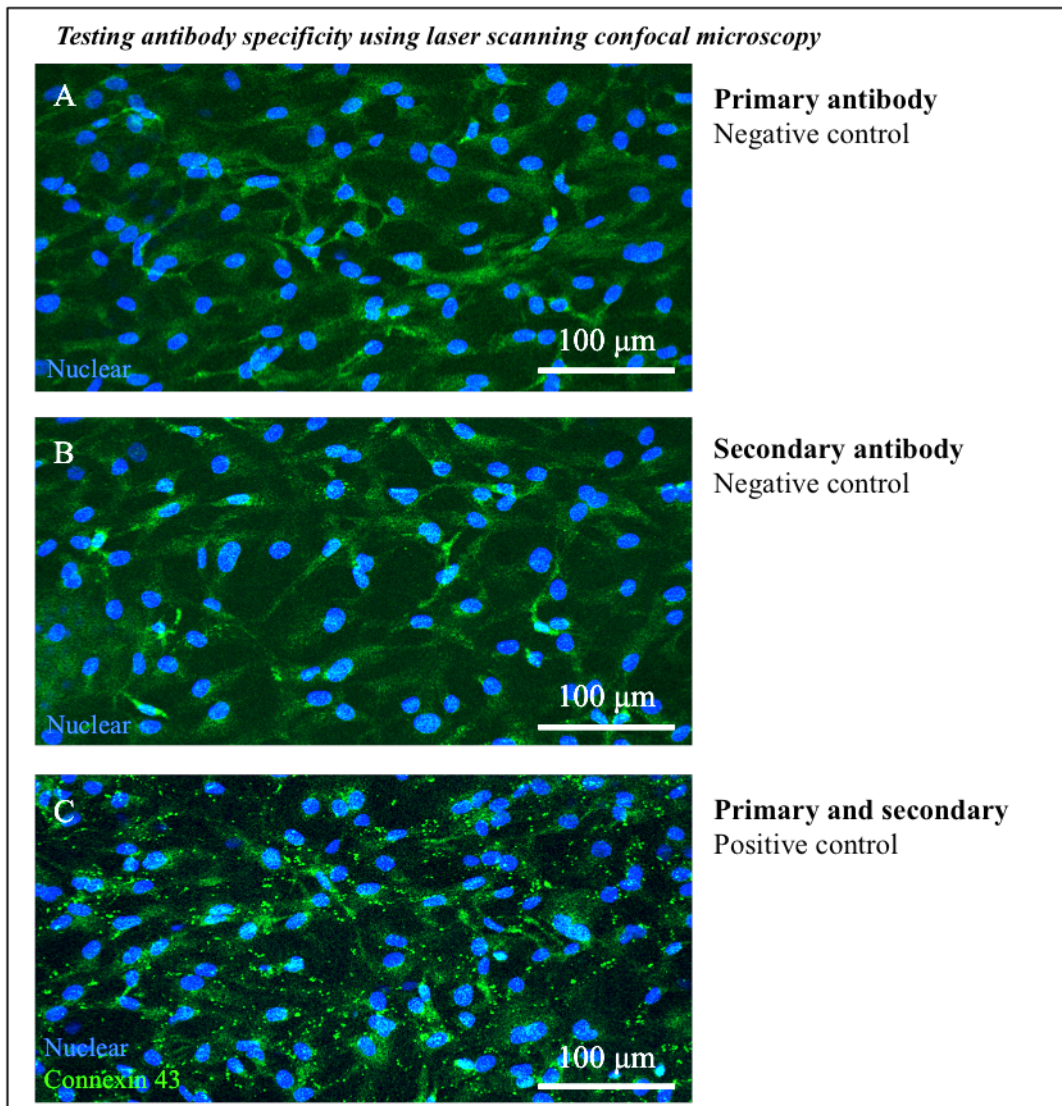


Figure 3.13: Cx43 antibody specificity was determined by staining cervical term amniotic membrane tissue in incubations of primary antibody only (A) secondary antibody only (B) and positive control primary and secondary antibody (C). When threshold was increased during image analysis, autofluorescence of mesenchymal cells is present in negative controls (A,B), however with the same threshold, connexin-43 plaques (0.1 -1 μm) can be seen using 1:4000 dilution Cx43 primary antibody and 1:400 dilution Alexa Fluor® 488 secondary antibody (C).

3.6 Second-harmonic generation imaging microscopy

Second-harmonic imaging microscopy utilises the non-linear optical effect known as second-harmonic generation (SHG). As above, the Leica TCS SP8 AOBS multi-photon confocal laser scanning microscope was used for image acquisition and the SHG signal was collected via the transmission detector and 430 – 450 nm barrier filter with a pump wavelength of 880 nm at 80 fs pulse width. To obtain SHG signals the 460/20 nm SHG filter (half 920 nm wavelength) was inserted. The pinhole was set to maximum throughout imaging. The SHG signal was collected sequentially with Cx43 and DAPI signals, therefore the laser was retuned automatically following collection of these signals.

3.7 Image analysis

3.7.1 Immunofluorescence data analysis

Full thickness volumes (approximately 150 μm) of amniotic membrane samples were acquired at 1.5 μm z-section intervals using the data acquisition system and Leica LAS X software; which can control the motorized stage containing the sample. **Figure 3.14** shows representative full thickness AM term explants imaged using optimal parameters for confocal laser scanning microscopy and second harmonic imaging microscopy. The parameters for laser power, detector gain, and offset remained constant for each sample so that direct comparisons could be made per patient and permit quantification. Data was collected a resolution of 1024 x 1024 and a speed of 600 Hz with bidirectional mode enabled to allow scanning in both directions. A line average of 3 was used in order to reduce background noise.

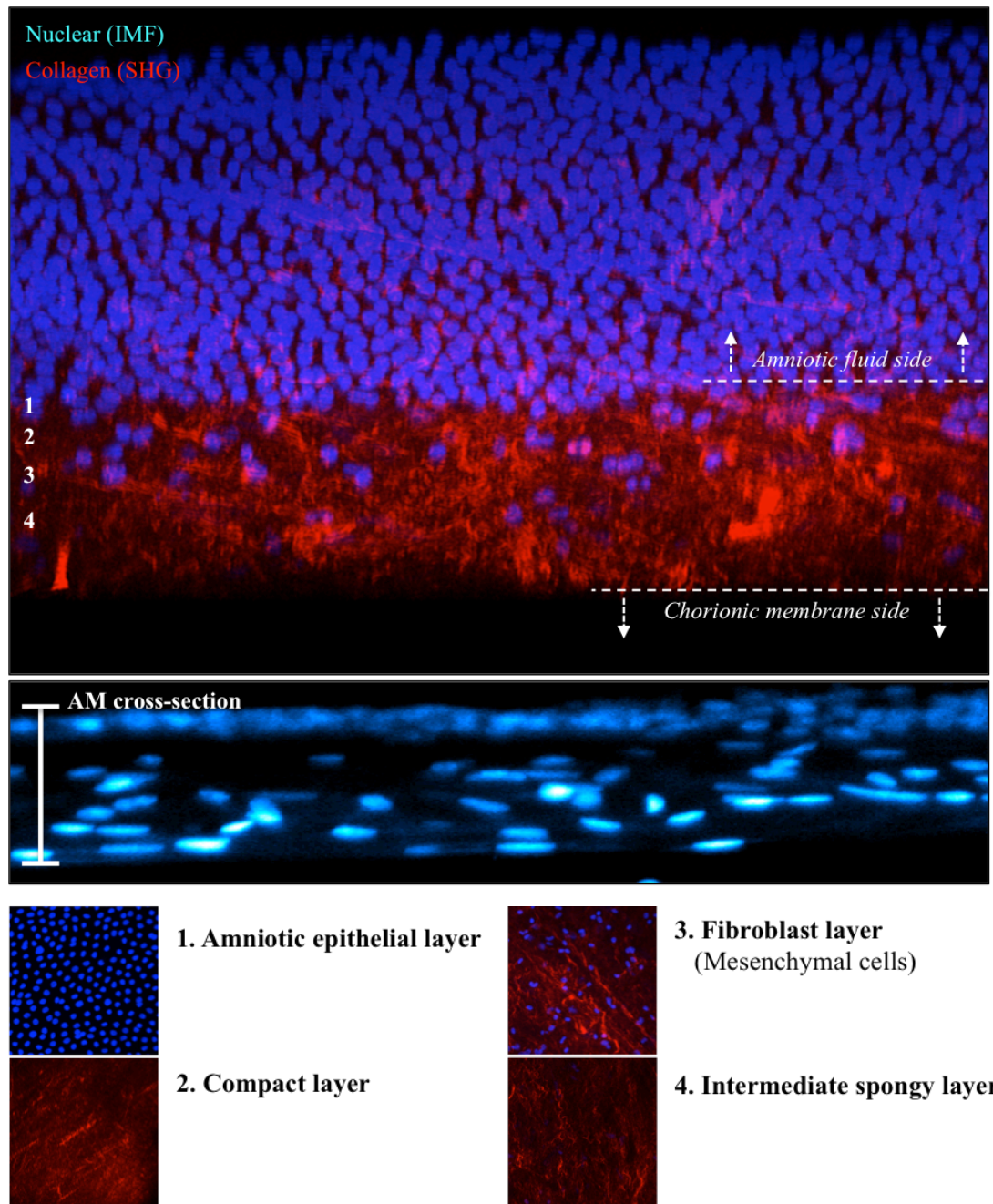


Figure 3.14: Optimal AM imaging parameters for confocal laser scanning immunofluorescence (blue – nuclei) and second harmonic generation microscopy (red – collagen). Example shows full thickness AM with separate layers including (1) amniotic epithelial layer, (2) compact layer, (3) fibroblast layer, and (4) intermediate spongy layer. The AM cross-section reveals nuclei staining for the epithelial cells of the epithelial layer (1) and mesenchymal cells of the fibroblast layer (3).

ImageJ (Fiji) was used to perform image analysis and quantification. Cx43 immunostaining levels were quantitatively evaluated per tissue area and per cell nuclei using a well-established pixel-counting method in control and wounded AM. Maximum projections were performed in the AM to examine the cell populations in the fibroblast and epithelial layer. The images were converted to binary images using identical threshold values and objects exceeding 2 pixels were counted to identify Cx43 positive pixels per tissue area (pixels per 500 μm^2 area of tissue) or per cell nuclei. Key steps taken to quantify both nuclei amount and Cx43 expression are shown in flow charts below (**Figure 3.15 and 3.16**). To quantify, initially the image was converted to binary and threshold adjusted with a dark background applied. Images were then converted to black and white and a particle analysis was performed given in pixel units. In order to remove background, 2-Infinity was applied, which removes noise of 2 pixel units or less. Results were enabled for total pixels per area in μm^2 and also total area coverage. Nuclei count was also carried out by thresholding and performing a particle analysis, however, smaller particles were excluded by applying 200-infinity and the “fill hole” parameter applied to avoid double counts. The “watershed” feature was also applied in order to separate nuclei that appeared to overlap and would have been miscounted.

Analysis of nuclei count

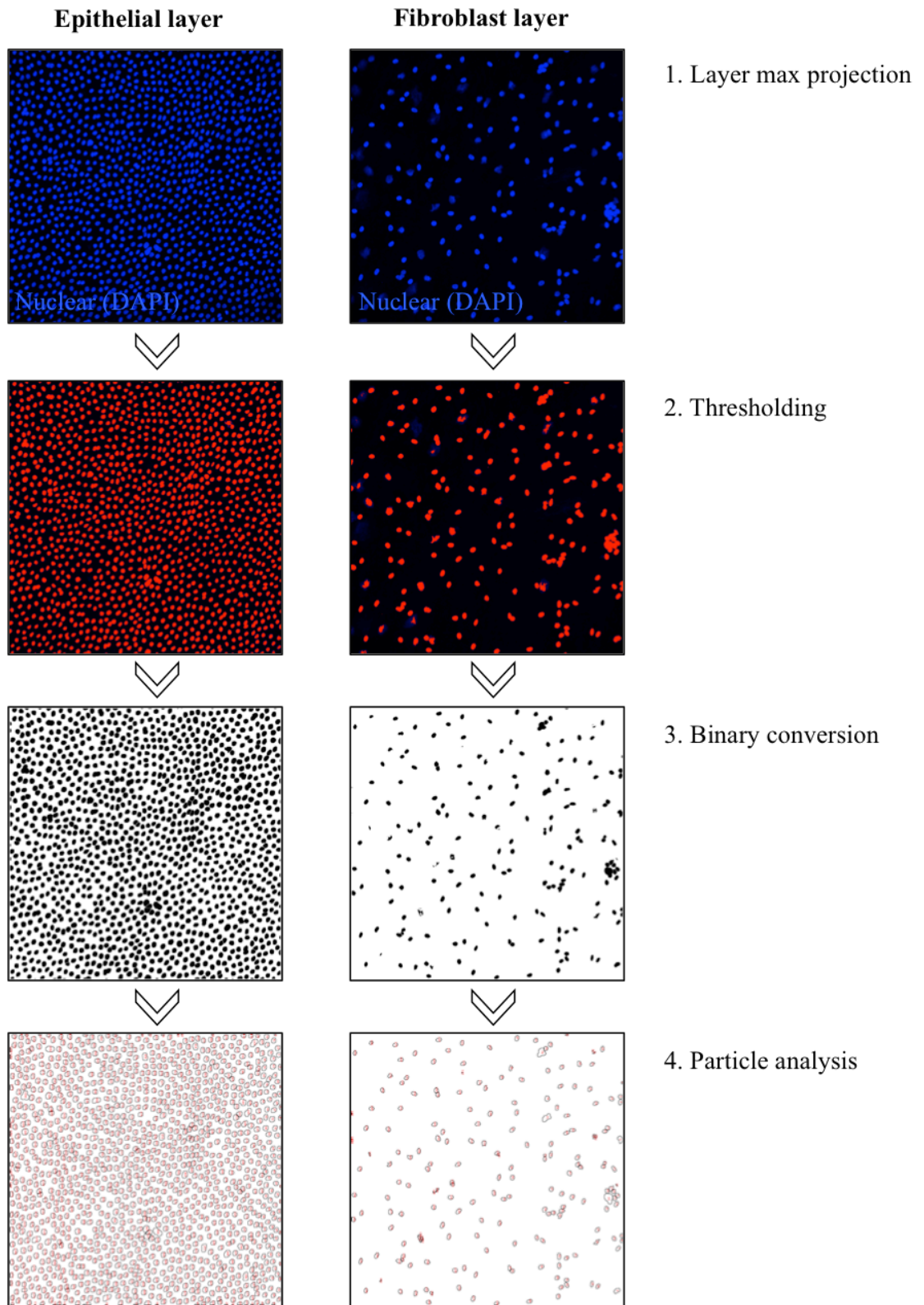


Figure 3.15: Key steps in image processing for nuclei count within epithelial and fibroblast layer of the amniotic membrane using ImageJ software.

Analysis of protein Cx43 plaque count

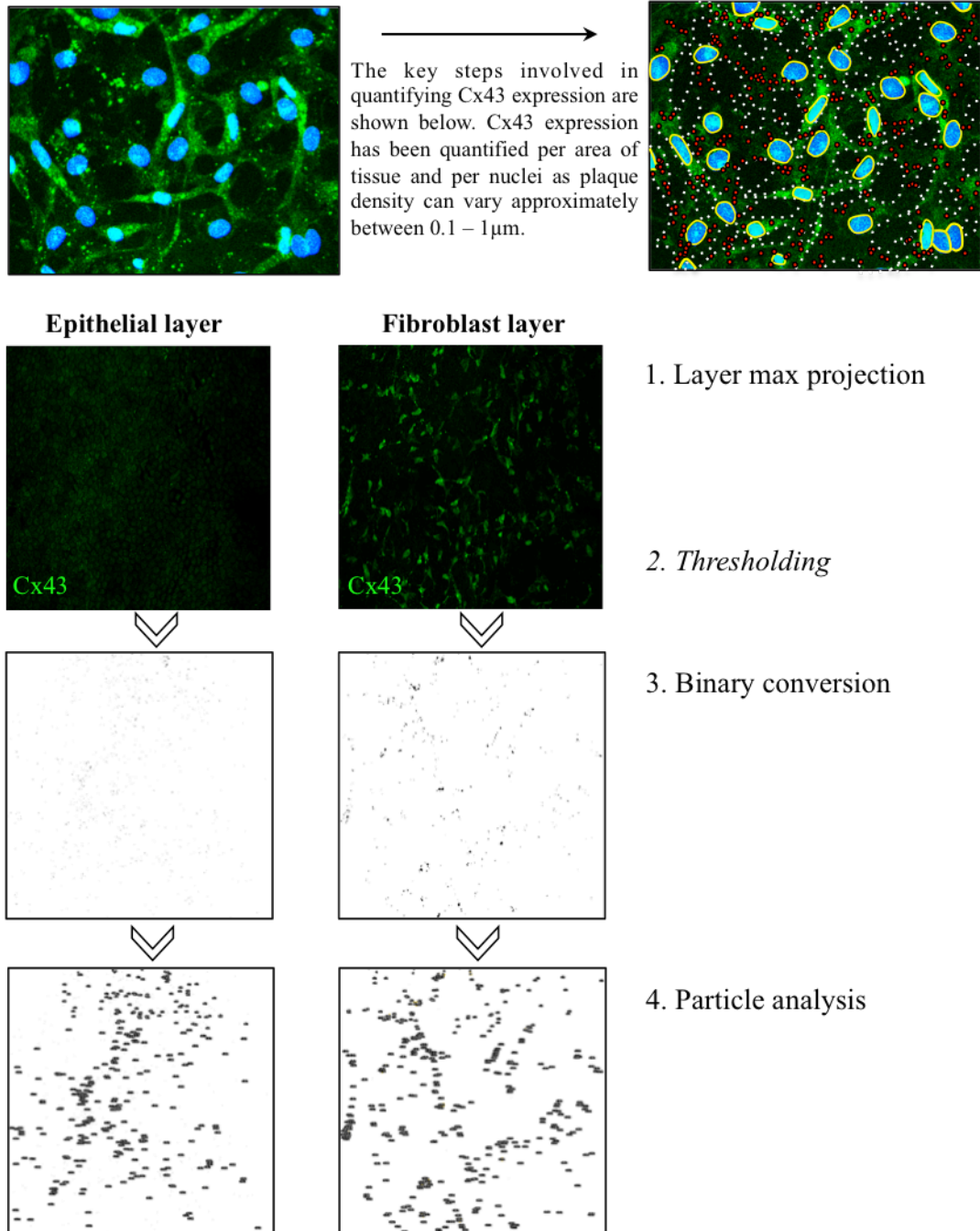


Figure 3.16: Key steps in image processing for Cx43 plaque count within epithelial and fibroblast layer of the amniotic membrane using ImageJ software.

3.8 Scanning electron microscopy

SEM was used to provide a view of the surface topography of tissue or self-assembled membranes. The technique allowed imaging of large areas (up to 50 μm^2) of sample to study microstructure and nanofibrous 3-D architecture up to a resolution of 3 nm and a magnification range between 20x and 30,000x. The SEM involved acceleration and focusing of electrons into a sample chamber from an optical column, which contains the electron gun and lenses. The sample is then scanned in a sequence of horizontal lines and the image is constructed after detection of secondary electrons that are ejected from specific points of the sample. A low acceleration voltage of 5 kV was used as the SEM beams were not required to penetrate the sample.

Human tissue samples were fixed in 4% paraformaldehyde for 2 hours at room temperature. Peptide amphiphile and amniotic fluid self-assembled membranes were fixed in 2.5% glutaraldehyde (0.1% NaCl) for 2 hours at room temperature and then washed three times in MilliQ water. Samples were then dehydrated in increasing percentages of ethanol for 10 minutes each in 20%, 50%, 70%, 90%, 96%, and 100%. Samples were then dried using the critical point drier (K850, Quorum Technologies, UK). The samples were mounted onto copper tape and placed on stub. The sample was then sputter coated with palladium/gold (30 nm). Samples were then placed onto the sample stage within the SEM chamber and then the vacuum environment was induced. The imaging was performed using an Inspect F50 (FEI Comp, Netherlands).

3.9 Histological analysis

3.9.1 Chemical fixation

Fetal membrane tissue was fixed in 4% paraformaldehyde for 2 hours at room temperature and then transferred to PBS and stored at 4°C. Fixation in 4% paraformaldehyde is ideal for a number of routine histological applications such as haematoxylin and eosin (H&E) staining. Due to the difficulty in maintaining a flat orientation of fetal membrane tissue, the tissue was fixed within a cassette sandwiched between 2 pieces of gauze before being submerged in 4% paraformaldehyde. If necessary

amniotic membrane was later separated from the chorionic membrane by gentle traction and dissected into approximately 2 cm x 2 cm specimens. PA membranes were fixed in 2.5% glutaraldehyde by applying directly to the *in vitro* fetal membrane wound model or within the PDMS channel with MilliQ water for 2 hours at room temperature and then transferred to PBS and stored at 4°C. The PA membranes were then washed four times with MilliQ water.

3.9.2 Tissue processing

Due to fetal membrane tissue being approximately 300 µM in thickness, the tissue was placed onto a small corkboard and pinned at each corner to maintain the orientation and prevent tissue curling. In the circumstance when fetal membrane wounds and tissue sealants were being examined it was at this point that a pin would be used to mark the wound edge/tissue sealant region with india ink to identify during tissue sectioning. Fixed tissue was then embedded in paraffin wax following dehydration by graded ethanol washes from 0% - 100% in order to prevent tissue distortion. This was then followed by xylene washes, which promotes efficient impregnation of the hydrophobic paraffin wax. During this process the water in fixed tissue is replaced with paraffin wax, which enables thin sections (5 µM) to be cut from the block using a sledge microtome and mounted onto glass slides.

3.9.3 Tissue staining

Haematoxylin and eosin (H&E) stain involves a routine procedure to identify cell types and cell components. Specifically, haematoxylin is a basic dye that stains the cell nucleus blue, and eosin is an acidic dye used to stain the cytoplasm and connective tissue different shades of red. The tissue is initially rehydrated by placing the glass slide into a bath of xylene for 8 minutes. The xylene bath was repeated twice and then the glass slide was placed into a series of ethanol baths including 100%, 90%, 80%, 70%, and 50% ethanol, with each bath being repeated twice to ensure rehydration.

After rehydration the slides were washed in water and then placed in a bath of haematoxylin for 8 minutes to stain cell nuclei. Excess stain was then removed by placing

the slides under a slow running tap for 8 minutes. The slides were then run through a brief series of graded ethanol washes (50%, 70%, 80%, 96%) for 30 seconds each. The slides were then placed in a bath of eosin for 2 minutes to stain cytoplasm and connective tissue. Following this, the slides were placed again in a bath of 96% ethanol for 30 seconds and then underwent 4 washes in 100% ethanol for 30 seconds each. The remainder of the work was then performed in a fume hood. To dehydrate fully, the slides were placed in 2 baths of xylene for 4 minutes each. The coverslip was then cleaned using xylene with a Pasteur pipette and the slide placed on a tissue face up. A drop of mounting solution (DPX) was placed on the slide and a cover slip (24 mm x 60 mm) placed on top. The cover slip was compressed until no bubbles were visible and left to dry overnight in the fume hood.

The Verhoeff's Van Gieson (EVG) stain was used to identify elastic fibres in fetal membrane tissue. The elastic fibres are stained blue-black and background stained yellow. As before, the tissue was de-paraffinised and hydrated to distilled water. The slides were then stained in Verhoeff's solution for 1 hour until tissue is completely black. The slides were then rinsed under the tap twice and differentiated in 2% ferric chloride for 2 minutes. Running the slides under the tap twice and then treating them with 5% sodium thiosulfate for 1 minute stopped differentiation. The slides were then washed under the tap for 5 minutes and counterstained in Van Gieson's solution for 5 minutes. The tissue was then dehydrated through to 100% ethanol and placed in 2 baths of xylene for 4 minutes each. As before, the cover slips were placed on top and compressed until no bubbles were visible.

3.10 Statistics

All results in this study were shown as the mean from replicates and individual experiments with error bars representing the mean +/- standard error of the mean. One-way or two-way analysis of variance (ANOVA) with Bonferroni-corrected post-hoc analysis was used to determine statistical significance of normally distributed data (confirmed by the Shapiro-Wilk normality test) between means (determined in SPSS software, version 24.0 IBM; Chicago, IL, USA) to reduce Type I errors where $\alpha = 0.05$. The number of patients and replicates are indicated in figure legends. In all comparisons

$P < 0.05$ was considered statistically significant for tests involving comparisons of wound edge vs. control amniotic membrane; strained vs. non-strained amniotic membrane; and treated vs. non-treated amniotic membrane groups. Densitometry analysis using ImageJ (Fiji) was performed for quantification of western blot bands and the mean grey value of 3 separate experiments determined for comparisons.

For gene expression statistical analysis, relative quantification of the target gene against a reference gene was performed in order to obtain relative expression ratio, which incorporated the PCR efficiency values (described previously in “PCR data analysis and optimisation” section). Briefly, PCR efficiencies for optimal primer pair concentrations were derived from standard curves ($n=3$) by preparing a ten-fold serial dilution of cDNA from a sample that represented the control. The real-time PCR efficiencies (E) of amplification for target genes were defined according to the relation, $E = 10[-1/\text{slope}]$. The R^2 value of the standard curves exceeded 0.99 and revealed efficiency percentage values ranging from 97.5–101%. Primer specificity was verified by examining the melting curves. Relative quantification of the target gene was estimated by normalising the target to the reference gene (GAPDH) and to the calibrator sample (patient matched control AM) by a comparative Ct approach. For each sample, the ratio of target Ct and reference Ct was calculated, as previously described^{175,176}. Ratios were expressed on a logarithmic scale (arbitrary units).

Chapter 4

Cx43 is overexpressed in human amniotic membrane after fetal surgery and artificial *in vitro* trauma

Chapter 4: Cx43 is overexpressed in human amniotic membrane after fetal surgery and artificial *in vitro* trauma

4.1 Introduction

This chapter investigates the expression of Cx43 in human amniotic membrane samples following fetal surgery and after *in vitro* trauma using an artificial fetal membrane wound model. Fetal membranes fail to heal after fetal surgery, resulting in increased incidence of iatrogenic PPRM, which occurs in approximately 35% of intra-uterine surgical cases. This can lead to severe lifelong complications including cerebral palsy and respiratory disorders. In order to develop successful iatrogenic PPRM preventatives and therapeutics it is important that research expands the current understanding behind human fetal membrane healing. This chapter furthers our understanding of human amniotic membrane wounds, by investigating the expression of Cx43, changes in cell morphology, and collagen orientation at the amniotic membrane wound edge. Previous research has shown Cx43 has an important role in normal wound healing, where it is initially downregulated. This is associated with the adoption of a cellular migratory phenotype, promoting cell migration across the wound edge. However, overexpression of Cx43 has been reported in chronic wounds that show limited or no healing, such as diabetic skin wounds and venous leg ulcers. To our knowledge, this chapter reports novel findings that show high Cx43 expression in amniotic membrane wounds following fetal surgery and *in vitro* trauma. Importantly, this could provide the premise for the development of a Cx43 targeted therapy that promotes amniotic membrane wound repair.

4.1.1 Gap junction structure and function

Gap junctions are specialised membrane channels composed of connexin proteins. Each connexin protein acts as a sub-unit, of which six make up a single hemichannel (also known as a connexon, **Figure 4.1**). They allow intercellular communication between adjacent cells through a hydrophobic channel (1 – 1.5 nm diameter), enabling passive diffusion of ions and metabolites of up to 1 kDa, including signalling molecules such as Ca^{2+} , IP_3 , cyclic AMP, cyclic GMP, and siRNA molecules¹⁷⁷⁻¹⁷⁹. Connexins have a highly

conserved structure amongst 21 known human genes, differing only slightly in regards to cytoplasmic domains that vary depending on interactions with connexin-associated proteins, such as cytoskeletal proteins, signalling molecules, adhesion molecules, phosphatases, and kinases including protein kinase B (PKB) also known as Akt¹⁸⁰⁻¹⁸². Human connexins are a large gap junction protein family that are most commonly named after their molecular weight and include: Cx23, Cx25, Cx26, Cx30.2, Cx30, Cx31.9, Cx30.3, Cx31, Cx31.1, Cx32, Cx36, Cx37, Cx40.1, Cx40, Cx43, Cx45, Cx46, Cx47, Cx50, Cx59, and Cx62¹⁸⁰.

4.1.2 Cx43 activation and plaque formation

Cx43 protein, encoded for by the *GJA1* gene, is the most ubiquitously expressed connexin, and the most commonly found within mammalian tissue. This signifies an important role in cell-cell communication, and with a short protein half-life of 1-3 hours, indicates the importance of correct Cx43 gene and protein expression in the dynamic regulation of multiple physiological events such as cell growth, cell differentiation, cell migration, and cell death^{183,184}. In a homomeric gap junction, six Cx43 proteins will form one connexon; therefore upon docking to an adjacent hemichannel, one gap junction will comprise 12 Cx43 proteins. Once Cx43 oligomerises into a connexon within the trans-golgi network it is trans-located to the plasma membrane where it can associate with other connexons to form a gap junction¹⁸⁵. It is important to note that these gap junctions do not exist in isolation, but are found in clusters that form gap junctional plaques within the cell membrane (**Figure 4.1a**)¹⁸⁶. When tissue is stained using specific Cx43 antibodies, and imaged using immunofluorescence confocal microscopy, these Cx43 plaques can form 0.1-1 μm puncta.

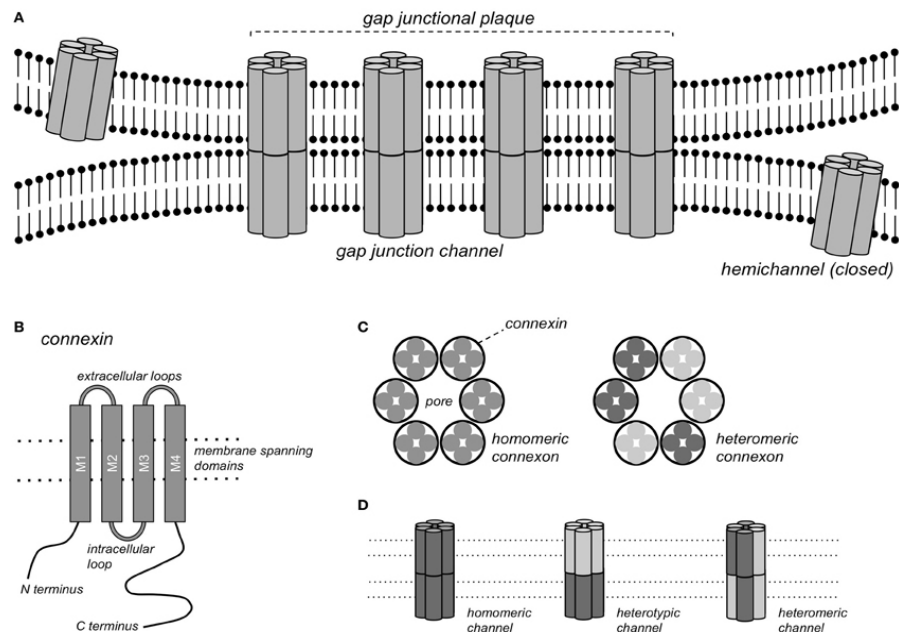


Figure 4.1: Schematic of gap junctional plaque and connexin structure. Gap junctions occur between adjacent cells after the docking of two hemichannels (A). Individual connexin proteins comprise four transmembrane domains, two extracellular loops, one intracellular cytoplasmic loop, and an N- and C- terminus (B). Hemichannels (connexons) can also exist in a homomeric or heteromeric forms, meaning all six connexin sub-units are the same isoform or a combination of different isoforms (C). Gap junctions can form between homomeric connexons of the same isoform (homomeric membrane channel), homomeric connexons of different isoforms (heterotypic membrane channel), and heteromeric connexons termed heteromeric membrane channels (D). Adapted from Verheule & Kaese (2013)¹⁰.

4.1.3 Cx43 activation regulates healing in wounded skin

Connexins play an important role in regulating the wound healing process¹⁸⁷⁻¹⁸⁹. Four key overlapping phases occur during wound healing, including (1) hemostasis, (2) inflammation, (3) proliferation and migration, and (4) remodelling. Cx43 downregulation is observed following cutaneous wounding¹²³. Cx43 expression in wound edge keratinocytes has been shown to decrease in the epidermis at 5 hours post-injury, continuing to decrease until negligible detection is found at 24 hours¹²³. This is concomitant with an increase in keratinocyte migration across the injury. Interestingly, compared to migrating keratinocytes at the leading wound edge, which show negligible Cx43 expression, the keratinocytes that are proliferating further back from the leading edge demonstrate comparably high Cx43 expression¹²³. A reduction in Cx43 has been linked to an absence of cell-cell communication, which pertains to keratinocyte migration, and once re-epithelialisation is complete, Cx43 levels return to original levels¹⁸⁷. Furthermore, Cx43 expression in wound edge dermal fibroblasts is also shown to decrease as early as 2 hours post-injury¹⁹⁰. This reflects the adoption of a migratory phenotype as the fibroblasts move into the wound to secrete granulation tissue.

Normal cutaneous wound healing involves a vasculature, and as such Cx43 levels have been studied in the endothelial cells of blood vessels¹⁹¹. It has been found that Cx43 is rapidly upregulated in blood vessel endothelial cells within the first 3 hours post-injury, which remains high during the inflammatory period¹⁹². The inflammation leads to swelling of the dermis and leakage of fluids, leukocytes, and proteins due to proinflammatory signals being released at the wound edge, which in turn correlates with Cx43 upregulation. This inflammatory response has been extensively studied in normal wound healing, with proinflammatory factors reported to favour the transformation of keratinocytes and fibroblasts into a migratory phenotype, promoting re-epithelialisation and granulation tissue secretion at the wound site¹⁹³. Degranulating platelets and mast cells initially secrete pro-inflammatory signals such as platelet-derived growth factor (PDGF) leading to recruitment of neutrophils and monocytes. Macrophages are then derived from monocytes, which engulf bacteria and other wound debris, as well as secreting fibroblast growth factor 2 (FGF-2) and transforming growth factor 2 (TGF- β 1). Interestingly, in embryonic wound healing the embryo cannot mount an inflammatory

response to injury, and it has been shown that wounds heal following contraction in a “purse-string” fashion, without scar formation, and without cell migration across the wound edge^{194,195}. In light of this, some research has emerged demonstrating that inflammation could in fact be more damaging to the wound healing process, and contribute to scar formation and destruction of healthy cells in adjacent tissue¹⁹⁶.

Similar to skin tissues, fibroblasts of the oral gingival mucosa express Cx43 as the predominant connexin¹⁹⁷. However, oral wound healing appears more rapidly than in cutaneous wounds, often with reduced scarring. Like in skin, Cx43 is rapidly downregulated in the leading wound edge epithelial and fibroblast cells, returning to basal levels at 60 days post-wounding¹⁹⁷. Interestingly, this group also found that suppressing Cx43 function in fibroblasts using the Cx43 mimetic peptide, Gap27, led to enhanced migration.

4.1.4 Cx43 and chronic wound healing

In contrast to normal cutaneous wound healing, there are several chronic wounds described in the literature that demonstrate changes in connexin expression, particularly Cx43¹⁹⁸. Diabetic wounds present with prolonged healing times due to the multiple damaging effects that hypoglycaemia and oxidative stress has on the tissue, which often results in the formation of ulcers. These ulcers show limited healing abilities, and interestingly, significantly upregulation of Cx43 protein and gene expression has been reported at the wound edge in venous leg ulcers, diabetic foot ulcers and pressure ulcers.

Venous leg ulcers

Venous leg ulcers present with sustained inflammation and atypical fibroblast and keratinocyte behaviour¹⁹⁹⁻²⁰¹. Cx43 expression in biopsies taken from human venous leg ulcers has been compared with healthy human skin punch biopsies¹²⁸. It was found that in healthy biopsies, Cx43 levels decreased at the wound edge, whereas in venous leg ulcer biopsies, higher Cx43 expression was observed throughout the entire dermis of the 4 mm biopsies. Furthermore, there was no evidence of Cx43 downregulation at the leading wound edge, where downregulation would typically lead to cell migration and healing.

Diabetic foot ulcers

In diabetic rat models, wounds show dramatic Cx43 upregulation in the keratinocytes of the leading wound edge, which leads to the formation of wound edge bulbs that contain non-migrating cells in the first 24 hours¹²⁶. Keratinocytes are only reported to migrate 72 hours post-injury, which correlates with Cx43 levels returning to normal. In human diabetic foot ulcer biopsies, fibroblasts in the dermal region show 10-fold increase in Cx43 expression compared to intact diabetic skin and non-diabetic skin wounds¹²⁴. Similarly this has also been reported in diabetic skin wound models of the rat where Cx43 upregulation in wound edge keratinocytes led to reduced cell migration¹²⁶.

Pressure ulcers

Pressure ulcers arise over a prolonged period of pressure to an area of skin that leads to ischemia, and tissue necrosis, typically over a bony prominence. They can also arise following repetitive pressure to the skin resulting in ischemia-reperfusion damage. Increased hemichannel activity and Cx43 upregulation has been noted in a pressure ulcer model²⁰². In pressure ulcer biopsies Cx43 was upregulated in the epidermis, with uneven expression reported at the wound edge¹⁹⁸. Overall, Cx43 was overexpressed by 10-fold when compared to patient matched intact skin. Cx43 expression in the dermis of pressure ulcers was substantially higher with a 57-fold increase at the leading wound edge compared to controls. Further away from the wound edge, Cx43 remained high, showing a 37-fold increase 1 mm away from the leading wound edge.

Taken together, chronic wounds show similarity in the striking upregulation of Cx43 linked with preventing fibroblast migration, and its downregulation appears to be pivotal in the ability of wounds to heal efficiently as seen in normal cutaneous wound healing. Furthermore, in wounds with privileged healing abilities such as the gingival mucosa and buccal membranes, there is rapid Cx43 downregulation at the wound edge, to almost negligible detection; resulting in rapid healing and reduced scarring. To date, the levels of Cx43 expression in wounded FM has not been investigated.

4.2 Methods

4.2.1 Fetal membrane used for fetal surgery study

Fetal membranes (n=18, **Table 4.1**) were collected from preterm and term deliveries following elective caesarean section after informed consent at University College Hospital London and University Hospital Leuven, Belgium. Women underwent fetoscopic surgery for treatment of twin-to-twin transfusion syndrome (TTTS, n = 16), fetal congenital diaphragmatic hernia (CDH, n = 1) and twin reversed arterial perfusion sequence (TRAPS, n = 1). The most common indication for fetoscopic intervention was TTTS (**Figure 4.2**). TTTS involves the uneven supply of blood from the placenta, which results in the two fetuses developing at different rates. There are 5 stages, with the severity increasing at each stage. Stage 1 involves imbalance of amniotic fluid, with a large amount around the recipient twin and smaller amount around the donor twin. Stage 2 involves the inability of the donor twin to produce urine, which is difficult to observe in the bladder via ultrasound examination. Stage 3 involves the imbalance of blood affecting the heart function in one or both fetuses. Stage 4 presents with signs of heart failure in one twin. Stage 5 involves death of one or both fetuses. Typically Stage III TTTS patients are considered for fetoscopic intervention.

Mean gestational age at surgical intervention was 23⁺³ weeks with a range of 15⁺⁰ – 29⁺³ weeks. Mean gestational age at delivery was 30⁺⁴ with a range of 23⁺⁰ – 37⁺⁴ and median GA of 30⁺⁶ weeks. Mean time from surgical intervention to delivery was 55 days with a range of 1 – 145 days (median: 42 days). Mean maternal age at delivery was 31 with a range of 20 – 39 years of age. From the sample group, four patients delivered within one week of surgical intervention (22.2%), six delivered between 8-50 days (33.3%), and eight delivered between 51-100 days (44.4%). From the sample group, 94% delivered preterm (less the 37 weeks) following fetoscopic surgery.

During the surgery, the fetoscopic entry site was created using a 10-Fr Teflon cannula (Cook Medical, Strombeek Bever, Belgium) and pyramidal trocar device (Karl Storz, Tuttlingen, Germany). At delivery, the fetoscopic defect site was identified by careful macroscopic survey of the fetal membrane, and the tissue around the wound was carefully

excised a long with control samples. One open fetal surgery case was collected, however the hysterotomy scar appeared infected and there was meconium presence in the amniotic fluid, likely leading to increased chance of infection. For this reason, the hysterotomy wound was removed from this study and data analysis focused completely on fetoscopic wound defects. A control region in the fetal membrane that was aligned in the same axis as the fetal defect and was at least 5 cm away from the wound edge was excised for comparison.

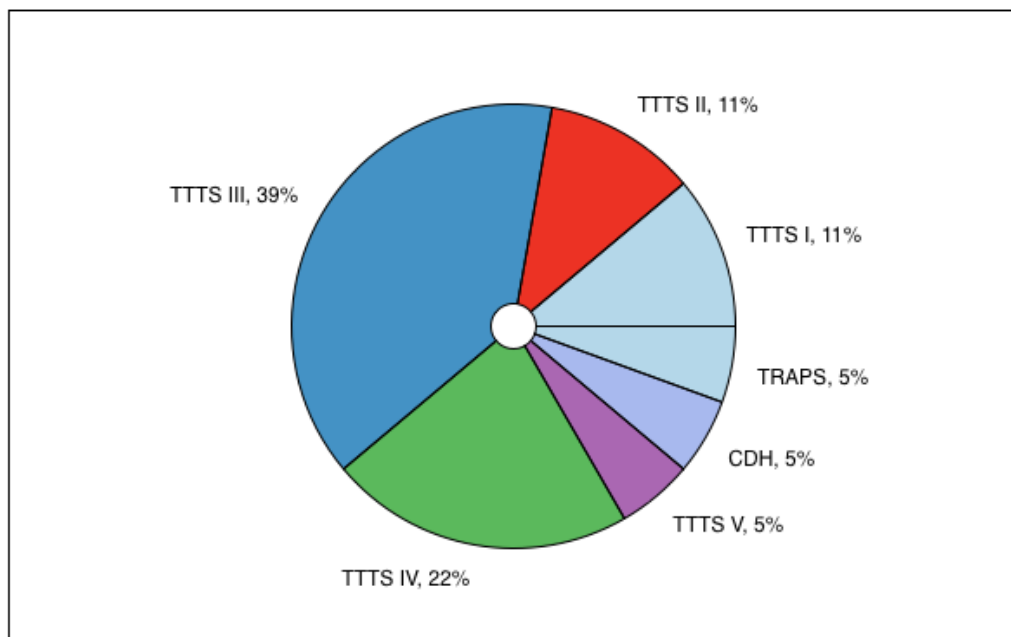


Figure 4.2: Reasons for fetoscopic surgery shown as a percentage. *TTTS*: twin-to-twin transfusion syndrome; *CDH*: congenital diaphragmatic hernia; *TRAPS*: twin reversed arterial perfusion sequence.

Table 4.1: Clinical information for patients undergoing laser ablation therapy.

Patient No.	Maternal age at delivery	Indication for surgery	GA at intervention	GA at delivery
Patient 1	39	TTTS stage I	24 ⁺⁰	35 ⁺⁵
Patient 2	28	TTTS stage I	19 ⁺³	29 ⁺⁴
Patient 3	28	CDH	28 ⁺¹	32 ⁺⁶
Patient 4	32	TTTS stage III	26 ⁺⁵	26 ⁺⁶
Patient 5	35	TTTS stage II	24 ⁺³	25 ⁺³
Patient 6	20	TTTS stage II	18 ⁺⁵	30 ⁺¹
Patient 7	34	TRAPS	15 ⁺⁰	35 ⁺⁰
Patient 8	33	TTTS stage III	22 ⁺²	23 ⁺⁰
Patient 9	29	TTTS stage III	21 ⁺⁶	35 ⁺⁵
Patient 10	36	TTTS stage V	19 ⁺³	37 ⁺⁴
Patient 11	33	TTTS stage III	25 ⁺³	31 ⁺⁵
Patient 12	29	TTTS stage IV	19 ⁺⁵	29 ⁺⁵
Patient 13	34	TTTS stage III	17 ⁺⁶	23 ⁺³
Patient 14	36	TTTS stage III	19 ⁺¹	27 ⁺⁵
Patient 15	33	TTTS stage IV	26 ⁺⁶	27 ⁺⁵
Patient 16	27	TTTS stage IV	29 ⁺³	33 ⁺³
Patient 17	33	TTTS stage III	27 ⁺³	32 ⁺⁴
Patient 18	23	TTTS stage IV	29 ⁺⁰	31 ⁺⁴

TTTS: twin-to-twin transfusion syndrome; CDH: congenital diaphragmatic hernia; TRAPS: twin reversed arterial perfusion sequence; GA: gestational age.

4.2.2 Fetal membranes used for the *in vitro* artificial fetoscopic trauma model

Fetal membranes (n=12) were collected from term deliveries following caesarean section after informed consent at University College Hospital London. Mean gestational age at delivery was 39^{+2} weeks with a range of $38^{+0} - 41^{+5}$ weeks (median: 39^{+1} weeks). Mean maternal age at delivery was 32 with a range of 23 – 38 years of age (median: 33 years). Indication for caesarean section (**Figure 4.3**) includes placenta praevia (low placenta), at least one previous caesarean section, previous stillbirth, breech position (fetal in bottom-down position) and medical reasons, in this case including two patients with heart conditions. One patient had both placenta praevia and previous caesarean section.

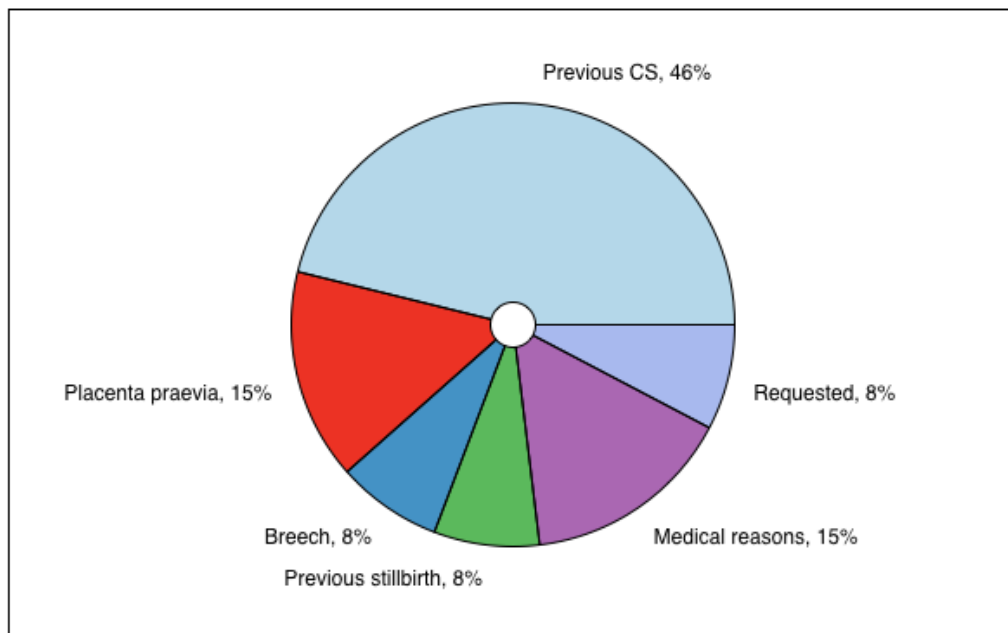
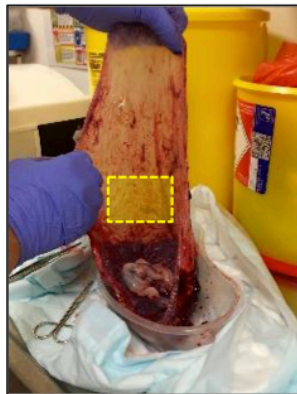


Figure 4.3: Indication for caesarean section shown as a percentage. These samples were used for developing the *in vitro* wound model and investigating amniotic membrane wound healing.

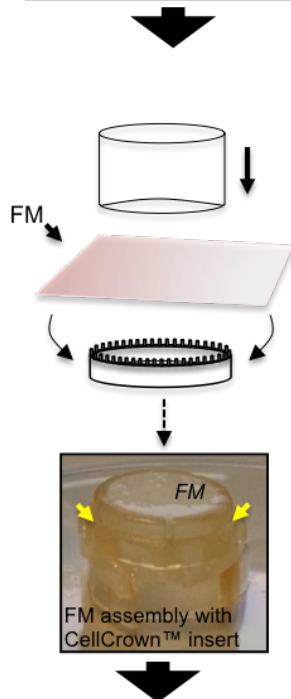
4.2.3 Development of artificial *in vitro* fetal membrane trauma model

In order to investigate fetal membrane wounds, an *in vitro* artificial fetoscopic trauma model was developed. The flow chart below shows the four key stages in preparing fetal membrane wounds and the steps taken to ensure consistency between experiments could be maintained.



Stage 1: Fetal membrane collection

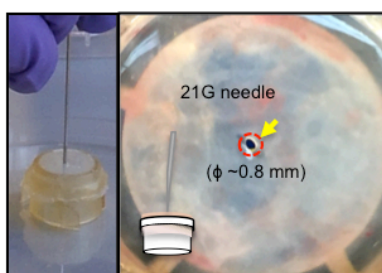
Fetal membrane was collected from term patients at University College Hospital London. Following delivery, Bobcock forceps were placed onto the lower edge of the membrane closest to the cervix. This allowed for sampling away from the zone of altered morphology (known to undergo morphological changes leading to membrane weakening in preparation for rupture). Samples were collected consistently from the membrane in the mid-zone of the fetal membrane closer to the placental disc (yellow box). Following dissection, the membrane was washed in sterile PBS and stored in DMEM+20% FCS. Membranes were left for up to 24 hours in an incubator (37°C, 5%CO₂) to adjust before being used for experiments.



Stage 2: Fetal membrane CellCrown™ assembly

Sterile CellCrown™ 12-well inserts were purchased from ©Scaffdex Oy (Tampere, Finland) and had undergone sterilisation by gamma radiation (25 kGy). Intact fetal membrane was placed with amniotic epithelial side faced upwards and the CellCrown™ outer ring was placed on top. For consistency the outer ring was placed on up to the notch indicated by the yellow arrows. Excess fetal membrane could be trimmed from the sides to allow for easy insertion into the 12-well plate.

Stage 3: Fetal membrane trauma

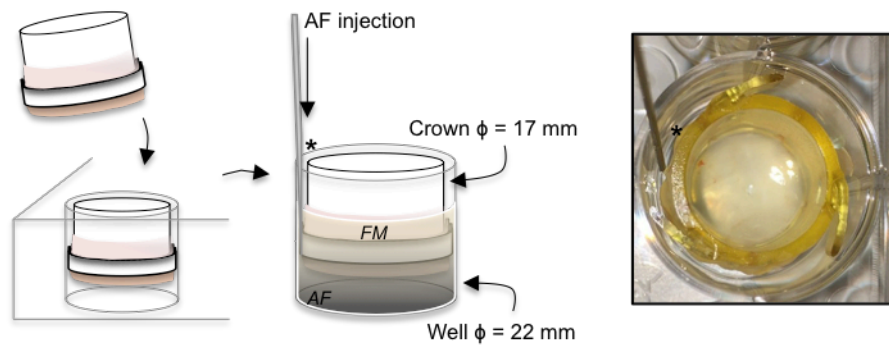


To create fetal membrane defects, a 21G needle was inserted into the fetal membrane previously assembled to the CellCrown™ insert. For consistency, the needle was inserted at 90° to the amniotic membrane surface and held in position for 2 minutes with the CellCrown™ positioned upright. The fetal membrane defect created was approximately 0.8 mm.



Stage 4: Fetal membrane wound incubation

Sterile CellCrown™ 12-well inserts assembled with wounded fetal membrane were placed into a sterile 12-well plate. Depending on the experiment, the fetal membrane was then incubated in DMEM + 20% FCS by injecting through the side until the fetal membrane was fully submerged. The final 12-well plate was then incubated at 37°C(5% CO₂). Following the incubation period, the fetal membrane was disassembled and immediately fixed for analysis.



4.3 Results: Investigation of AM trauma after fetoscopic surgery

4.3.1 Scanning electron microscopy of wounded fetal membranes after fetoscopic surgery

Initial observation of the fetal membrane at the macroscopic and microscopic level was important to understand the features of the wound in both amniotic and chorionic membrane fetoscopic defects (**Figure 4.4**). This specific case shows the macroscopic and microscopic appearance of a fetoscopic wound after 71 days since fetoscopic surgery, with delivery occurring preterm at 29⁺⁴ weeks gestation by caesarean section. Electron micrographs of the fetal membrane defect following fetoscopic surgery show the insufficiency of fetal membranes to heal. The defect size was approximately 3 mm in diameter for both AM and CM layers, however this varied due to the irregular defect shape. Thickened wound edges were seen specifically in the AM. The increase in folding at the wound edge in the AM could be a result of increased tensile properties causing the wound edges to retract more than is seen in the CM at the time of laparoscope entry. In comparison, the CM did not appear to have the same thickened edges and the wound margin was more irregular. Extracellular matrix fibres were exposed at the wound edge in both AM and CM, visible at 10,000 x magnification (**Figure 4.4c**). Nanofibres appeared more compact in the AM than the CM.

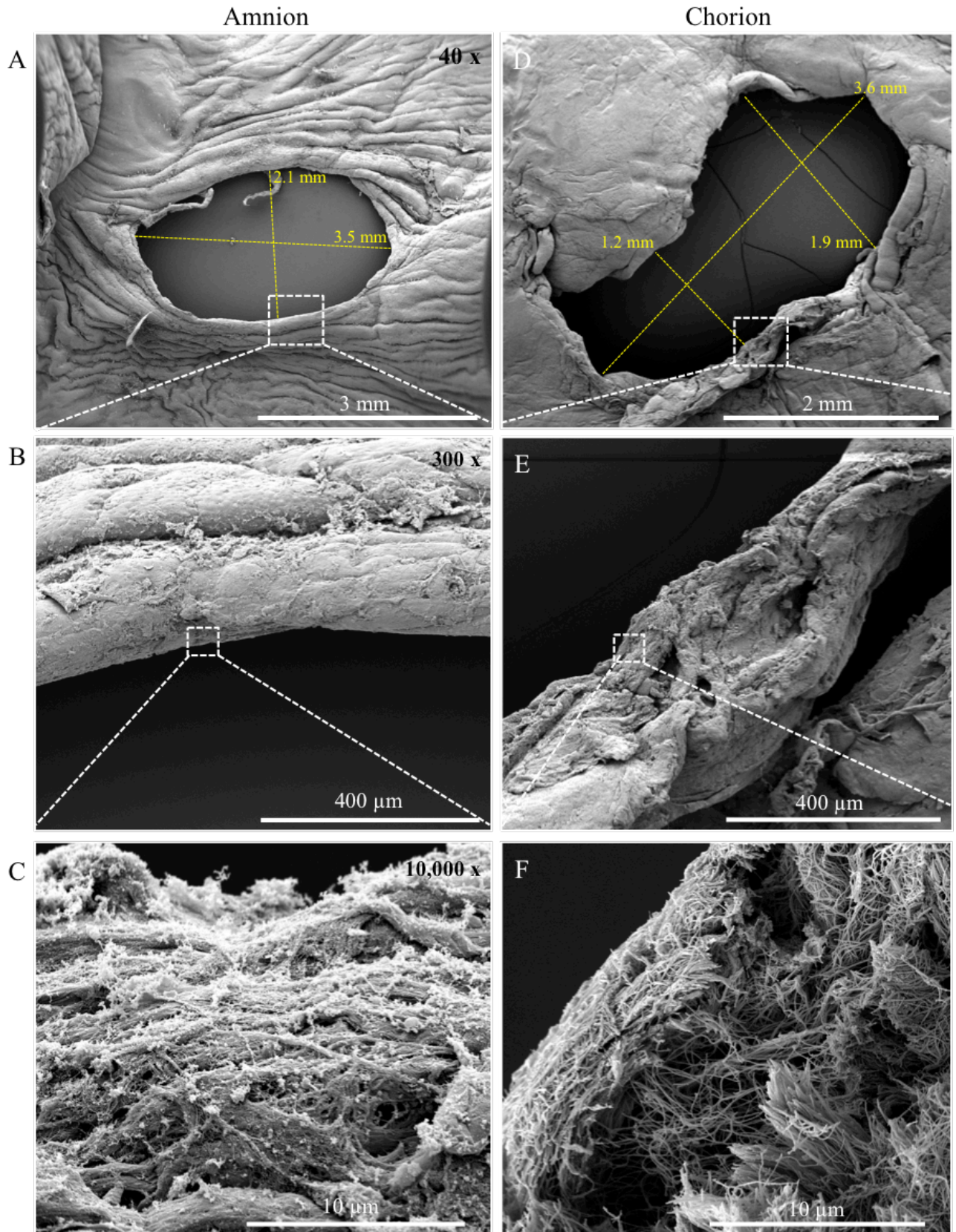


Figure 4.4: Electron micrograph of the fetal membrane wound following fetoscopic surgery. The amniotic membrane wound (A) appears to have a thickened bulb at the wound edge (B) compared to the chorionic membrane wound (D,E). Extracellular matrix nanofibres can be seen in the amniotic membrane (C) and chorionic membrane (F) at 10,000 x magnification. This electron micrograph shows that the wound persists with absent healing even 71 days since fetoscopic surgery in both membrane layers. Fetoscopic surgery was performed at 19^{+3} weeks gestation and delivery was at 29^{+4} days.

4.3.2 Cell morphological changes in wounded AM after fetoscopic surgery

No morphological changes were observed in cuboidal amniotic epithelial cells when comparing wound edge (comprising up to 500 μm from wound margin) to control regions (> 5 cm from wound margin). In contrast, mesenchymal cells of the fibroblast layer exhibited increased polarisation at the wound edge compared to control (**Figure 4.5a-f**). Polarisation occurred in parallel to the wound margin. Mesenchymal cells in the control region did not show the same morphology, although they were not completely rounded but slightly oval. The epithelial layer could be seen to curl over at the wound margin around the perimeter of the entire defect (**Figure 4.5g**), which could occur following removal of the laparoscope. Mesenchymal cells of the fibroblast layer appeared to form more clustered regions at the wound edge, with highly dense areas seen within approximately 200 μm of the wound margin. Amniotic epithelial “bulbs” were observed at the wound edge consistently around the perimeter of the wound margin (**Figure 4.5h, i**). These were a continuation of the epithelial surface and appeared to be aggregates of epithelial cells, having possibly attempted to crawl over the wound bed as seen during the typical re-epithelialisation stage of wound healing

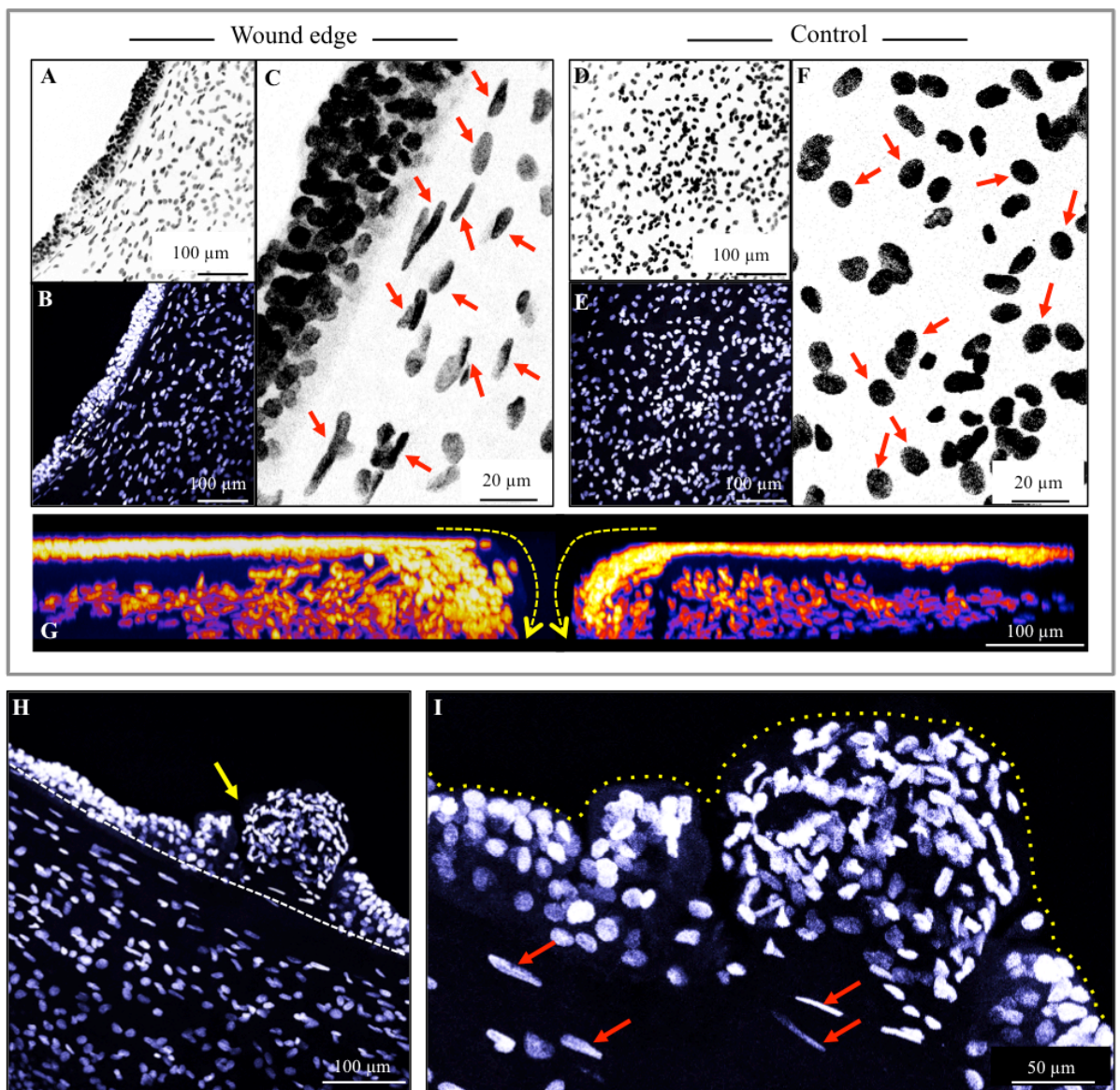


Figure 4.5: Immunofluorescence confocal laser scanning microscopy of wounded amniotic membrane fetoscopic surgery and representative control region with nuclear staining using DAPI. The wound edge amniotic membrane shows polarised mesenchymal cells that orientate tangential to the wound margin (A, B, C, red arrows). In comparison, control amniotic membrane taken from at least 5 cm away from the wound site in the same axis shows more rounded mesenchymal cell nuclei (D, E, F, red arrows). Cross-sectional image analysis reveals amniotic epithelial cell curling at the wound edge (yellow arrows) and a dense region of mesenchymal cells close to the wound edge (approximately 200 μm from the leading wound edge). The wound distance depicted in “G” is not to scale and wound margins have been moved together. Another feature at the amniotic membrane wound edge are epithelial cell bulbs, which appear to be aggregates of amniotic epithelial cells (H). Polarised mesenchymal cell nuclei (red arrows) can also be seen behind the epithelial cell bulb (I, dotted yellow outline). Dotted white lines indicate wound margins.

4.3.3 Quantification of mesenchymal cell polarisation in the wounded AM after fetoscopic surgery

Quantification of mesenchymal cell nuclei (**Figure 4.6**) shows increased polarisation at the wound edge compared to patient matched controls (**Figure 4.6, insert**, $p < 0.001$). Three patients were used in the analysis, with wound edge nuclei ($n=107$) compared with patient matched control ($n=100$). Overall, there was a 124.9% increase in polarity at the wound edge (within 200 μm of the wound margin). In wound edge nuclei, y-axis dimensions ranged from 7.215 μm – 38.991 μm , and x-axis dimensions ranged from 2.581 μm – 9.467 μm . In control regions (>5 cm from wound edge) mesenchymal nuclei y-axis dimensions ranged from 7.42 μm – 18.625 μm , and x-axis dimensions ranged from 4.132 μm – 14.502 μm . Mean wound edge mesenchymal nuclei dimensions were 15.8 μm by 5.3 μm . Mean control mesenchymal nuclei dimensions were 12 μm by 8.35 μm .

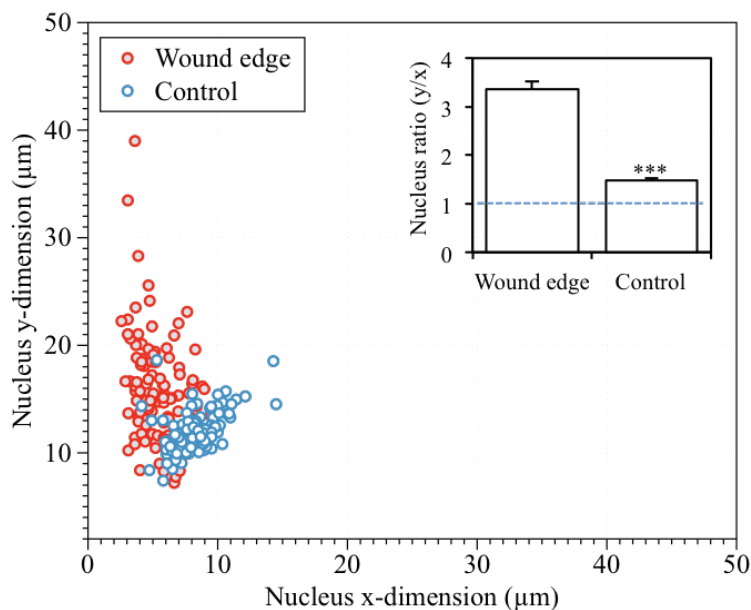


Figure 4.6: Quantification of mesenchymal cell nuclei morphology at the wound edge (<100 μm from wound margin) and control (>5 cm from wound edge) in amniotic membrane following fetoscopic surgery. Wound edge nuclei ($n=107$, red) were measured from 3 different patients along with control nuclei ($n=100$, blue) from patient matched control regions. Red dots indicate individual wound edge sample point and blue dots indicate individual control sample points. Y-axis indicates the longest distance measured per cell (μm) and x axis-indicates the corresponding x-axis dimension (μm), measured perpendicular to the nuclear y-axis. Insert shows overall y/x ratio with a value of 1 indicating a complete sphere (dotted blue line). Values further away from 1 indicate increased nuclear polarisation. The wound edge nuclei show increased polarity compared to control nuclei ($***p < 0.001$).

4.3.4 Changes in Cx43 and COX-2 gene expression in AM wounds after fetoscopy

Cx43 (GJA1) gene expression increased approximately four-fold in wounded AM compared to control AM ($P < 0.001$, **Figure 4.7**). Similarly, pro-inflammatory cytokine cyclooxygenase-2 (COX-2) gene expression increased approximately three-fold in wound edge samples compared to control ($p < 0.001$). Collagen type I (COL1A1) gene expression showed no significant changes when comparing wound edge and control samples. Analysis included four patients ($n = 12-18$ replicates) where error bars represent the standard error of the mean. Gene expression was normalised to patient matched control samples and presented as a ratio value with gene amplification efficiency values taken into account during fold change calculation.

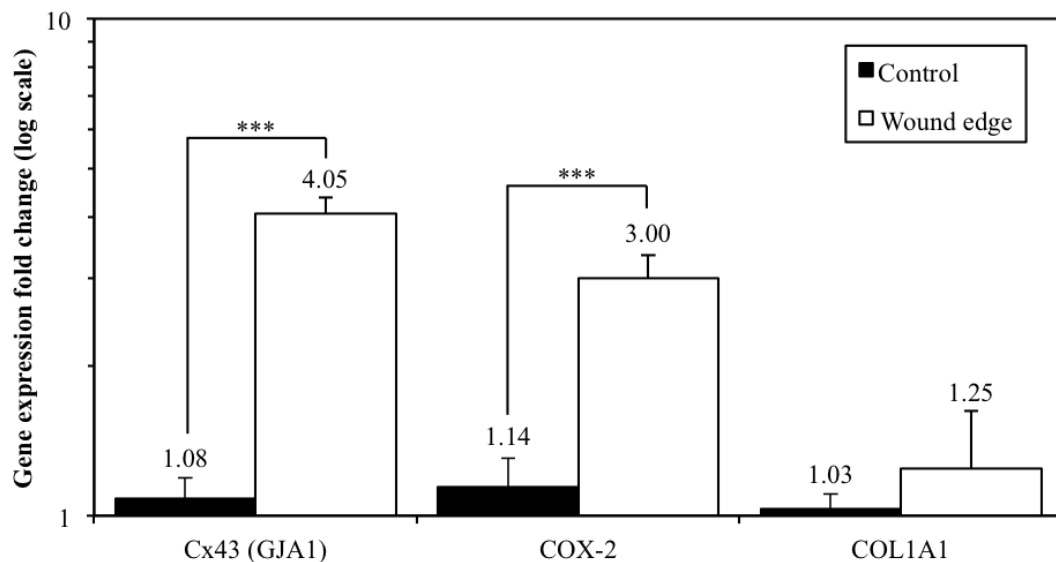


Figure 4.7: Gene expression fold change for Cx43 (GJA1), COX-2, and COL1A1 with y-axis presented as logarithmic scale. Cx43 and COX-2 gene expression increased approximately 4-fold and 3-fold in wound edge samples, compared to patient matched controls, respectively (both $p < 0.001$). No difference was reported in COL1A1 gene expression. Analysis included four patients, with 12-18 replicates performed during analysis per patient.

4.3.5 Changes in Cx43 protein expression in wounded AM after fetoscopic surgery

Typical Cx43 staining showed puncta of approximately 0.1–1 μm sized plaques (**Figure 4.8**). Representative images from a human fetoscopy patient show Cx43 plaques are predominantly expressed in wound edge mesenchymal cells of the fibroblast layer compared to basal Cx43 expression levels of control tissue (imaged at least 5 cm from the wound margin) control. Furthermore, Cx43 plaques are negligible in the epithelial layer of both wound edge and control regions.

Cx43 positive pixels were quantified per tissue area (pixels per 500 μm^2 area of tissue) and per cell nuclei (**Figure 4.9**). Overall, 8 patients were included in analysis, with 8-10 replicates per patient for both wound edge and patient matched control regions. Analysis of Cx43 protein quantification as pixels per 0.5 mm^2 and per cell nuclei showed no difference in epithelial cells in control AM compared to wound edge AM. Epithelial cells showed negligible Cx43 protein expression, virtually non-detectable, in both control and wound edge samples. Quantification of Cx43 per area showed mesenchymal cells expressed higher Cx43 protein levels compared to epithelial cells in both control ($P < 0.05$) and wound edge AM ($P < 0.001$). Cx43 protein expression was higher in mesenchymal cells at the wound edge compared to patient matched control regions ($P < 0.001$). Similarly, quantification of Cx43 pixels per cell nuclei showed higher expression in mesenchymal cells compared to epithelial cells in both control ($P < 0.05$) and wound edge ($P < 0.05$) samples. Cx43 expression per cell increased in wound edge mesenchymal cells compared to control mesenchymal cells ($P < 0.05$).

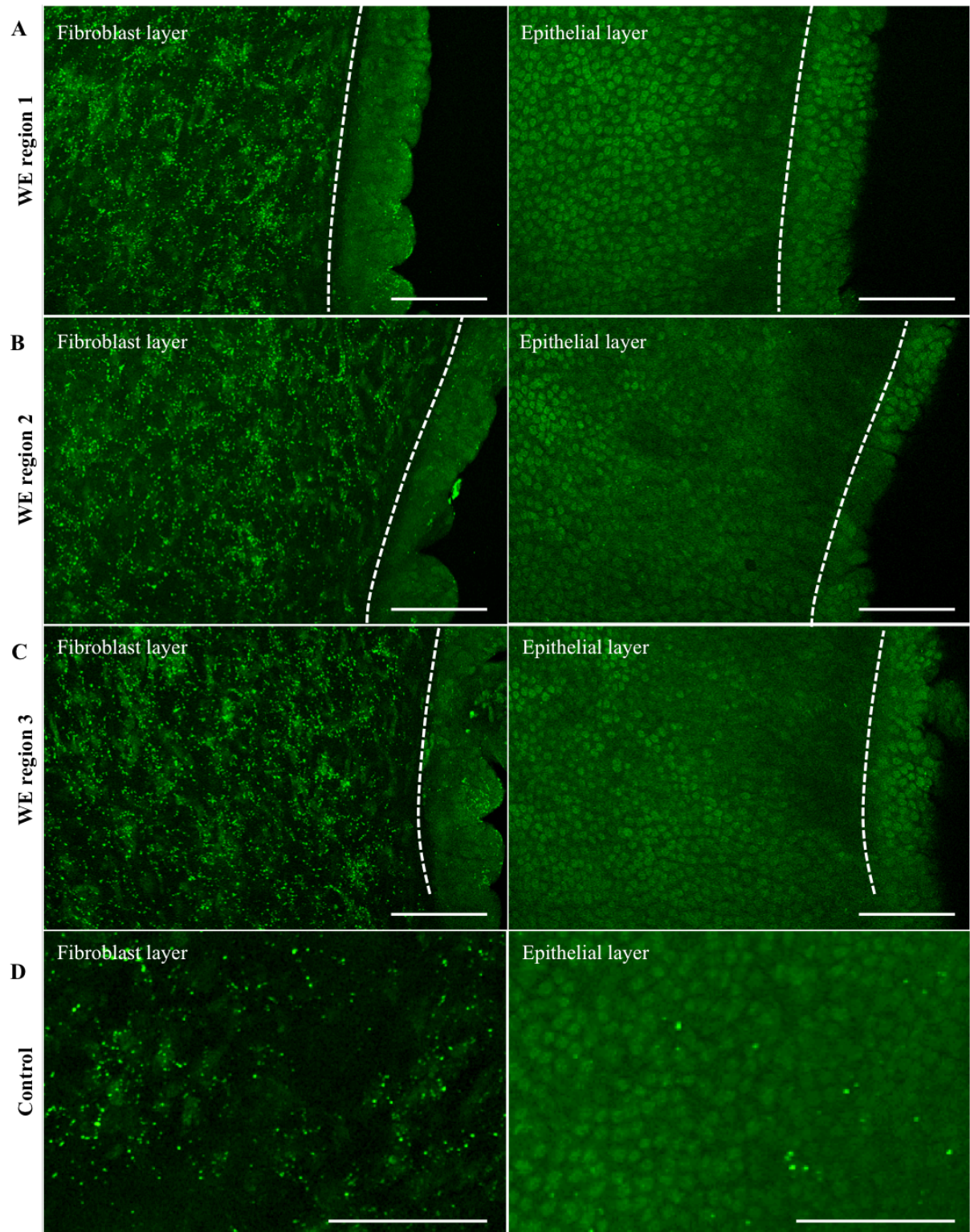


Figure 4.8: Human amniotic membrane fetoscopy patient Cx43 staining at wound edge (WE) and control regions. Typical Cx43 puncta of approximately $0.1 - 1 \mu\text{m}$ sized plaques (3 different wound edge regions shown A-C) that are predominantly expressed in the mesenchymal cells of the fibroblast layer. Cx43 puncta is still evident at basal expression levels in the control regions (>5 cm) from the wound margin (D). However negligible Cx43 staining is observed in the epithelial layers for both wound edge and control regions. Wound margin indicated by the dotted white line. Scale bars = $100 \mu\text{m}$.

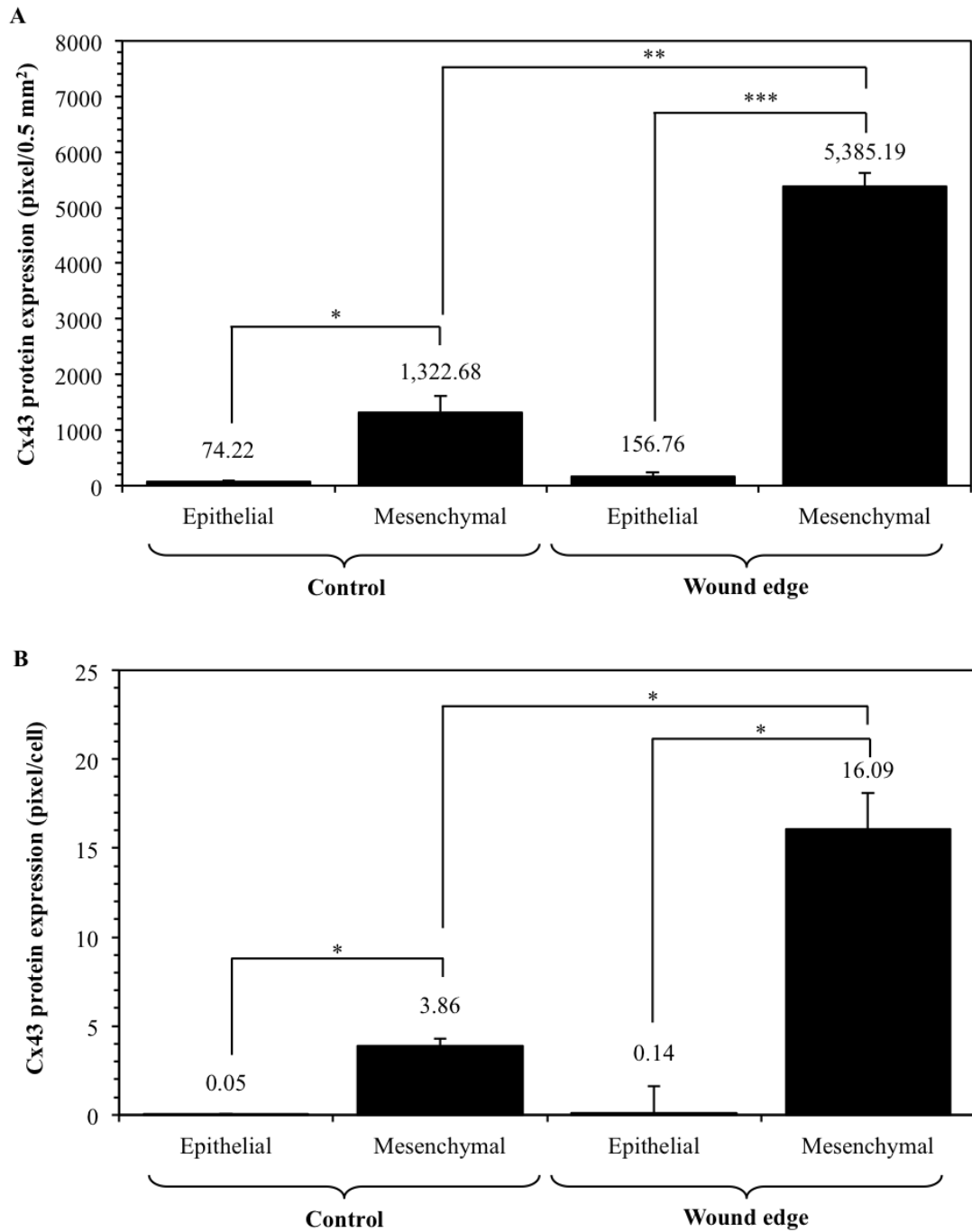


Figure 4.9: Cx43 protein quantification per area (A) and per cell nuclei (B). Quantification was performed using ImageJ particle analysis to quantify pixels per area and cell nuclei. No difference is reported in Cx43 expression in the epithelial layer of wound edge and control AM. Cx43 expression is higher in mesenchymal cells compared to epithelial cells in both control and wound edge AM. Cx43 expression is higher in the fibroblast layer of the wound edge compared to control fibroblast layers. Eight patients were involved in analysis with 8-10 replicates per patient. Statistical significance is indicated as * $p < 0.05$, ** $p < 0.01$, *** $p < 0.001$.

4.3.6 Collagen alignment and intensity in wound edge vs. control regions

Comparison of SHG intensity (presented in arbitrary units across an area of approximately 425 x 425 μm sample region) shows an increase in intensity at the wound edge regions compared to control (**Figure 4.10a**, representative patient with 10 replicates around perimeter of wound edge). Overall, there was a five-fold SHG signal intensity increase in wound edge regions compared to patient matched controls (**Figure 4.10b**, n=8 patients, $p<0.001$)

To infer the preferred collagen alignment direction, we performed an orientation distribution analysis using *ImageJ*. SHG images were converted to binary and 2D orientation analysis performed using the directionality plugin. Collagen fibres showed increased organisation at the wound edge (**Figure 4.11a**), where fibres aligned tangential to the wound edge, similarly to the tangential alignment of the mesenchymal cell nuclei. Control regions showed more typical disorganised and “basket-shaped” fibre orientation that is interwoven throughout the imaged region in random fashion (**Figure 4.11b**). Surface intensity plots of wound edge (**Figure 4.11c, e**) and control regions (**Figure 4.11d, f**) show the formation of a thicker, highly aligned collagen ring at the wound margin that could be seen around the perimeter of the wound edge. Representative histogram analyses of wound edge (**Figure 4.11g**) and control regions (**Figure 4.11h**) show a higher amount of collagen fibre alignment at the wound edge compared to control regions.

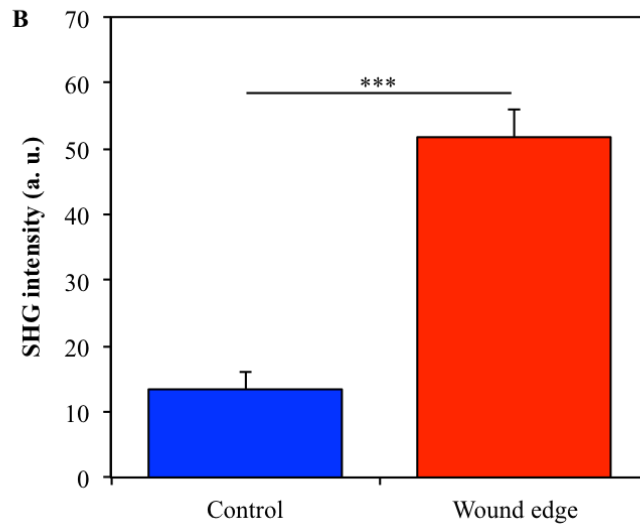
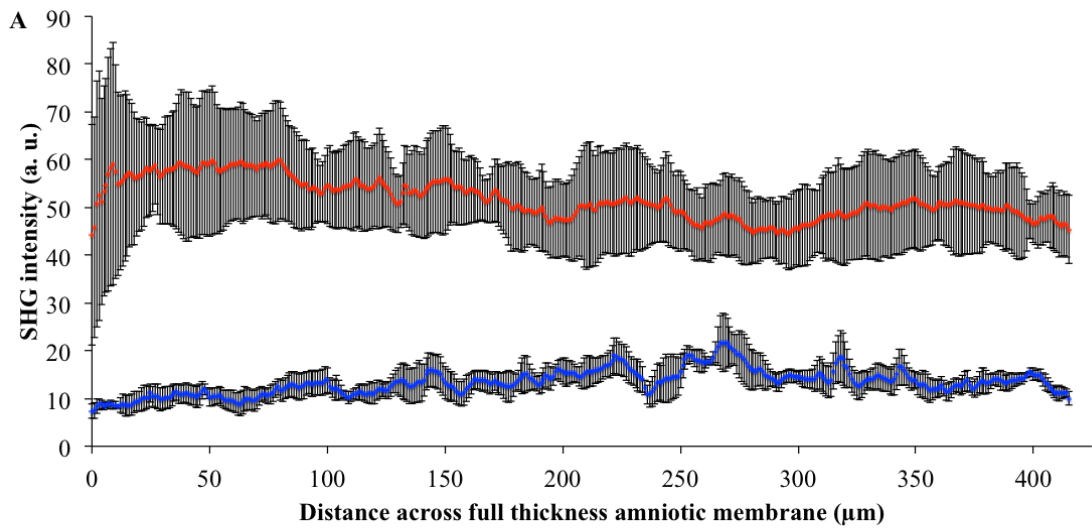


Figure 4.10: Second harmonic generation signal intensity in wound edge and control specimens across full thickness amniotic membrane samples approximately $425 \mu\text{m}^2$. Figure shows representative SHG profile with 10 replicates around perimeter of wound edge (within $500 \mu\text{m}$ of wound margin, A). There was an approximately five-fold mean SHG signal intensity increase in wound edge regions compared to patient matched controls ($N=8$ patients, B). Error bars represent mean \pm SEM, where statistical significance is indicated by $***p < 0.001$.

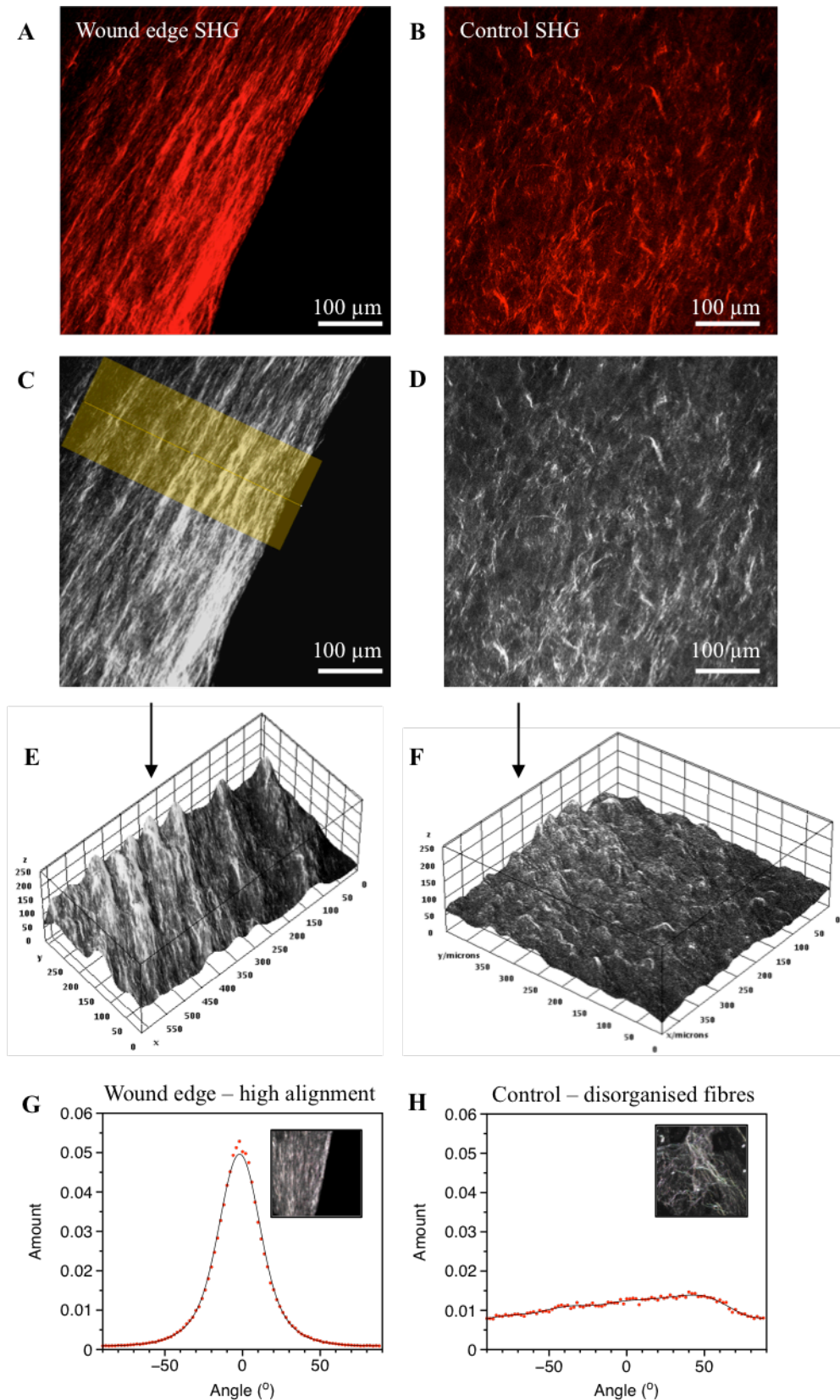


Figure 4.11: Second harmonic generation imaging analysis of collagen density SHG signal intensity in wounded amniotic membrane compared to control. AM collagen fibres were aligned parallel to the wound margin (A,C) compared to disorganized fibres in AM control regions (B,D). Surface intensity plots show formation of a ring of collagen at the wound edge, which had higher intensity (E) compared to patient matched control AM (F). Histogram analysis shows increased collagen alignment at the wound edge (G) compared to control regions (H).

4.4 Results summary

- 94% of patients (17/18) who underwent fetoscopy delivered preterm (less than 37 weeks gestation). Mean gestational age at delivery was 30^{+4} weeks (range: 23^{+0} – 37^{+4} ; median: 30^{+6} weeks). Mean duration from surgical intervention to delivery was 55 days. From the sample group, 22.2% delivered within 1 week following surgical intervention.
- Electron micrographs reveal the absent healing of fetal membrane wounds (~3 mm in diameter) following fetoscopy for intrauterine fetal surgery, even up to 71 days post-surgery. High magnification electron micrographs at the wound edge reveals a dense ECM network in both amnion and chorion that appears to be denser in the amnion.
- Following fetoscopy, the defect diameter is similar in amnion and chorion layers, however, the defect shape is irregular in the chorion compared to the amnion, which may be due to increased elasticity of the amnion.
- Wound edge mesenchymal cells are polarised and arranged in a tangential orientation around the perimeter of the wound margin. In comparison, control region (more than 5 cm from the wound edge) mesenchymal cells are oval shaped and arranged in random orientations.
- The wound edge appears to have a higher density of mesenchymal cells within approximately 200 μm of the wound margin, indicating a higher rate of proliferation, compared to control regions.
- Cx43 and COX-2 gene expression is upregulated in amniotic membrane wound edge specimens compared to patient-matched control regions (more than 5 cm from the wound edge). COL1A1 did not show a statistically significant difference in wound edge samples compared to patient-matched control regions.

- Cx43 protein expression (per area and per nuclei) increased in amniotic membrane mesenchymal cells at the wound edge compared to control regions. No statistically significant difference in Cx43 protein expression was reported in amniotic epithelial cells at the wound edge compared to control regions.
- SHG intensity increased in wounded amniotic membrane compared to control regions. This could indicate a change in density of collagen at the wound edge compared to control regions. The density of collagen appears to increase without a change in mRNA collagen, therefore increased collagen intensity could result from increased content per area unit and not through increased synthesis of collagen.
- Collagen fibres, indicated by SHG signals, showed increased alignment at the wound edge, and were organised tangential to the wound margin in a similar fashion to mesenchymal cell polarisation. In contrast, control SHG signals were arranged in random orientations, and fibres were shorter compared to bundles of fibres at the wound edge.

4.5 Results: Investigation of AM wounds after *in vitro* artificial trauma

4.5.1 Cell morphological and Cx43 changes in AM after trauma

In control AM region, mesenchymal cell nuclei showed no change in morphology. In wound edge samples, mesenchymal cell nuclei were polarised in a similar fashion to AM after fetoscopic surgery samples (**Figure 4.12a, c**). They lined up tangential to the wound edge within approximately 200 μm from the wound margin and around the full perimeter of the wound (**Figure 4.12e, f**). In control AM, mesenchymal cell nuclei were oval shaped (**Figure 4.12b, d**). The epithelial surface curled over at the leading wound edge from 2 hours, which was more profound at 168 hours (**Figure 4.12g, h**). However, no epithelial “bulbs” were discovered after *in vitro* trauma, which were a common feature in fetoscopic surgery samples. Furthermore, unlike the epithelial layer in fetoscopy surgery samples, which expressed negligible Cx43 protein, there appears to be a higher level of Cx43 protein expression after *in vitro* trauma in amniotic epithelial cells (**Figure 4.12i, inserts**). This could be due to term fetal membrane being used and therefore highlights Cx43 expression could vary with gestational age.

Temporal changes in Cx43 protein expression were quantified per area (0.5 mm^2) and per cell nuclei (**Figure 4.12i and Figure 4.13a, b**). Cx43 temporal expression was investigated at 2, 12, 24, 168 hours (7 days), after *in vitro* trauma in the AM. Cx43 protein expression in the wound edge increased in mesenchymal cells from 2 hours to 12 hours, and the levels were sustained for up to 168 hours. Cx43 protein expression was higher in mesenchymal cells at the wound edge compared to control mesenchymal cells from 12 hours, sustained for up to 168 hours. Interestingly, at 2 hours there is a decrease in Cx43 at the wound edge in mesenchymal cells compared to control mesenchymal cells when quantifying Cx43 per area. This was not the case in Cx43 per cell nuclei, which indicates that Cx43 plaque size may decrease overall at 2 hours post-trauma. However, the number of plaques may remain constant until 12 hours where an increase in Cx43 protein is seen at the wound edge. Furthermore, when quantifying Cx43 protein expression per area, there was an increase ($P < 0.001$) from 24 hours to 168 hours; however, this was not replicated per cell nuclei. This could indicate Cx43 plaque size is increasing but not necessarily the number of Cx43 plaques.

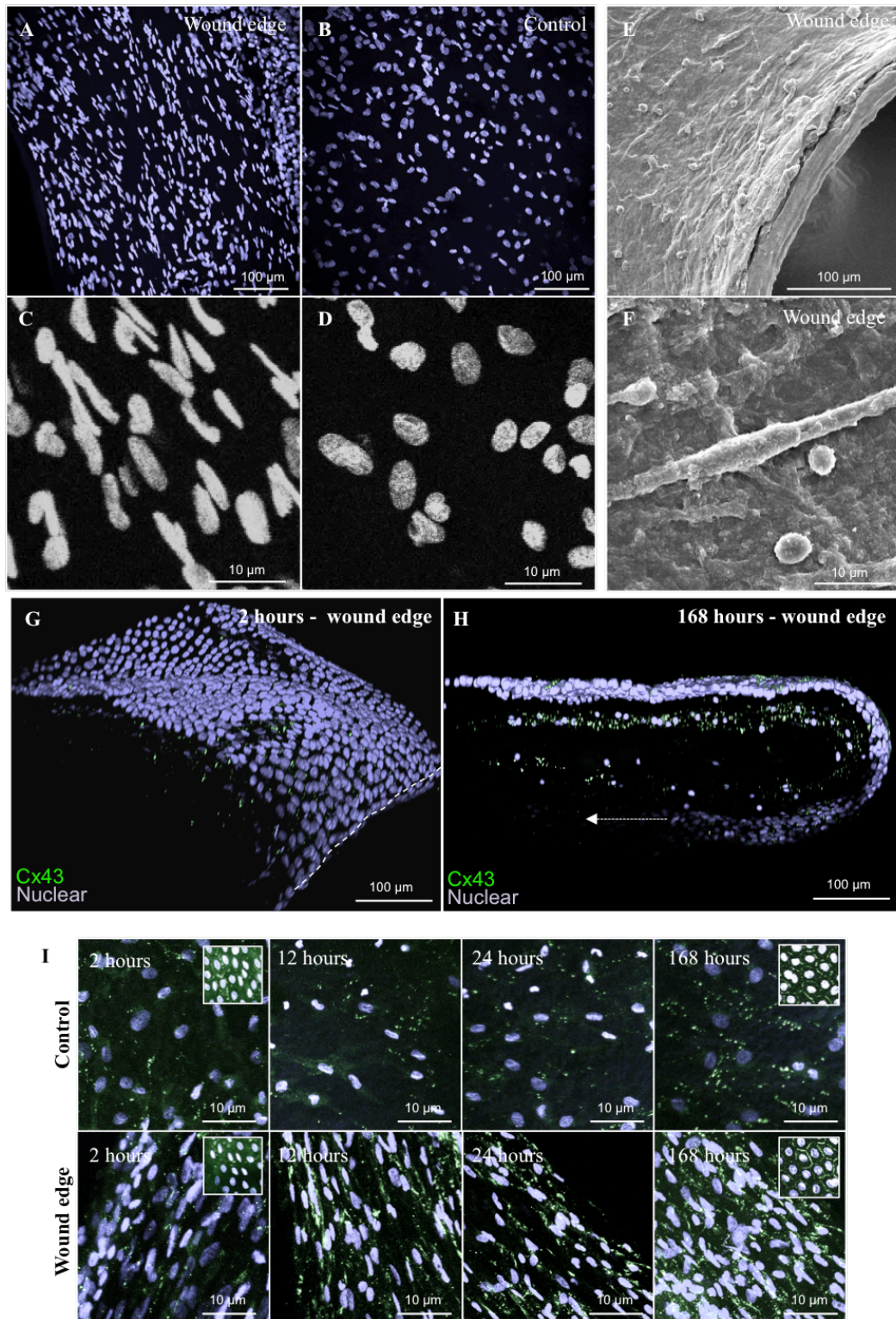


Figure 4.12: Immunofluorescence confocal laser scanning microscopy of nuclei morphology and Cx43 protein expression. Mesenchymal nuclei was polarised at the wound edge (A, C) compared to oval shaped mesenchymal nuclei in control AM regions (B, D). Scanning electron microscopy shows polarised mesenchymal cells of the fibroblast layer at the wound edge (E,F). Epithelial curling can be seen at the wound edge from 2 hours to 168 hours (G, H). Cx43 protein expression can be seen at the wound edge and patient matched control AM region at 2, 12, 24, and 168 hours post-trauma. Cx43 protein expression increases from 2 – 12 hours, which is sustained to 168 hours in the mesenchymal cells of the fibroblast layer.

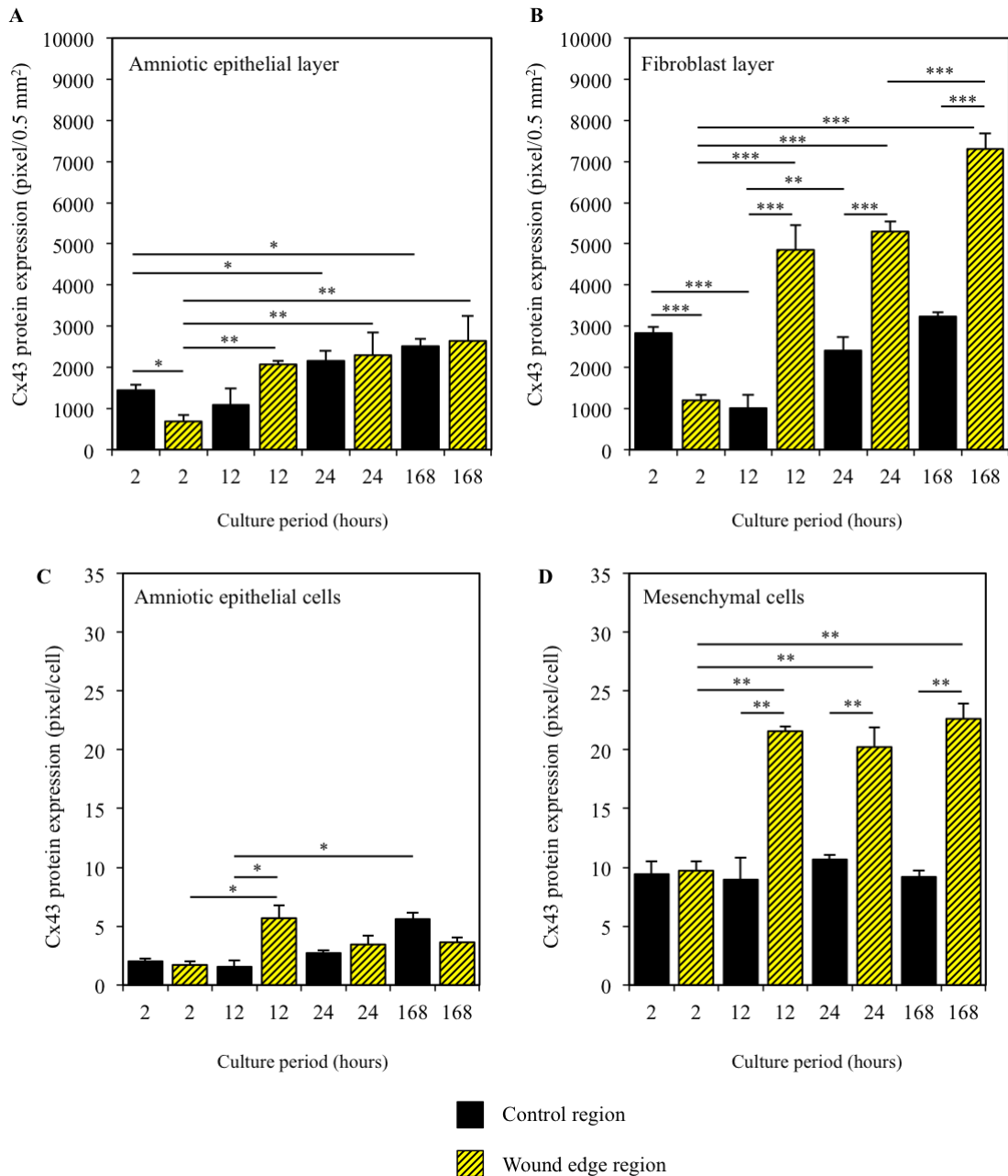


Figure 4.13: Cx43 protein quantification per area (0.5 mm^2 , A and B) and per nuclei (C and D) following in artificial vitro trauma of human amniotic membrane. Cx43 protein levels increase from 2 hours to 12 hours in the wound edge of the amniotic membrane, which is maintained at high levels for 168 hours post-trauma. Analyses included $N=12$ patients with 8-10 replicates per fetal membrane. Mean gestational age at delivery was 39^{+2} weeks. Error bars represent mean \pm SEM, with statistical significance is indicated as $*p<0.05$, $**p<0.01$, $***p<0.001$.

4.5.2 Collagen alignment in wound edge and control AM after *in vitro* artificial trauma

Collagen alignment increased from 24 hours to 168 hours at the wound edge (**Figure 4.14a, b**). Similar to fetoscopic surgery wounds, fibres aligned tangential to the wound edge around the perimeter of the wound (**Figure 4.14a**). Histogram analysis shows collagen fibres were more aligned at the wound edge compared to control regions (>5 cm from wound edge, **Figure 4.14a**). Control regions reflected that seen in fetoscopic surgery patients where fibres were shorter and more disorganised in an interwoven fashion.

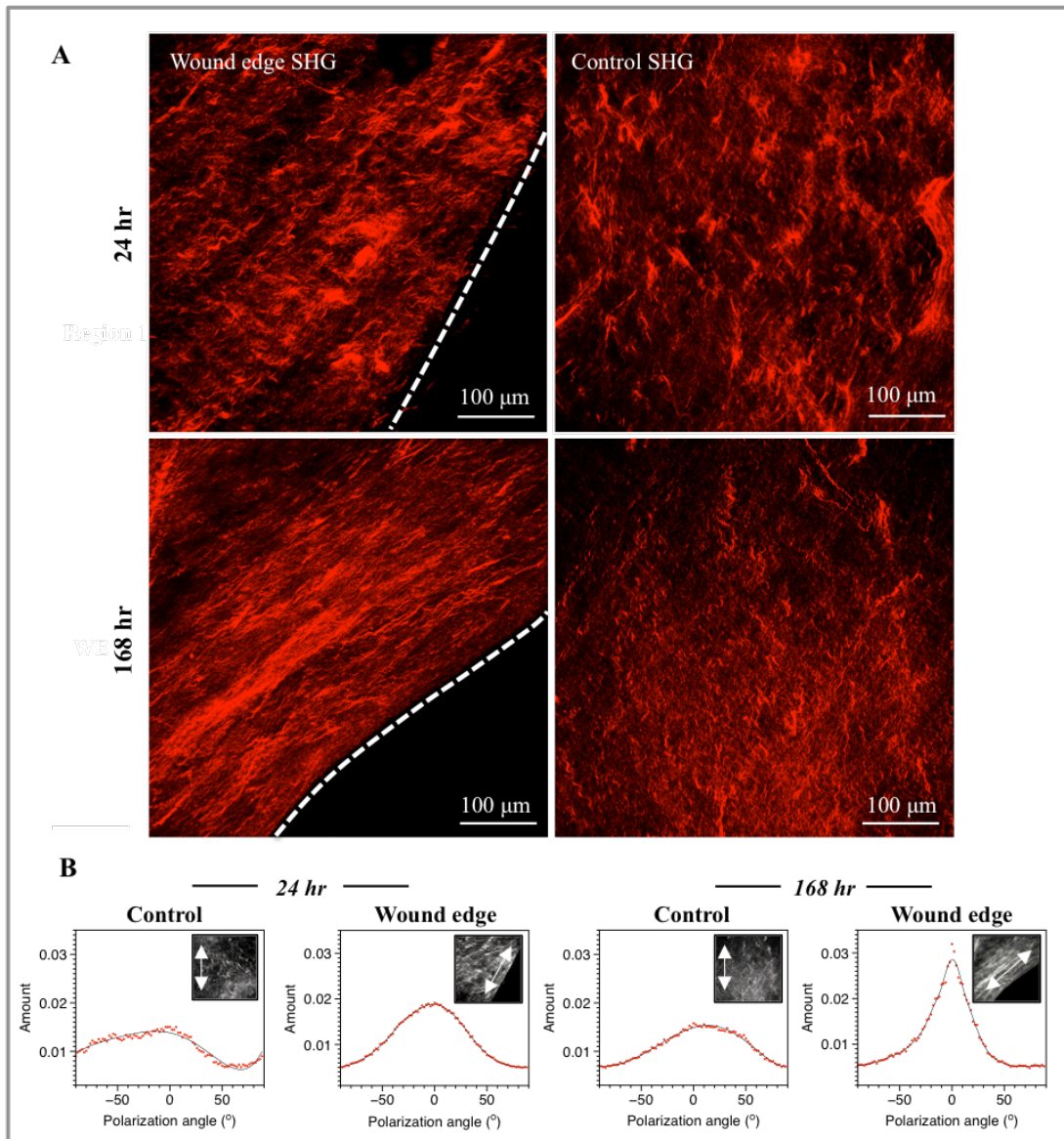


Figure 4.14: Second harmonic generation imaging analysis of collagen alignment in wound edge AM compared to control AM following artificial *in vitro* trauma. At 24 hours, collagen fibres in the wound edge showed basket-shaped bundles. However, at 168 hours, fibres were aligned tangential to the wound edge in AM (A). In control AM, collagen fibres showed typical disorganized interwoven fibres. However, at 168 hours, the fibres appeared shorter and less dense in the AM (A). Histogram analysis shows alignment increased in wound edge at 168 hours compared to both control and wound edge AM at 24 hours, which showed some alignment compared to control AM (B).

4.6 Results summary

- Human fetal membranes can be cultured within the artificial fetal membrane trauma model to investigate reproducible defects of approximately 0.8 mm in diameter for 7 days.
- The amniotic epithelial layer curls over at the wound margin, which appears more profound at day 7 compared to 2 hours, indicating epithelial cell migration around the perimeter of the wound margin.
- Amniotic membrane epithelial cells do not change morphology at the wound edge; and control region mesenchymal cells (more than 5 cm from wound edge) have an oval shaped morphology occurring in random orientations.
- Amniotic membrane mesenchymal cells polarise towards the wound edge and express greater levels of Cx43 protein expression compared to control AM.
- Cx43 puncta of 0.1-1 μm is reported in both amniotic epithelial cell and mesenchymal cell populations, indicating variability in Cx43 plaque size.
- Cx43 protein expression (per area and per nuclei) at the wound edge increases between 2-12 hours in the fibroblast layer, which is maintained and increases further at 168 hours after artificial trauma.
- Cx43 protein expression is higher in amniotic epithelial cells at the wound edge compared to control regions at 12 hours, however, whilst Cx43 increases in both wound edge and control amniotic epithelial cells, there is no difference reported at 24 and 168 hours. Interestingly, there is an initial decrease in Cx43 protein expression at the wound edge in amniotic epithelial cells compared to control (per area) at 2 hours but not when quantified per epithelial nuclei. This could indicate that Cx43 plaque size may decrease whilst the number of Cx43 plaques remains unchanged.

- SHG reveals that collagen fibres in control amniotic membrane are arranged in a disorganised orientation at both 24 and 168 hour incubation periods. However, in control tissue at 24 hours, collagen fibres appear longer and more defined, compared to 168 hours where fibres are finer and shorter, indicating partial degradation over the 7 day incubation period.

4.7 Discussion

This study set out to investigate the AM wound following fetoscopic intra-uterine fetal surgery and *in vitro* trauma. Specifically, changes at the wound edge in cell morphology, Cx43 expression, and collagen orientation were examined and compared to patient matched control regions of the AM without trauma. Furthermore, the study developed an *in vitro* model for creating reproducible fetal membrane defects that could be incubated for up to 7 days to assess wound healing and provide data which could be compared with that obtained in AM wounds after fetoscopic procedures.

The inability of AM to heal following injury, both *in utero* following fetoscopic surgery, and *in vitro* following trauma is demonstrated in this study. Within the cohort of fetoscopy patients, no spontaneous healing of the fetal membrane was observed. The study documents key changes in cell morphology observed at the wound edge. Polarisation of mesenchymal cells of the fibroblast layer was evident within approximately 200 µm from the wound margin. The mesenchymal cells orientate in a tangential fashion to the wound margin, indicative of that reported during embryonic wound healing and wound contraction mechanisms of healing. Aggregates of epithelial cells extending from the amniotic membrane epithelial surface is also evident in fetoscopy wounds, although these were not evident following *in vitro* trauma up to 7 days. We show Cx43 expression in AM, and how overexpression is reported at the wound edge compared to patient matched control regions.

During investigation of *in vitro* amniotic membrane trauma, Cx43 protein expression per area decreased at 2 hours post-injury, however then dramatically increased at 12 hours, which was sustained for up to 168 hours, when compared to amniotic membrane regions away from the wound edge. Cx43 protein expression per cell remained unchanged at 2 hours post-injury, however, it then increased at 12 hours and was sustained for 168 hours. This indicates that whilst the amount of Cx43 plaques per cell remains unchanged at 2 hours post-injury, the size of Cx43 plaques is initially decreased, before a striking upregulation is observed at 12 hours post-injury. In addition to high Cx43 protein expression at the wound edge, Cx43 and COX-2 gene expression is also found to be upregulated at the wound edge. COX-2 mRNA levels increase in response to

inflammatory cytokines and therefore indicates a level of inflammation occurring at the wound edge compared to control regions. The study further demonstrates changes in collagen alignment by the use of second harmonic generation imaging. It was found that high-resolution collagen imaging could be performed in the AM, obtained using transmission geometry for SHG signal collection. This is an improvement on previous attempts to image collagen fibres, which have relied on backscattered geometry, and does not provide the resolution obtained in the present study³. Indeed, the use of SHG imaging has provided novel findings and shown high alignment of collagen fibres at the wound edge. Collagen fibres align tangential to the wound margin in the same fashion as mesenchymal cell polarisation around the perimeter of the wound. In contrast, control regions show disorganised and shorter collagen fibres arranged in an interwoven fashion.

Previous studies have documented human fetal membrane healing through studying histological changes after fetoscopic surgery^{162,164}. However, limited detail is provided, with the studies stating observation of thickened rounded edges and little macroscopic evidence of tissue remodelling. In contrast to Papanna *et al.*, who reports disordered orientation of collagen fibres at the trocar site, the present study reports conflicting evidence with highly aligned collagen fibres that orientate tangential to the wound margin around the full perimeter of the wound¹⁶⁴. However, this study provides supporting evidence regarding the thinning of collagen fibres distal from the wound site. This could be explained by increased deposition of granulation tissue at the wound edge leading to observation of mature thick collagen. The ability of second harmonic generation imaging using transmission geometry to visualise collagen fibres also provides a higher resolution and level of detail not attainable through histological examination, which could explain why this was not previously reported. Increased collagen deposition noted at the AM wound edge following fetoscopic surgery for TTTS and after *in vitro* trauma is in agreement with a recent study showing increased collagen staining intensity at the wound edge following open fetal surgery for myelomeningocele¹⁶⁵. The picrosirius red stain is associated with type I collagen, which increased in surgical regions ($13.22 \pm 2.84\%$, N=10) compared to control non-surgical regions ($6.16 \pm 1.09\%$, N=10) from the same patient. Other previous studies have used cell monolayer models to study repair kinetics of human fetal membranes²⁰³⁻²⁰⁵. The effect of mechanical injury on repair mechanisms of amniotic epithelial and mesenchymal cell monolayers found increased ability of epithelial cells to repair, usually

within around 40 hours, compared to mesenchymal cell monolayers²⁰⁴. Furthermore, Devlieger *et al.*, discovered gestational age dependent repair kinetics of fetal membrane defects using a monolayer model developed using amniocytes obtained from human fetal membranes²⁰⁵. Although the study only investigated healing up to 48 hours, it was reported that proliferation at the monolayer wound edge increased as well as in monolayers derived from preterm tissue²⁰⁵.

Interestingly, traits from both normal cutaneous wound healing and embryonic wound healing are reported in this study. These include overexpression of COX-2, which is reported in the pro-inflammatory phase of normal cutaneous wound healing. Furthermore, tangential alignment of both mesenchymal cells and collagen fibres of the fibroblast layer is indicative of that seen in “purse-string” wound contraction mechanisms reported in embryonic wound healing¹⁹⁶. Interestingly, “purse-string” wound contraction occurs before the embryo is able to mount an inflammatory-mediated wound healing response, and contraction allows healing without the need for cell migration over the wound bed, and without the secretion of scar tissue¹⁹⁶. However, we report both the alignment of mesenchymal cells at the wound edge and an increase in collagen intensity, which indicates the secretion of granulation tissue. The overexpression of Cx43 at the wound edge, could inhibit mesenchymal cell migration, leading to the highly aligned ring of collagen and tangentially orientated mesenchymal cells at the wound edge, indicative of that seen in “purse-string” wound healing. However, further studies are needed to determine the mechanisms of wound healing in the AM.

To my knowledge this is the first study to investigate Cx43 expression in the AM and after trauma. Comparison with the literature is therefore limited, although similar findings have been reported in other chronic wounds that show a lack of healing, specifically diabetic foot ulcers, venous leg ulcers, and pressure ulcers¹⁹⁸. Interestingly, striking upregulation of Cx43 expression is reported in wound edge biopsies of chronic wounds compared to intact skin. Furthermore, Cx43 overexpression at the wound edge is also contradictory to that seen during normal cutaneous wound healing, where a reduction in Cx43 is reported. In addition, wounds that show a privileged healing response such as the gingival mucosa membrane of the mouth, show a rapid reduction of Cx43 at the wound edge¹⁹⁷.

Cx43 has been linked with the regulation of cell migration, and with a short half-life of 1-3 hours indicates a key regulatory role in wound healing dynamics. Overexpression of Cx43 is linked to poor wound healing outcomes in chronic wounds. However, knockdown of Cx43 using Cx43asODNs leads to the adoption of a migratory phenotype and has been shown to accelerate wound healing¹²⁸. Interestingly, knockdown of Cx43 leads to a decrease in cell adhesion and proliferation, whilst promoting cell migration, a necessary step in efficient wound healing. Furthermore, increased lamellipodial protrusions that assist migration occur following Cx43 knockdown, associated with increased Rac-1 and RhoA GTPase activity.

The negligible Cx43 protein expression observed in the AM epithelial layer of fetoscopy patients could indicate other cell-cell proteins dominate preterm (less than 37 weeks gestation) such as tight junctions and anchoring junctions including adherens and desmosomes. However increased Cx43 expression in epithelial cells was noted after artificial *in vitro* trauma. This could be due to gestational differences as term tissue (37-42 weeks gestation) was used *in vitro* in contrast to fetoscopy patient studies that had a mean gestational delivery age of 30⁺⁴ weeks. Unexpectedly, collagen type I expression did not change. This could be explained by the presence of different collagen types and other collagen types dominating in the amniotic membrane which may explain the increased SHG intensity seen at the wound edge which is known to detect collagen types I and III, which are known to exist in the amniotic membrane²⁰⁶. However, it should be noted that gene expression levels do not always correlate with protein levels and can be influenced by post-translational modifications.

The main cohort of patients had undergone fetoscopic surgery for TTTS. Treatment of congenital diaphragmatic hernia and twin-reversed arterial perfusion sequence involves a fetoscopic procedure similar to TTTS treatment, and therefore these fetal membrane defects were also included in analyses. Consultation with the fetal surgeon and careful macroscopic survey of the membranes after delivery enabled the quick location of laparoscope entry within 20 minutes of delivery for each patient. Due to the nature of the surgery, consented fetoscopy patients were often discharged from UCLH to return home to distant locations in England. Initially, this provided a noticeable constraint to the study, however this was partially alleviated by contacting other hospitals and obtaining letters of access for sample collection. Furthermore, a collaborative effort with University

Hospital Leuven, Belgium, provided another avenue for collection. Indeed, the mean time from fetoscopy surgery to delivery was 55 days, therefore a concerted effort to track patient's progress was necessary but often sample collection could not occur due to unpredictable and emergency delivery often occurring overnight after women presented with PPROM.

During development of the artificial *in vitro* trauma model, an area of FM away from the zone of altered morphology between the mid-zone and placental disc was dissected for consistency. The zone of altered morphology is known to undergo biochemical changes in preparation for parturition and in turn affects the mechanical integrity. Furthermore, FM were taken from term patients who had undergone elective caesarean section and had not gone into labour. Therefore, any changes in biochemistry and mechanical integrity that could arise following contractions was avoided. It should be noted that patient variability is likely to result in some differences, however this could not be avoided and therefore ample fetal membranes were collected and replicates performed during analyses to minimise this concern.

Intra-uterine fetal surgery rates are increasing for fetal conditions. Therefore, the importance of research into FM healing is important in order to more effectively design preventatives and reduce future iatrogenic PPROM rates. This study provides an in-depth examination of the AM defect following fetal surgery and *in vitro* trauma. Characterisation of the wound edge and identification of Cx43 overexpression provides an important foundation for the development of future therapies and iatrogenic PPROM preventative strategies. Furthermore, the inability of FM to heal has often been described as the "Achilles' heel" of fetal surgery with no explanation yet provided. For the first time we implicate Cx43 overexpression in thwarting the ability of AM to heal once injured, and therefore the effects of Cx43 modulation in AM healing could provide therapeutic options for preventing iatrogenic PPROM.

Chapter 5

**Molecular self-assembly of peptide amphiphile
membrane macrostructures triggered by amniotic
fluid for sealing human fetal membrane defects**

Chapter 5: Molecular self-assembly of peptide amphiphile membrane macrostructures triggered by amniotic fluid for sealing human fetal membrane defects

5.1 Introduction

This chapter outlines previous clinical and experimental attempts that have been made to seal fetal membrane defects. Currently there is no clinically available method to seal fetal membrane defects following fetal surgery that reduces the rate of PPRM or improves perinatal outcome. The results of this chapter highlight a novel approach towards sealing fetal membrane defects and could provide the basis for the development of a new therapeutic for PPRM prevention and treatment.

5.1.1 Previous approaches for sealing fetal membrane defects

There has been a resurgence in attempts to seal and repair fetal membranes over the past decade with the histological identification of absent fetal membrane healing by Gratacos *et al.*, and the recent reports of the amniotic membrane being a potential source of stem cells^{162,207-209}. To date, fibrin-based sealants (the amniopatch), gelatin sponges, and collagen amniografts have been used clinically in an attempt to seal the hole in the FM of patients following spontaneous and iatrogenic PPRM²¹⁰⁻²¹³. Experimental attempts to seal fetal membrane defects following fetoscopy also include the use of gelatin sponges, collagen plugs, and fibrin-based glues²¹⁴⁻²¹⁹. Other innovative approaches have also been tested including decellularised human amniotic membrane, bioactive small intestinal submucosa membranes, and more recently innovative synthetic hydrogels that seek biological inspiration from the mussel and sandcastle worm highly adhesive secretions^{168,220-224}. However, attempts for both treatment of PPRM and experimental methods for iatrogenic PPRM prevention have had limited success with inconsistent outcomes.

5.1.1.1 Sealants used clinically for spontaneous PPRM

Fibrin-based sealants used to treat PPRM

Table 5.1 shows a summary of the publications describing sealants used clinically. Initial descriptions of the use of fibrin-based sealants to prevent leakage of amniotic fluid after spontaneous PPRM involved the intracervical injection of maternal platelets that activate thrombin and the coagulation process. This was combined with a cervical cerclage to prevent the resulting fibrin clot from leaking out²²⁵. The resulting fibrin clot produced through the conversion of fibrinogen to fibrin in the presence of thrombin was thought to act as a glue to prevent amniotic fluid leakage and reduce the risk of ascending bacterial infection. This strategy was later refined and referred to as the amniopatch procedure, developed by Quintero *et al.*, in an attempt to improve outcome²¹⁴. The intra-amniotic injection of platelets was immediately followed with cryoprecipitate, which contains fibrinogen, fibronectin, and clotting factors (factor VIIIc, factor XIII, von Willebrand factor) to help stabilise the fibrin plug after it adheres to the damaged AM^{226,227}. However successful prevention of amniotic fluid leakage was not achieved in all cases following treatment between 16-24 weeks of gestation, resulting in poor clinical outcome for one third of cases^{214,228}. Other research groups tested the ability of fibrin-based sealants to prevent fluid leakage and seal artificially punctured fetal membranes in a modified syringe model²²⁹. Combinations of Aminocaproic acid and aprotinin that inhibit fibrinolysis for prolonging clot life, a commercially available preparation (Tisseel, Baxter Corp; Glendale, California) of fibrinogen, thrombin, and aprotinin, and platelets alone were tested. The commercially available Tisseel and cryoprecipitate/thrombin combinations performed best to prevent fluid leakage.

Major limitations of fibrin-based strategies have since emerged and include the inconsistency of outcomes between groups, which report approximately a 51-61% fetal survival rate^{212-214,216,230,231}. The technique of intra-amniotic injection was also performed blind, and therefore targeting of the fibrin clot to the FM rupture is not always possible. These strategies were also associated with chorioamnionitis, pulmonary hypoplasia, intrauterine fetal death, acute fetal bradycardia, development of amniotic bands, severe respiratory distress syndrome, and maternal pulmonary edema^{216,218,230}. Furthermore, the procedure to prepare fresh blood products is expensive and lengthy, and further

complicated by safety procedures that can take up to 48 hours to resolve. Although some achievements were made with an average of 10 weeks from procedure to delivery, the patient sample size is often small with research regularly referring to single patient outcomes. The overall survival rate reported is poor (51-61%) and the association with intrauterine fetal deaths highlighted the potentially harmful effects of introducing blood-clotting factors into the intra-amniotic region. Recent cohort studies confirmed that the success reported by the amniopatch procedure in some studies should be approached cautiously^{228,232}. Contradictory results show a success rate of 63.5% in iatrogenic PPRM patients compared to 21.4% reported by Sung *et al.*, who reported an even lower success rate of 11.8% after amniopatch treatment for spontaneous PPRM patients^{228,232}.

Regarding treatment of spontaneous PPRM using the amniopatch procedure, difficulty lies in locating site of rupture, the variation in defect size, and the increased chance of infection, meaning the standardisation of protocols often varies in clinical practice. In addition, success of the amniopatch procedure is often defined as cessation of amniotic fluid leakage and restoration of normal amniotic fluid volume, therefore it is important to note these studies do not address whether the structural integrity of the fetal membranes have been functionally restored. Follow up studies involving histological analysis would prove beneficial in evaluating the true sealing potential of the amniopatch procedure.

Table 5.1: Fibrin-based strategies for sealing fetal membrane defects.

Species	Sealant	Model	Key findings	Study
Human PPRM (n=19)	Fibrin glue	Tested clinically	Intracervical application. 60% survival rate reported between 1979 and 1982 ²²⁵ .	Genz <i>et al.</i> , (1979) ²¹³
Human PPRM (n=26)	Fibrin adhesion TISSUCOL®	Tested clinically	Repeated intracervical application up to six times until ceasing of AF leakage. 65% survival rate reported. However, most surviving neonates occurred in patients who were >26 weeks gestation.	Baumgarten & Moser (1986) ²²⁵
Human iPPROM (n=1)	Amniopatch	Tested clinically	Patient was readmitted with PPRM 4 days after umbilical-cord ligation of monoamniotic acardiac twin via fetoscopic guidance. Transabdominal Intra-amniotic injection of a platelet-cryoprecipitate plug. AF volume was restored. Final outcomes not provided.	Quintero <i>et al.</i> , (1996) ²²⁶
Human	Fibrin glue	FM explants	The effect of fibrin glue on FM tensile strength examined. Fibrin glue increased tensile rupture in wounded FM explants. However, this remained lower than non-wounded control FM.	Harmanli <i>et al.</i> , (1998) ²³³
Human iPPROM (n=7)	Amniopatch	Tested clinically	Restoration of AF volume n=3. Sudden fetal death n=2. Oligohydramnios persisted in 1 patient with AF leakage. Miscarriage occurred in 1 patient with no further leakage. Transabdominal intra-amniotic injection of platelets and cryoprecipitate.	Quintero <i>et al.</i> , (1999) ²¹²
Human PPRM (n=12)	Fibrin glue	Tested clinically	Intracervical application. Survival rate=53.8% Patients with poor prognosis (<24 weeks) selected.	Sciscione <i>et al.</i> , (2001) ²³⁰
Human	Platelets, Tisseel & thrombin	FM explant syringe model	Wounds created with a 20 gauge needle. Fibrin/thrombin-based combination best candidate for preventing AF leakage.	Reddy <i>et al.</i> , (2001) ²²⁹

Human, sPPROM (n=4) iPPROM (n=4)	Platelet, fibrin glue, and collagen slurry injection.	Tested clinically	More success in treating iPPROM than spontaneous PPROM. Spontaneous PPROM patients: n=2 delivered preterm within 2 days, n=1 fetal demise, n=1 delivered 31 weeks with respiratory distress syndrome. iPPROM patients: n=3 delivered viable infants at 26, 32, and 34 weeks, n=1 further membrane rupture with fetal termination.	Young <i>et al.</i> , (2004) ²¹⁶
Human, PPROM (n=5)	Amniopatch	Tested clinically	AF volume restoration in 4 of 5 patients who underwent CVS between 12-18 weeks gestation. Fetal demise occurred (n=3) at 1, 2, and 26 days post-procedure. Only one viable infant delivered.	Cobo <i>et al.</i> , (2007) ²³⁴
Human PPROM (n=1)	Amniopatch	Tested clinically	Amniocentesis at 3 weeks after PPROM at 18 weeks gestation. Viable infant delivered at 38 weeks.	Mandelbrot <i>et al.</i> , (2009) ²³⁵
Human iPPROM (n=3)	Amniopatch	Tested clinically	Restored AF volume in 2 patients within 7 days. One patient required 2 nd procedure to restore membranes. All 3 patients delivered viable infants. One infant born at 30 weeks gestation.	Pathak <i>et al.</i> , (2010) ²³⁶
Human sPPROM (n=1-7) iPPROM (n=19-24)	Amniopatch	Tested clinically	Very low survival reported (14.3%). One patient delivered viable infant at 39 weeks gestation. TWO CENTRE STUDY: Procedure restored membranes in 58%. Overall neonatal survival was 55%. Restoration of AF volume achieved in 12 patients (63.2%) who delivered at a mean of 35 weeks gestation. SUCCESS RATE between 15-23 weeks gestation: sPPROM (11.8%) vs iPPROM (36.4%).	Ferianec <i>et al.</i> , (2011) ²³⁷ Kwak <i>et al.</i> , (2013) ²³⁸ Richter <i>et al.</i> , (2013) ²³⁹ Chmait <i>et al.</i> , (2017) ²²⁸ Sung <i>et al.</i> , (2017) ²³²

Gelatin and collagen based sealing strategies used for treating PPROM

Strategies other than fibrin-based sealants have been attempted to improve PPROM clinical outcome and include the use of gelatin sponge (**Table 5.2**). In much the same way, the gelatin sponge, known as Gelfoam, is used to prevent amniotic fluid leakage from the amniotic cavity²¹⁸. However, the technique has been described as a complex and aggressive form of PPROM prevention, which did not yield promising clinical outcomes²⁴⁰. Sudden fetal death was also associated with this technique that involved constant replenishment of amniotic fluid by amnioinfusion, cervical cerclage, administration of Gelfoam, and a combination of antibiotics with perioperative tocolysis. Further amnioinfusion were often required to maintain amniotic fluid volume and therefore with low neonatal survival rates reported, it remains an unpopular clinical option.

Collagen amniograft have also been tested clinically in spontaneous PPROM. The collagen amniograft is placed over the defect endoscopically and sealed in place using fibrin glue. This technique is more involved compared to instillation of fibrin glue or gelatin plugs and requires a lengthy surgery time (approximately 2.5 hours). Furthermore, the continued inflation of the amniotic cavity using carbon dioxide was required, putting the fetus at more risk.

Table 5.2 Gelatin and collagen based PPROM sealing strategies

Species	Sealant	Model	Key findings	Study
Human	Gelatin sponge plug	Syringe model	Gelatin sponge was able to prevent AF leakage when the wound diameter was >7 mm.	O'Brien <i>et al.</i> , (2001) ²⁴¹
Human sPPROM (n=14) iPPROM (n=1).	Gelfoam and amnioinfusion	Tested clinically	Administration of gelatin sponge into amniotic cavity. Intervention occurred between 13-21 weeks gestation. Overall neonate survival was 30%. 2 intrauterine fetal deaths.	O'Brien <i>et al.</i> , (2002) ²⁴⁰
Human sPPROM (n=1).	Collagen amniograft	Tested clinically	Collagen graft was endoscopically placed over a 2 cm defect and sealed in place with fibrin glue. AF leakage persisted 14 days post-procedure. Viable infant delivered at 30 weeks gestation.	Quintero <i>et al.</i> , (2002) ²⁴²

To date, there has been limited success in improving clinical outcomes to treat women after spontaneous PPROM²¹³. Whilst improvements have been made regarding fibrin-based sealants and development of the amniopatch, the safety and efficacy are not well established due to small patient groups, lack of comparative control groups, and contradictory results between different research centres. Furthermore, clinical attempts to use gelatin sponge plugs and collagen amniografts have been associated with low neonatal survival and low patient groups, making it difficult to foresee the true efficacy and safety for use in the clinic. Before translation to the clinic, the development of sealing strategies for treating PPROM should be thoroughly investigated by improvement of *in vitro* cell and tissue explant mode followed by studies in animal models prior to implementation within organised pre-clinical trials that have appropriate control groups. It is important to note that the use of fibrin-based glues, gelatin sponges, and collagen amniografts discussed so far have been used clinically as a treatment following rupture of membranes after spontaneous PPROM making it difficult to design approaches that can seal the fetal membrane defect with an irregular shape and size.

5.1.1.2 Tissue engineering strategies for iatrogenic PPROM prevention

Iatrogenic PPROM occurs in 30% of patients following fetoscopic surgery²⁴³. It has been reported that PPROM does not always occur following fetoscopy possibly due to sliding of the amniotic and chorionic membranes over one another and adherence of the fetal membrane wound edges to the underlying myometrium^{129,162}. Nevertheless, iatrogenic PPROM presents an on-going challenge for the field of intrauterine fetal surgery, where it is often termed the “Achilles’ heel” of intrauterine surgical intervention.

Many technical and biological challenges have hindered the development of fetoscopic wound sealants for healing the wounds in the fetal membranes. For example, sealants must take into consideration the size of the fetal membrane defect (approximately 250 µm in thickness; 5 mm diameter) when acting as a plug to prevent amniotic fluid leakage. Localisation and accessibility of the fetoscopic wound may be challenging, since the wounds created after fetoscopic surgery can lead to tears that are irregular in shape and size. Therefore, the plugging material must favourably be injectable and remain stable in a wet environment that will contain amniotic fluid and often the presence of maternal and fetal blood. Furthermore, as previously reported in **Chapter 4**, there is an absence of fetal membrane healing, which further complicates the potential of previously used sealants to integrate efficiently with the native tissue and induce healing mechanisms in the wound^{244,245}.

To date, very few studies exist regarding prophylactic sealing of fetoscopic puncture sites in the clinic. As described in the previous section for treatment of PPROM (**5.1.1.1 Sealants used clinically for spontaneous PPROM**) fibrin-based sealants have also been tested for prevention of iatrogenic PPROM. Injection of platelets, followed by fibrin glue and powdered collagen slurry was administered endoscopically following cord ligation for twin-to-twin transfusion syndrome or amniocentesis (**Table 5.3**). From the 8 patients, 6 progressed with no evidence of amniotic fluid leakage for 8 weeks or more²¹⁶. Since, the use of gelatin sponge plug has been tested clinically for sealing fetoscopic defects following fetoscopy for twin-to-twin transfusion syndrome¹³¹. However, there was no improvement in patient outcome when compared to patients that did not receive the gelatin sponge plug. Furthermore, a larger retrospective cohort study (n=134) has confirmed no significant difference in iatrogenic PPROM rates in patients who received gelatin sponge plug (39% progressed to iPPROM) compared to those that did not (34% progressed to iPPROM)²¹¹. More recently, the collagen plug has been tested clinically in

patients following fetoscopic endoluminal tracheal occlusion for congenital diaphragmatic hernia²¹⁰. From 54 patients who received the collagen plug, 48% developed PPROM; and of the 87 who did not receive the collagen plug, 39% went on to develop iPPROM.

Table 5.3: Collagen and gelatin plug strategies for prevention of iPPROM

Species	Sealant	Model	Key findings	Study
Sheep (n=5) Rhesus monkey (n=5)	Gelatin sponge plug (Gelfoam)	Sheep and rhesus monkey fetoscopy model.	Gelatin sponge plug placed in fetal membrane wound endoscopically. Rapid swelling of the plug reported. All sheep fetuses survived intervention. 2 primate fetuses were aborted. Histological analysis of membranes was not performed.	Luks <i>et al.</i> , (1999) ²⁴⁶
Rabbit (n=32 does, with 288 sacs).	Fibrin sealant, autologous maternal blood plug and collagen plug	Mid-gestational fetoscopy rabbit model.	Fetoscopy wound closure technique occurred at day 22 and harvested at day 32. Amnion resealed in 20-44% of controls when surgically closed. However, none of tested techniques significantly improved outcome.	Deprest <i>et al.</i> , (1999) ²⁴⁷
Fetal rabbit (n=36)	1. human amnion membrane (n=23) 2. collagen foil (n=16) 3. collagen plug (n=19) 4. collagen plug with cultured amnion cells (n=19).	Mid-gestational fetoscopy rabbit model.	Fibrin sealant was additionally administered following insertion of plugging technique. Resealing occurred in 58-64% of cases in all but the human amnion alone technique as defined by restoration of amniotic fluid at day 30 gestation. No sealing technique was significantly better than the other.	Papodopoulos <i>et al.</i> , (2006) ²⁴⁸
Rabbit	Platelet-enriched collagen plug with amniotic fluid cells (n=44) and without amniotic fluid cells (n=32).	Mid-gestational fetoscopy rabbit model.	Fetoscopy needle puncture occurred at day 23 gestation before plugging with collagen plug with or without amniotic fluid cells. Cell proliferation was increased in collagen plugs enriched with amniotic fluid cells. N=14/44 of collagen plugs with amniotic fluid cells remained. N=18/32 of collagen plugs without amniotic fluid cells remained.	Liekens <i>et al.</i> , (2008) ²⁴⁹
Human	Gelatin sponge plug (Gelfoam).	Tested clinically.	No difference in outcome after gelatin sponge plugging of fetoscopic port site compared to patients who did not receive gelatin sponge.	Papanna <i>et al.</i> , (2010) ¹³¹

Human (n=134).	Absorbable gelatin sponge plug	Tested clinically. Retrospective cohort study for patients undergoing fetoscopy.	Gelatin sponge placed in 74 patients. 60 patients did not receive the gelatin plug. There was no difference in iPPROM rates. 39% of patients who received gelatin plug developed iPPROM. 34% of control patients who did not receive gelatin plug developed iPPROM.	Papanna <i>et al.</i> , (2013) ²¹¹
Human	Collagen plug imbued with fibrinogen and plasma	FM explant model.	Amniotic fluid leakage decreased by 1/3 rd with plasma and fibrinogen addition. Some fibrin formation occurred in fibrinogen and plasma soaked collagen plugs.	Engels <i>et al.</i> , (2013) ²⁵⁰
Human (n=141)	Lyostypt collagen plug (B. Braun)	Single centre cohort study for patients undergoing fetoscopic endoluminal tracheal occlusion for congenital diaphragmatic hernia.	Collagen plug is rolled into cylinder and placed into membrane defect. N=54 received collagen plug N=87 did not receive collagen plug. 48% of patients who received collagen plug experienced PPROM. 39% of patients who did not receive a plug experienced PPROM.	Engels <i>et al.</i> , (2014) ²¹⁰

Other than these limited clinical studies, preclinical assessment of sealing strategies has mainly focused on the mid-gestational rabbit model. Fibrin-based sealants and collagen plugs also showed limited clinical success in the mid-gestational rabbit model²⁴⁷⁻²⁵⁰. Other strategies have included the use of bioactive membranes from porcine small intestine and decellularised human amnion (**Table 5.4**)^{168,170,224}. More recently, efforts have been made to adopt the favourable approach of injectable sealants as opposed to the placement of 3D biomaterial plugs such as collagen and acellular amnion scaffolds.

Table 5.4: Other strategies for sealing fetal membrane defects for prevention of *iPPROM*

Species	Sealant	Model	Key findings	Study
Human	Laser welding	FM explant model. In vitro laser welding.	Cryoprecipitate, 50% albumin, and polytetrafluoroethylene (e-PFTE) used as solder medium. Amniotic membrane laser welding successful in 82.6% of membranes when using e-PFTE compared to 10.7% when using cryoprecipitate. 100% unsuccessful using albumin as solder medium.	Mendoza et al., (1999) ²⁵¹
Rabbit (n=20 does, n=100 gestational sacs).	Bioactive membrane (porcine small intestine)	Mid-gestational fetoscopy rabbit model.	N=50 fetoscopic wounds were sealed with biocompatible matrix derived from porcine small intestine containing TGFB and FGFB. Membrane integrity restored in 70% after plug insertion compared to 41% in control sacs that did not receive plug. Amniotic band observed in one treated sac.	Devlieger et al., (2003) ²²⁴
Rabbit (n=8 does).	Acellular human amnion	Mid-gestational fetoscopy rabbit model.	75% of sacs treated with decellularised term human amnion showed amniotic integrity compared to 25% in control sacs that did not receive plug.	Mallik et al., (2007) ¹⁶⁸
Rabbit	Engineered native amniotic scaffold and polyesterurethane scaffolds (DegraPol)	Mid-gestational fetoscopy rabbit model.	AF volume was significantly higher in the DegraPol sealed sacs compared to unclosed sacs. Integration of plugs improved when using amniotic membrane scaffold compared to DegraPol. Epithelialisation and proliferation indices improved with amniotic membrane scaffold as a sealant.	Ochsenbein-Kolble et al., (2007) ¹⁷⁰
Human	Precipitated egg white	Syrnige FM explant model.	Study suggests egg white can seal defects for up to 2 weeks in this model. However, whilst there is statistical significance between control and test group regarding amount of fluid leakage over 24 hours, the difference was approximately 5 mL, which is not necessarily clinically significant.	Mendez-Figueroa et al., (2010) ²⁵²

The new approaches include the use of bioinspired polymer hydrogel biomimetics involving mussel and sandcastle worm adhesives, with the primary function to act as a separation barrier and prevent amniotic fluid leakage (**Table 5.5**)^{172,220-223,253,254}. Liquid sealants tested *in vitro* by Bilic *et al.*, include cyanoacrylate glues and polyethylene glycol (PEG)-based hydrogel-type polymers. Based on previous reports demonstrating interfacial bonding to other tissues, and the ability to gel *in situ*, the synthetic PEG-based hydrogels investigated were a photopolymerisable gel used in the lung for closure of pulmonary air leaks, the commercially available SprayGel used previously as an anti-adhesion barrier for myomectomy, and the mussel-mimetic adhesive sealant. The bioinspired mussel-mimetic is a catechol-functionalised PEG that forms hydrogels via crosslinking by oxidation after mixing with a cross-linking solution, sodium periodate. The strong adhesive properties of this mussel-mimetic derive from the 3,4-dihydroxyphenylalanine (DOPA) amino acid found in high concentrations in the mussel foot, allowing strong underwater adhesion. The other liquid sealants tested included Dermabond and Histoacryl, which are alkyl-cyanoacrylate glues, known to strongly adhere to wet tissue via amniotic polymerisation of hydrogel groups. The alkyl-cyanoacrylate glues appeared to severely damage the amniotic membrane epithelial layer, with one showing significant cytotoxicity. The photopolymerisable gel and SprayGel PEG-based hydrogel lacked adhesion to the fetal membrane. However, the DOPA-functionalised PEG hydrogel showed improved adhesion to the fetal membrane with lower apoptosis levels and without disrupting the amniotic epithelial layer²²⁰.

Since first investigating the adhesive properties of the mussel-mimetic glue, it has been further tested on elastomeric membranes and *in vitro* inflation devices that subject the fetal membranes to physiological levels of compression and tension. However, after examination in the mid-gestational rabbit model, fetal survival outcome was not significantly different to control sacs that did not receive the adhesive²⁵³.

Similarly, the sandcastle worm is another marine creature that secretes a proteinaceous glue that helps bond sand grains underwater to form a protective shell. The strong adhesion is due to the polyacidic and polybasic properties of the proteins found in the secretions. By replicating the chemistry and molar ratios using synthetic poly(meth)acrylate copolymers, the group were able to achieve an adhesive complex coacervate that improved sealing in an *in vitro* syringe model. The glue has since been

tested in a Yucatan miniature swine model. However, unexpectedly the swine fetal membrane showed self-healing properties likely due to its vasculature, and therefore the swine model was unable to show a difference in fetal survival.

Table 5.5: *Bioinspired tissue adhesive strategies for sealing fetal membrane defects*

Species	Sealant	Model	Key findings	Study
Human	Photopolymerised PEG (pPEG) and catechol-functionalised PEG (cPEG) mussel-mimetic hydrogel sealant.	Sealing tested <i>in vitro</i> using a cellerator device to stretch out fetal membrane.	Only poly(ethylene glycol)-based hydrogel mussel mimetic hydrogel sealant showed non-disruptive and non-toxic bonding to fetal membranes.	Bilic <i>et al.</i> , (2010) ²²⁰
Elastomeric membranes	Mussel-mimetic tissue adhesive.	Inflation device.	Poly(ethylene glycol)-based hydrogel used to seal elastomeric membrane defects. A critical burst pressure of 48 mbar reached after sealing.	Haller <i>et al.</i> , (2011) ²²¹
Human	Mussel-mimetic tissue adhesive.	Inflation device.	Poly(ethylene glycol)-based hydrogel reached burst pressure of 60 mbar, comparable with fibrin glue alone.	Haller <i>et al.</i> , (2012) ²²²
Human	Sandcastle worm mimetic tissue adhesive.	Syringe FM explant model.	The study develops a method to test fluid leakage. Addition of amniotic membrane patch and adhesive was used to seal artificially punctured fetal membranes. The sealant and membrane patch withstood an additional 12g compared to membrane patch alone.	Mann <i>et al.</i> , (2012) ²²³
Rabbit	Mussel mimetic tissue adhesive.	Mid-gestational rabbit fetoscopy model.	Fetal survival no different in treated groups. Comparable to fibrin glue control.	Kivelio <i>et al.</i> , (2013) ²⁵³
Swine	Sandcastle worm mimetic tissue adhesive.	Yucatan miniature pig fetoscopy model.	No difference in fetal survival in treated groups. Spontaneous healing of control defects reported in the swine model, therefore proving to be an inadequate model.	Papanna <i>et al.</i> , (2015) ¹⁷²

In summary, there are advantages to the new liquid sealants under development compared to the previous use of 3D biomaterial plugs, which include the injectable capabilities and the ability to adhere in a wet/moist environment. However, there are many limitations associated with the previous attempts to seal fetal membrane defects. In particular, the use of miniature swine models is not helpful due to their spontaneous FM healing rate. The use of the mid-gestational rabbit model is not ideal, as the rabbit amniotic sac does not adhere to the decidua and myometrium as it does in human systems. The gestational age of the rabbit is also very short in comparison to humans with term being at 30 days. Therefore any sealing method can only be tested for up to 7 days before delivery and harvesting of the sample. Furthermore, the use of synthetic bioinspired liquid sealants require crosslinking agents such as sodium periodate, which acts as a strong oxidizing reagents that enable polymerization and formation of hydrogels. This chemical is a strong irritant and the effects on fetal membranes after 24 hours has not been reported. It is therefore necessary to investigate more long-term cytotoxicity and efficacy *in vitro* and in animal models other than the Yucatan miniature swine model before clinical testing can be proposed.

The development of future sealants would benefit from being injectable and functional in a wet and dynamically mechanical environment. However, a tissue engineering approach that could facilitate the introduction of wound healing factors and inhibitors that enhance healing could improve liquid sealants that not only provide a barrier for prevention of amniotic fluid leakage but also induce healing mechanisms and promote repair in the fetal membranes.

5.1.2 Potential peptide amphiphiles for sealing defects in the fetal membranes

Peptide amphiphiles (PAs) have a widespread interest in tissue engineering, regenerative medicine, and drug delivery, due to their ability to inter- and intra-molecularly self-assemble into highly ordered nanostructures with bioactive functionality. The use of PAs has not before been explored in the context of FM regeneration and the ability to use these systems to signal native cells presents an interesting opportunity.

PAs are small synthetic molecules that contain both hydrophobic and hydrophilic domains, typically comprised of three regions: (1) Hydrophobic, (2) Peptide, and (3) Charged group domain (**Figure 5.1**).

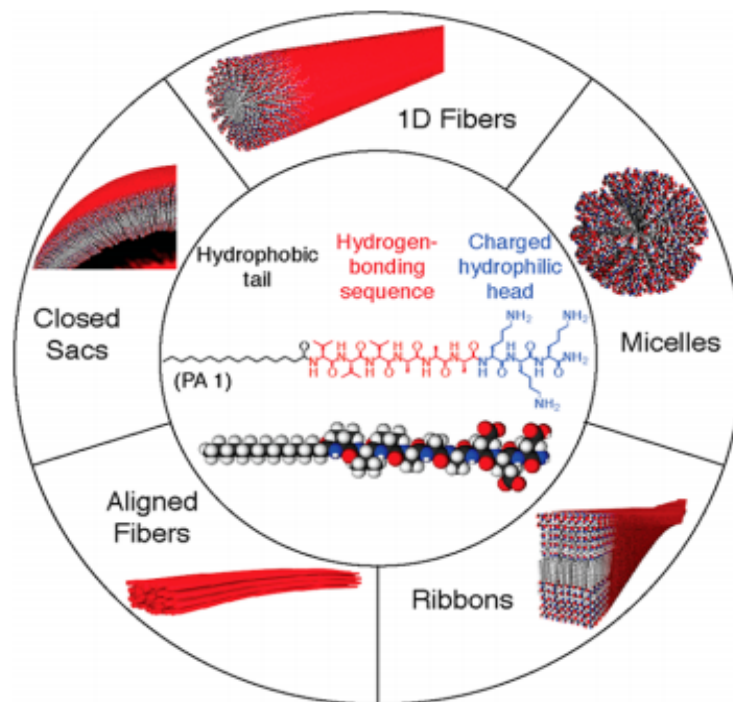


Figure 5.1: Peptide amphiphiles are composed of three key regions including the hydrophobic alkyl tail, the β -sheet forming peptide domain, and the charged amino acid group domain. The amphilocity is provided by the combined hydrophilic nature of the alkyl tail and peptide domain with the hydrophilic charged group of amino acids. This interesting property enables the formation of 1D nanofibres, micelles, closed sacs, aligned fibres, and ribbons. Adapted from Hendricks et al., (2017)¹¹

The hydrophobic domain consists of a long alkyl tail that varies in length and consists of various groups facilitating integration of bioactive epitopes onto the surface of the self-assembled nanostructure.

The peptide domain forms a β -sheet that is adjacent to the hydrophobic alkyl tail with intermolecular hydrogen bonding due to the short peptide sequence that contains hydrophobic amino acids. The ability to form intermolecular hydrogen bonds as β -sheets assists the formation of self-assembled 1D nanofibres, which are then responsible for the formation of 3D nanofibre networks.

The charged group domain is adjacent to the hydrophobic β -sheet forming region and contains charged amino acids which promotes solubility and facilitates PA design in response to changes in pH and electrolyte levels due to the charged amino acids acting as weak acids and bases. This triggers formation of 1D nanofibres and therefore the design of this domain is important in regulating the formation of 3D nanofibre networks once in contact with a physiological solution. The pH and salt-responsive property has inspired the addition of a fourth region, termed the bioactive epitope, which is adjacent to the charged group domain and has previously incorporated bioactive regions including cells, DNA, and growth factors that can form self-assembled PA nanofibre networks with biofunctionality once injected into a physiological environment.

5.1.3 Molecular self-assembly

According to IUPAC Recommendations (2013), molecular self-assembly is the “*spontaneous and reversible organisation of molecular entities by non-covalent interactions*” further defined as “*a process in which a system of pre-existing components, under specific conditions, adopts a more organized structure through interactions between the components themselves*”²⁵⁵.

Self-assembled hydrogels differ from conventional covalently cross-linked polymer hydrogels, as they do not require cross-linking or polymerisation to undergo gelation. Instead self-assembled hydrogels typically form following charge screening due to multivalent ions in solution, and therefore are not determined by covalent interactions. As previously described, PAs can self-assemble to form 1D high-aspect-ratio nanofibres, closed sacs, micelles, ribbons, and aligned fibres, with emergent potential in tissue engineering applications for soft and hard tissue regeneration²⁵⁶.

5.1.4 Liquid-liquid interfacial systems for a tissue engineering approach

The study of molecular organisation at the interface has previously been investigated between an air and water interface classically known as the Langmuir-Blodgett film; and between solid and liquids, for example the self-assembling monolayer formed by dissolving liquids on a solid surface²⁵⁷⁻²⁵⁹. Another example is the layer-by-layer deposition of polymers at a liquid interface²⁶⁰. Interestingly, the aqueous liquid-liquid interface has also been investigated using unassembled solutions of PAs and other solutions including polysaccharide hyaluronic acid, growth factors, and elastin-like polypeptides (**Figure 5.2a, b**)^{4,14,15}. Hyaluronic acid is a non-sulfated glycosaminoglycan (GAG) that is highly negative and found in connective tissues, whilst elastin-like polypeptides are also negatively charged and engineered to share structural characteristics with proteins such as tropoelastin. Hyaluronic acid and elastin-like polypeptides are both high molecular weight molecules that have been shown to co-assemble with positive PAs (PA-K3) via strong electrostatic interactions to form solid membranes at the liquid-liquid interface (**Figure 5.2a**)^{4,8,261}.

PAs have previously been tested with solutions of synovial fluid demonstrating gel formation at physiological pH for biomedical applications (**Figure 5.2a**)¹³. PA-K molecules, used at 1% (w/v), with branched RGDS sequences to promote cell adhesion, enabled the formation of gels when mixed in a 1:1 ratio with synovial fluid. However, no studies exist involving liquid-liquid interface systems of other physiological solutions such as blood and amniotic fluid when combined with solutions of PAs. Recently, PA-based gels have been used to investigate wound regeneration for diabetic skin wounds and full thickness skin burns (**Figure 5.2c**)^{17,18}. For example, a heparin-mimetic PA gel formed using negatively charged GAG-PA and positively charged PA-K, which was topically applied to a diabetic mouse wound model, reported to accelerate diabetic wound healing by promoting angiogenesis¹⁷. The same group also used the heparin-mimetic PA gel to treat full thickness burn injuries in a mouse model and demonstrated an increased rate of repair following topical application¹⁸.

A major benefit of PAs regarding *in situ* fetal membrane sealing and regeneration is that they can exist in an unassembled state in solution with very low viscosity, and then be easily injected to interact with a physiological solution such as amniotic fluid and maternal blood. The presence of key physiological factors in the amniotic fluid (AF) could induce PA self-assembly to form cylindrical nanofibres leading to complex 3D nano-architectures for mimicking the fetal membrane extracellular matrix, which is highly dense and contains a complex anisotropic collagenous matrix.

In summary, the use of PAs to form highly complex 3D nanostructures is of growing interest for developing new therapies for biomedical applications. Regarding fetal membrane sealing for the prevention and treatment of iatrogenic and spontaneous PPRM, PA-based gels offer advantages over previously attempted sealing techniques as they can be injected and when combined with physiological solutions self-assemble to form stable gels that microscopically mimic the extracellular matrix. The ability to design and alter the sequence of PA provides a never before ability to optimise the desired gel properties in applications such as fetal membrane wound sealing. Furthermore, previous complications include the ability of gels to remain stable and functional in a wet environment. As PAs form stable gels at the liquid-liquid interface this could help to address this complication. In addition, the ability to present bioactive epitopes in high density at the surface of self-assembled PA nanofibres alludes to the possibility of

designing therapies that not only act as a barrier to prevent amniotic fluid leakage but also if targeted correctly, can promote wound repair in a tissue that has absent wound healing. For the first time we propose the use of synthetic peptide amphiphiles that self-assemble to form 3D nanofibrous networks with potential to mimic amniotic membrane extracellular matrix microstructure.

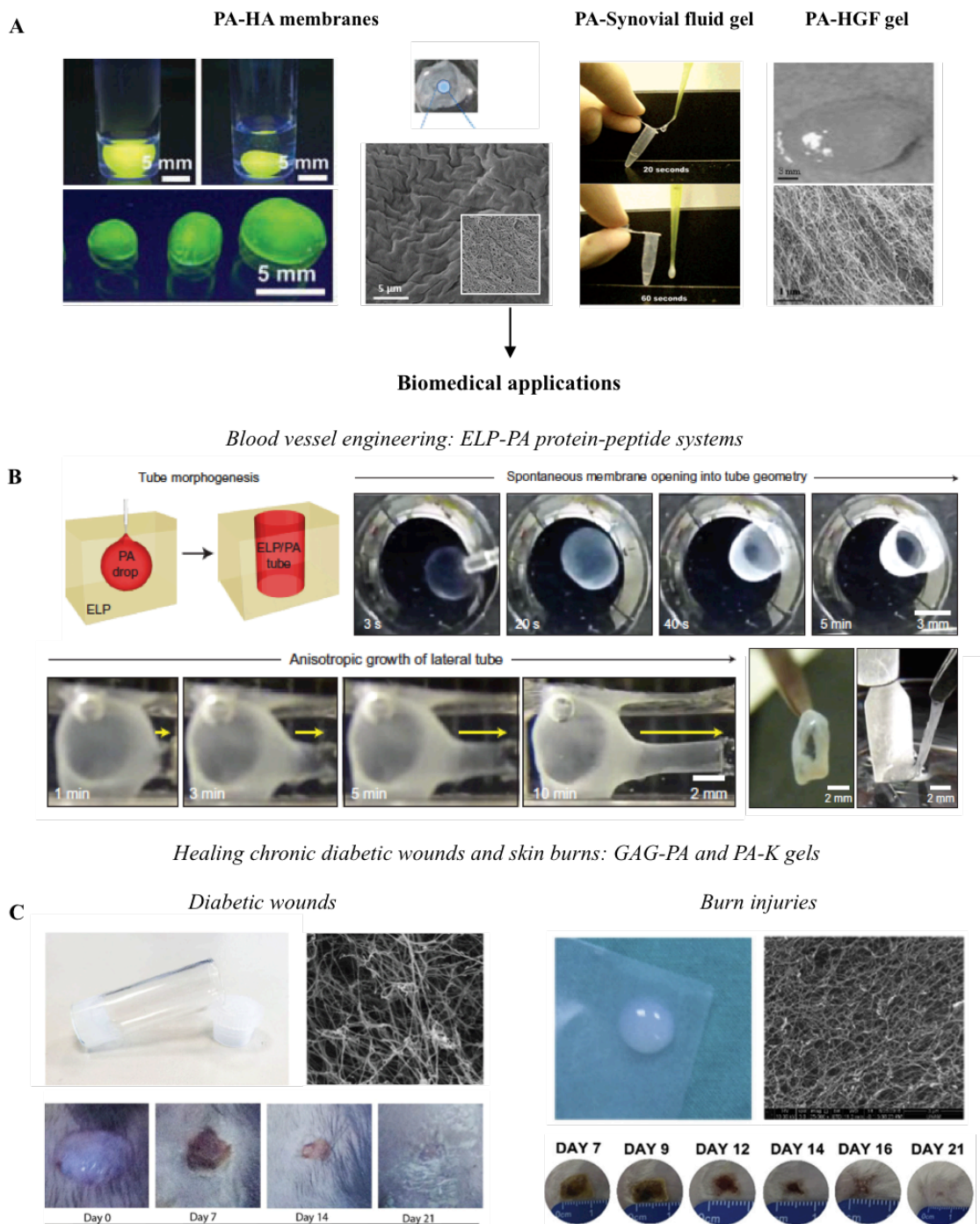


Figure 5.2: Peptide amphiphile gels and biomedical applications. Self-assembling peptide amphiphile gels formed when combined with a variety of solutions including polysaccharides, growth factors, and physiological solutions (A). Self-assembly peptide amphiphile systems have also been used for engineering of blood vessels using protein-peptide elastin-like polypeptide (ELP) – PA systems (B) and for the topical application of PA gels for diabetic wound and burn injury regeneration (C). Adapted from: Capito et al., (2008)⁴; Ferreira et al., (2013)⁸; Guler et al., (2006)¹³; Hosseinkhani et al., (2006)¹⁴; Inostroza-Brito et al., (2015)¹⁵; Senturk et al., (2017)¹⁷ and Yergoz et al., (2017)¹⁸.

5.2 Methods

5.2.1 Amniotic fluid collection

Human amniotic fluid (AF) was used to study formation of macroscopic structures, if any, with solutions of positively charged peptide amphiphiles (PAs) at the liquid-liquid PA-AF interface. AF was collected from women undergoing fetoscopic laser ablation of placental vascular anastomoses for twin-to-twin transfusion syndrome in mid-trimester pregnancies, and following amniodrainage for polyhydramnios, and amniocentesis for diagnostic genetic testing. Mid-trimester human AF was used to form macroscopic structures at the PA-AF interface.

5.2.2 Fetal membrane collection

Fetal membranes (n=9) were collected from term deliveries following elective Caesarean section to test the potential of PA-AF membranes for sealing FM defects using the *in vitro* FM wound model. Mean gestational age at delivery was 39^{+1} weeks with a range of 38^{+3} – 41^{+2} weeks (median: 39^{+3} weeks). Mean maternal age at delivery was 32 with a range of 25 – 39 years of age (median: 34 years). The indication for caesarean section (**Figure**

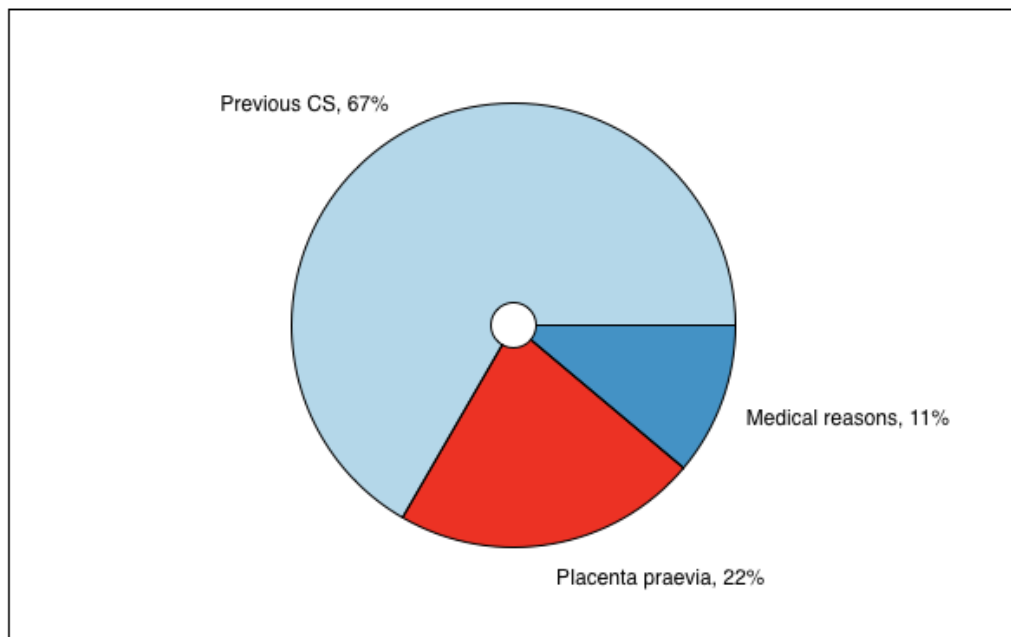


Figure 5.3: Indication for caesarean section shown as a percentage. These samples were used for testing peptide amphiphile sealing potential and toxicity within our *in vitro* wound model.

5.3) includes placenta praevia, history of at least one previous caesarean section, and maternal medical reasons.

5.2.3 PDMS fluidic device fabrication

Polydimethylsiloxane (PDMS) fluidic channels were used for the formation of self-assembled macroscopic structures at the liquid-liquid PA-AF interface. PDMS was used as it is a hydrophobic and inert material, providing a large contact angle between liquid droplets. PDMS channels were formed using a novel method established within our laboratory (**Figure 5.4**). First, a 10:1 ratio of silicone elastomer and crosslinking agent was thoroughly mixed. Air bubbles were removed using a vacuum desiccator. The resulting mixture was cured for 45 minutes at 60°C. For PDMS channels, a bottom layer was partially cured and a second layer was deposited. After the first layer is fully cured and the second layer partially cured, 2 mm capillary tubes were inserted into the PDMS. After complete curing for a total of 45 minutes at 60°C, the capillary tubes were carefully removed to reveal 2 mm channels.

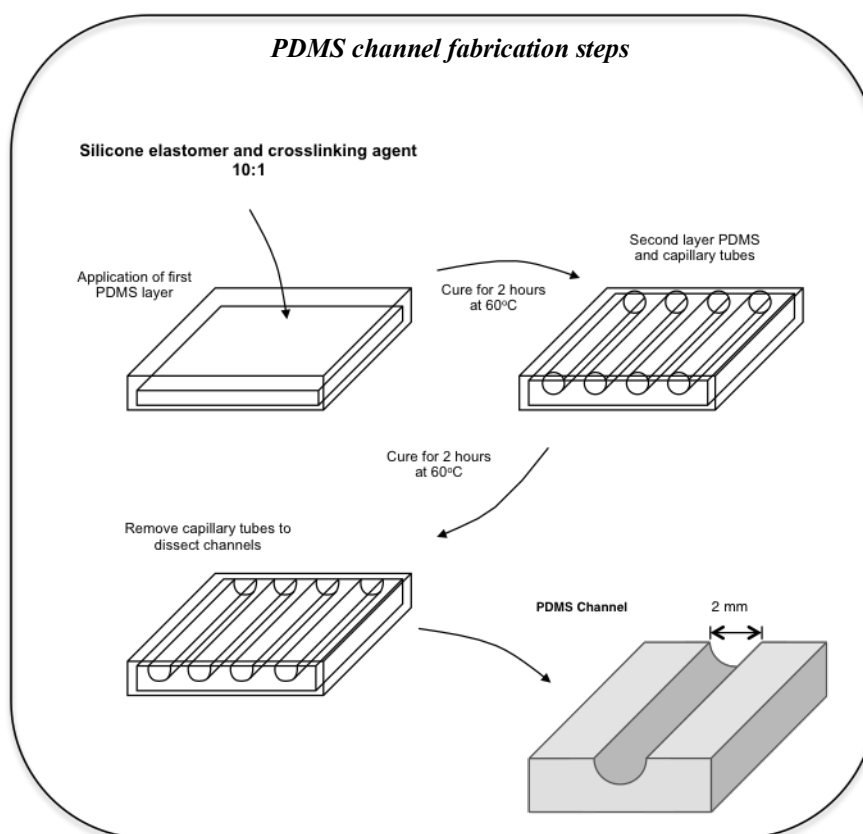


Figure 5.4: Fabrication of PDMS channels for investigating formation of self-assembling membranes between amniotic fluid and peptide amphiphile solutions. The channels are 2 mm in diameter and provide a hydrophobic and inert surface for the study of liquid-liquid interfacial systems.

5.2.4 Self-assembly of PA-AF macrostructures

AF was either used immediately after collection or stored at 4°C in a sterile sealed container for up to 7 days before being transferred to -20°C. Self-assembly of macroscopic structures were studied using 0.5-2% (w/v) PA solutions with unaltered human AF. PDMS channels were used (**Figure 5.5a**) as a fluidic device to study the liquid-liquid interface self-assembling systems and prepare membranes in a reproducible, hydrophobic and inert environment. Within the PDMS channel, PA and AF solutions were combined in equal volumes using a range of 5-15 μL throughout experimentation. Using PDMS channels also allowed for small quantities of PA solution to be tested. AF (\sim 5-15 μL) was first pipetted into the left side of a channel and then an equal volume of PA solution (\sim 5-15 μL) into the opposite side and left to form an interface. Self-assembly was also tested by injecting either PA or AF into a larger volume of the other solution. Furthermore, the PA solution sealing ability was also tested with human fetal membrane defects in the *in vitro* FM wound model (**Figure 5.5b-e**).

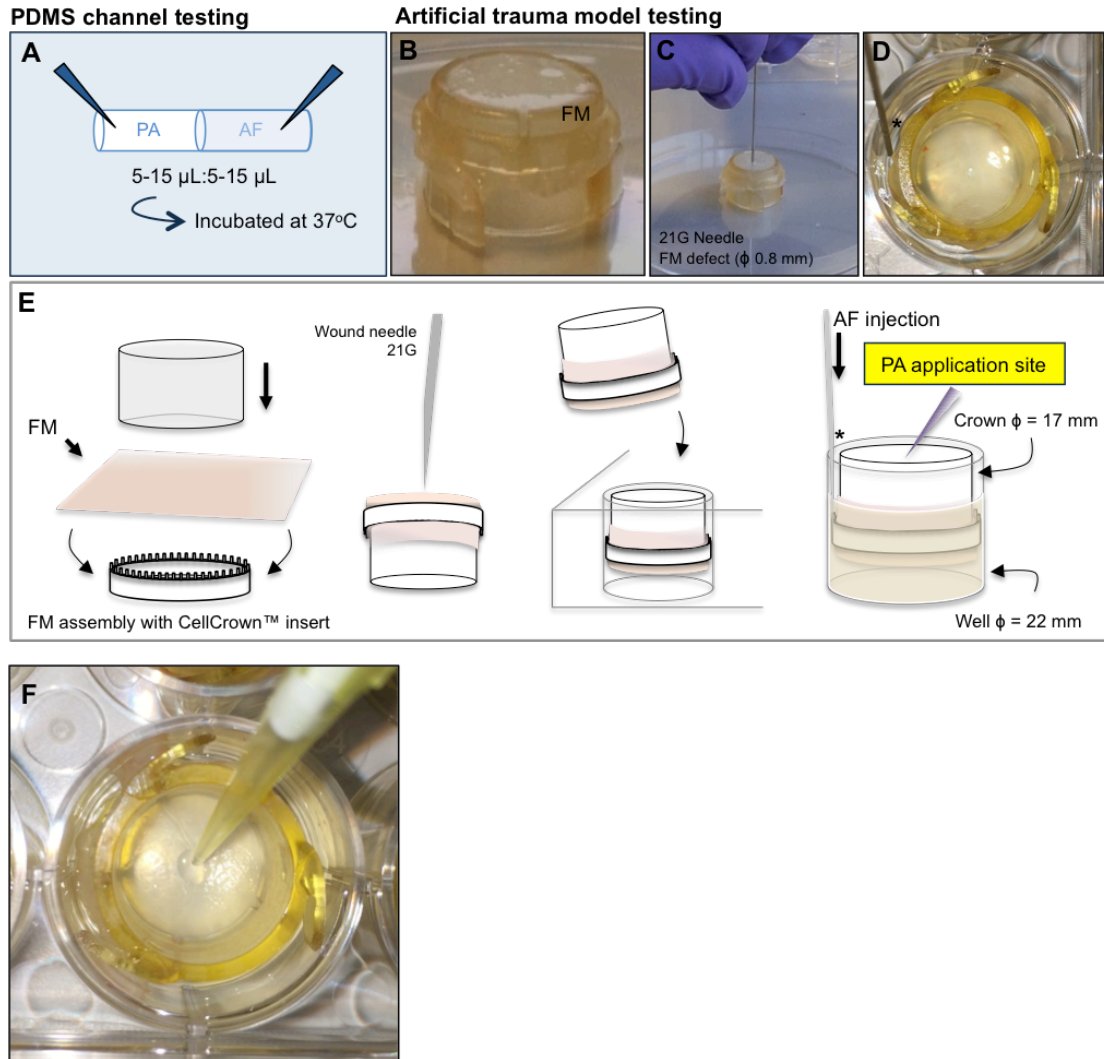


Figure 5.5: Methods used to test the self-assembly of macrostructures at the amniotic fluid and peptid amphiphile interface. Self assembly was tested in PDMS channels (A) and within the artificial fetal membrane trauma model to test sealing capabilities (B-E). Fetal membranes (FM) were collected from term placentas from women undergoing elective caesarean section between 37 and 42 weeks of gestation. The FM was excised into square tissue explants (approx. 30 x 30 mm) and assembled with the crown insert (B). A 21 Gauge needle was used to create a 0.8 mm diameter FM defect (C). The FM crown model was transferred into the tissue culture plate and amniotic fluid (AF) injected into the well (D) to cover the area below the FM explant (* indicates AF injection site, schematic). Peptide amphiphile (PA) was applied to the FM defect from above (E, schematic, F). Self-assembly was also tested by injection of AF or PA into larger volumes of the other solution (not shown here).

5.2.5 PA synthesis and purification

Solid phase peptide synthesis (SPPS) using an automated peptide synthesizer (CS Bio, USA) was used for peptide amphiphile (PA) synthesis. The standard 9-fluorenylmethoxycarbonyl (Fmoc) protection chemistry on a 4-methylbenzhydrylamine (MBHA) Rink Amide resin (Novabiochem Corporation, UK) was used. Amino acid couplings were performed using four equivalents (4 mmol) of Fmoc-protected amino acids (Novabiochem Corporation, UK), four (4 mmol) equivalents of 1-hydroxybenzotriazol (HOBT, Carbosynth Limited, UK) and six (6 mmol) equivalents of *N,N'*-diisopropylcarbodiimide (DIC, Sigma-Aldrich, UK) for 1h. Fmoc deprotections were performed with 20% piperidine (Sigma-Aldrich, UK) in *N,N*-dimethylformamide (DMF). Following Fmoc removal from the final amino acid residue, the alkyl tail moiety (palmitic acid, C₁₆H₃₂O₂, Calbiochem, UK) was conjugated to the free N-terminus. The alkylation reaction was accomplished by using four equivalents of the fatty acid, four equivalents of HOBT, and six equivalents of DIC in DMF/dichloromethane. The reaction was allowed to proceed overnight and pursue until obtaining a negative Kaiser test. PA cleavage from the resin and deprotection were carried out with a mixture of trifluoroacetic acid (TFA, Sigma-Aldrich, UK)/triisopropylsilane (TIS, Alfa Aesar, UK)/water (95:2.5:2.5) for 3h at room temperature. After filtration of the cleaved mixture, TFA was removed by rota-evaporation and the resulting viscous peptide solution was precipitated with cold diethylether at -20°C. The precipitate was collected by centrifugation, washed twice with cold diethylether, allowed to dry overnight, suspended in water, and lastly freeze-dried.

Peptide purification was carried out using 2545 binary gradient preparative High-Performance Liquid Chromatography (Waters, USA) with a 2489 UV/Visible detector (Waters, USA) using a C18 column (Atlantis Prep OBD T3 Column, Waters, USA) and a water/acetonitrile (0.1% TFA) gradient. In the case of positive peptides the TFA counter-ions were exchanged by sublimation from 0.01 M hydrochloric acid. Finally, the peptides were dialyzed against deionized water using 500 MWCO dialysis tubing (Spectrum Europe B.V., The Netherlands) to remove salts, lyophilized to obtain a fluffy powder, and stored in closed containers at -20°C until use. The mass of the peptides was confirmed by electrospray ionisation (ESI, Thermo LXQ, Thermo Scientific, USA) and

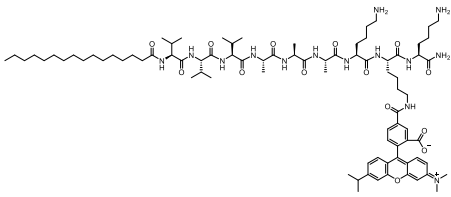
matrix-assisted laser desorption ionisation-time of flight mass spectrometry (MALDI-TOF MS, Applied Biosystems 4800 Proteomics Analyzer (TOF/TOF) mass spectrometer).

5.2.6 PA subtypes and properties

The PAs used in the present study and their corresponding sequence, molecular weight, isoelectric point, and zeta-potential are shown in **Table 5.6**.

Table 5.6: The molecular details of the peptide amphiphiles used in the present study.

Peptide sub-type	Peptide sequence	M_w	pI	ζ (mV)
PA-K2	C ₁₅ H ₃₁ CONH- VVVAAAKK- CONH ₂	1.0224	10	67.8±5.2
PA-K3	C ₁₅ H ₃₁ CONH- VVVAAAKKK- CONH ₂	1.1506	10.3	67.5±3.3
PA-K4	C ₁₅ H ₃₁ CONH- VVVAAAKKKK- CONH ₂	1.2788	10.5	66.6±4.0
PA-E3	C ₁₅ H ₃₁ CONH- VVVAAAEIII- CONH ₂	1.1531	3.7	-33.1±3.0

<p>PA-K4(TAMRA)</p> 	<p>C₁₆- VVVAAAKKK- K(TAMRA)- CONH₂</p>	<p>1.537</p>	<p>n/a</p>	<p>n/a</p>
---	--	--------------	------------	------------

PA: peptide amphiphile; K: lysine; E: glutamic acid; M_w: molecular weight; pI: isoelectric point; ζ: zeta-potential (mV).

5.2.7 Fluorescently labelled peptide amphiphile self-assembly

Fluorescently labelled peptide amphiphile was used to study direction of self-assembling membrane growth and discern the direction that PA was flowing. The peptide used was PAK3 (2%) with addition of the Fluorescent PA-K4(TAMRA) diluted to 0.01% in PAK3 solution. The epifluorescence Leica DMI 4000B Fluorescence microscope was used to produce a time-lapse of fluorescently labelled PA by placing PDMS channel under the microscope and imaging the interaction between the 2 solutions.

5.2.8 ζ-potential measurement (ζ) for amniotic fluid charge

All ζ-potential measurements were performed after resuspension of the PAs at a concentration of 1mM in cell diluent (HEPES 10 mM supplemented with 0.9% NaCl, pH 7.4). After loading the samples in folded capillary cells, measurements were performed at 25°C using a ζ-sizer instrument (Nano-ZS Zen 3600, Malvern Instruments, UK). For each PA, three separate samples were measured with at least five runs per sample.

5.3 Results

Amniotic fluid (AF) suspensions from 2nd trimester patients were used for these experiments and mixed with dilute aqueous PA solution at varying concentrations (0.5 – 2%). Positively charged PAs were used as 2nd trimester AF is known to contain proteins (0.16 – 10 g/L) and growth factors that have negative charge²⁶². Overall net negative charge was confirmed by measuring Zeta-potential (mV, **Figure 5.6a**). Furthermore, GAGs that are highly negatively charged molecules were detected in 2nd and 3rd trimester AF samples (n=10, **Figure 5.6b**). A higher amount of GAG was detected in the 3rd trimester towards term (mean GA: 31⁺²; median GA: 30⁺³; range 29⁺¹-33⁺⁴; n=12), compared to 2nd trimester AF (mean GA: 17⁺¹; median GA: 18⁺⁴; range: 15⁺³-23⁺⁶; n=10).

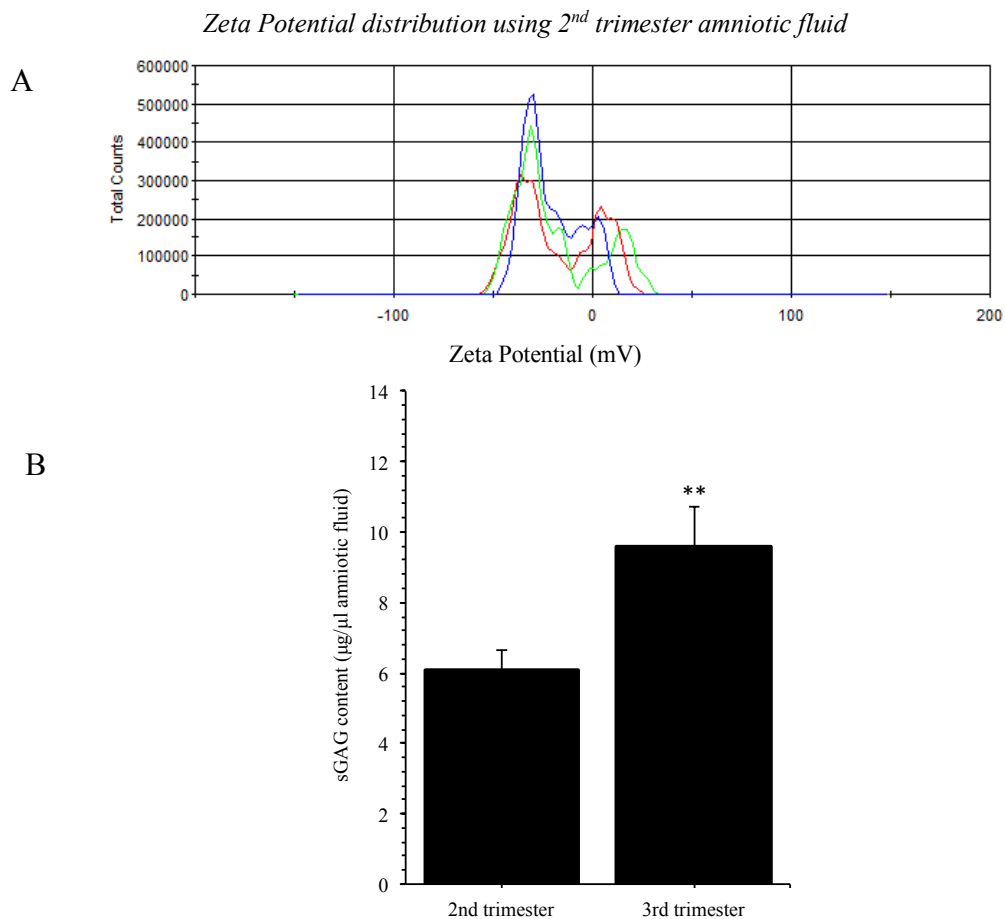


Figure 5.6: Confirmation of negatively charged amniotic fluid suspensions and presence of highly negatively charged long unbranched polysaccharide glycosaminoglycans. 3rd trimester amniotic fluid (n=12) contained higher GAG content compared to 2nd trimester (n=10). Error bars represent mean \pm SEM, where ** $p < 0.01$.

For self-assembly experiments, 2nd trimester amniotic fluid (mean GA: 17⁺¹; median GA: 18⁺⁴; range: 15⁺³-23⁺⁶) was used throughout, as this is the period of pregnancy where intrauterine fetal surgery and PPROM complications commonly occur.

5.3.1 Peptide amphiphile – amniotic fluid (PA-AF) systems

Peptide amphiphiles containing three lysine residues in the charged group domain (PAK3) have been commonly used to investigate self-assembly of 1-D cylindrical nanofibres^{4,15}. We decided to investigate PAK3, a positive PA, when combined with human amniotic fluid, which is comprised of a multitude of negatively charged proteins. We further investigated changes in the number of lysine residues contained in the PA sequence, which changes the overall positive charge of the PA and therefore predicted to influence electrostatic screening when combined with human amniotic fluid.

PDMS fluidic channels were used to study the initial interface between PAs with varying numbers of lysine residues (PA-K2, -K3, -K4) and mid-trimester amniotic fluid (**Figure 5.7**). Membrane formation can be seen instantly in PA-K2, -K3, -K4, and amniotic fluid systems, at 5 seconds (**Figure 5.7a, b, c**), which possibly acts as a diffusion barrier formed via strong electrostatic interactions. Self-assembly of macrostructures occurred in PAK2-AF and PAK3-AF systems, however PAK4-AF system resulted in a paste-like substance. The PAK2-AF system resulted in a very weak gel following a 6-hour incubation period, which easily disintegrated.

The resulting gel from the PAK3-AF system was stable, and appeared to be solid, containing no fluid in the centre. Following a 6-hour incubation period the gel from the PAK3-AF system (**Figure 5.7d, e, f**) formed within the PDMS fluidic device or when PAK3 solutions were injected into larger AF volumes, formed a stable and solid gel that could be manipulated without disintegrating after contact. Injection of PAK3 (~50 µL) at 2% (w/v) into a larger solution of human amniotic fluid (up to 50 mL) for longer time periods also resulted in formation of a solid gel at 24 hours when incubated at 37°C (**Figure 5.7g**). Interestingly, an overall negative PA, PAE3, also formed a very weak gel that could not be manipulated and which readily disintegrated upon contact.

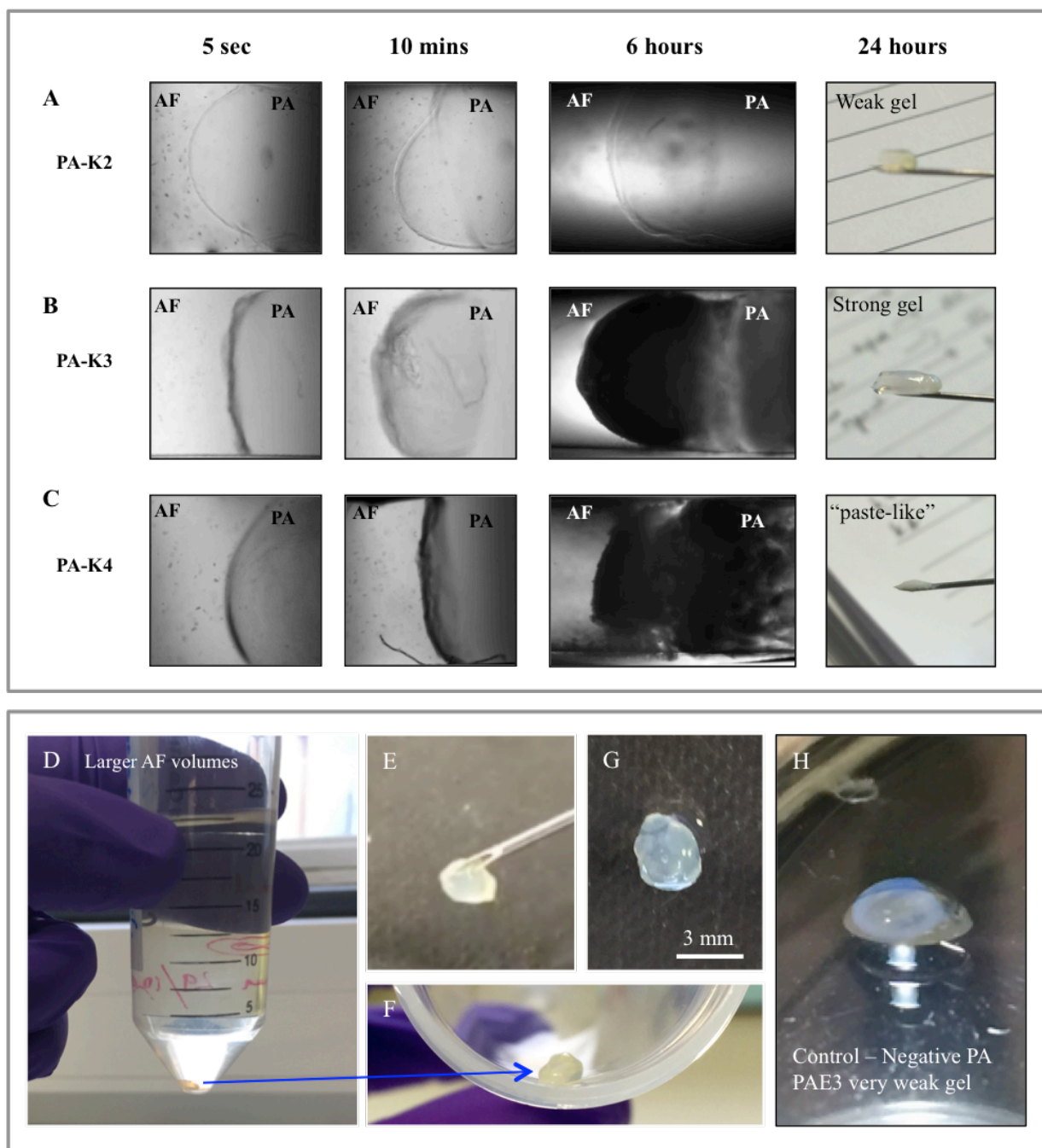


Figure 5.7: Peptide amphiphile and amniotic fluid macrostructure self-assembly. PAs with varying lysine residues self-assembled with AF to form membranes that developed to form macrostructures with different structural stabilities. PAK2-AF system (A) resulted in a weak gel at 24 hours. PAK3-AF system (B) resulted in a stable gel that could be handled without disintegrating. PAK4-AF system (C) resulted in a paste-like substance. PAK3-AF system also resulted in stable gels when the PAK3 solution (2% w/v) was injected into larger AF volumes and incubated for 6 hours (D, E, F), and remained stable at 24 hours (G). PAE3-AF system formed a weak gel that easily disintegrated upon contact after 6 hours (H).

Following closer investigation of gel formation, it is clear that after self-assembly of an initial PAK3-AF interface (**Figure 5.8a, b**) the direction of gelation occurs towards the PA solution until the entire PA solution becomes engulfed (**Figure 5.8c**), opposite of that reported by Capito *et al.*, where solutions of the hyaluronic acid are engulfed by the PAK3 solution during gelation⁴.

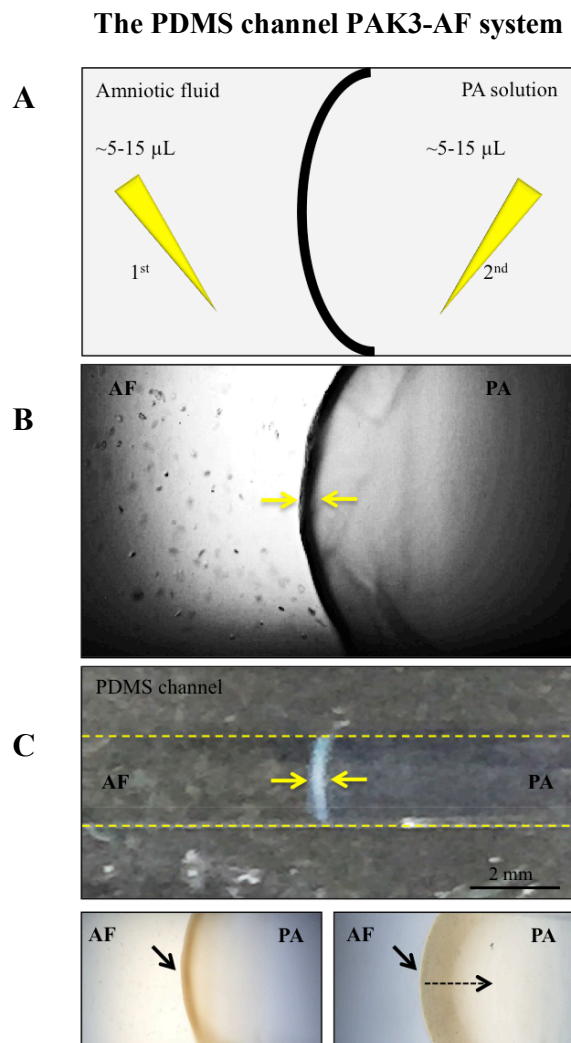


Figure 5.8: Formation of self-assembling membranes at the PAK3-AF interface using PDMS channels as a fluidic device. A schematic showing the typical procedure involving first pipetting $\sim 5\text{-}15\ \mu\text{L}$ of amniotic fluid to the left side of the channel and then introducing the same volume of the PAK3 (2% w/v) solution to the right side of the channel (A). A typical membrane as seen through a light microscope (B) and with no instrumentation (C). Following formation of an initial dense membrane at the PAK3-AF system interface, the formation of a gel occurs in the direction of the PA solution as shown by comparing self-assembly at 10 mins (C, left) and 2 hours (C, right).

To confirm direction of membrane growth and gelation, the positively charged PAs including PAK2, PAK3, and PAK4 were injected into solutions of AF; and solutions of AF were injected into solutions of the PAs for comparison (**Figure 5.9a,b**).

Following initial self-assembly of membranes at the interface, it is clear the direction of macrostructure growth and self-assembly is towards the PA solution. For all variation of PAs, membrane growth moved towards the PA solution. This self-assembly phenomenon occurred rapidly in all circumstances, where the volumes of PA solutions injected (~5 μL) are completely engulfed within minutes. The initial membrane formation appears rapidly, and gel formation increases in density from 5 seconds to 10 minutes, originating from the PA-AF interface. In contrast, injection of AF (~5 μL) into a solution of the PA led to macrostructure formation towards the PA solution, but did not engulf the entire volume of AF over the same time period, indicating that the amount of self-assembly and macrostructure formation is dependent upon PA volume.

Regarding the mechanism of gelation, it appears there are three distinct stages involved in the PA-AF system (**Figure 5.9c**). Initial membrane formation at the interface leads to rapid gelation via strong electrostatic interactions and rapid diffusion of ions across the diffusion gradient. This is then followed by a third stage, where the gel appears to increase in density beginning at the PA-AF interface and moving towards the centre of the PA solution, perhaps elicited by the slower diffusion of macromolecules within the amniotic fluid across the diffusion gradient. Furthermore, fluorescently labelled PAK4 conjugated with a TAMRA fluorophore did not mix with amniotic fluid when combined, and instead clear separation from the amniotic fluid solution is evident (**Figure 5.9d**). The initial interface between the PA solution and amniotic fluid appears to move in the direction of the amniotic fluid. This may be due to the formation of a gel and expansion against the sides of the channel as the membrane grows. However the initial PA-AF interfacial membrane that forms upon contact, prevents mixing of the two solutions.

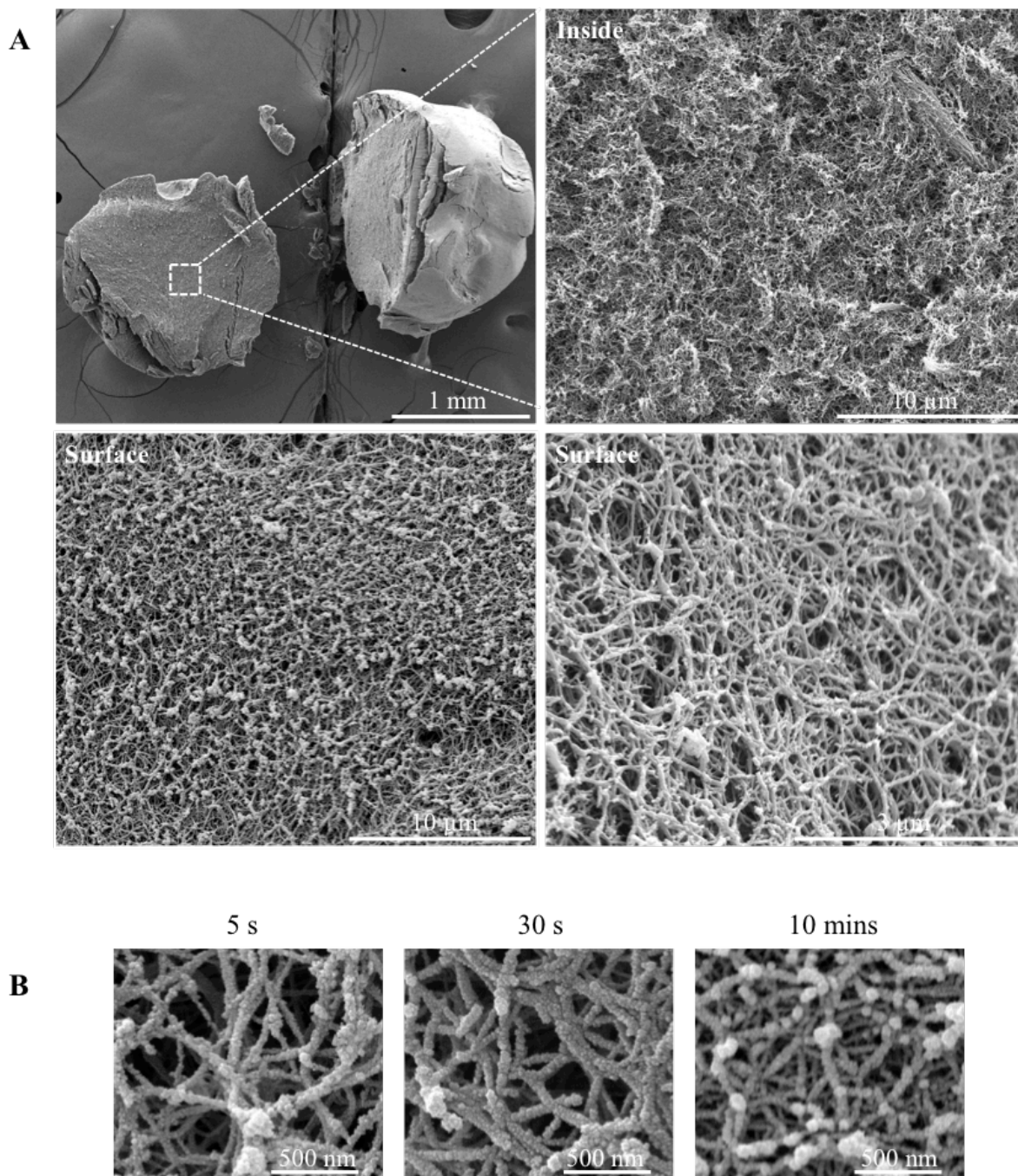
5.3.2 PAK3-AF self-assembling system: membrane microstructure

Scanning electron micrographs of PAK3-AF macrostructures after 24 hours, formed by injection of PAK3 (2% w/v) into AF revealed a highly dense 3D nanofibrous network that mimics the dense native ECM of the fetal membrane (**Figure 5.10a**). After separating the PAK3-AF macrostructure using a scalpel and then dissecting open the structure, it is clear that the self-assembly of a nanofibre network occurs throughout the full thickness of the macrostructure, confirming that the macrostructure does not contain a fluid-filled centre. Throughout the PAK3-AF gel, the nanofibres are well-defined and arranged in random orientations. The surface of the PA-AF membrane in direct contact with the amniotic fluid side contains a dense network of well-defined nanofibres that appear to be coated in a rough layer of droplets. It is likely these are microscopic lipid droplet corpuscles found within the amniotic fluid, and are too large to diffuse through the initial membrane that self-assembles upon contact between the AF and PAK3 aqueous solution.

Rapid fixation of the PAK3-AF system did not show a well-defined membrane, however, it was possible to produce electron micrographs of fixed nanofibres during the early fixation period of 5 seconds to 10 minutes. Nanofibres of less than 100 μm are shown at 5 seconds, 30 seconds, and 10 minutes (**Figure 5.10b**). The density of nanofibres also appears to increase from 5 seconds to 10 minutes.

Further analysis of membrane microstructure reveals a rough surface at the PAK3-AF interface, on the AF side, following 24 hours (**Figure 5.11a**). Further evidence of amniotic fluid organic components attached to the surface of the membrane is found at 24 hours. Towards the PA side of the gel, the organic components are absent, revealing well-defined nanofibres arranged in random orientations (**Figure 5.11b**). Nanofibres are approximately 84 nm in diameter. Furthermore, cross-sectional analysis of PAK3-AF self-assembled gels reveal a highly dense PAK3-AF interfacial membrane (**Figure 5.11c; region 2**), with nanofibres mostly arranged perpendicular to the surface. This highly dense membrane is approximately 2 μm in thickness, consistent with the increased autofluorescence of PA membranes observed using confocal microscopy (**Figure 5.11c, inset**). The surface, originally in contact with the amniotic fluid (**Figure 5.11c; region 1**) also contains droplets that are likely to be organic components of the AF. Beyond the

highly dense membrane, the nanofibre network is less dense and contains well-defined nanofibres arranged in random orientations consistently through the full thickness of the gel (**Figure 5.11c; region 3**).



Rapid initial membrane formation

Figure 5.10: Electron micrographs of PAK3-AF system following injection of PAK3 aqueous solution into AF. Injection of PAK3 into AF results in formation of a gel composed of well-defined nanofibres that are randomly orientated throughout the full thickness of the gel (A). The surface of the PAK3-AF gel contains organic components. Early fixation of PAK3-AF system shows formation of nanofibres as early as 5 seconds (B). The self-assembling nanofibre network appears to increase in density from 5 seconds to 10 minutes (B).

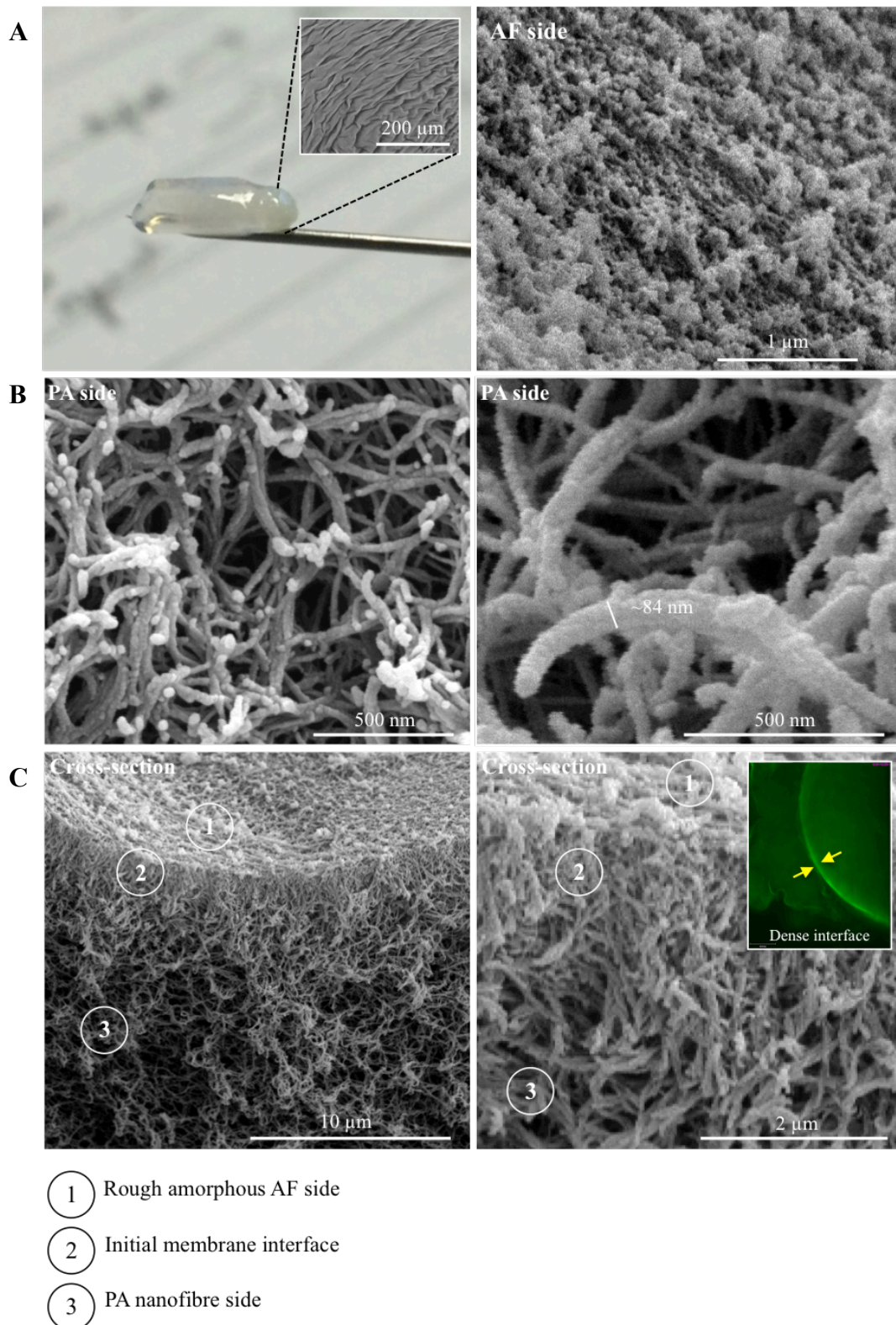


Figure 5.11: Electron micrographs of PAK3-AF system formed within the PDMS fluidic device. Following a 24-hour period, the PAK3-AF gels showed a rough amniotic fluid surface containing organic components (A). The PAK3 side contains well-defined nanofibres of approximately 84 nm in diameter and organised in random orientations (B). The PAK3-AF interface contains a highly dense region of nanofibres (region 2) arranged perpendicular to the surface (region 1), spanning a thickness of approximately 2 μm consistent with that shown from increased PA autofluorescence at the liquid-liquid interface using confocal microscopy. Adjacent to the perpendicular fibres is a less dense nanofibre network.

5.3.3 Self-assembled PAK3-AF membranes for sealing artificial fetal membrane wounds

Following formation of a stable gel using the PAK3-AF system, the ability to effectively seal FM defects was tested using the artificial FM trauma model developed previously for studying the expression of Cx43 (**Chapter 4**). Briefly, after assembling term FM within the crown insert, the tissue was wounded using a sterile 21G needle to create a 0.8 mm defect. The PAK3 (2% w/v, ~10 μ L) was then carefully applied to the top (chorionic membrane wound side) of the FM wound with amniotic fluid being injected until in contact with the inner AM surface (~2 mL). Therefore, the PA was exposed to the AF present within the FM wound margins on the AM side of the FM, as would occur in fetoscopic procedures if this technique was applied clinically. This would allow the PAK3 to initiate self-assembly of cylindrical nanofibres and formation of a 3-D nanofibrous network. After 24 hours incubation (37°C), the PAK3-AF system resulted in gel formation across the fetal membrane wound. The wound margins were not visible on the chorionic membrane side (**Figure 5.12a, c**). However, the wound outline could be seen on the AM side (**Figure 5.12b**). Following fixation with paraformaldehyde (4%) the PAK3-AF gel appears dark red.

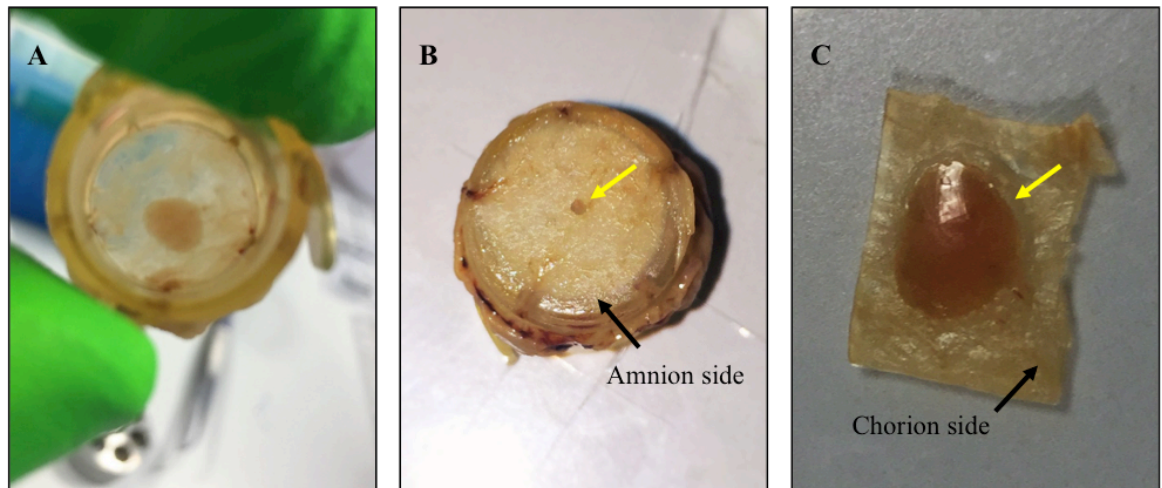


Figure 5.12: Sealing of fetal membrane defects using the PAK3-AF system in the artificial fetal membrane trauma model. PAK3 aqueous solution (2% w/v) was applied over the wound from above. The wound margin cannot be seen on the chorionic membrane side (A, C), however is clearly visible on the amniotic membrane side. The PAK3 solution has self-assembled to form a macroscopic plug (yellow arrows) in the presence of amniotic fluid, sealing the fetal membrane defect over a 24 hour period.

Sealing of artificial fetal membrane defects can be seen using electron micrographs (**Figure 5.13**). Fetal membrane remains mostly viable (**Figure 5.13a, green**) following a 24-hour culture period and creation of a 0.8 mm defect (**Figure 5.13a, b**). However, following initial trauma there is a small boundary of cells (~5 cell layer thick) that are non-viable (**Figure 5.13a, red**). Sealing of the artificial defect (**Figure 5.13c**) can be observed at high magnification, which shows some promising integration of native fetal membrane ECM nanofibres with the self-assembled nanofibres of the PA-based sealant, following 24 hours incubation with amniotic fluid (**Figure 5.13c-i**).

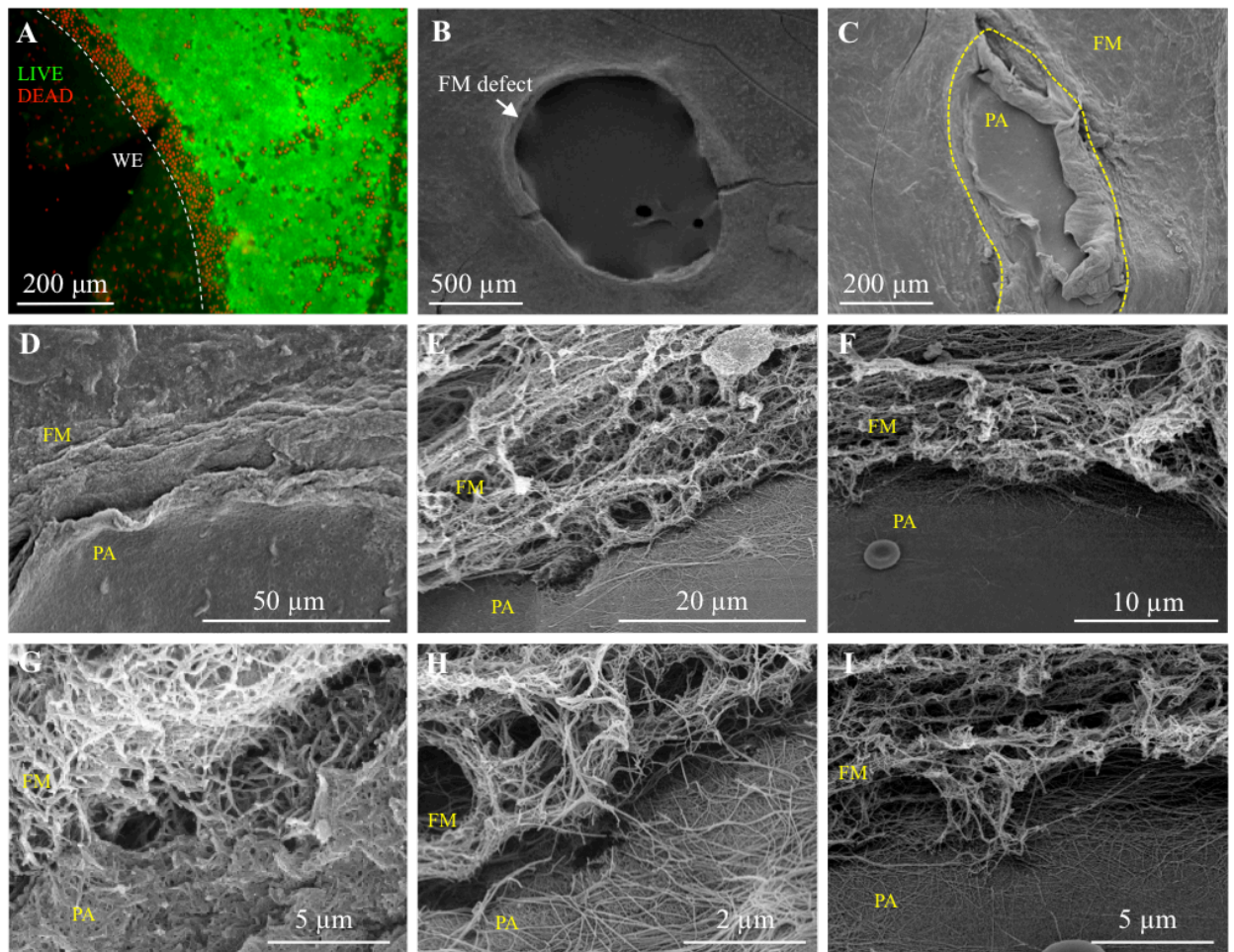


Figure 5.13: Electron micrographs of fetal membrane defects sealed using the PAK3-AF system using the artificial fetal membrane trauma model. The fetal membrane used for these experiments contained viable cells over a 24 hour period (A) with a small 2 – 5 cell layer thick boundary of non-viable cells due to initial trauma following wound creation. A control fetal membrane defect of approximately 0.8 mm shows absent healing following 24 hours (B). Following PAK3 application, sealing at the wound margin occurs (C, yellow line). Microstructure analysis reveals integration of human fetal membrane ECM nanofibres with self- assembled PAK3 nanofibres following 24 hour incubations (D, E, F). Higher magnification shows close association between the self-assembled PAK3-AF gel and the native fetal membrane ECM nanofibres.

5.3.4 Histological analysis of sealed fetal membrane defects

After wounding the fetal membrane using a 21G needle, the histological analysis of control samples reveals the non-healing nature of the fetal membrane (**Figure 5.14a**). The 0.8 mm defect was located using India ink to mark the wound margin prior to tissue sectioning. Cross-sectional H&E staining shows viable cells within the loosely conjoined amniotic membrane and chorionic membrane layers. The amniotic epithelial layer

remains intact, showing cuboidal amniotic epithelial cells covering the stromal layers that contain dispersed mesenchymal cells. The amniotic epithelial layer is clearly adhering to the chorion membrane, which contains a higher density of fibroblast and trophoblast cells dispersed within the stromal layers.

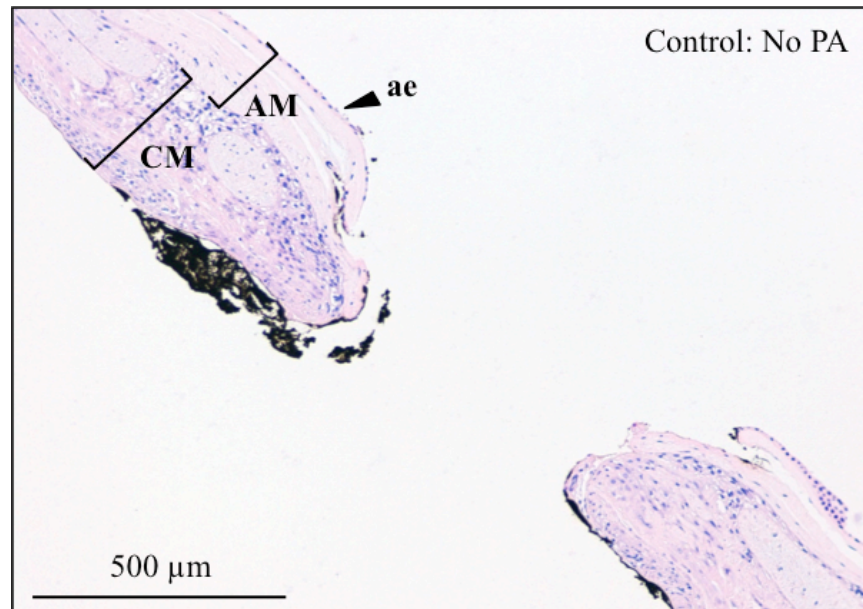


Figure 5.14: Cross-sectional histological H&E staining of the human fetal membrane showing clearly the amniotic membrane (AM) and chorionic membrane (CM) layers, and the non-healing nature of the fetal membrane wound. The amniotic epithelial (ae) layer remains intact following sectioning, and no amniochorion separation can be seen. The wound was identified using india ink.

Application of PAK3 to the defect site results in self-assembly of a nanofibrous structure that completely seals the fetal membrane defect at both the amniotic membrane and chorionic membrane regions, showing no evidence of amniochorion separation (**Figure 5.15 b, c**). The PAK3-AF gel also appears to be present on the surface of the chorionic membrane where residual amniotic fluid may have been present. A layer of PAK3-AF gel has also formed on the underside, adhering to the amniotic membrane surface, which may result following injection of PAK3 along the fetal membrane wound and during the early stages of membrane formation at the PAK3-AF interface (**Figure 5.15b, c**). Biocompatibility of the PA-based gel appears promising, as the PA on the surface of the amniotic membrane does not damage the layer, leaving the amniotic epithelial layer structurally intact with no ruptures present. The PAK3-AF gel also did not appear to damage the integrity of the cell-dense chorionic membrane layer. The structural integrity of the amniotic epithelial layer can be seen at higher magnification, indicating successful biocompatibility (**Figure 5.15a**).

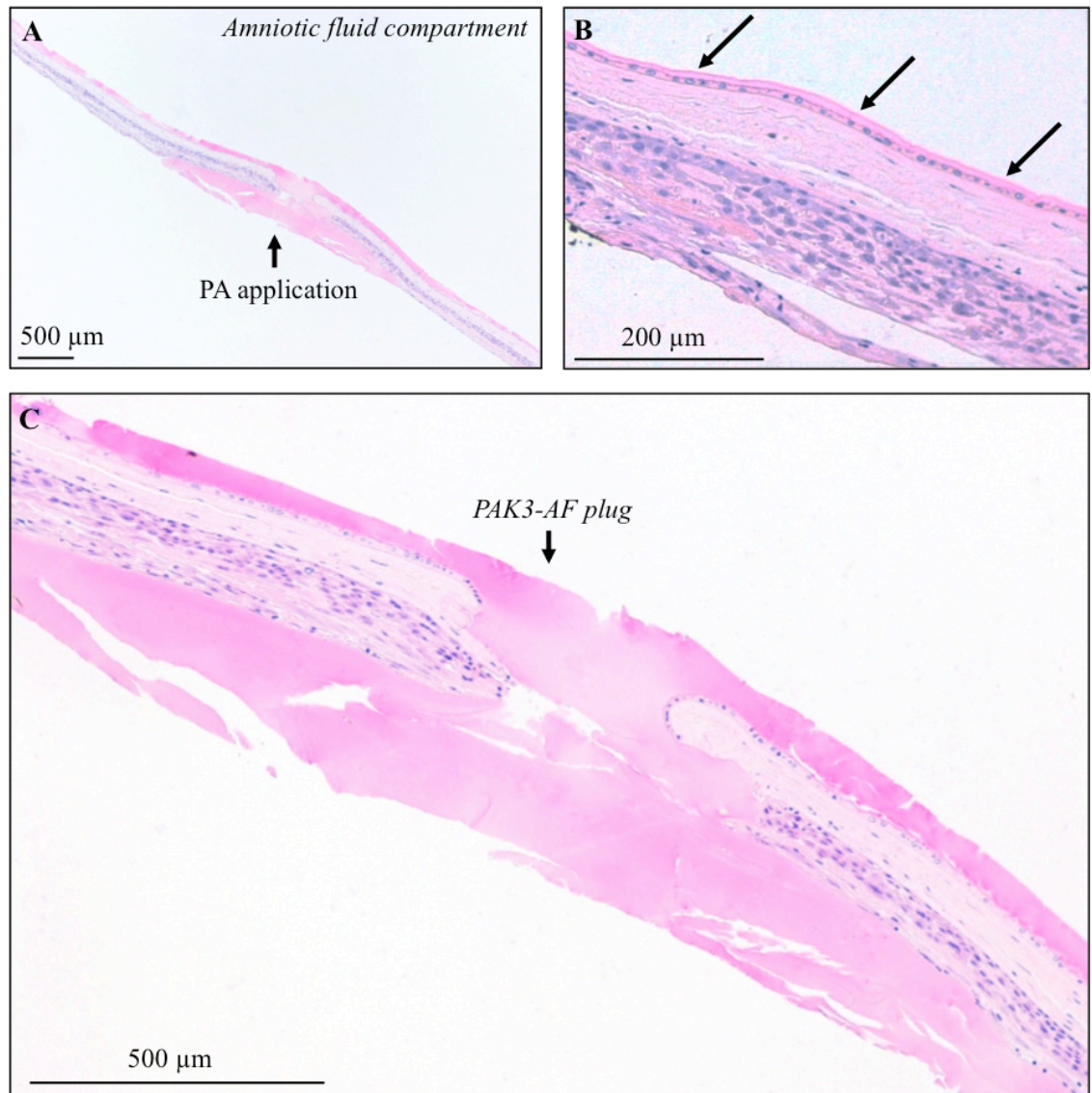


Figure 5.15: Histological analysis of fetal membrane explants and PAK3-AF plug. Following PAK3 application, the PAK3-AF self-assembling nanofibrous structure can be seen plugging the fetal membrane defect (A, C), which also appears to be biocompatible following a 24 hour incubation period, with no sign of fetal membrane structural damage or loss of integrity to the amniotic epithelial layer (arrows, B). Histological analysis is representative for $n=6$.

5.3.5 Peptide amphiphile toxicity testing with fetal membrane specimens

Cell viability of PA application was tested after fresh fetal membrane was allowed to stabilise after 24 hours in DMEM (**Figure 5.16**). Fetal membrane explants were then treated with 2% (w/v) solutions of PAK2, PAK3, PAK4, and PAE3, for 2 hours and then replaced with DMEM for the remainder of the 24-hour incubation period. Control tissue was incubated in DMEM and AF for 24 hours with no PA exposure. Following 24 hours, cell viability remained high in DMEM (92%) and AF (78.4%) incubations. Increasing the number of lysine residues within the PA molecules appears to increase toxicity. PAK2 (72.4%) and PAK3 (69.8%) incubations showed high cell viability compared to PAK4 (43.1%) exposure. Incubations with negative PAE3 containing the glutamic acid residue showed high cell viability after 24 hours (81%). Percentage cell viability is shown as the mean of the placental and cervical fetal membrane samples. For each PA incubation condition (n=3), the mean percentage viability was calculated from 3 replicate cell counts from different field views of approximately 0.5 mm².

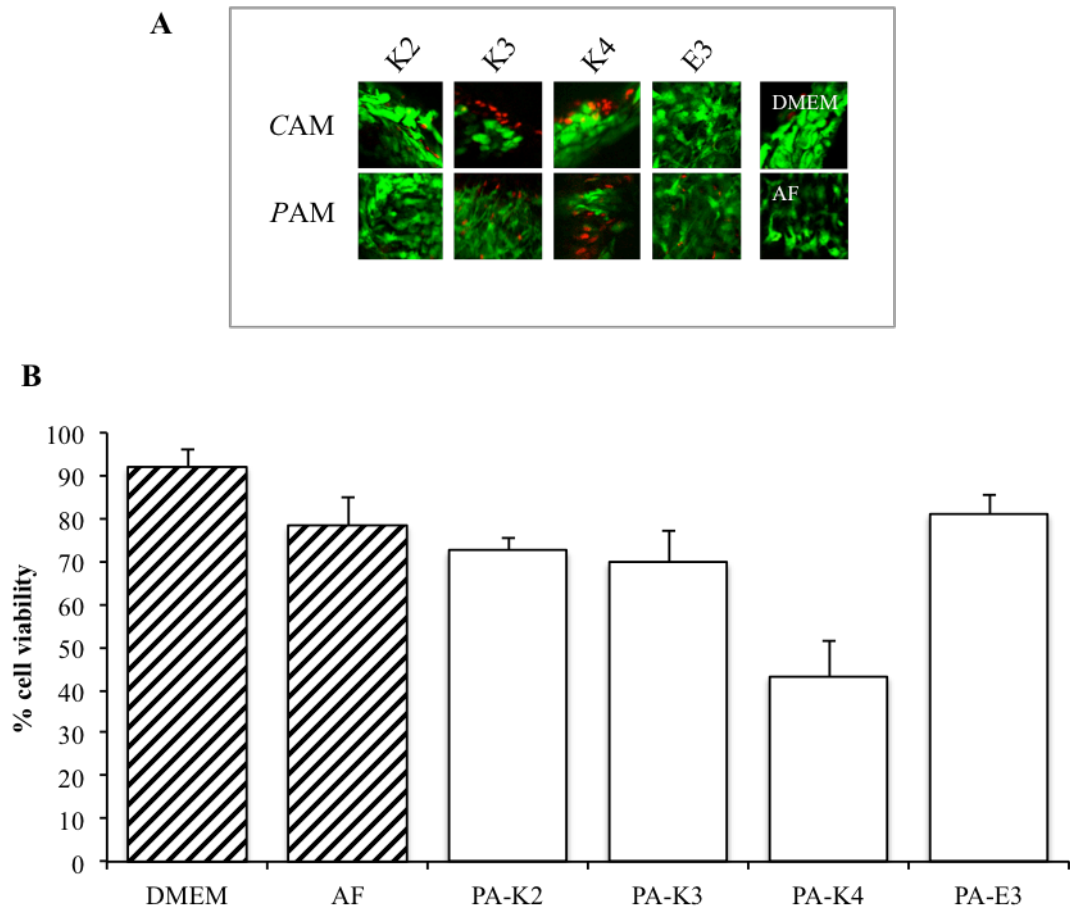


Figure 5.16: Fetal membrane cytotoxicity testing of peptide amphiphile subtypes. Cervical (CAM) and placental (PAM) amniotic membrane explants were separated and analysed separately following live/dead staining (A). Percentage cell viability is shown as the mean between PAM and CAM (B). Percentage cell viability remained high in DMEM (92%) and amniotic fluid (AF, 78.4%). When treated with PA, percentage cell viability remained high in PAK2 (72.4%), PAK3 (69.8%), and PAE3 (81%). Percentage cell viability was lowest after PAK4 incubations (43.1%). For each PA condition, 3 AM explants were incubated and live/dead staining measured in triplicate per AM explant. Error bars represent standard error of the mean.

5.4 Results summary

- The amniotic fluid is known to contain a multitude of proteins and growth factors that have overall negative net charge. Here, we confirm the overall negative charge and report the presence of long unbranched negatively charged polysaccharides sulfated glycosaminoglycans (sGAG). Interestingly, the levels of sGAG increases in third trimester gestational age amniotic fluid compared to mid-trimester amniotic fluid.
- Positively charged peptide amphiphiles self-assemble when combined with human amniotic fluid to form 1D cylindrical nanofibres (~84 nm in diameter). These 1D cylindrical nanofibres form a complex 3D nanofibrous network that mimics the native ECM of the amniotic membrane.
- Varying the number of lysine residues within the peptide amphiphile molecule changes the overall charge and effects the physical properties of the resulting macrostructure when combined with amniotic fluid. PAK2-AF system resulted in a weak gel, whilst PAK4-AF systems resulted in a paste-like substance. However, PAK3-AF systems resulted in a novel strong gel that could be manipulated without disintegration.
- Formation of the PAK3-AF gel started with a thin membrane at the liquid-liquid interface, acting as a physical barrier, separating the two solutions. Membrane growth then occurred in the direction of the PA solution until the PA solution has undergone complete gelation or the amniotic fluid solution has been depleted.
- It is likely that electrostatic complexation and differences in the osmotic pressures contributed to the direction of gelation towards the PA solution. Further diffusion of macromolecules across the diffusion barrier in the PAK3-AF system could have occurred over time, which appears to have increased self-assembly nanofibre formation towards the PA solution and therefore increase nanofibre density over time.

- The PAK3-AF system was tested in the artificial fetal membrane trauma model, and successfully sealed defects of approximately 0.8 mm, adhering to the fetal membrane surface. High magnification electron micrographs reveal close integration of PA nanofibres with the native fetal membrane ECM.
- Histological and cell viability analysis reveals promising PAK3-AF biocompatibility with no disruption to the amniotic epithelial layer and percentage cell viability similar to that of DMEM and AF incubated control fetal membrane.

5.5 Discussion

This study set out to investigate the potential of a novel sealing strategy based on the molecular self-assembly of peptide amphiphiles and complexation with physiological molecules present within the amniotic fluid. We examined the interaction between positive PA molecules, which contained a varying number of lysine residues (i.e. PA-K2, PA-K3, and PA-K4) and fresh human mid-trimester amniotic fluid for the potential formation of self-assembled 1-D cylindrical nanofibres that could mimic the native fetal membrane ECM within the PA-AF system. Using an optimal PAK-AF system, we examined the approach within the artificial fetal membrane trauma model. Biocompatibility and cytotoxicity of the PA-AF system was examined using histological analysis and cell viability assays.

The present study demonstrated the formation of a self-assembling nanofibrous 3-D structure after combining PA (PAK3) and human amniotic fluid. The formation of well-defined 1-D cylindrical nanofibres was reported as early as 5 seconds in the PAK3-AF system. Using PDMS designed fluidic channels of approximately 2 mm diameters, it was possible to observe the spontaneous formation of a self-assembled membrane at the PA-AF interface. The PA-AF membranes propagate towards the PA solution indicated by decreased transparency towards the PA solution and away from the original membrane interface. In contrast, no changes in transparency were observed in the AF regions over time following co-assembly of PA and AF.

Varying the number of lysine residues present within the charged group region of the PA resulted in changes in the outcome of the physical properties following incubations of the PA-AF combinations with AF. The PAK2-AF system resulted in the formation of a weak gel that disintegrated upon contact. However, the PAK3-AF system resulted in a more stable gel that could be manipulated without disintegrating. The PAK4-AF system did not form a gel, and instead resulted in a paste-like substance. Interestingly, during the initial membrane formation reported (5 seconds – 10 minutes) instantaneous distinct membranes can be seen, which propagate towards the PA solution and increases in density originating from the PA-AF interface. This membrane growth continues until the entire PA solution within the channel is engulfed. Following this primary finding the

PAK3-AF system was tested in larger amniotic fluid volumes, which also resulted in the formation of stable gel following the 6 – 24 hour incubations reported. Using PDMS fluidic channels, it was possible to highlight the direction of self-assembling membrane growth over time. This was confirmed by injecting solutions of PA or AF into larger volumes of the other solution. As suspected from the PDMS fluidic channel experiments, following initial membrane formation, the self-assembly of a larger macrostructure continued in the direction of the PA solution. Injecting smaller volumes of PA into AF led to complete gelation of the PA solution confirmed using scanning electron microscopy; however, injection of a smaller volume of AF into PA solutions did not lead to complete gelation of the PA solution, suggesting that complete gelation only occurs if sufficient AF volume is present within the system.

Membrane growth in all PAK-AF systems is likely to occur following diffusion of macromolecules across the initial membrane barrier formed following rapid electrostatic screening between the positively charged PAK molecules and the negatively charged macromolecules present in the amniotic fluid. In addition, the two solutions do not combine, confirmed from fluorescently labelled PA, and therefore provides supporting evidence for the formation of a diffusion barrier at the AF-PA interface leading to macromolecule diffusion towards the PA solution. Interestingly, the PAE3-AF system also formed a weak gel that disintegrated on contact. This indicates that whilst the amniotic fluid is mainly composed of negatively charged molecules, electrostatic screening may still occur with positive components of amniotic fluid, and the positive moieties of AF proteins. Following charge complexation and the formation of a diffusion barrier, changes in charge density within the PA-AF system affects the final physical properties of the PA-AF gel. For example, similarities can be drawn between a previously published system using elastin-like polypeptides (ELPs) and PAs¹⁵. A lower charge density using ELP5-PAK2 resulted in thinner and more transparent membranes similar to that seen within the PAK2-AF system described here; which shows thinner membranes that show increased transparency compared to the PAK3-AF and PAK4-AF systems. Furthermore, increasing the charge density using an ELP5-PAK4 system led to a weaker membrane compared to the ELP5-PAK3 system, similar to that seen in the PAK4-AF system described here, which leads to the formation of a very weak membrane that disintegrates upon contact and resembles a paste-like substance compared to a more stable PAK3-AF system. Other than the electrostatic screening between amniotic fluid

components and the PA solutions, the difference in osmotic pressures likely plays an important role in gelation. Following initial membrane formation at the PA-AF interface the osmotic pressure gradient may influence the movement of fluid to the PA solution across the diffusion barrier and enhance self-assembly. It is likely that the changes in osmotic pressures may have assisted in gel formation and initial electrostatic complexation between negatively charged PA molecules and positively charged amniotic fluid protein moieties within the PAE3-AF system.

Contrary to Capito *et al.*, the PA-AF membrane formation does not appear as defined as the PAK3-Hyaluronic acid (HA) system liquid-liquid interface, although some similarities can be drawn⁴. It is likely that similar mechanisms of membrane formation occur between the AF components and the PAK3 solution. This group first described electrostatic complexation upon contact between the two solutions that simultaneously results in self-assembly of PA nanofibres, and consequently creates an immediate physical barrier separating the two solutions. The diffusion of the high molecular weight polysaccharide HA macromolecules through the physical barrier into the PA solution leads to the nanofibre orientating perpendicular to the interface, similar to the findings reported in the present study. Interestingly, the findings from PAK3-HA systems also report a rough amorphous layer on the surface with resemblance to the PA-AF system, although another region containing nanofibres parallel to the surface is not reported in the present study^{4,8,15,261}. Furthermore, it is clear that at the PA-AF interface, there is a highly dense arrangement of nanostructures likely due to the increased concentration of amniotic fluid components such as polysaccharides at the interface. This then clearly becomes less dense with increasing distance from the interface as the diffusion of macromolecules is slowed.

The significance of these findings are highlighted after the successfully sealing of a fetal membrane wound defect, tested within the artificial fetal membrane trauma model. Electron micrographs and histologic analysis show successful sealing at the defect site, revealing a close association between self-assembled PA nanofibres and the dense native ECM nanofibre network. This is a novel sealing method that we believe has not previously been reported. Furthermore, the self-assembly of PAs has also not previously been investigated using this physiological solution (i.e. amniotic fluid). Compared to other sealing strategies and synthetic hydrogel sealants tested, the PA-based plugging

strategy shows good biocompatibility and low toxicity using the PAK3-AF system²²⁰. Currently, there is no clinically available method to seal fetal membrane defects following fetal surgery and previous attempts including bioactive membrane scaffolds, collagen plugs, gelatin sponges, and synthetic hydrogels have provided disappointing results^{210,211,220,223,239}. Importantly, the PAK3-AF system could be used to develop a therapy for sealing human fetal membrane defects that is easily injectable and shows promising biocompatibility. Furthermore, optimisation and scaling up of this technology could provide an option to seal larger defects that are of more irregular sizes and occur following spontaneous PPRM. In addition, the PA-AF plugging strategy could provide a safer alternative to the amniopatch, which involves the injection of high concentrations of platelet rich plasma and cryoprecipitate²⁶³. This method is associated with low efficacy and fetal complications including sudden fetal death, acute bradycardia, and amniotic band syndrome, linked to its direct effect on the fetus. However, as the PA does not combine with the AF and instead forms an instantaneous physical barrier at the PA-AF interface, these risks could be preventable.

Chapter 6

Mechanotransduction mechanisms that induce fetal membrane weakening and tissue damage

Chapter 6: Mechanotransduction mechanisms that induce fetal membrane weakening and tissue damage

6.1 Introduction

This chapter investigates the mechanotransduction that leads to tissue weakening in AM subjected to repetitive cyclic tensile strain. The mechanisms by which the fetal membrane weakens are not well understood. Potential upstream therapeutic targets are elucidated and the effect of inhibiting these targets on fetal membrane weakening factors and ECM components are investigated. Importantly, by further defining fetal membrane weakening mechanisms in response to repetitive cyclic tensile strain it is possible to identify potential targets for developing preventatives and treatments for PPRM.

There is likely to be similarities between the biological fetal membrane weakening pathways leading to PPRM and the area of the fetal membrane known to undergo focal weakening due to biochemical alterations in healthy term delivery known as the zone of altered morphology (ZAM, see **section 1.4**). Normal physiological changes occur in the area of the fetal membrane overlying the cervix in synergy with cervical ripening in order to prepare for parturition. Whilst the fetal membrane weakening processes observed towards term in the ZAM are likely to be similar with that observed in PPRM, the upstream cellular signalling pathways and etiology remain poorly understood.

6.1.1 Factors associated with fetal membrane weakening

The main morphological changes occurring in fetal membranes prior to parturition in the ZAM are: (1) swelling of the stromal layers, specifically the spongy (intermediate) layer connecting the amnion to the chorion; (2) reduction in thickness of the decidua cellular layers, specifically the cytotrophoblast layer of the chorion; and (3) disruption between the amnion and chorion. There are several fetal membrane weakening factors reportedly associated with these alterations (**Figure 6.1**). Matrixmetalloproteases (MMP-1, MMP-3 and MMP-9), cyclooxygenase-2 (COX-2), interleukins (IL-1, IL-6, IL-8), prostaglandin E₂ (PGE₂), oxidative stress (p38 MAPK), and pro-apoptosis factors have been associated

with an important role in PPROM^{12,264}. Our group have previously shown that repetitive cyclic strain increases the expression of Cx43, also known to increase in the myometrium following uterine stretch^{86,89}. Increase in Cx43 expression in the amniotic membrane was associated with an increase in COX-2 gene expression, PGE₂ release, and glycosaminoglycan (GAG) content, concomitant with a decrease in collagen and elastin content.

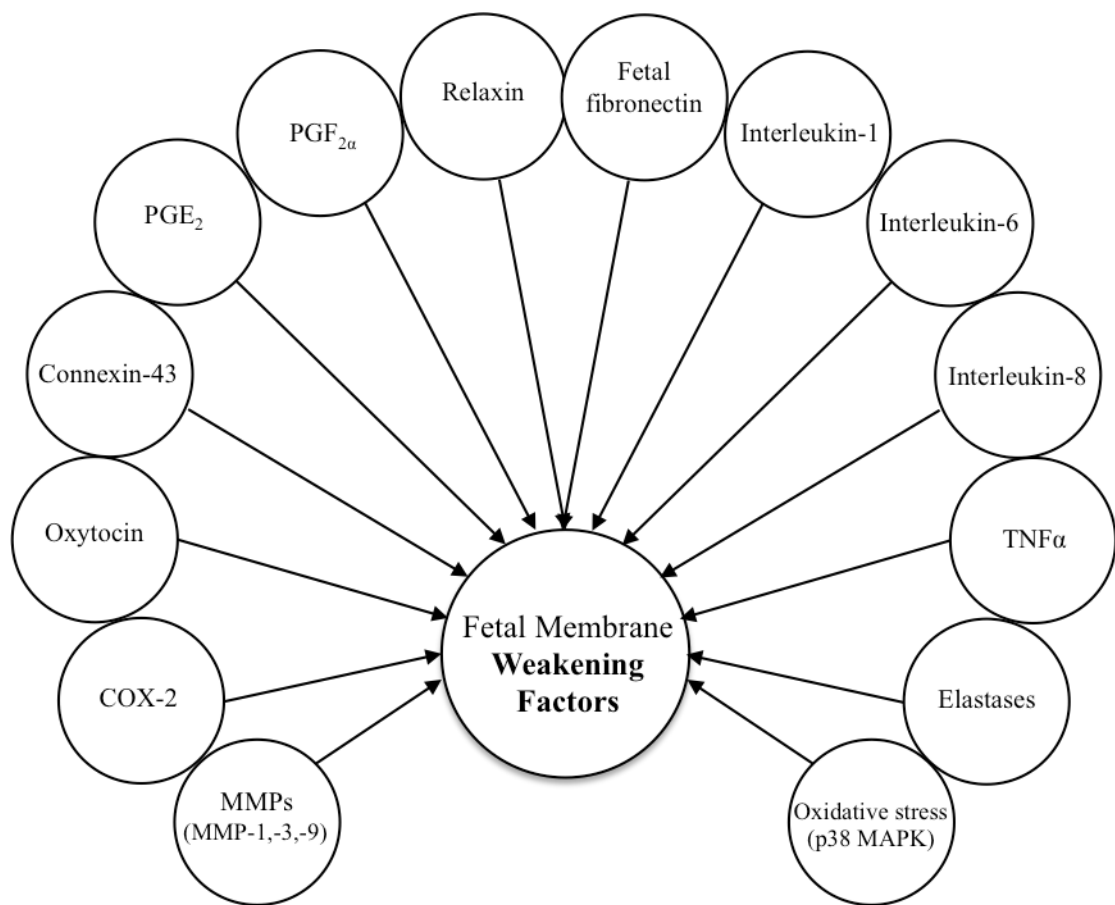


Figure 6.1: List of reported fetal membrane weakening factors

The primary signals which initiate the inflammatory process and lead to AM weakening are unclear (**Figure 6.1**). The principal factors are MMPs, which degrade collagen and reduce mechanical strength³². Indeed, an increase in MMP-9 with a decrease in TIMP-1 has been linked with a reduction in tensile strength of fetal membranes³³. It is suggested that these changes occur due to a “host inflammatory response” in the fetal membrane, but are also found at higher levels in the amniotic fluid of PPROM patients³³.

Interestingly, MMP-9 amniotic fluid concentration is higher in PPROM patients compared to preterm birth patients who did not rupture their membranes³³. Furthermore, MMP-9 specifically degrades collagen type IV, which is found at high levels in basement membranes, suggesting that this layer of the amniotic membrane could play a key role in overall membrane integrity. PGE₂ is one known factor that contributes towards an increased production of MMP-1 and MMP-3 in fibroblast cells. MMPs have also been increased in amniocytes following IL-1 and TNF α exposure²⁶⁵.

Furthermore, MMP activity induced by reactive oxygen species (ROS) has been linked to PPROM²⁶⁶. Recently, mechanistic differences have been made between spontaneous preterm birth and PPROM²⁶⁷. When comparing preterm birth patients, those that had PPROM showed higher oxidative stress with reduced antioxidant enzymes compared to patients who had not ruptured their membranes. DNA damage and cellular senescence was higher in PPROM, indicated by an increase in stress-dependent p38 MAPK activity. Further differentiation between PPROM patients and preterm birth patients who have not ruptured their membranes involve increased activity of apoptosis pathways mediated by TNF α in PPROM patients³³. The IL-6 cytokine and respective receptor have also been shown to increase in PPROM patients due to a reduction in soluble gp130, a protein that inhibits IL-6 signalling²⁶⁸. Overall, the pathological signalling mechanisms that lead to PPROM are not well understood. It is important that research expands on the upstream biological pathways that lead to increased apoptosis in the ZAM region and collagen degradation, which can ultimately cause FM rupture.

6.1.2 Mechanotransduction mechanisms in fetal membranes

It has previously been proposed that overdistension of the uterus can predispose pregnant women to preterm birth. Indeed, uterine overdistension has been linked with preterm labour, mediated by inflammation as found in human and non-human primates¹¹¹. Women are more likely to deliver preterm if they are carrying twin or higher order multiple pregnancies (54%)²⁶⁹. Polyhydramnios (over production of amniotic fluid) also increases the likelihood of preterm delivery²⁷⁰. Other uterine structural abnormalities such as unicornuate also increase the risk of preterm delivery²⁷¹. Furthermore, studies have indicated that the FM does not have a high structural reserve, meaning that during

physiological loading, the FM is close to its failure stress and therefore failure is likely to be easily mediated during labour contractions due to the low structural reserve²⁷². Interestingly, this could indicate that even small increases in stretch to the fetal membrane or overdistension of the uterus leading to fetal membrane stretch could initiate fetal membrane weakening pathways in preterm gestations prior to labour contractions.

A variety of *in vitro* mechanical stretching devices have been used to study FM biomechanics and the mechanotransduction of FM weakening pathways. The types of experimental setup include devices that enable uniaxial, biaxial, inflation, and puncture testing (**Figure 6.2**)^{1,30,273,274}. For example, uniaxial stretching of amniocytes increased IL-1 β , IL-6 and IL-8 cytokines at 11% static stretch for up to 6 hours¹¹¹. Interestingly, these cytokines also increased in the amnion of women who had polyhydramnios in addition to increased TNF- α transcription factor expression. Furthermore, uniaxial static stretch of cultures amniocytes led to increased expression of COX-2 and the transcription factors AP-1 and NF-kB, which is also observed in myometrial cells^{114,275}. Burst testing is achieved by pressure acting perpendicular to the fetal membrane surface and has proved useful for the study of deformation behaviour on FM microstructure³. Furthermore, puncture testing has proved useful in measuring changes in FM strength after development of inflammation/infection and abruption *in vitro* models⁵.

Taken together, these systems enable *in vitro* analysis of FM biomechanics and weakening mechanisms, and so far have highlighted the importance of understanding the inflammation/infection pathways, and understanding the effect of possible exposure to thrombin, which could lead to FM weakening. However, these systems have mainly focused on the use of static strain to the FM. Due to the dynamic nature of amniotic fluid volumes and uterine overdistension, we propose that the use of our cyclic tensile strain system that mimics labour contractions (cycles of 1 min CTS; 9 min rest, for 24 hours, 1Hz) would provide an important contribution to the study of FM weakening mechanotransduction. This system would help to decipher mechanisms that lead to FM rupture preterm, whilst also providing an *in vitro* opportunity to examine therapeutic options to prevent PPRM.

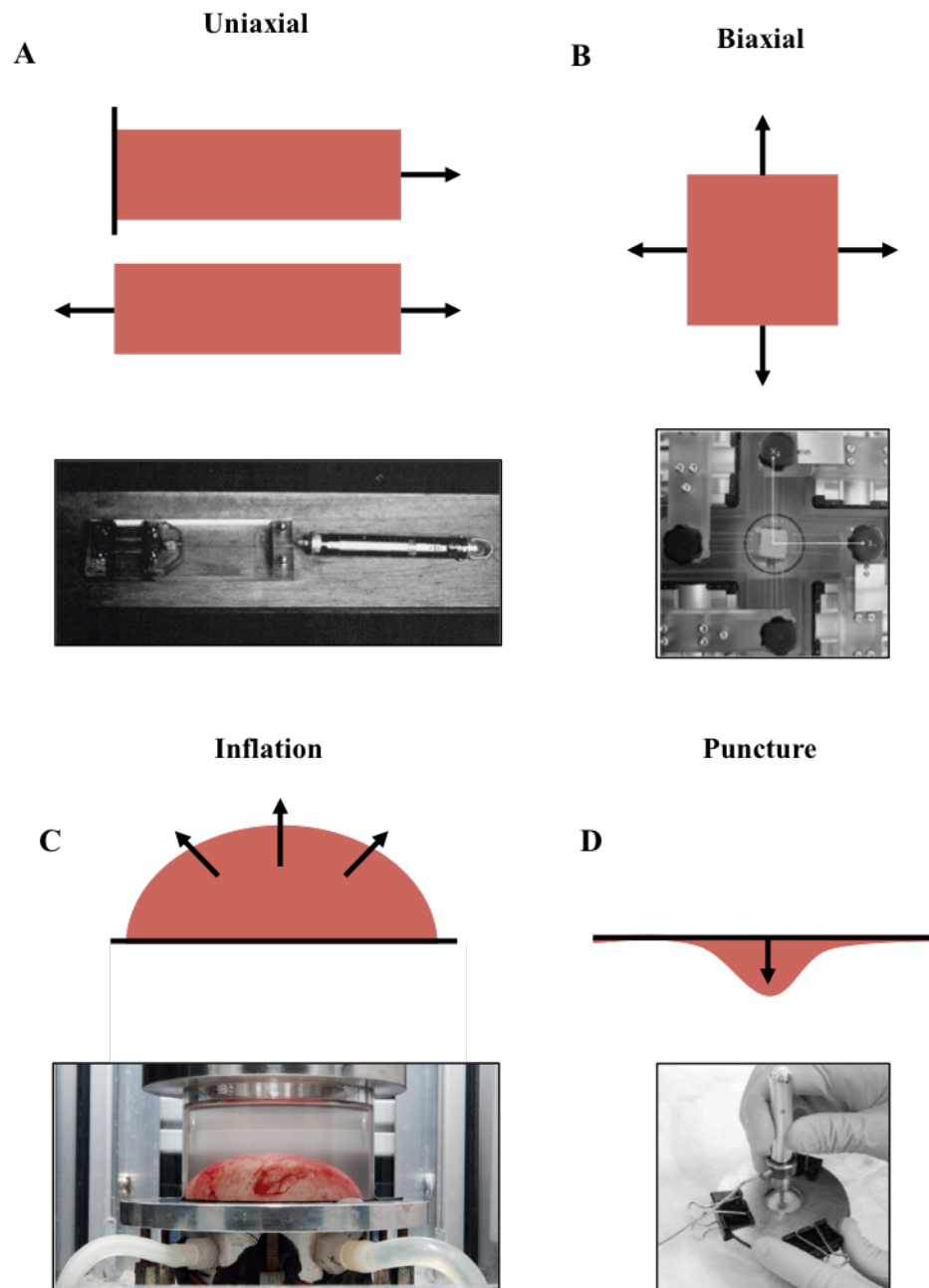


Figure 6.2: Types of *in vitro* mechanical testing devices used for studying mechanotransduction and mechanical properties of fetal membranes. Testing devices include uniaxial (A) biaxial (B) inflation (C) and puncture testing (D). Adapted from Buerzle et al., (2003)¹; Maradny et al., (1996)⁹; Mauri et al., (2016)³; and Oyen et al., (2004)¹⁶.

6.2 Methods

6.2.1 Patient recruitment

Human placentas were collected from University College Hospital London after written informed consent. The fetal membranes were separated from the placenta obtained from term patients who underwent elective caesarean section (between 37 and 42 weeks gestation). Women with placenta praevia, multiple pregnancy, antepartum haemorrhage, PPRM, fetal growth restriction, clinical chorioamnionitis, meconium, and maternal diabetes were excluded from the study. Ethical approval was granted by the Joint UCL/UCLH Committees on the Ethics of Human Research (Ref: 14/LO/0863).

6.2.2 Uniaxial cyclic tensile strain loading using the ex-vivo bioreactor system

AM was separated from the chorionic membrane by gentle traction and dissected into 5 mm x 20 mm PAM and CAM strips in a cell culture hood. Following cyclic tensile strain, preliminary experiments confirmed high AM cell viability for all conditions used in the present study (**Figure 6.3**). All amniotic membrane (AM) explants were dissected and inserted into the mechanical stretching apparatus in the same orientation for all patients (**Figure 6.4**). In order to remain consistent, fibre orientation was always cut in the parallel orientation so that strain would occur consistently in the direction of the fibres as shown during preliminary SHG analysis of collagen fibre orientation (**Figure 6.5**).

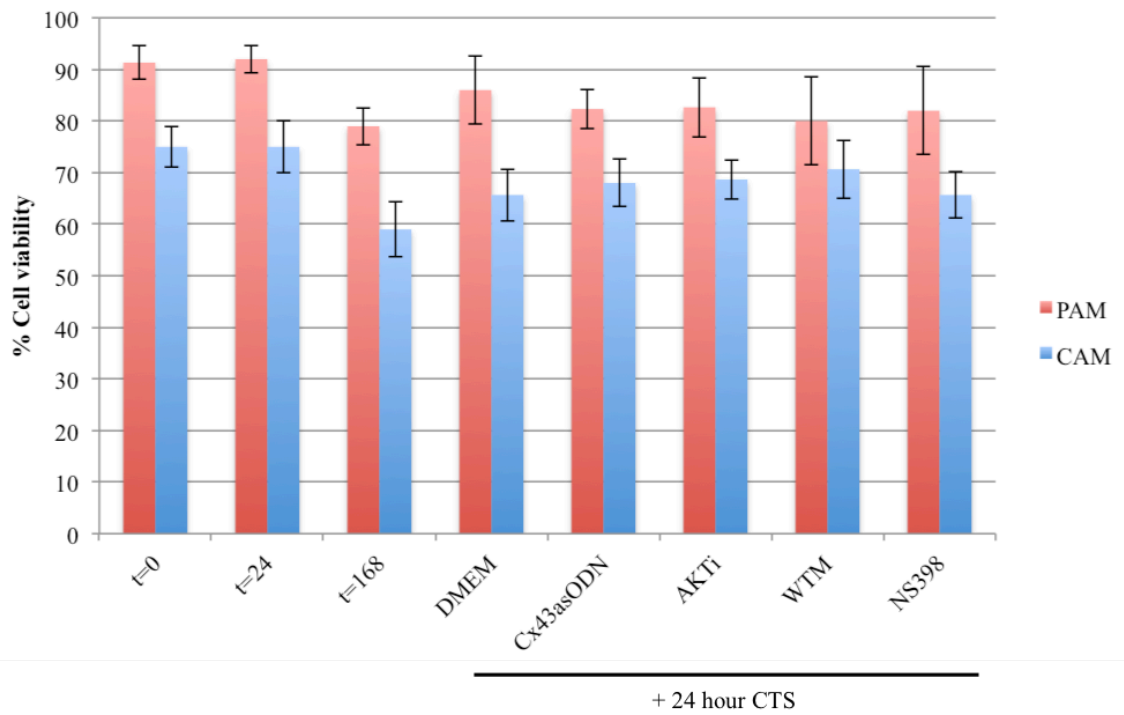
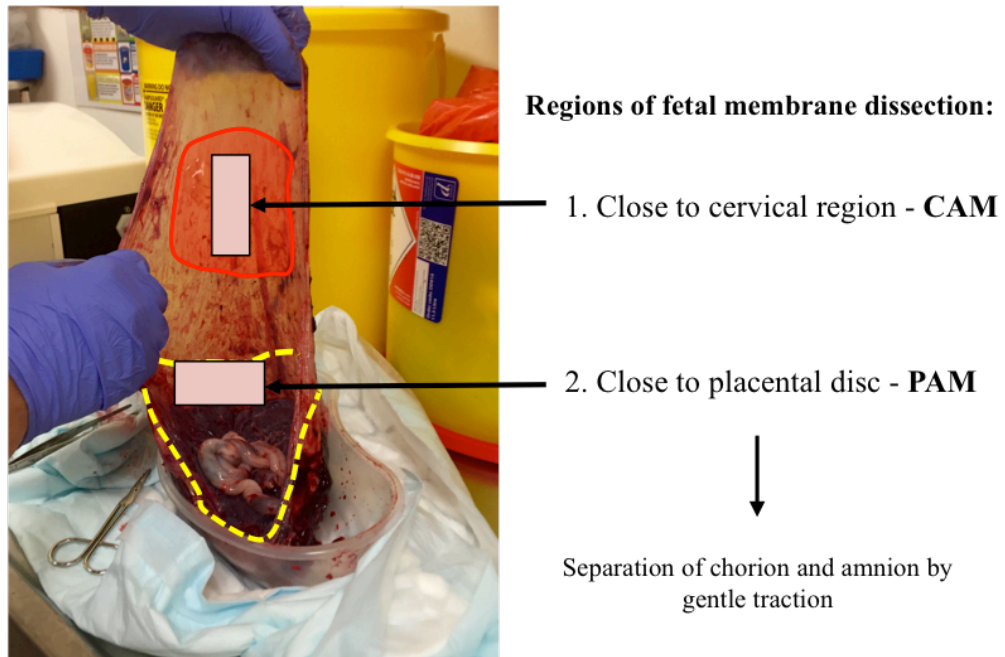


Figure 6.3: Cell viability analysis performed for mechanotransduction studies in both CAM and PAM tissue regions. Cell viability was measured using Live/dead assay in amniotic membrane for tissue at $t=0$ hours, $t=24$ hours, and $t=168$ hours incubation in DMEM. Cell viability was also assessed in tissue following 24 hours cyclic tensile strain in the ex-vivo bioreactor system when incubated with DMEM, Cx43asODNs, AKTi, WTM, and NS-398. Error bars represent mean and standard deviation of 3 tissue regions from 3 separate donors.



Dissection of amniotic membrane strips:

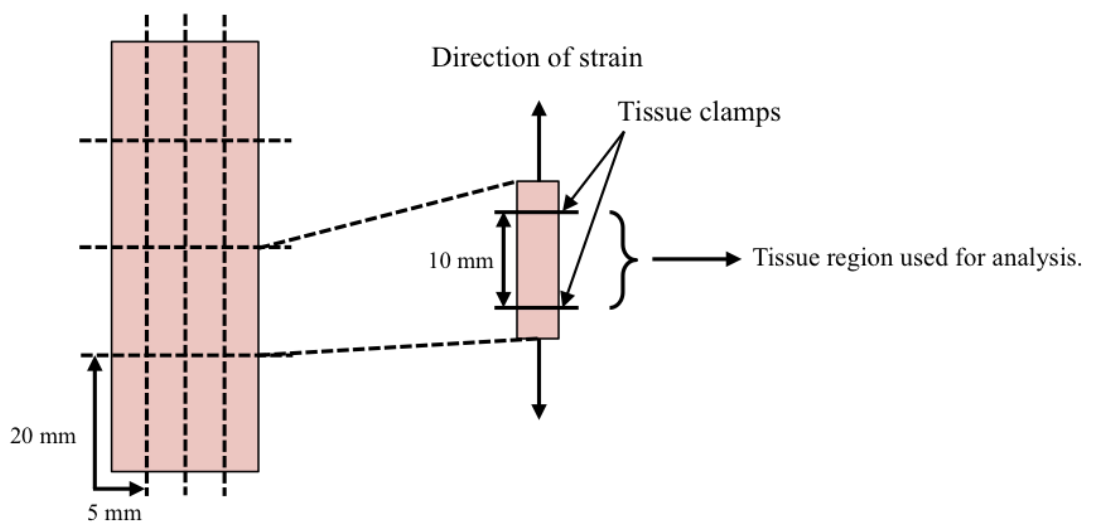


Figure 6.4: Method of fetal membrane dissection. AM was separated from the chorionic membrane by gentle traction and dissected into 5 mm x 20 mm PAM and CAM strips in a cell culture hood. All amniotic membrane (AM) explants were dissected and inserted into the mechanical stretching apparatus in the same orientation for all patients. Only tissue exposed to DMEM during cyclic tensile strain experiments was dissected and used for analysis.

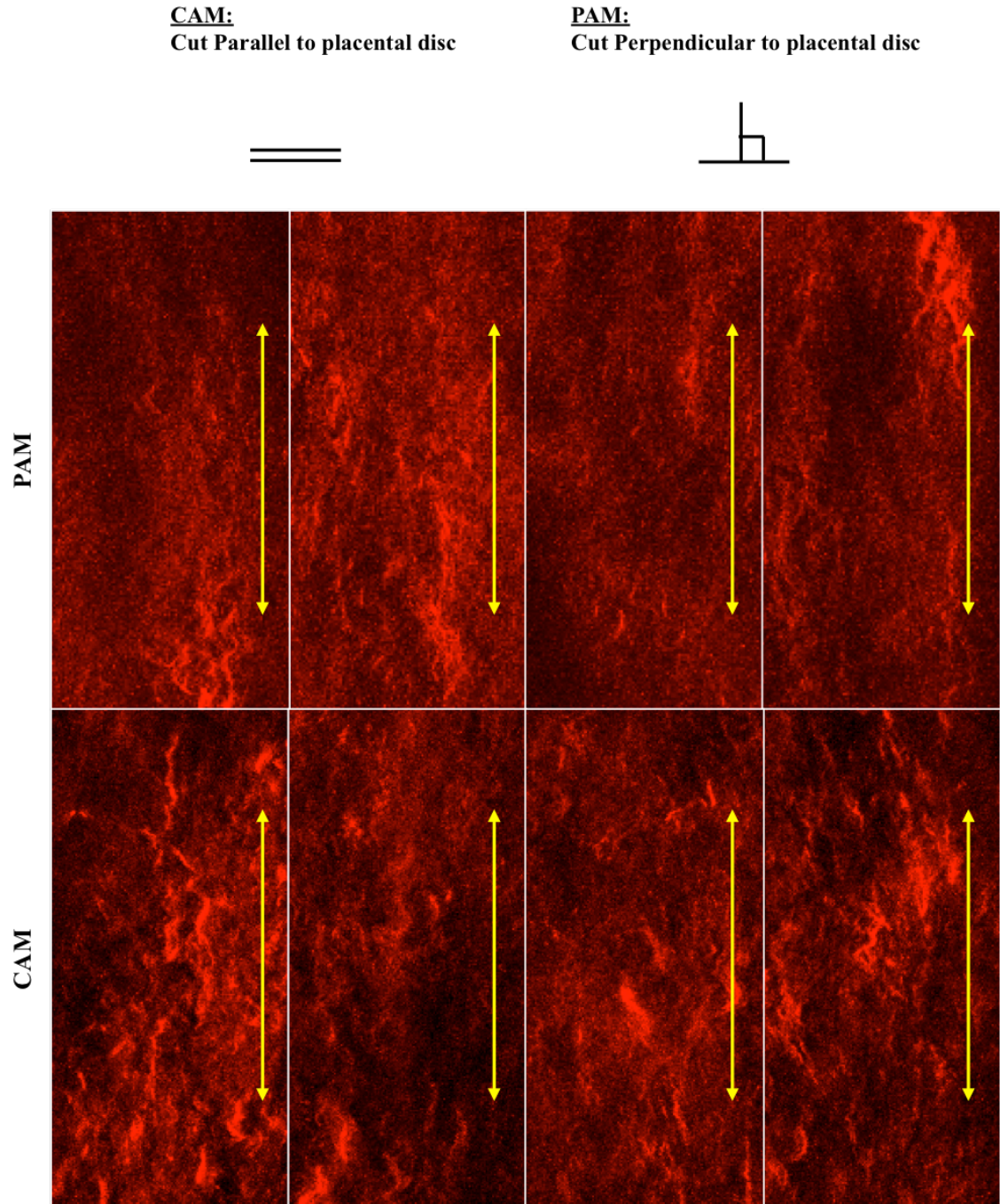


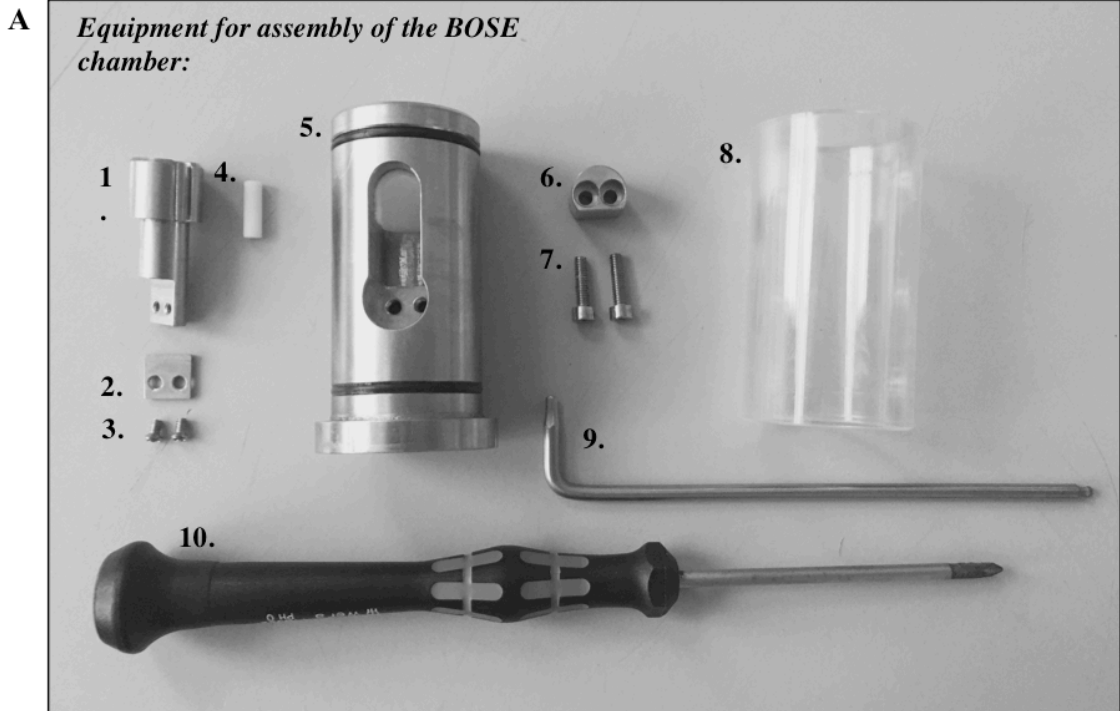
Figure 6.5: Second harmonic generation imaging microscopy of CAM and PAM specimens. Collagen fibre orientation as defined by SHG imaging was shown to align in parallel to the placental disc and transition towards a perpendicular orientation towards the cervical region. AM explants were loaded into the ex-vivo bioreactor chambers and strained in the same direction for consistency (yellow arrows).

During dissection the tissue was prevented from drying out by placing in sterile DMEM solution. To perform uniaxial cyclic tensile strain experiments the AM was clamped into the tissue chamber using the equipment in **Figure 6.6a**. All equipment was sterilized using an autoclave and opened only in the cell culture hood. Assembled chambers were filled with DMEM+20%FCS supplemented with 5 µg/ml penicillin and 5 µg/ml streptomycin. Some experiments involved incubation of the tissue with pharmacological agents, and if so it was at this point that they were added using a syringe with final concentrations having been established in the literature including 25 µM AKTi (selectively targets AKT-1/2 isoforms), 50 nM wortmannin (WTM, non-specific PI3-kinase inhibitor), 10 µM Cx43 antisense or sense oligodeoxynucleotides (Cx43asODNs/Cx43sODNs), and 10 µM NS-398 (selective COX-2 inhibitor).^{182,276-278} Once samples were loaded into the custom-made stainless steel mechanical loading chamber (**Figure 6.6b**), with a grip-to-grip distance of 30 mm they were loaded into the mechanical testing rig and fixed into the Bose machine (BOSE Enduratec, UK, Mechanical Test Systems Incorporation, **Figure 6.7**).

The *ex-vivo* BOSE bioreactor system set-up (**Figure 6.7**) has been routinely used in our laboratory and optimised for uniaxial cyclic strain of the AM as previously described.^{86,279} Uniaxial cyclic tensile strain experiments involved cyclic strain at a frequency of 1 Hz with samples exposed to 2% strain. Strain was applied in blocks of 1 minute strain (60 cycles) in a sinusoidal waveform, and rest (~0% strain) held for 9 minutes (540 cycles) repeated for 24 hours (144 blocks); which simulate contraction cycles induced during the onset of labour. A maximum of 16 loading chambers were connected to an actuator arm and secured within the BOSE loading frame (BOSE Corporation, Eden, Prairie, Minnesota, USA), which was housed within a humidified incubator (5%CO₂, 37°C). The loading chambers were each loaded with 2 mL of DMEM. Unstrained control specimens were incubated within the BOSE system's incubator within separate tubes but did not undergo CTS.

Following CTS experiments, the BOSE chambers (maximum 16 per experiment) were dismantled and media samples were drawn up from the chamber using a syringe. The glass cover was removed from the mechanical testing chamber and the stationary bottom grip tissue holder released to allow the movable upper grip tissue holder to be removed from the main chamber. The 1 mm thick plate was then removed and only the tissue

exposed directly to strain and DMEM, approximately 5 mm x 10 mm, was dissected for storage. The tissue underneath the movable upper grip and stationary bottom grip that was not exposed to strain was discarded. Depending on the experiment the tissue was now fixed or snap frozen in liquid nitrogen and stored at -80°C.



1. Movable **upper grip** that attaches to mechanical rig
2. 1 mm thick plate for tissue attachment to the upper grip
3. Top clasp screws to secure plate to top upper grip and fix tissue in position
4. Polyethylene pin to prevent rotation of the top holder during stretch
5. BOSE chamber
6. Stationary **bottom grip** that inserts into BOSE chamber
7. Bottom tissue grip screws to fix tissue in position
8. Glass case for securing on the main BOSE chamber
9. Allen key for bottom grip tissue holder screws (7)
10. Philips head screwdriver for upper grip screws (3)

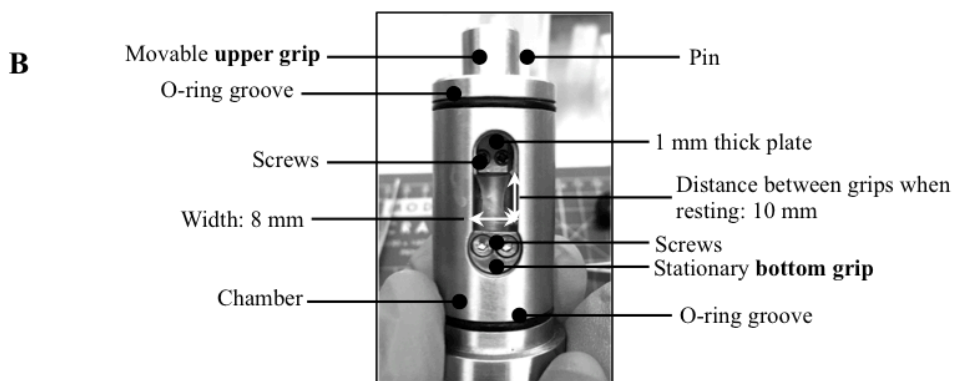


Figure 6.6: Equipment used to assemble individual BOSE chambers (A) and assembly of BOSE chamber containing amniotic membrane clamped between the movable upper grip and stationary bottom grip (B). In order to secure amniotic membrane tissue between upper and bottom grips, the tissue is placed on the lower end of the movable upper grip and then secured in place with the 1 mm thick plate. The upper grip containing the tissue is then placed inside the chamber and the tissue is placed between the 2 bottom grip screw holes which is then secured in place by inserting the bottom grip. Once the tissue is secure, the glass cover is put on and DMEM injected through the pin hole. The top and bottom O-ring grooves prevent leakage of the DMEM. The movable upper grip is then connected to the actuator arm.

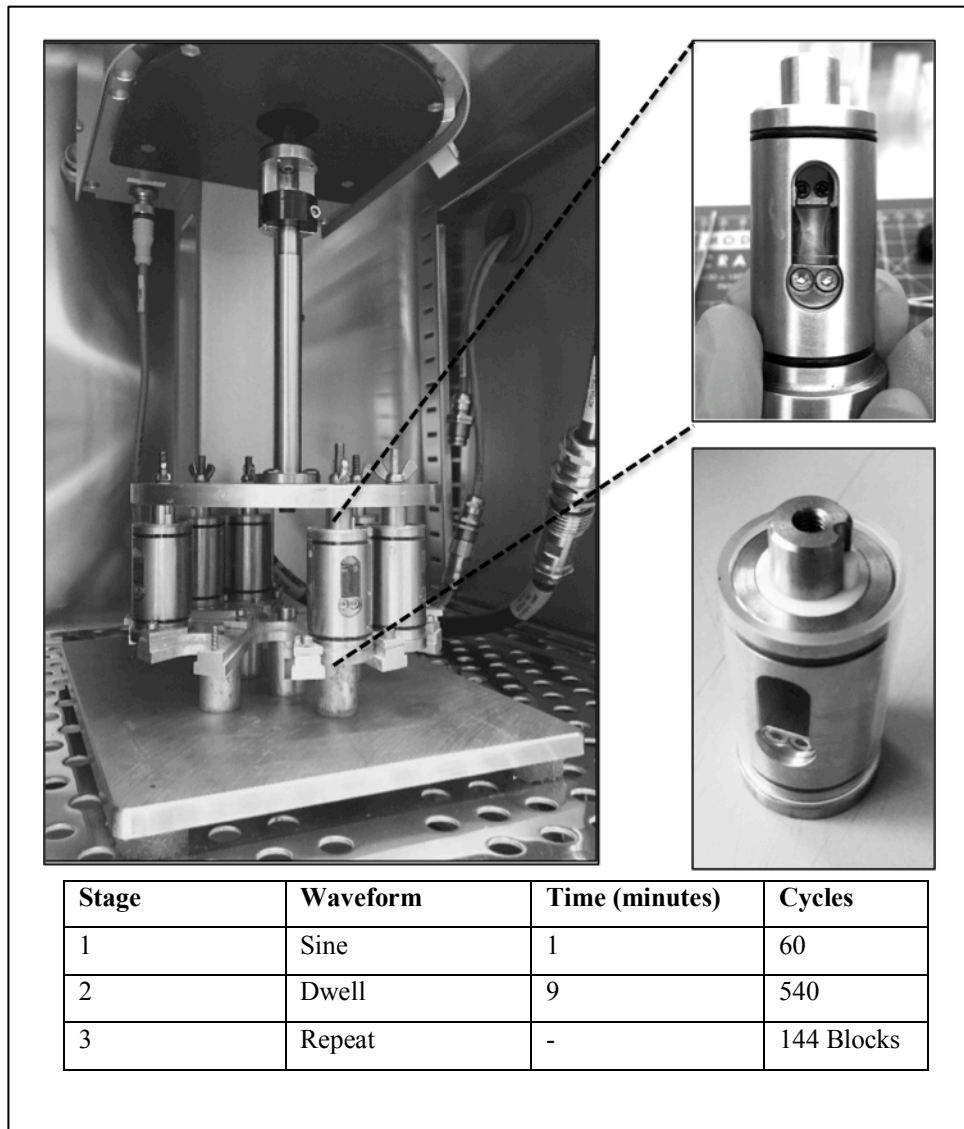


Figure 6.7: Bose chamber system with individual chambers containing dissected AM tissue undergoing cyclic tensile strain. Bose system experimental set-up involved a frequency of 1 Hz and 144 Blocks were used to allow cyclic tensile strain of tissue for 24 hours with cycles of 1 minute strain and 9 minutes rest. Sine waveform represents strained and dwell represents unstrained conditions. Total sine cycles = 8,640. Total dwell cycles = 12,960.

6.3 Results

6.3.1 Understanding fetal membrane weakening mechanisms

To test the hypothesis that repetitive cyclic tensile strain can lead to changes in the amniotic membrane ECM proteins and levels of weakening factors, amniotic membrane was repetitively stretched using an ex-vivo bioreactor, and experiments performed to measure collagen, elastin, sulfated glycosaminoglycan (sGAG) content and release of Prostaglandin E₂, and total MMP activity. The effect of inhibiting stretch activated pathways and pro-inflammatory pathways on cyclic tensile strain induced changes were also investigated to determine if these typical weakening mechanisms that occur during repetitive cyclic tensile strain could be perturbed. Experiments were performed to inhibit Cx43, AKT (protein kinase B), PI3-kinases, and cyclooxygenase-2 (COX-2).

6.3.1.1 The effect of cyclic tensile strain on glycosaminoglycan content

AM was exposed to 24 hours of 2% CTS in cycles of 1 minute CTS and 9minutes rest at a frequency of 1 Hz. These data show that sGAG synthesis increased following CTS (**Figure 6.8**) in both cervical AM (CAM, $P < 0.001$), and placental AM (PAM, $P < 0.001$). Levels of sGAG were also increased in non-strained CAM tissue compared to patient-matched PAM tissue ($P < 0.05$). There was no difference in sGAG content between CAM and PAM tissue that had undergone CTS for 24 hours ($P > 0.05$).

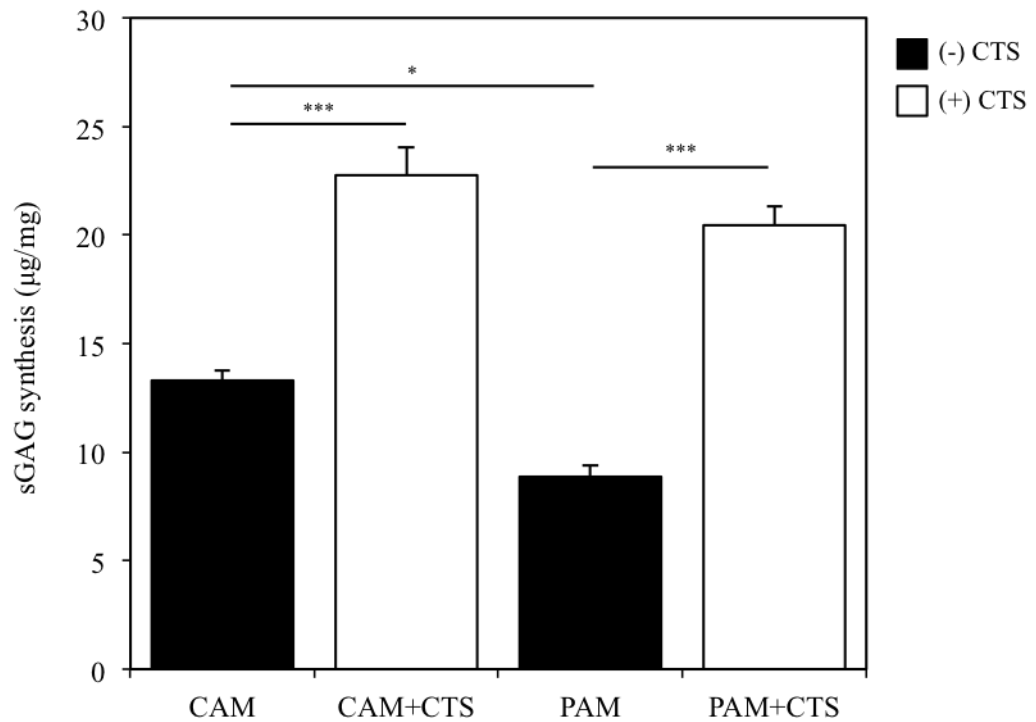


Figure 6.8: The effect cyclic tensile strain (CTS) on cervical (CAM) and placental (PAM) amniotic membrane sulfated glycosaminoglycan content. Amniotic membrane was exposed to cycles of 1 minute strain and 9 minutes rest for 24 hours at a frequency of 1 Hz and compared to non-strained patient matched controls. Error bars represent mean \pm SEM, where *** $p < 0.001$, * $p < 0.05$. $N = 16$ amniotic membrane samples per condition from $N = 4$ patients.

6.3.1.2 The effect of cyclic tensile strain on collagen content

Collagen content in AM was quantified by hydroxyproline assay, which is an important component of the collagen triple helix structure. Collagen content decreased in CAM ($P < 0.001$) and PAM ($P < 0.001$) following CTS for 24 hours (**Figure 6.9a**). Collagen content was higher in PAM tissue compared to CAM tissue in non-strained control AM ($P < 0.001$). Following CTS for 24 hours collagen content remained higher in PAM compared to CAM tissue ($P < 0.05$). Second harmonic generation (SHG) imaging of collagen fibres revealed decreased SHG intensity (arbitrary units) over time in both CAM and PAM tissue following CTS suggesting repetitive CTS increases degradation of collagen within the AM (**Figure 6.9b**).

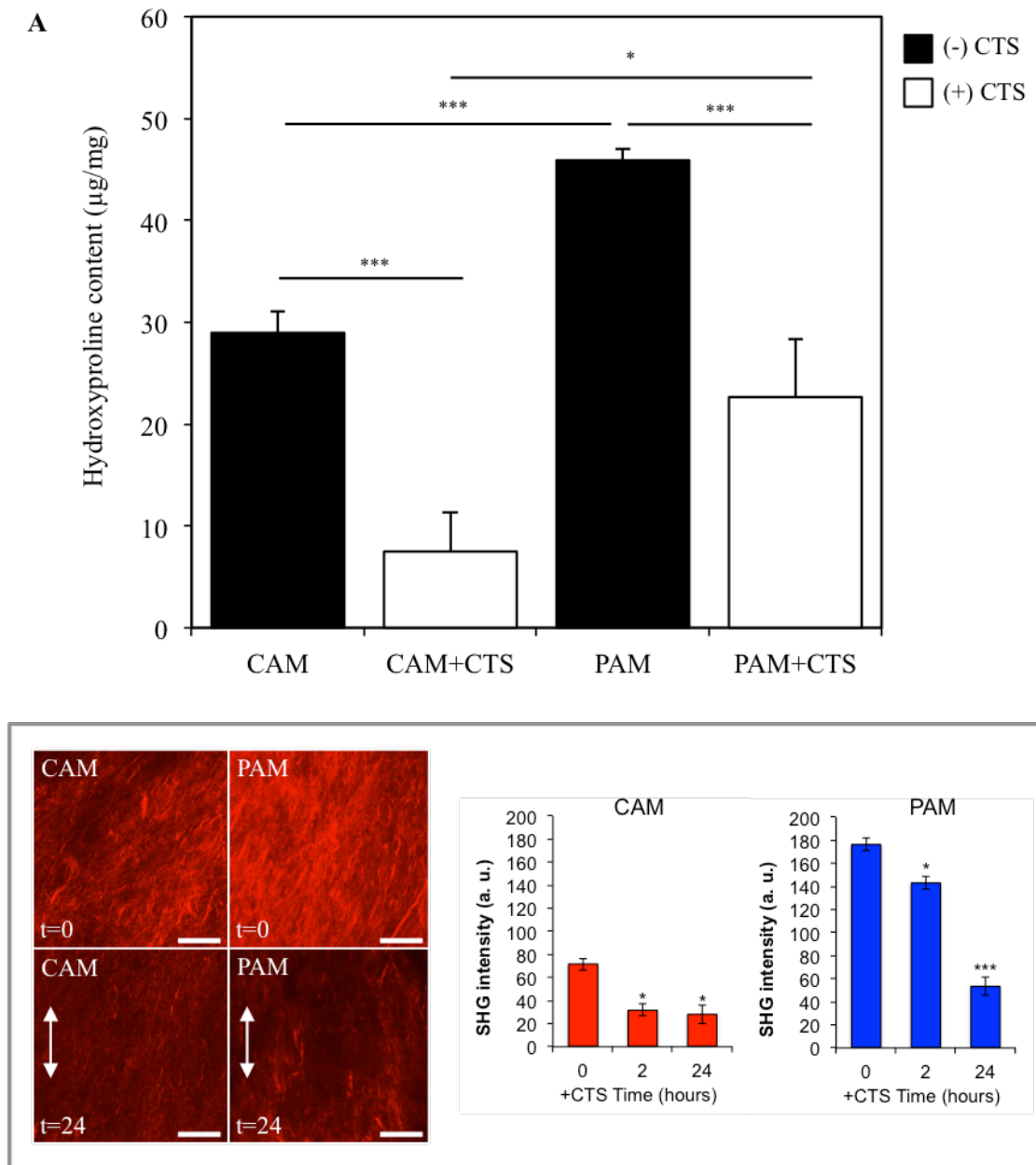


Figure 6.9: The effect cyclic tensile strain on collagen content in cervical (CAM) and placental (PAM) amniotic membrane. Amniotic membrane was exposed to cycles of 1 minute strain and 9 minutes rest for 24 hours at a frequency of 1 Hz and compared to non-strained patient matched controls (A). SHG intensity was higher in PAM tissue compared to CAM tissue and decreased in both CAM and PAM tissue over time in response to CTS. Error bars represent mean \pm SEM, where *** $p < 0.001$, * $p < 0.05$. $N = 16$ amniotic membrane samples per condition from $N = 4$ patients. SHG analysis was performed on bisected amniotic membrane samples from $N = 2$ patients with 5 separate fields of view used for analysis in each condition.

6.3.1.3 The effect of cyclic tensile strain on elastin content

There was a decrease in CAM elastin content following CTS for 24 hours compared to non-strained CAM tissue ($P < 0.05$, **Figure 6.10**); whilst elastin content also decreased in PAM tissue following 24 hours of CTS compared to non-strained PAM tissue ($P < 0.05$). Interestingly, in unstrained control tissue, elastin content did not change in PAM tissue compared to CAM tissue ($P > 0.05$).

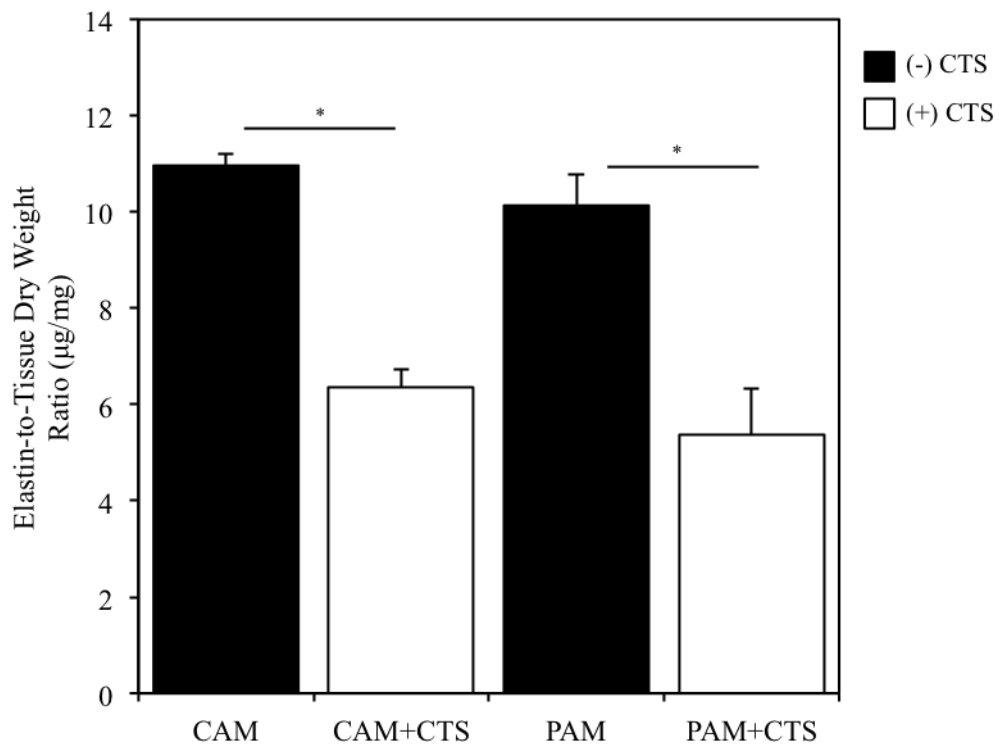


Figure 6.10: The effect of cyclic tensile strain on cervical (CAM) and placental (PAM) amniotic membrane elastin content. Amniotic membrane was exposed to cycles of 1 minute strain and 9 minutes rest for 24 hours at a frequency of 1 Hz and compared to non-strained patient matched controls. Error bars represent mean \pm SEM, where $*p < 0.05$. $N=16$ amniotic membrane samples per condition from $N=4$ patients.

6.3.1.4 The effect of cyclic tensile strain on prostaglandin E₂ release

These data show increased PGE₂ release following 24 hours CTS in both CAM and PAM strained tissue (both $P < 0.001$, **Figure 6.11**). There was no difference in levels of PGE₂ release when comparing CAM and PAM strained tissue ($P > 0.05$). However, in non-

strained control tissue, CAM tissue released higher amounts of PGE₂ into tissue media compared to non-strained PAM tissue ($P < 0.001$).

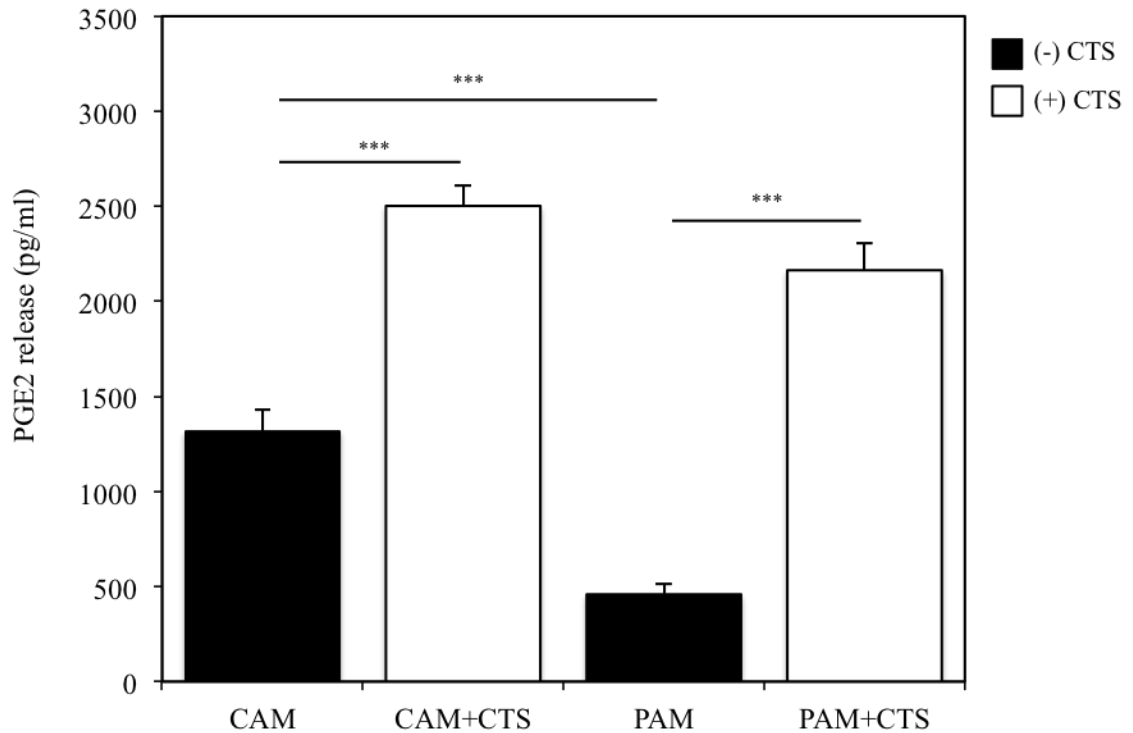


Figure 6.11: The effect of cyclic tensile strain on cervical (CAM) and placental (PAM) amniotic membrane prostaglandin E_2 release. Amniotic membrane was exposed to cycles of 1 minute strain and 9 minutes rest for 24 hours at a frequency of 1 Hz and compared to non-strained patient matched controls. Error bars represent mean \pm SEM, where *** $p < 0.001$. $N = 24$ amniotic membrane samples per condition from $N = 6$ patients.

6.3.1.5 The effect of cyclic tensile strain on total MMP activity

Similarly to PGE₂ data, total MMP activity increased following 24 hours of CTS for both CAM and PAM tissue measured from incubated media samples (both $P < 0.001$, **Figure 6.12**). There was no difference in total MMP activity between strained PAM and CAM tissue ($P > 0.05$). Interestingly, in non-strained control tissue, CAM tissue released higher amounts of MMP into tissue media compared to PAM tissue ($P < 0.05$). These data indicate that there are significant differences between CAM and PAM regions of the AM, likely due to the zone of altered morphology present at term and located in the AM region overlying the cervix.

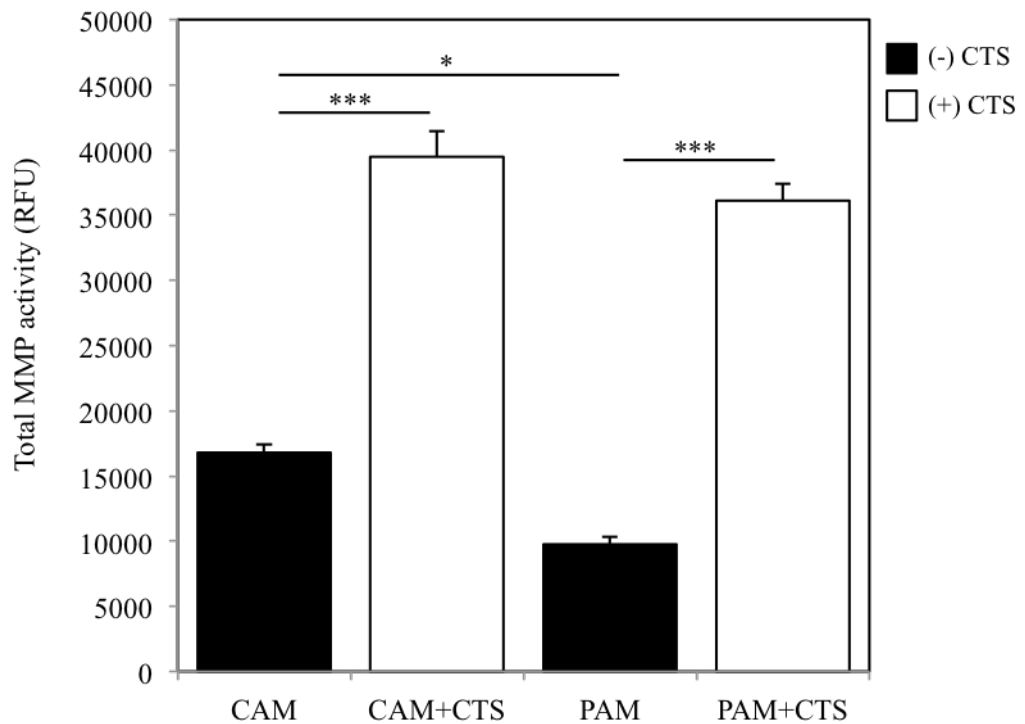


Figure 6.12: The effect of cyclic tensile strain on cervical (CAM) and placental (PAM) amniotic membrane total MMP activity (RFU). Measurements were taken using fresh DMEM, taken immediately after cyclic tensile strain with patient matched controls. Amniotic membrane was exposed to cycles of 1 minute strain and 9 minutes rest for 24 hours at a frequency of 1 Hz and compared to non-strained patient matched controls. Error bars represent mean \pm SEM, where *** p <0.001, * p <0.05. $N=24$ amniotic membrane samples per condition from $N=6$ patients.

6.3.1.6 Inhibition of AKT and Cx43 activation

Following 2% CTS for 24 hours activation of Cx43 and AKT-1/2/3 was investigated by comparison with non-strained control tissue in both CAM and PAM regions. These data show increased protein expression of Cx43 and AKT-1/2/3 in both CAM and PAM tissue regions following CTS (**Figure 6.13** and **Figure 6.14**). When normalised to GAPDH these data show increased activation of AKT-1/2/3 in PAM and CAM tissue (both $P < 0.05$); and increased activation of Cx43 in PAM and CAM tissue (both $P < 0.01$) when compared to non-strained tissue at 24 hours incubation. Inhibition of AKT-1/2/3 is

achieved using 25 μ M isozyme specific AKT-1/2 inhibitor, which is a well-established concentration in the literature¹⁸². Inhibition of Cx43 was achieved using 10 μ M Cx43asODNs in serum-free media to reduce degradation rate, and is a well-established concentration¹²⁴. Whilst this was the first time Cx43 and AKT inhibition is reported in fetal membranes, these concentrations resulted in sufficient knockdown, and therefore used for further experiments investigating the inhibition of these pathways. Interestingly, inhibition of AKT was most efficacious in CAM and PAM samples that underwent repetitive CTS compared to strained CAM and PAM tissue that were not exposed to AKTi (both $P < 0.001$). Incubation with Cx43asODNs resulted in Cx43 knockdown in both CAM and PAM regions during both strained ($P < 0.001$) and non-strained ($P < 0.05$) conditions compared to CAM and PAM tissue not exposed to Cx43asODNs.

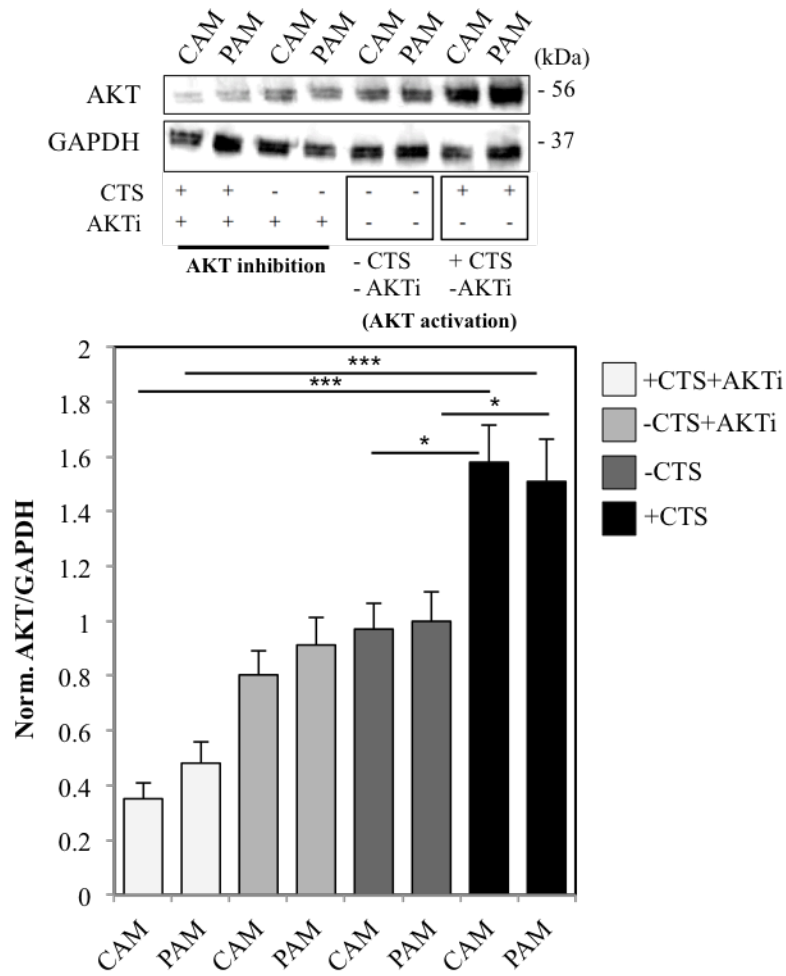


Figure 6.13: Activation and inhibition and AKT-1/2/3 protein expression. Normalisation of AKT to GAPDH using densitometry analysis reveals increased expression of AKT after mechanical stimulation following cyclic tensile strain for 24 hours. AKT is inhibited during CTS when incubated with AKTi. Error bars represent the mean \pm SEM where $*p < 0.05$; $***p < 0.001$, $N = 3$ patients with 3 AM samples per condition.

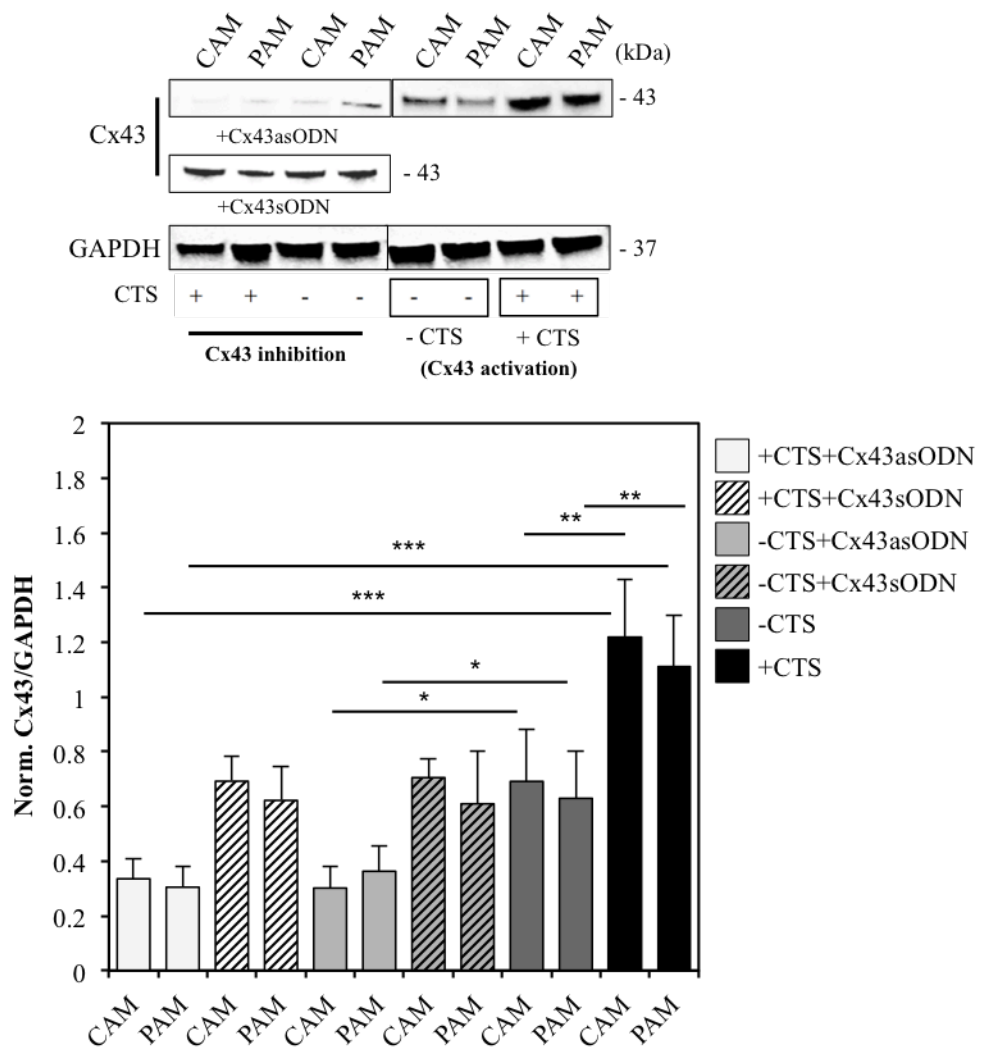


Figure 6.14: Activation and inhibition and Cx43 protein expression. Normalisation of Cx43 to GAPDH using densitometry analysis reveals increased expression of Cx43 after mechanical stimulation following cyclic tensile strain for 24 hours. Cx43 is inhibited during CTS and non-strained conditions when incubated with Cx43asODNs, confirmed following incubations with Cx43sODN as a negative control. Error bars represent the mean \pm SEM where * $p < 0.05$; ** $p < 0.01$; *** $p < 0.001$, $N = 3$ patients with 3 AM samples per condition.

6.3.1.7 Targeting mechanotransduction pathways reduces fetal membrane weakening factors

Isozyme-specific AKT-1/2 inhibition

Following incubations with isozyme-specific AKT-1/2 inhibitor (**Figure 6.15**), sGAG content reduced when incubated with AKTi for 24 hours in non-strained CAM ($P < 0.05$) but did not show statistically significant reduction in sGAG content in PAM tissue for non-strained conditions ($P > 0.05$). However, incubations with AKTi during CTS resulted in reduction of sGAG content in PAM regions ($P < 0.01$) but not in CAM regions ($P > 0.05$). Conversely, collagen content was higher in both CAM ($P < 0.05$) and PAM ($P < 0.01$) therefore reducing collagen degradation typically seen during 24 hours of CTS. However, elastin content did not show any statistically significant changes when incubated with AKTi in both strained and non-strained conditions. Furthermore PGE₂ release dramatically decreased in strained and non-strained CAM samples when incubated with AKTi (both $P < 0.001$). PGE₂ release also decreased in PAM tissue media samples that had undergone CTS ($P < 0.001$), although no change occurred in non-strained PAM tissue media samples when treated with AKTi, likely due to the relatively low PGE₂ levels reported in non-strained PAM tissue media. Similarly, total MMP activity reduced in CAM tissue media for both non-strained and strained conditions when incubated with AKTi (both $P < 0.001$). Although total MMP activity was only reported to reduce in PAM tissue media samples incubated with AKTi during CTS compared to non-treated PAM controls during CTS ($P < 0.01$). Whereas no difference in total MMP activity was reported in non-strained PAM tissue media samples when treated with AKTi; likely due to relatively low total MMP activity occurring in non-treated and non-strained PAM tissue media samples.

Cx43 inhibition using Cx43asODNs

Following incubations with Cx43asODNs (**Figure 6.16**) these data show a decrease in sGAG content in response to 24 hours CTS when incubated with Cx43asODNs in both CAM and PAM tissue (both $P < 0.001$). In non-strained control tissue there was no difference in sGAG content when incubated with Cx43asODNs for 24 hours ($P > 0.05$). Collagen content increased returning close to normal levels when incubated with

Cx43asODNs during CTS in both CAM and PAM tissue (both $P < 0.05$). There was no difference in collagen content reported in non-strained CAM and PAM tissue incubated with Cx43asODNs when compared with non-treated control CAM and PAM tissue. Furthermore, no changes in elastin content were reported when incubated with Cx43asODNs in PAM and CAM for strained and non-strained conditions. Both PGE_2 and total MMP activity were reduced in CAM and PAM tissue media samples that were incubated with Cx43asODNs during CTS compared to non-treated tissue (all $P < 0.001$). PGE_2 levels decreased in non-strained CAM tissue media treated with Cx43asODNs compared to non-treated ($P < 0.01$) but no difference was reported in PAM tissue media. Total MMP activity reduced in both CAM and PAM non-strained tissue media when incubated with Cx43asODNs compared to non-treated tissue media samples (CAM: $P < 0.001$; PAM: $P < 0.01$).

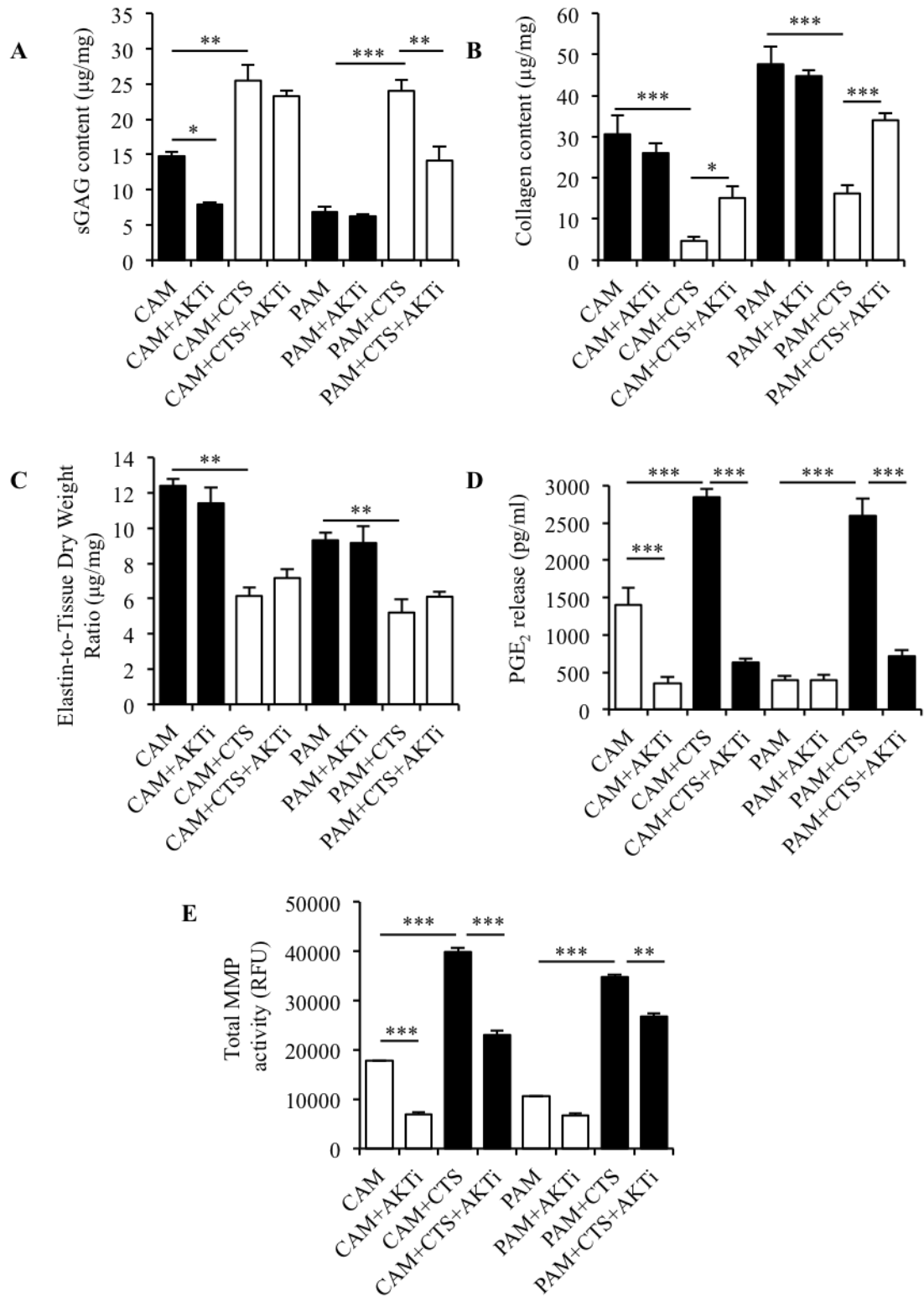


Figure 6.15: The effect of cyclic tensile strain and inhibition of AKT on cervical (CAM) and placental (PAM) amniotic membrane GAG (A), collagen (B), and elastin (C) production; and release of PGE₂ (D) and total MMP (E). Error bars represent mean \pm SEM, where *** p <0.001, ** p <0.01, * p <0.05. $N=8$ amniotic membrane samples per condition from $N=4$ patients (GAG, collagen, and elastin assays). $N=12$ amniotic membrane samples per condition from $N=6$ patients (PGE₂ and MMP assays).

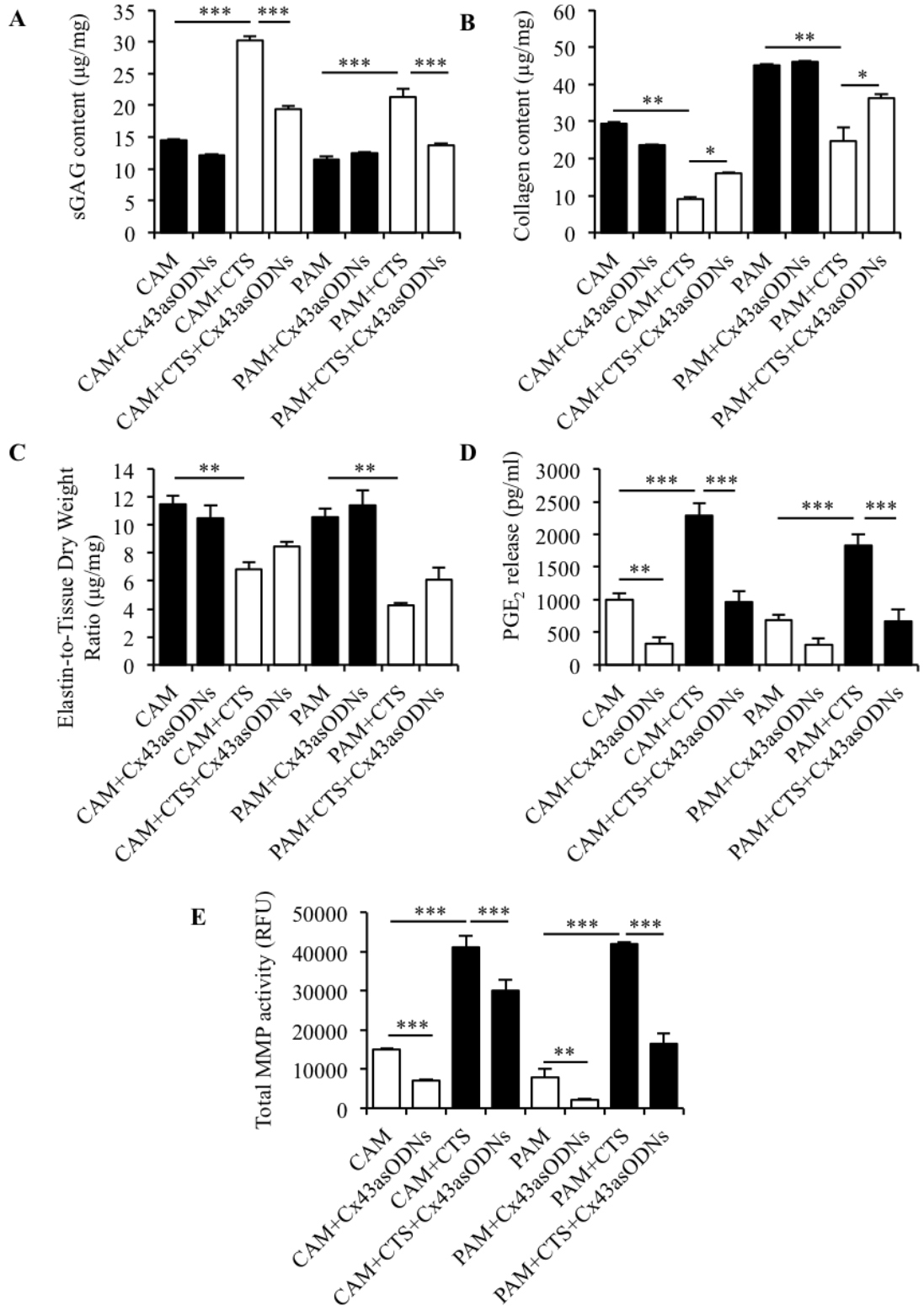


Figure 6.16: The effect of cyclic tensile strain and inhibition of Cx43 on cervical (CAM) and placental (PAM) amniotic membrane GAG (A), collagen (B), and elastin (C) production; and release of PGE₂ (D) and total MMP (E). Error bars represent mean \pm SEM, where *** p <0.001, ** p <0.01, * p <0.05. $N=8$ amniotic membrane samples per condition from $N=4$ patients (GAG, collagen, and elastin assays). $N=12$ amniotic membrane samples per condition from $N=6$ patients (PGE₂ and MMP assays).

Non-specific PI3-kinase inhibition

Non-specific inhibition of PI3-kinases using wortmannin (WTM, **Figure 6.17**) decreased sGAG content in PAM tissue that had undergone CTS for 24 hours compared to non-treated strained PAM tissue ($P < 0.001$). However, no difference in sGAG content was noted in CAM tissue treated with WTM. Furthermore, no difference in sGAG content was reported in non-strained tissue treated with WTM compared to non-treated tissue. Collagen content in strained CAM and PAM tissue increased when incubated with WTM compared to non-treated strained controls (both $P < 0.01$). However, no difference in collagen content occurred in non-strained CAM and PAM tissue when treated with WTM for 24 hour incubations. No difference in elastin content is reported for WTM incubations within all conditions, compared to non-treated controls. PGE₂ release decreased in CAM and PAM tissue that had undergone CTS and were treated with WTM (both $P < 0.001$). PGE₂ release also decreased in non-strained CAM tissue when treated with WTM for 24 hour incubations compared to non-treated CAM tissue ($P < 0.001$); whilst no difference was reported in PAM treated tissue. Similarly, total MMP activity decreased in CAM and PAM tissue that had undergone CTS and were treated with WTM (both $P < 0.001$). Similar to PGE₂ changes, total MMP activity reduced in non-strained CAM tissue media when treated with WTM for 24 hour incubations compared to non-treated CAM tissue ($P < 0.001$); whilst no difference was reported in PAM tissue treated with WTM.

6.3.2 Targeting pro-inflammatory pathways reduces fetal membrane weakening factors

Cyclooxygenase-2 (COX-2) inhibition using NS-398

Blocking COX-2 using NS-398 (**Figure 6.18**) reduced sGAG content in CAM and PAM tissue that had undergone CTS compared to non-treated CAM and PAM strained tissue (CAM: $P < 0.001$; PAM: $P < 0.01$). In non-strained CAM tissue, sGAG content decreased when incubated with NS-398 compared to non-treated CAM tissue ($P < 0.01$); whilst no difference was reported in PAM tissue. Collagen content increased in CAM tissue that had undergone CTS when treated with NS-398 compared to non-treated strained CAM tissue ($P < 0.05$); however, no difference was reported under the same conditions with PAM tissue. No difference in collagen content was reported in non-strained CAM and

PAM tissue treated with NS-398, compared to non-treated controls. Interestingly, elastin content increased in CAM and PAM tissue that had undergone CTS when incubated with NS-398, compared to non-treated strained CAM and PAM tissue (both $P < 0.01$). No difference in elastin content was reported in non-strained conditions when CAM and PAM tissue was incubated with NS-398. PGE₂ and total MMP activity dramatically decreased in CAM and PAM tissue media samples that had undergone CTS and were incubated with NS-398 compared to non-treated strained CAM and PAM tissue media samples (all $P < 0.001$). PGE₂ release decreased in non-strained CAM tissue when treated with NS-398, compared to non-treated CAM tissue ($P < 0.001$); however, no difference in PGE₂ was reported in PAM tissue media samples. Furthermore, these data show total MMP activity decreased in non-strained CAM and PAM tissue media samples when treated with NS-398 and compared to non-treated CAM and PAM tissue media samples (both $P < 0.001$).

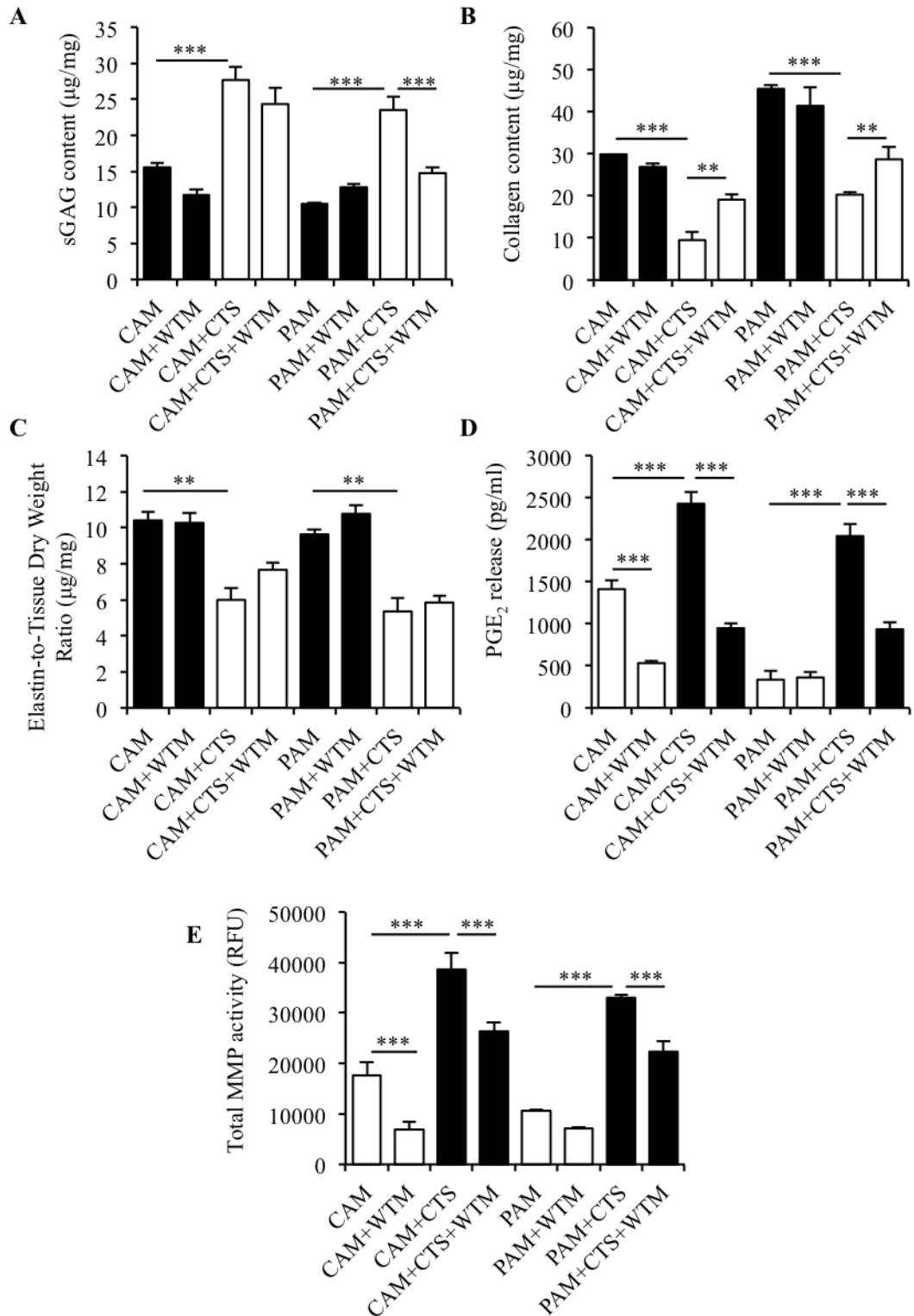


Figure 6.17: The effect of cyclic tensile strain and inhibition of PI3-kinase on cervical (CAM) and placental (PAM) amniotic membrane GAG (A), collagen (B), and elastin (C) production; and release of PGE₂ (D) and total MMP (E). Error bars represent mean \pm SEM, where *** $p < 0.001$, ** $p < 0.01$, * $p < 0.05$. $N = 8$ amniotic membrane samples per condition from $N = 4$ patients (GAG, collagen, and elastin assays). $N = 12$ amniotic membrane samples per condition from $N = 6$ patients (PGE₂ and MMP assays).

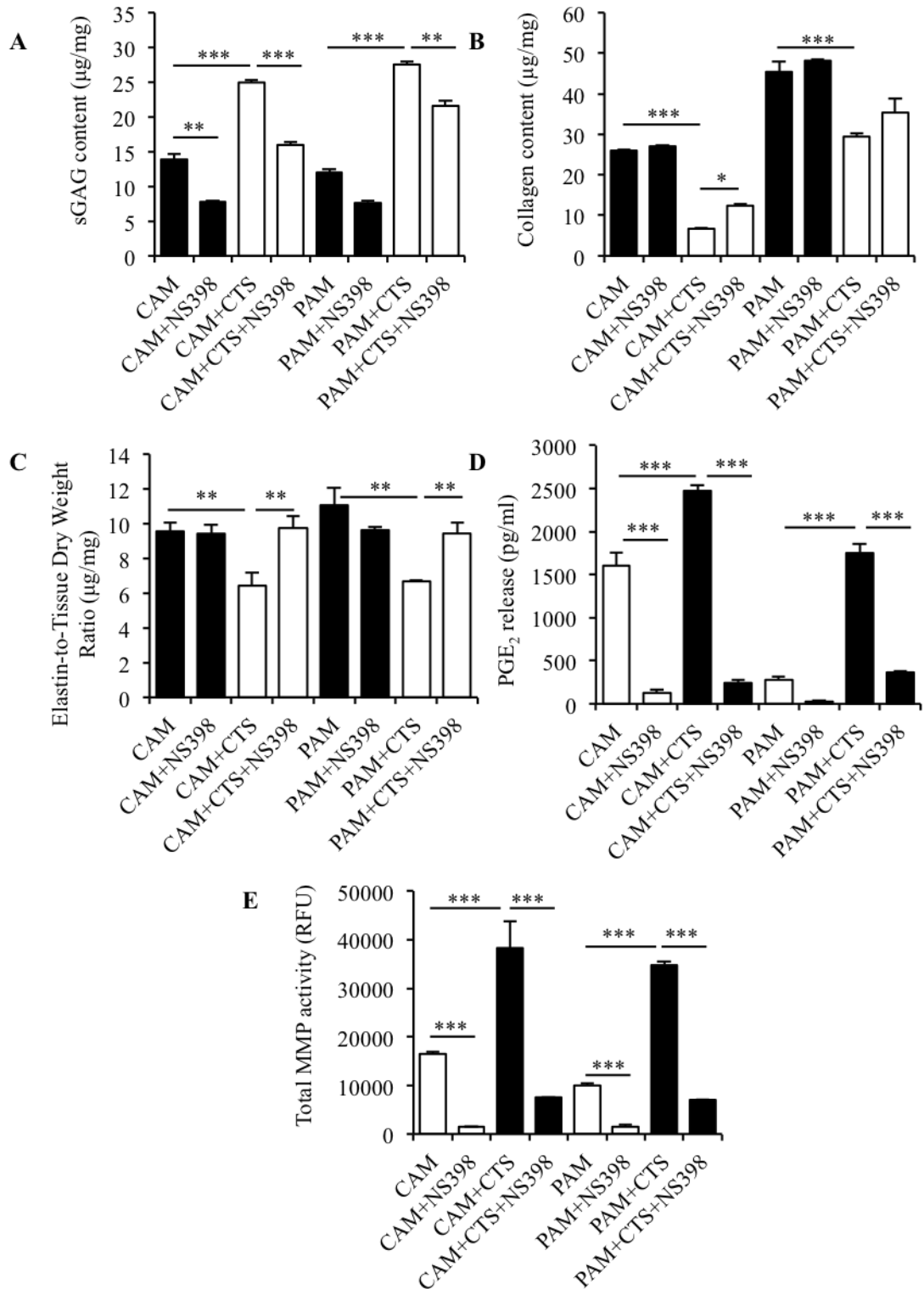


Figure 6.18: The effect of cyclic tensile strain and inhibition of cyclooxygenase-2 on cervical (CAM) and placental (PAM) amniotic membrane GAG (A), collagen (B), and elastin (C) production; and release of PGE₂ (D) and total MMP (E). Error bars represent mean \pm SEM, where *** p <0.001, ** p <0.01, * p <0.05. $N=8$ amniotic membrane samples per condition from $N=4$ patients (GAG, collagen, and elastin assays). $N=12$ amniotic membrane samples per condition from $N=6$ patients (PGE₂ and MMP assays).

6.4 Results summary

A summary of percentage changes following cyclic tensile strain experiments can be seen in **Tables 6.1 – 6.5**.

- Sulfated glycosaminoglycan (sGAG) content increases in both cervical (CAM) and placental (PAM) amniotic membrane samples following 2% cyclic tensile strain for 24 hours compared to non-strained controls. In non-strained samples sGAG content is higher in CAM regions compared to PAM samples.
- Following 2% cyclic tensile strain for 24 hours, collagen content decreases in both CAM and PAM samples compared to non-strained control. In non-strained control samples, PAM contained higher collagen content compared to CAM samples. SHG intensity also decreased in both PAM and CAM samples following 2% cyclic tensile strain for 24 hours.
- Elastin content decreased in PAM samples but not CAM samples following cyclic tensile strain for 24 hours. In non-strained control samples, elastin content was higher in PAM samples compared to CAM.
- PGE₂ and total MMP release increased in CAM and PAM samples following cyclic tensile strain for 24 hours. In non-strained control samples, PGE₂ and total MMP activity in media from CAM specimens contained higher PGE₂ and total MMP activity compared to PAM after 24 hours.
- Cyclic tensile strain induced activation of Cx43 and AKT-1/2/3 after 24 hours compared to non-strained samples in both PAM and CAM specimens.
- Inhibition of isozyme specific AKT-1/2 kinase, non-specific PI3-kinase, and Cx43 expression suppressed the effect of cyclic tensile strain on synthesis of sGAG and release of PGE₂ and total MMP activity. Degradation of elastin and collagen also diminishes following inhibition of these pathways.

- Inhibition of COX-2 also reduced the effects of cyclic tensile strain on synthesis of sGAG, and release of PGE₂ and MMP. Degradation of elastin and collagen also diminished following inhibition of COX-2 activity.
- Inhibiting pro-inflammatory and stretch-activated pathways may reduce cyclic tensile strain induced fetal membrane weakening by reducing MMP/PGE₂ induced degradation of collagen and elastin. Swelling and softening of amniotic membrane induced by sGAG content can also be reduced by inhibiting these pathways.

Table 6.1: Overall response to repetitive cyclic tensile strain of the human amniotic membrane given as a percentage change for GAG, collagen, elastin, PGE₂ and total MMP activity (values represent mean \pm SEM).

Measurement	AM region	-CTS	+CTS	% change
GAG	CAM	13.30 (\pm 0.45)	22.75 (\pm 1.28)	+71.05
	PAM	8.86 (\pm 0.55)	20.45 (\pm 0.89)	+130.81
Collagen	CAM	28.96 (\pm 2.05)	7.48 (\pm 3.86)	-74.17
	PAM	45.89 (\pm 1.17)	22.65 (\pm 5.69)	-50.64
Elastin	CAM	10.96 (\pm 0.25)	6.35 (\pm 0.34)	-42.06
	PAM	10.13 (\pm 0.65)	5.37 (\pm 0.94)	-46.99
PGE ₂	CAM	1318.27 (\pm 119.96)	2615.41 (\pm 87.71)	+98.40
	PAM	458.85 (\pm 55.44)	2163.67 (\pm 139.16)	+371.54
MMP	CAM	16784.13 (\pm 632.29)	39442.50 (\pm 1968.36)	+135.0
	PAM	9751.25 (\pm 587.02)	36109.50 (\pm 1311.76)	+270.31

Table 6.2: Overall summary for AKTi treated human amniotic membrane tissue with patient-matched controls following cyclic tensile strain. Given as a percentage change (values represent mean \pm SEM).

Measurement	AM region	-AKTi			+AKTi		
		-CTS	-CTS	% change	+CTS	+CTS	% change
GAG	CAM	14.77 (± 0.55)	7.87 (± 0.35)	-46.72	25.46 (± 2.19)	23.26 (± 0.86)	-8.64
	PAM	6.75 (± 0.78)	6.14 (± 0.32)	-9.04	24.0 (± 1.52)	14.12 (± 1.99)	-41.17
Collagen	CAM	30.61 (± 1.91)	26.04 (± 0.98)	-14.93	4.68 (± 0.40)	15.11 (± 1.17)	+222.86
	PAM	47.63 (± 1.75)	44.74 (± 0.57)	-6.07	16.20 (± 0.78)	34.01 (± 0.71)	+109.94
Elastin	CAM	12.39 (± 0.38)	11.41 (± 0.91)	-7.91	6.15 (± 0.48)	7.16 (± 0.53)	+16.42
	PAM	9.31 (± 0.46)	9.15 (± 0.93)	-1.72	5.20 (± 0.78)	6.11 (± 0.31)	+17.50
PGE ₂	CAM	1399.67 (± 233.17)	344.90 (± 91.40)	-75.36	2844.02 (± 114.48)	629.67 (± 46.15)	-77.86
	PAM	386.49 (± 68.15)	391.97 (± 69.12)	+1.42	2594.85 (± 234.70)	714.28 (± 83.73)	-72.47
MMP	CAM	17765.28 (± 69.15)	6939.96 (± 312.94)	-60.94	39823.36 (± 731.9)	23007.55 (± 933.46)	-42.23
	PAM	10623.68 (± 102.25)	6790.40 (± 445.33)	-36.08	34755.46 (± 753.64)	26743.92 (± 689.39)	-23.05

Table 6.3: Overall summary for Cx43asODN treated human amniotic membrane tissue with patient-matched controls following cyclic tensile strain. Given as a percentage change (values represent mean \pm SEM).

Measurement	AM region	+Cx43asODNs			+Cx43asODNs		
		-CTS	-CTS	% change	+CTS	+CTS	% change
GAG	CAM	14.46 (± 0.21)	12.10 (± 0.20)	-16.32	30.21 (± 0.62)	19.41 (± 0.45)	-35.75
	PAM	11.50 (± 0.47)	12.45 (± 0.29)	+8.26	21.32 (± 1.34)	13.72 (± 0.30)	-35.65
Collagen	CAM	29.36 (± 0.53)	23.59 (± 0.04)	-19.65	9.04 (± 0.19)	15.99 (± 0.17)	+76.88
	PAM	45.07 (± 0.48)	46.02 (± 0.18)	+2.11	24.67 (± 1.45)	36.24 (± 1.12)	+46.90
Elastin	CAM	11.49 (± 0.58)	10.50 (± 0.89)	-8.62	6.83 (± 0.50)	8.46 (± 0.36)	+23.87
	PAM	10.53 (± 0.63)	11.38 (± 1.12)	+8.07	4.25 (± 0.18)	6.09 (± 0.89)	+43.29
PGE ₂	CAM	1004.89 (± 95.68)	321.06 (± 95.70)	-68.05	2286.71 (± 186.41)	963.03 (± 172.10)	-57.89
	PAM	686.41 (± 78.80)	308.50 (± 102.98)	-55.06	1827.61 (± 172.35)	667.13 (± 188.90)	-63.50
MMP	CAM	15110.42 (± 211.40)	6931.90 (± 381.82)	-54.13	41090.66 (± 2797.26)	30029.81 (± 2716.5)	-26.92
	PAM	7885.58 (± 208.29)	2182.06 (± 106.77)	-72.33	41927.96 (± 495.74)	16435.53 (± 2515.75)	-60.80

Table 6.4: Overall summary for wortmannin treated human amniotic membrane tissue with patient-matched controls following cyclic tensile strain. Given as a percentage change(values represent mean \pm SEM).

Measurement	AM region	+WTM			+WTM		
		-CTS	-CTS	% change	+CTS	+CTS	% change
GAG	CAM	15.52 (± 0.63)	11.77 (± 0.71)	-24.16	27.67 (± 1.87)	24.33 (± 2.31)	-12.07
	PAM	10.45 (± 0.25)	12.76 (± 0.43)	+22.11	23.51 (± 1.88)	14.76 (± 0.86)	-37.22
Collagen	CAM	29.88 (± 0.17)	26.89 (± 0.91)	-10.01	9.50 (± 1.94)	19.12 (± 1.23)	+101.26
	PAM	45.47 (± 0.94)	41.43 (± 4.28)	-8.88	20.30 (± 0.58)	28.70 (± 1.19)	+41.38
Elastin	CAM	10.40 (± 0.51)	10.27 (± 0.52)	-1.25	5.99 (± 0.63)	7.66 (± 0.40)	+27.88
	PAM	9.63 (± 0.28)	10.77 (± 0.43)	+11.84	5.35 (± 0.72)	5.85 (± 0.37)	+9.35
PGE ₂	CAM	1407.37 (± 106.03)	528.59 (± 28.32)	-62.44	2428.03 (± 137.25)	948.39 (± 54.99)	-60.94
	PAM	330.16 (± 106.32)	366.33 (± 54.55)	+10.96	2043.17 (± 138.91)	935.07 (± 87.39)	-54.23
MMP	CAM	17693.06 (± 2514.33)	6842.50 (± 1063.69)	-61.33	38610.65 (± 3324.55)	26366.81 (± 1666.79)	-31.71
	PAM	10542.63 (± 410.53)	7142.97 (± 299.56)	-32.25	33032.10 (± 467.14)	22327.77 (± 2143.37)	-32.41

Table 6.5: Overall summary for NS-398 treated human amniotic membrane tissue with patient-matched controls following cyclic tensile strain. Given as a percentage change (values represent mean \pm SEM).

Measurement	AM region	+NS-398			+NS-398		
		-CTS	-CTS	% change	+CTS	+CTS	% change
GAG	CAM	13.86 (± 0.77)	7.73 (± 0.23)	-44.23	24.95 (± 0.36)	15.97 (± 0.40)	-35.99
	PAM	12.0 (± 0.48)	7.67 (± 0.19)	-36.08	27.54 (± 0.43)	21.60 (± 0.67)	-21.57
Collagen	CAM	25.97 (± 0.06)	27.03 (± 0.06)	+4.08	6.70 (± 0.13)	12.37 (± 0.15)	+84.63
	PAM	45.39 (± 1.03)	48.15 (± 0.14)	+6.08	29.42 (± 0.28)	35.35 (± 1.44)	+20.16
Elastin	CAM	9.56 (± 0.52)	9.43 (± 0.49)	-1.36	6.45 (± 0.76)	9.74 (± 0.70)	+51.01
	PAM	11.06 (± 1.02)	9.63 (± 0.18)	-12.93	6.68 (± 0.18)	9.44 (± 0.65)	+41.32
PGE ₂	CAM	1599.42 (± 159.50)	128.90 (± 35.39)	-91.94	2474.06 (± 69.12)	242.66 (± 40.65)	-90.19
	PAM	276.96 (± 38.43)	31.81 (± 5.43)	-88.51	1751.53 (± 102.16)	365.48 (± 15.55)	-79.13
MMP	CAM	16569.03 (± 434.77)	1545.25 (± 199.87)	-90.67	38248.32 (± 1558.38)	7540.90 (± 183.38)	-80.28
	PAM	9956.32 (± 443.2)	1508.99 (± 322.38)	-84.84	34725.55 (± 669.11)	7013.39 (± 129.43)	-79.80

6.5 Discussion

The mechanotransduction mechanisms leading to fetal membrane weakening and rupture are unknown. Physiologically, it is known that a combination of stretch and pre-weakened tissue facilitated by biochemical alterations leads to the initiation and rupture of the fetal membranes. However, it is likely that similar pathways play a role in weakening and rupture of preterm tissue that occurs in PPRM, although upstream mediators and detailed pathways are yet to be detailed. Investigations have primarily focused on the influence of pro-inflammatory cytokines, ECM degradation by MMPs, oxidative stress, and apoptosis on PPRM, developing from inflammation/infection and thrombin-induced weakening due to placental bleeding (abruption) pathways.

The present study were to investigate the effect of repetitive CTS on AM weakening mechanisms using an *ex-vivo* bioreactor; and investigate the effects of inhibiting Cx43 and Akt (also known as protein kinase B, known to stabilise Cx43 gap junctions) on the outcome of AM weakening mechanisms. Furthermore, we investigate the inhibition of PI3 kinase (known to be the major mode of Akt activation) and selectively inhibit COX-2, an enzyme rapidly expressed in response to cytokines and pro-inflammatory mediators.

The present study demonstrates definitive changes following repetitive cyclic tensile strain in major ECM components including sulfated GAG, collagen, and elastin, as well as changes in the release of weakening factors associated with pro-inflammatory pathways (PGE₂ and MMPs). It is well known that amniotic membrane in the region overlying the cervix undergoes biochemically mediated weakening in preparation for parturition, therefore analysis was performed on both this tissue (termed cervical amniotic membrane, CAM) and tissue close to the placenta (within 3 cm of the placental disc, PAM).

In response to 24 hours CTS, sulfated GAG content increases in both CAM and PAM tissue regions, whilst collagen and elastin content decreases in both regions of the amniotic membrane. Whilst the reduction of collagen and elastin content in response to repetitive CTS can result in weakened structural and elastic properties of the fetal membrane, the relationship between elevated GAG content and FM weakening could be detrimental to FM mechanical integrity by promoting tissue softening due to enhanced

proteoglycans. Interestingly, total GAG content during cervical ripening has been reported to increase with increased gestational age and parturition, concomitant with a reduction in collagen, where fibres appear thinner and more dispersed^{280,281}. It is likely that in the amniotic membrane, the changes in sGAG content will effect the organisation of collagen and lead to increased fetal membrane softening. Importantly, GAGs are long unbranched polysaccharides that contain negatively charged repeating disaccharide units. This property attracts Na⁺ ions, which is beneficial in tissues such as cartilage, as it creates a hydrostatic pressure leading to swelling of the tissue providing enhanced protection to compressive forces. However, whilst enhanced GAG content in the FM is probably a normal physiological response that occurs during cervical ripening in a healthy pregnancy, the pathways involved are also likely to occur in preterm tissue regarding cases of PPROM. Furthermore, the alterations in amniotic membrane ECM components are accompanied by an increase in both PGE₂ and total MMP activity within tissue secretions for both CAM and PAM regions. PGE₂ is known to increase in the cervix during cervical ripening and induces remodelling of cervical connective tissue by increased production of proteoglycans²⁸². We report similar mechanisms in the fetal membrane following repetitive cyclic tensile strain where increased PGE₂ levels enhance sGAG synthesis, and in turn this softening of the amniotic membrane leads to a reduction of collagen mediated by over production of MMP demonstrated in both PAM and CAM strained tissue. This repetitive mechanical stimulation could activate stretch-responsive proteins that initiate a pro-inflammatory response leading to overstimulation of ECM degradation pathways.

Interestingly, static stretch of cultured amniotic cells leads to enhanced expression of COX-2 and PGE₂ synthesis induced the pro-inflammatory transcription factor activator protein-1 (AP-1) and nuclear factor- κ B (NF- κ B)¹¹⁴. Previous studies also show increased expression of COX-2, oxytocin receptor, and Cx43 in the myometrium^{89,90,283}. Indeed, stretch of the uterus, and myometrium are likely to play a role in activation of pro-inflammatory pathways that lead to normal ECM degradation and FM rupture in healthy pregnancies. However, it has been reported that overdistension of the myometrium can contribute to the occurrence of preterm delivery⁹⁴. Importantly overdistension of the uterus will also contribute to stretching of the fetal membranes and increase the risk of activating stretch sensitive inflammatory pathways that induce ECM degradation in the amniotic membrane.

We report differences between the two regions of term amniotic membrane (CAM and PAM) that were not subjected to repetitive cyclic tensile strain and instead incubated for 24 hours. It was found that in CAM regions, there was elevated sGAG associated with reduced collagen content compared to PAM regions. In addition, elevated PGE₂ release and MMP activity is reported in CAM tissue secretions even without repetitive mechanical stimulation compared to PAM regions. These findings can be explained by the formation of a zone of altered morphology (ZAM) that overlies the cervix and weakens in preparation for parturition, whilst tissue distal from the ZAM is not affected. The ZAM is characterised by swelling of the collagenous layers in the amnion and thinning of the cell-dense chorionic trophoblast later with a reduced thickness of the overall FM. This specific area is also associated with increased MMP activity and cellular apoptosis. We also report a reduced SHG intensity in CAM regions compared to PAM, which reduces further with repetitive mechanical stimulation. The fibres are thinner and appear to reduce in length following increased periods of cyclic tensile strain. This area of tissue is specifically programmed to rupture at term and therefore similar mechanisms activated in the ZAM could be induced by overdistension and repetitive cyclic tensile strain leading to weakened fetal membrane and increasing the risk of PPRM.

Summarising the findings for the amniotic membrane response to repetitive cyclic tensile strain (**Figure 6.19**) using an *ex-vivo* bioreactor system, we report an increase in amniotic membrane sGAG synthesis with a reduction in collagen and elastin content; concurrent with an increase in MMP activity and PGE₂ release. Furthermore, we see a distinct difference in CAM and PAM amniotic membrane regions, indicating activation of pro-inflammatory induced ECM degradation in the cervical region marked by elevated sGAG synthesis and reduced collagen content whilst total MMP activity and PGE₂ release is also elevated, compared to placental amniotic membrane regions from the same donor.

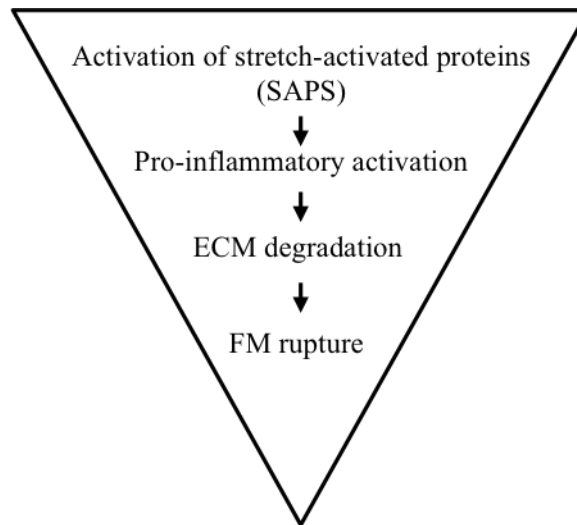


Figure 6.19: Putative flow of major events that could lead to fetal membrane rupture in response to stretch and activation of stretch-activated proteins (SAPs).

Previously, we have demonstrated increased Cx43 and COX-2 expression in response to repetitive cyclic tensile strain²⁸⁴. Here, we confirm activation of Cx43 in response to stretch, but also show activation of Akt (also known as protein kinase B). Akt is well known to be involved in a pathway called PI3K-Akt pathway, involving interaction with phosphatidylinositol 3-kinase (PI3K), and Akt activation is known to play a role in forming larger stable Cx43 gap junctional plaques²⁸⁵. The functional relationship between Akt and Cx43 has recently been evidenced in other cell types, where Cx43 gap junction channel opening during mechanical stimulation results from phosphorylation of Cx43 by Akt¹⁸². However, the presence and activation of Akt in amniotic membrane has not been reported, and here we show increased expression of Akt for the first time in addition to increased expression of Cx43.

After demonstrating an increase in Cx43 and Akt expression in response to repetitive cyclic tensile strain, associated with disruption of amniotic membrane matrix composition that could lead to FM rupture, studies were performed to investigate the inhibition of Cx43 and the PI3-Akt pathways as well as COX-2 mediated inflammatory pathways. For the first time we report on the inhibitory effects of Cx43asODNs and AKTi on AM matrix composition and production of inflammatory factors PGE₂ and MMP during free swelling and cyclic tensile strain conditions in an ex-vivo bioreactor model. Further experiments

involving the inhibitory effects of wortmannin and NS-398 on PI3-kinase and COX-2 pathways, respectively, are also reported for the first time. These data show that inhibition of PI3-Akt pathways dampens cyclic tensile strain induced softening involving increased GAG synthesis of the amniotic membrane in placental AM tissue, but is not statistically significant in cervical AM regions. Interestingly, it appears that inhibition of the PI3-Akt pathway during cyclic tensile strain decreases the amount of collagen degradation, which is concomitant with a reduction in MMP activity and PGE₂ release during tissue strain in both CAM and PAM tissue regions. However, there is no marked effect on elastin content when inhibiting the PI3-Akt pathways in both free-swelling and strained tissue. Furthermore, the inhibitory effects of Cx43asODNs on matrix composition and FM weakening factors reveal striking similarities to inhibition of PI3-kinase and Akt, leading to a reduction in collagen degradation reduced AM softening mediated by reduction in GAG content, and a reduction in MMP and PGE₂ release in both CAM and PAM regions during cyclic tensile strain. Selective inhibition of COX-2 using NS-398 led to the only changes observed in elastin content during cyclic tensile strain. COX-2 is rapidly expressed in response to pro-inflammatory molecules and is responsible for the first step in prostanoid synthesis, including PGE₂. By selectively inhibiting COX-2 we report a decrease in both collagen and elastin degradation, which returns close to basal levels, as well as reduced tissue softening mediated by enhanced GAG synthesis concurrent with a reduction in MMP/PGE₂ release to almost negligible levels in both tissue regions during free swelling and mechanically stimulated conditions.

Limited studies have attempted to delineate pathways associated with fetal membrane weakening that could provide avenues for future PPRM therapeutics. However, recent studies by Kumar *et al.*, have provided strong evidence towards the involvement of inflammation/infection and decidual bleeding/abruption pathways linking to PPRM^{5,286}. This group described an overlap between these two FM weakening pathways and by modelling inflammation using TNF- α and abruptio using thrombin, they show induction of Granulocyte-macrophage colony-stimulating factor (GM-CSF) on the choriodecidual side leading to FM weakening. Interestingly, they also demonstrate reduced fetal membrane weakening via inflammation and abruptio pathways by blocking the action of GM-CSF. Furthermore, targeting this pathway using progestogen has been explored with promising results, however the optimal progestogen is still under

investigation²⁸⁷. Importantly, the increase in GM-CSF is observed only on the choriodecidua side of the FM exposed to TNF- α or thrombin as and not the amnion side⁵.

Whilst the inflammation/infection and abruption pathways can lead to FM weakening involving increased production of GM-CSF in the choriodecidual side of the FM, we provide interesting FM weakening evidence specific the amnion only, in response to repetitive mechanical stimulation (summarised in **Figure 6.20**). Future studies involving GM-CSF and its activation in response to cyclic tensile strain could provide fruitful in understanding the relationship between the choriodecidual side and amnion side of the FM leading to overall weakening of the fetal membrane. The findings presented here provide the premise to explore stretch-activated pathways that could lead to FM weakening and rupture. Further optimisation of agents using dose-responsive studies are required and for longer time periods (up to 1 week). Combining these findings with rupture strength testing in the future will be beneficial in characterising how the inhibitory effects of such agents translates to changes in the physical properties of the FM. Overall, we provide a novel avenue of research in the development of therapeutics for preventing PPROM.

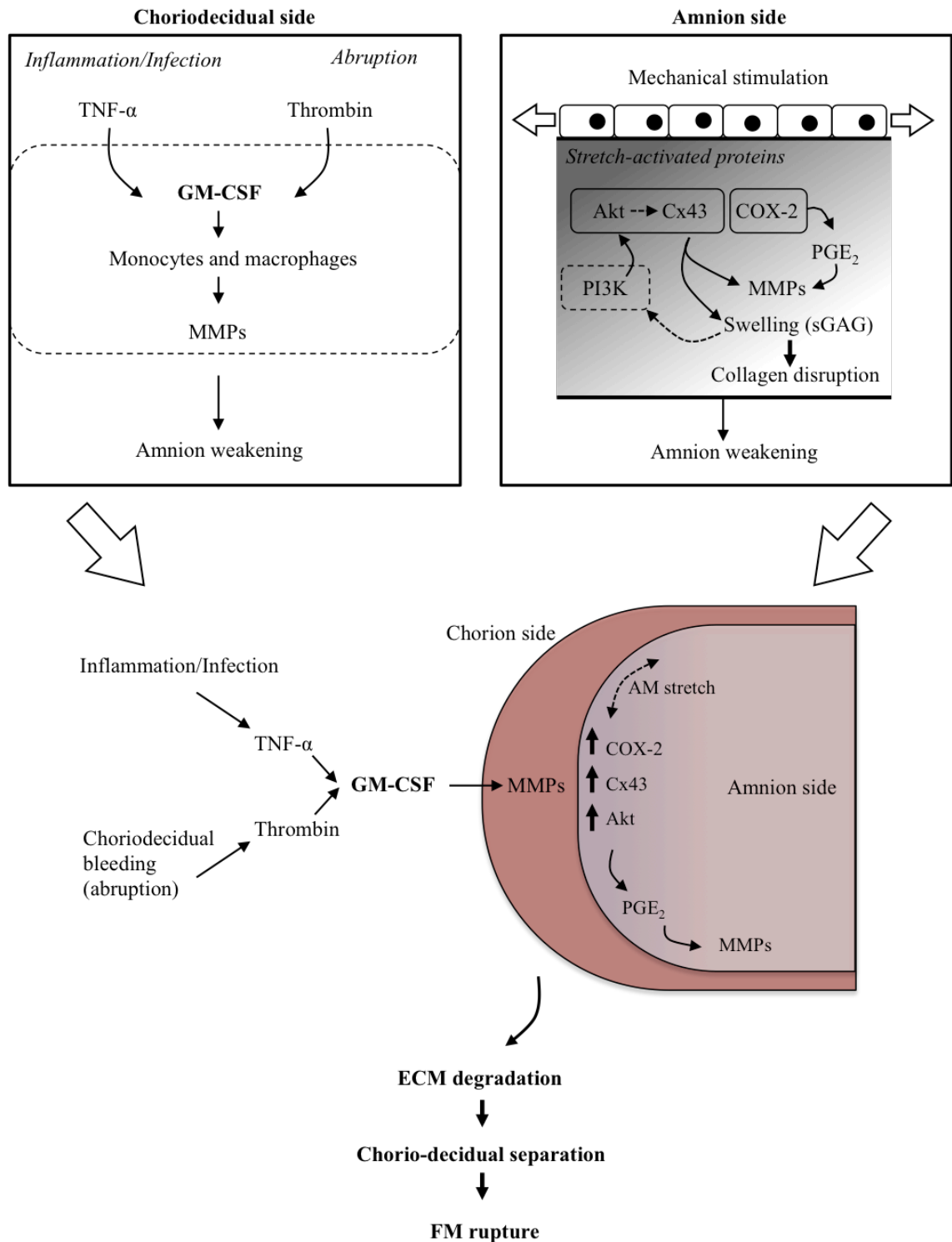


Figure 6.20: Synergy of events that lead to fetal membrane rupture following activation of stretch-activated inflammatory pathways. Previously identified fetal membrane weakening pathways described by Kumar et al., and development of stretch-activated fetal membrane weakening pathways could synergistically work towards ECM degradation, choriodecidual separation, and fetal membrane rupture. An improved understanding of these mechanisms could lead to the further development of therapeutics for preventing PPRM. GM-CSF pathway figure adapted from Kumar et al., (2014)⁵.

Chapter 7

Final Discussion and Future Prospects

Chapter 7: Final Discussion and Future Prospects

The development of approaches to repair AM would benefit PPRM patients who have ruptured their membranes at early gestational age. Prolonging the latency period from rupture of membranes to delivery is imperative for improving clinical outcome. Future research is needed to reduce preterm birth rates and alleviate the large socio-economic impact. Difficulty resides with the multifactorial etiology of PPRM, which complicates research efforts. The present study utilised a multidisciplinary approach to investigate the mechanotransduction mechanisms of FM weakening and potential strategies to repair the AM after fetoscopic surgery and artificial *in vitro* trauma.

7.1 Cx43 is overexpressed in AM after fetoscopic surgery and artificial *in vitro* trauma and delays cell migration and repair

Examination of fetoscopic defects revealed no spontaneous healing in all cases, leaving a wound with a diameter of ~3 mm, that exhibited thickened wound margins indicating tissue remodelling at the wound edge. These thickened wound edges have previously been reported in human FM¹⁶².

We demonstrate significantly enhanced Cx43 protein plaque formation that range in size from 0.1 to 1 μm , similar to that observed in skin tissue. Examination of Cx43 protein and gene expression shows significantly increased expression in the wound edge of the AM and limits the ability of mesenchymal cells to adopt a migratory phenotype. The overexpression of Cx43 may slow down cell migration as observed during normal cutaneous wound healing.

We observed polarisation of mesenchymal cells in the wound edge of the AM that was tangential to the highly aligned collagen fibres. These traits are only found at the wound margin, with control AM revealing rounded mesenchymal cells and randomly orientated collagen bundles. Interestingly, collagen SHG intensity increased towards the wound edge of the AM, and contributes to the thickened wound edge observed macroscopically in the AM. The polarised mesenchymal cells at the wound margin are indicative of the “purse-string” wound healing contraction mechanisms seen in embryonic wound healing and leads to the hypothesis that wound healing mechanisms

are present in human AM. However, the resulting trauma after fetoscopy surgery could leave a wound that is too large and beyond the limits of FM repair capabilities.

Development of an artificial *in vitro* trauma model enabled further investigation of AM trauma in FM collected from women at term pregnancies. When term AM are wounded *in vitro* (~0.8 mm diameter defects), we demonstrate striking similarities in Cx43 protein and gene expression when compared to preterm AM after fetoscopy surgery. We observed temporal changes in mesenchymal cell morphology and collagen fibre orientation such that these traits were tangential to the wound edge in the AM after 168 hours of trauma. The levels of Cx43 gene and protein expression were significantly enhanced in the wounded AM after 168 hours of trauma when compared to control AM. It is possible that the “purse-string” wound healing contraction mechanisms could potentially be undergoing an attempt to repair the damaged AM. However, even with smaller wounds (0.8 mm), term tissue in the present model was unable to mount a successful wound healing response after 7 days of culture. The levels of Cx43 expression in wounded AM compared to control AM may likely complicate wound healing dynamics and limit the migration of mesenchymal cells that is required for effective wound contraction and secretion of new granulation tissue. *In summary, the identification of a putative target Cx43 is an important key finding that if knocked down, could enhance human AM repair and prevent iatrogenic PPRM.*

7.2 Development of a new PA-based sealing strategy for human AM repair

We developed a novel PA-based strategy for sealing FM defects after artificial trauma. Combining solutions of human amniotic fluid with the FM induced self-assembly and formation of a 3D nanofibrous architecture that closely mimics the ECM of native FM. Indeed, self-assembling PA gels have previously provided promising results for healing diabetic wound and burn injuries^{17,18}. To our knowledge, this is the first study reported to induce spontaneous temporal self-assembly of FM in the presence of amniotic fluid.

The present study shows that the PAK3-AF system is optimal in sealing FM defects compared to PA systems that have too few (<3) or too many lysine residues (>3). For example, the PAK2-AF system formed a comparably weak gel that disintegrated upon manipulation, whereas the PAK4-AF system did not form a stable gel. The PAK3-AF system provides a promising starting point for PA-based rapidly self-assembling

biomaterial that is biocompatible and potentially could lead to the development of an injectable model utilised in a clinical setting. This would allow injection through a 10-Fr cannula, and optimal functionality within a wet environment.

7.3 Mechanotransduction mechanisms that induce AM weakening and production of inflammatory mediators leading to ECM damage

The potential therapeutic targets that could influence mechanotransduction and induce weakening in the AM leading to ECM damage were explored. AM explants were subjected to CTS in the presence and absence of chemical inhibitors that influence the Cx43 (Akti, Cx43 asODNs, PI3K), inflammatory (COX-2, PGE₂) and repair pathways (Collagen, GAGs, elastin). Mounting evidence links overdistension of the uterus to PPROM and preterm labour, mediated by inflammation, choriodecidual separation and FM rupture¹¹¹. Twin or higher order multiple pregnancies, polyhydramnios (over production of amniotic fluid), and uterine structural abnormalities have been associated with increased PPROM and preterm delivery incidence^{269,270,288}. With this in mind, a repetitive CTS regimen was used to investigate potential weakening of the AM over a 24 hour period in tissue collected from term pregnancies.

CTS significantly increased GAG synthesis, MMP activity and PGE₂ release in CAM and PAM compared to unstrained control membranes. This response was paralleled with an associated reduction in collagen (SHG and protein levels) and elastin content in CAM and PAM subjected to CTS when compared to unstrained control membranes. Previously, we have shown that CTS leads to increased COX-2 and Cx43 in AM²⁸⁴. Similar mechanotransduction mechanisms induced within the present *ex-vivo* FM explant bioreactor model could be activated following in utero stretch forces. In utero stretch forces stem from polyhydramnios, overdistension of the uterus, twin or higher order multiple pregnancies, or uterine structural abnormalities, and could cause AM strain and induce biochemical AM changes associated with increased expression of the stretch sensitive proteins Cx43/AKT, and pro-inflammatory enzyme COX-2. Inhibition of molecules using Cx43asODNs (specific targeting of Cx43), AKTi (specific targeting of AKT-1/2), NS398 (selective COX-2 inhibition), and WTM (non-specific targeting of PI3-kinases) perturb the effect of CTS-induced AM damage, and provide potential therapeutic targets for further research. Whilst it has been shown that PGE₂ and MMPs are key factors involved in parturition and FM rupture, the upstream mechanisms are

unknown. We have established a model that enhanced PGE₂ and MMPs in response to CTS. This system has provided a reproducible environment in which to study the effects of inhibiting potential targets and develop therapeutics for prevention of FM weakening mechanisms. Potential therapeutic options to prevent FM weakening have previously been investigated. By modelling TNF α -induced inflammation and bleeding through thrombin exposure, Kumar *et al.*, has identified Granulocyte-Macrophage Colony-Stimulating Factor (GM-CSF) as a potential target to prevent MMP induced damage originating from the choriodecidua side⁵. Recent investigations revealed that GM-CSF levels increase on the choriodecidua side but not in the outer amnion layer in response to TNF-alpha and thrombin⁵. This group was able to show that 3 progestogens (progesterone, 17-alpha hydroxyprogesterone caproate, and medroxyprogesterone acetate) can block production of GM-CSF, which is involved in the FM weakening pathway. 17-alpha hydroxyprogesterone caproate is available for clinical use during PPRM treatment. However, it has recently been reported that this progestogens is not optimal in the inhibition of FM weakening involving GM-CSF activation²⁸⁷. Whilst these reports show promise in targeting choriodecidual factors that lead to FM weakening, this chapter provides additional therapeutic targets for further investigation regarding FM weakening specific to the AM.

7.4 Implications and future research

7.4.1 Identification of targets for mechanotransduction and FM weakening

Future research will be performed to explore FM weakening mechanisms in more detail. Following on from the mechanotransduction mechanisms defined in this thesis, key areas of future research include the investigation of our CTS loading conditions on preterm tissue. Whilst we have focused investigations on term AM, naturally the next step would be to complement these studies with tissue obtained from preterm deliveries, including samples obtained from women with and without preterm contractions. This would inform on whether the mechanotransduction mechanisms observed in term tissue are replicated in preterm tissue that has not been exposed to labour contractions. Further investigations of preterm tissue that has been exposed to preterm labour contractions would complement these studies and help to define whether the mechanisms elucidated within our *ex-vivo* FM explant bioreactor correspond to PPRM patients.

In obtaining these preterm samples, the next steps would be to investigate expression of Cx43. We have shown that Cx43 is a stretch-sensitive protein and its activation is linked with AM weakening mechanisms. It is likely that there are gestational age dependent differences in expression of Cx43 and therefore future research would develop a Cx43 profile throughout gestation. Furthermore, differences in Cx43 expression will be investigated in samples obtained from PPRM patients with preterm tissue from patients who have not ruptured their membranes. This would make an important comparison and help to identify whether Cx43 expression is abnormally expressed in PPRM tissue at sites of rupture. Due to the many risk factors associated with PPRM, it will be critical to develop an extensive database where comparisons of Cx43 levels can be compared depending on race/ethnicity, maternal age, parity, previous preterm birth history, and medical condition, all of which could influence FM weakening and lead to PPRM. In the future, this could give a strong indication on whether Cx43 levels vary in patients with greater risk of PPRM.

Furthermore, the relationship between Cx43 and AKT will be explored further. Whilst we cannot claim in this thesis that Cx43 and AKT act synergistically or through separate CTS-induced AM weakening mechanisms, the evidence provided in this thesis leads to further research questions. The next steps would be to further define their connection, if any. Indeed, research in other cell types suggests a strong link between

AKT and Cx43. For example, mechanical stress in osteocytes leads to Cx43 hemichannel opening, required for remodelling processes¹⁸². Recent evidence suggests Cx43 is phosphorylated by AKT, which enhances their interaction causing increased hemichannel opening¹⁸². To our knowledge, AKT phosphorylation of Cx43 has not been investigated in the AM. This provides an exciting opportunity to explore the hypothesis that mechanisms leading to hemichannel opening could lead to the initiation of FM weakening. Further research is required to identify whether Cx43 is phosphorylated by AKT in AM following CTS. This could help to improve our understanding on AM weakening mechanotransduction mechanisms following CTS, and postulate a potential mechanism (**Figure 7.2**). This will provide a new area for development of therapeutics that prevent AM weakening mechanotransduction mechanisms.

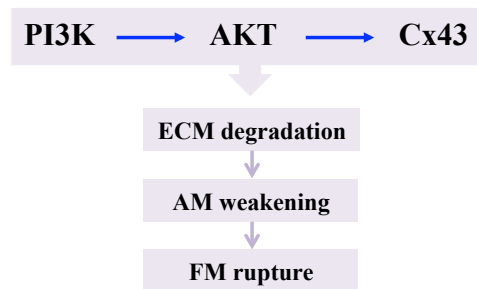


Figure 7.2: Potential mechanotransduction mechanism leading to FM rupture. Future work will investigate the relationship between AKT and Cx43.

To investigate this we will conduct further functional pharmacological studies in the AM following CTS. Important questions will include whether AKT directly phosphorylates Cx43 at a known phosphorylation site (S373). Previous research has shown that Cx43 can be phosphorylated by AKT at the S373 site²⁸⁹. This then leads to reduced interaction with the tight junction protein, Zonula occludens-1 (ZO-1) suggesting activation of a “molecular switch” which leads to increased Cx43 plaque size and communication²⁸⁹.

To complement these studies, mechanical strength testing will also be an important addition to confirm whether the biochemical changes induced by inhibiting potential therapeutic targets correlates to changes in mechanical strength in both preterm and term AM. Rupture strength (N) will be tested following culture of AM with therapeutic agents within the *ex-vivo* FM explant bioreactor model. To do this AM will be removed from the *ex-vivo* bioreactor after CTS cultured with or without therapeutic agents. Both the AM from close to the cervix and placenta will be mechanically tested

after cultures as these two regions have been shown to have different rupture strengths in term FM³⁰. The cervical fetal membrane is shown to have a rupture strength of around 5 N whilst FM distal from the cervical region has a rupture strength of 8 N. Importantly, AM samples from PPRM patients will be cultured using therapeutic agents and then mechanically tested to identify changes in rupture strength that may occur as a result of inhibiting AM weakening mechanisms. To perform mechanical testing the MTS Bionix100 (MN, USA) mechanical testing system with a 50N cell load will be used. This will allow strain to failure (rupture strength), tangent modulus, and ultimate tensile stress to be identified. Ultimately this work is required to establish whether culturing with therapeutic agents can impact AM strength to help develop therapies to prevent and treat PPRM.

7.4.2 Pharmacological strategies for the induction of healing mechanisms and repair of FM defects

Future research will aim to explore ways to restore the normal functionality of AM. The induction of healing will be investigated by selective targeting of Cx43. PPRM incidence increases following fetal surgery, therefore as we have identified high expression of Cx43 in AM after trauma (both preterm and term), the next steps would be to develop strategies to heal and repair AM by targeting this protein. By using Cx43asODNs we have identified that Cx43 knockdown perturbs the effect of CTS-induced ECM damage, however, this thesis does not investigate the effect of Cx43asODN application to AM after trauma. Therefore, future work will investigate the modulation of Cx43 on AM healing. To investigate the effect of Cx43asODNs on AM healing, we will use Pluronic-F127 gel as a delivery vehicle. Whilst this is not ideal in a clinical environment, Pluronic gel will allow the slow release of Cx43asODNs to the AM wound (over a period of 24 hours) in order to examine whether AM healing is enhanced. Pluronic gel has been used as a delivery vehicle for slow release of Cx43asODNs before, and has successfully enhanced wound healing in rat diabetic skin wound models by promoting cell migration¹²⁶. These promising results in other chronic wounds provide rationale to investigate Cx43 targeting in AM defects.

To examine Cx43 modulation on AM healing, future studies will initially use a variety of models to reflect the physiological environment (**Figure 7.3**). Initially, our artificial in vitro FM explant trauma model. Leading on from this, the development of a FM inflation

model would further test repair extent by comparing burst pressures with healed and non-healed AM. Finally, AM healing could be examined within the ex-vivo CTS bioreactor model, where delivery of Cx43asODNs can be introduced through 21G needle using pluronic gel or another adhesive sealant as a delivery vehicle.

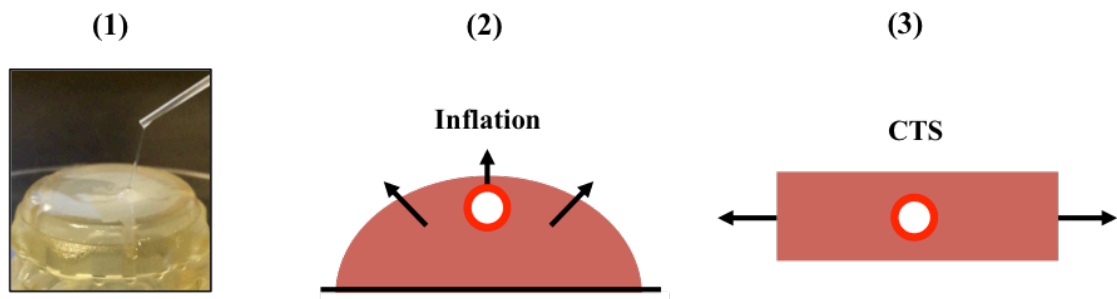


Figure 7.3: Models that will be used in future research to investigate repair of the AM. Initially, experiments will be conducted using the artificial in vitro trauma model (1), then progress to an inflation device (2) and ex-vivo bioreactor model (3).

Another option which may be more appropriate in a clinical environment is the use of Cx43asODN coated collagen scaffolds²⁹⁰. Recently, these have been developed to promote healing of chronic wounds and show an 85% downregulation of Cx43 at the wound edge in rat wounds²⁹⁰. Furthermore, they show superior release over Pluronic F127 gel, by providing continuous release of Cx43asODNs over a period of 7 days. Cx43asODN coated collagen scaffolds is an area of research that will be explored for healing of the AM. Regarding iatrogenic defects following fetal surgery, scaffolds could be implanted through a laparoscope and surgically inserted into a fetoscopic defect.

Successful targeting of Cx43 at the wound edge in AM could promote AM repair by accelerating cell migration by reducing cell adhesion and proliferation¹²⁸. Knockdown of Cx43 enhances Rac-1 and RhoA GTPase activation, which is associated with changes in cytoskeletal proteins, specifically leading to increased lamellipodial protrusions. By decreasing levels of Cx43 at the wound edge of the AM epithelial and mesenchymal cells, future research will examine whether AM wounds can overcome their limited healing capacity.

7.4.3 Strategies for sealing the AM using tissue engineering models

Fetal membrane repair is a new research area for tissue engineering approaches. The repair of numerous other tissues have benefited from tissue engineering approaches, which usually adopt a variety of scaffold materials with or without the presence of cells. As discussed previously, sealing of FM defects could be combined with a pharmacological approach by coating collagen scaffolds with Cx43asODNs²⁹⁰. In a clinical environment these could be introduced through a laparoscope following fetoscopic surgery and surgically placed in the FM defect. Whilst future research will examine the potential of this approach, previous research regarding collagen plugs for FM sealing has had limited success, and do not reduce the rate of PPROM²¹⁰. Future investigations will aim to develop a biomaterial that can be combined with bioactive functionality to enhance FM repair.

In this thesis we explored the use of self-assembling PAs that are injectable in solution and form a scaffold upon contact with a physiological solution (i.e. amniotic fluid). Whilst the PA solution ultimately forms the scaffold material, future research will explore the potential of a PA-based gel and cell mixture to stimulate tissue repair mechanisms. Furthermore, future work will aim to develop a PA that shows increased adhesiveness and functions in a wet environment. In addition, conjugation of Cx43 mimetic peptides or silencing technologies to PA molecules could be explored to further enhance repair capacity by promoting migration of native mesenchymal cells found at the AM wound edge. Display of bioactive epitopes on PA molecules is an exciting avenue of research that can be exploited to further enhance FM wound healing capacity.

In the future, predictive PPROM models could help to develop personalised treatment following fetal surgery. For example, a recent study identified that the likelihood of PPROM increases with elevated lactic acid and MMP-8 in the amniotic fluid measured during fetal surgery²⁹¹. The present study provides an improved understanding on the absence of AM healing, and the mechanotransduction mechanisms behind AM weakening. Furthermore, a novel FM sealing strategy is explored for the prevention of PPROM after fetal surgery.

List of publications

Barrett, D. W.; David, A. L.; Thrasivoulou, C.; Mata, A.; Becker, D. L.; Engels, A. C.; Deprest, J. A.; Chowdhury, T. T. *Connexin 43 is overexpressed in human fetal membrane defects after fetoscopic surgery*. Prenatal Diagnosis **2016**, 36 (10), 942-952.

- Editor's choice for original article in October 2016.

Barrett, D. W.; Kethees, A.; Thrasivoulou, C.; Mata, A.; Virasami, A.; Sebire, N. J.; Engels, A. C.; Deprest, J. A.; Becker, D. L.; David, A. L.; Chowdhury, T. T. *Trauma induces overexpression of Cx43 in human fetal membrane defects*. Prenatal Diagnosis **2017**, 37 (9), 899-906.

Engels, A. C.; Joyeux, L.; Van der Merwe, J.; Jimenez, J.; Prapanus, S.; **Barrett, D. W.**; Connon, C.; Chowdhury, T. T.; David, A. L.; Deprest, J. *Tissuepatch is biocompatible and seals iatrogenic membrane defects in a rabbit model*. Prenatal Diagnosis **2017** (Accepted article).

National and international conference contributions

Oral presentations

Barrett, D. W.; David, A. L.; Thrasivoulou, C.; Mata, A.; Becker, D. L.; Engels, A. C.; Deprest, J. A.; Chowdhury, T. T. *Overexpression of Cx43 in human fetal membrane defects following fetal surgery*. Institute for Women's Health. UCL, London

Date: Tuesday 14th June 2016.

Barrett, D. W.; David, A. L.; Thrasivoulou, C.; Mata, A.; Becker, D. L.; Engels, A. C.; Deprest, J. A.; Chowdhury, T. T. *Connexin 43 is overexpressed in human fetal membrane defects after fetoscopic surgery*. International Society for Prenatal Diagnosis and Therapy. Berlin, Germany.

Date: Monday 11th July 2016.

Barrett, D. W.; Kethees, A.; Thrasivoulou, C.; Mata, A.; Virasami, A.; Sebire, N. J.; Engels, A. C.; Deprest, J. A.; Becker, D. L.; David, A. L.; Chowdhury, T. T. *Trauma induces overexpression of Cx43 in human fetal membrane defects*. International Society for Prenatal Diagnosis and Therapy. San Diego, USA.

Date: Monday 10th July 2017.

Barrett, D. W.; Mata, A.; David, A. L.; Chowdhury, T. T. *Understanding the mechanisms behind fetal membrane weakening after repetitive cyclic tensile strain*. The Royal College of Obstetricians & Gynecologists, London.

Date: Friday 9th February 2018.

Poster presentations

Institute for Bioengineering Launch Event.

Bioengineering therapies for healing the human fetal membrane. Queen Mary University of London, School of Engineering and Materials Science.

Date: Thursday 8th October 2015.

The Industrial Liason Forum.

Bioengineering therapies for healing the human fetal membrane. Queen Mary University of London, School of Engineering and Materials Science.

Date: Thursday 29th October 2015.

The Industrial Liason Forum.

Connexin 43 is overexpressed in human amniotic membrane defects following fetal surgery. Queen Mary University of London, School of Engineering and Materials Science.

Date: Friday 11th November 2016.

Rosetrees Trust PhD symposium.

Connexin 43 is overexpressed in human amniotic membrane defects following fetal surgery. Blizard Institute, Queen Mary University of London.

Date: Wednesday 21st September 2016.

Rosetrees Trust 30th Anniversary Symposium.

Trauma induces overexpression of Cx43 in human fetal membrane defects. UCL Great Ormond Street Institute of Child Health.

Date: Thursday 14th September 2017.

Barrett, D. W.; Mata, A.; David, A. L.; Chowdhury, T. T. *Understanding the mechanisms behind fetal membrane weakening after repetitive cyclic tensile strain.*

The Royal College of Obstetricians & Gynecologists, London.

Date: Thursday 8th February 2018.

List of Awards

Young Investigator Award

Winner of the Malcolm-Ferguson Smith Young Investigator 2017 award presented by the Prenatal Diagnosis journal for the article published on “Connexin 43 is overexpressed in human fetal membrane defects after fetoscopic surgery”. Received \$1000 for travel expenses and invitation to present research at the ISPD conference in San Diego 2017. *Received Monday 10th July 2017.*

Research Project Grant (3 year PDRA)

Provided pilot data for research grant award (£148,863) – SPARKS and GOSH children’s medical research charity grant application accepted for new project on “Innovative bioengineering approach to heal the fetal membrane for iatrogenic PPROM prevention” *Accepted August 2017.*

Oral Presentation Award

2nd place for oral presentation in the annual Institute for Women’s Health (UCL) conference. *Received Tuesday 14th June 2016.*

Poster Presentation Award

1st place in the Rosetrees Trust PhD symposium poster presentation. *Received Wednesday 21st September 2016.*

Scientific photography award

- 2nd place in SEMS inspiring research photo competition. *December 2015.*
- 3rd place in QMUL summer graduate festival 2016 research photography competition. *July 2016.*

Travel Grant Awards

- Awarded two separate travel awards (£500) for conference travel expenses from the British Society for Cell Biology.
Received June 2016 and June 2017.
- Awarded \$1000 from Prenatal Diagnosis journal after receiving Malcolm-Ferguson Smith Young Investigator award.
Received July 2017.
- Queen Mary Postgraduate Research Fund (QMPGRF): Total value: £587.
Received June 2017.

Other activities

- Completion of “Introduction to good clinical practice” e-learning course.
Completed Sunday 18th May 2014.
- Completion of Research Governance Framework course.
Completed Thursday 22nd January 2015.
- Completion of 210 hours of researcher development activities for the Queen Mary Diploma of Researcher Development (Q-Dip) award.
October 2017.

Certificate of Completion

David Barrett

has completed

Introduction to Good Clinical Practice (GCP) e-learning course

**A practical guide to ethical and scientific quality
standards in clinical research**

on 18 May 2014

Modules completed

Introduction to Research in the NHS
Good Clinical Practice and Standards in Research
Study Set-up and Responsibilities
The Process of Informed Consent
Data Collection and Documentation
Safety Reporting
Summary



References

1. Buerzle W, Haller CM, Jabareen M, et al. Multiaxial mechanical behavior of human fetal membranes and its relationship to microstructure. *Biomechanics and modeling in mechanobiology* 2013;12:747-62.
2. Sozen B, Can A, Demir N. Cell fate regulation during preimplantation development: a view of adhesion-linked molecular interactions. *Developmental biology* 2014;395:73-83.
3. Mauri A, Perrini M, Mateos JM, et al. Second harmonic generation microscopy of fetal membranes under deformation: normal and altered morphology. *Placenta* 2013;34:1020-6.
4. Capito RM, Azevedo HS, Velichko YS, Mata A, Stupp SI. Self-assembly of large and small molecules into hierarchically ordered sacs and membranes. *Science (New York, NY)* 2008;319:1812-6.
5. Kumar D, Moore RM, Nash A, et al. Decidual GM-CSF is a critical common intermediate necessary for thrombin and TNF induced in-vitro fetal membrane weakening. *Placenta* 2014;35:1049-56.
6. Pansky B. *Review of Medical Embryology*: McGraw-Hill; 1982.
7. Marieb EN, Hoehn K. *Human anatomy & physiology*. 9th ed ed: Boston: Pearson; 2013.
8. Ferreira DS, Marques AP, Reis RL, Azevedo HS. Hyaluronan and self-assembling peptides as building blocks to reconstruct the extracellular environment in skin tissue. *Biomaterials Science* 2013;1:952-64.
9. Maradny EE, Kanayama N, Halim A, Maehara K, Terao T. Stretching of fetal membranes increases the concentration of interleukin-8 and collagenase activity. *American journal of obstetrics and gynecology* 1996;174:843-9.
10. Verheule S, Kaese S. Connexin diversity in the heart: insights from transgenic mouse models. *Frontiers in pharmacology* 2013;4:81.

11. Hendricks MP, Sato K, Palmer LC, Stupp SI. Supramolecular Assembly of Peptide Amphiphiles. *Accounts of chemical research* 2017;50:2440-8.
12. Parry S, Strauss JF, 3rd. Premature rupture of the fetal membranes. *The New England journal of medicine* 1998;338:663-70.
13. Guler MO, Hsu L, Soukasene S, Harrington DA, Hulvat JF, Stupp SI. Presentation of RGDS Epitopes on Self-Assembled Nanofibers of Branched Peptide Amphiphiles. *Biomacromolecules* 2006;7:1855-63.
14. Hosseinkhani H, Hosseinkhani M, Khademhosseini A. Tissue Regeneration through Self-Assembled Peptide Amphiphile Nanofibers 2006.
15. Inostroza-Brito KE, Collin E, Siton-Mendelson O, et al. Co-assembly, spatiotemporal control and morphogenesis of a hybrid protein-peptide system. *Nature chemistry* 2015;7:897-904.
16. Oyen ML, Cook RF, Calvin SE. Mechanical failure of human fetal membrane tissues. *Journal of materials science Materials in medicine* 2004;15:651-8.
17. Senturk B, Demircan BM, Ozkan AD, et al. Diabetic wound regeneration using heparin-mimetic peptide amphiphile gel in db/db mice. *Biomater Sci* 2017;5:1293-303.
18. Yergoz F, Hastar N, Cimenci CE, et al. Heparin mimetic peptide nanofiber gel promotes regeneration of full thickness burn injury. *Biomaterials* 2017;134:117-27.
19. Bourne GL. The microscopic anatomy of the human amnion and chorion. *American journal of obstetrics and gynecology* 1960;79:1070-3.
20. Bourne G. The foetal membranes. A review of the anatomy of normal amnion and chorion and some aspects of their function. *Postgraduate medical journal* 1962;38:193-201.
21. Bourne GL. The anatomy of the human amnion and chorion. *Proceedings of the Royal Society of Medicine* 1966;59:1127-8.
22. Tabatabaei M, Mosaffa N, Nikoo S, et al. Isolation and partial characterization of human amniotic epithelial cells: the effect of trypsin. *Avicenna journal of medical biotechnology* 2014;6:10-20.

23. Gupta A, Kedige SD, Jain K. Amnion and Chorion Membranes: Potential Stem Cell Reservoir with Wide Applications in Periodontics. *International journal of biomaterials* 2015;2015:274082.
24. Lei J, Priddy LB, Lim JJ, Masee M, Koob TJ. Identification of Extracellular Matrix Components and Biological Factors in Micronized Dehydrated Human Amnion/Chorion Membrane. *Advances in wound care* 2017;6:43-53.
25. Gulamhusein AP, Beck F. Development and structure of the extra-embryonic membranes of the ferret. A light microscopic and ultrastructural study. *Journal of anatomy* 1975;120:349-65.
26. Avila C, Santorelli J, Mathai J, et al. Anatomy of the fetal membranes using optical coherence tomography: part 1. *Placenta* 2014;35:1065-9.
27. Severi FM, Bocchi C, Voltolini C, Borges LE, Florio P, Petraglia F. Thickness of fetal membranes: a possible ultrasound marker for preterm delivery. *Ultrasound in obstetrics & gynecology : the official journal of the International Society of Ultrasound in Obstetrics and Gynecology* 2008;32:205-9.
28. Benirschke K, Burton G, Baergen R. *Anatomy and Pathology of the Placental Membranes. Pathology of the Human Placenta. Sixth Edition* ed. New York, NY: Springer New York; 2012:321-79.
29. McLaren J, Malak TM, Bell SC. Structural characteristics of term human fetal membranes prior to labour: identification of an area of altered morphology overlying the cervix. *Human reproduction (Oxford, England)* 1999;14:237-41.
30. El Khwad M, Stetzer B, Moore RM, et al. Term human fetal membranes have a weak zone overlying the lower uterine pole and cervix before onset of labor. *Biology of reproduction* 2005;72:720-6.
31. Bou-Resli MN, Al-Zaid NS, Ibrahim ME. Full-term and prematurely ruptured fetal membranes. An ultrastructural study. *Cell and tissue research* 1981;220:263-78.
32. Malak TM, Bell SC. Structural characteristics of term human fetal membranes: a novel zone of extreme morphological alteration within the rupture site. *British journal of obstetrics and gynaecology* 1994;101:375-86.

33. Menon R, Fortunato SJ. The role of matrix degrading enzymes and apoptosis in rupture of membranes. *Journal of the Society for Gynecologic Investigation* 2004;11:427-37.
34. El Khwad M, Pandey V, Stetzer B, et al. Fetal membranes from term vaginal deliveries have a zone of weakness exhibiting characteristics of apoptosis and remodeling. *Journal of the Society for Gynecologic Investigation* 2006;13:191-5.
35. Ibrahim ME, Bou-Resli MN, Al-Zaid NS, Bishay LF. Intact fetal membranes. Morphological predisposal to rupture. *Acta obstetrica et gynecologica Scandinavica* 1983;62:481-5.
36. Verbruggen SW, Oyen ML, Phillips AT, Nowlan NC. Function and failure of the fetal membrane: Modelling the mechanics of the chorion and amnion. *PloS one* 2017;12:e0171588.
37. Nunes V, Cross J, Speich JE, Morgan DR, Strauss JF, 3rd, Ramus RM. Fetal membrane imaging and the prediction of preterm birth: a systematic review, current issues, and future directions. *BMC pregnancy and childbirth* 2016;16:387.
38. Malak TM, Bell SC. Distribution of fibrillin-containing microfibrils and elastin in human fetal membranes: a novel molecular basis for membrane elasticity. *American journal of obstetrics and gynecology* 1994;171:195-205.
39. Hieber AD, Corcino D, Motosue J, et al. Detection of elastin in the human fetal membranes: proposed molecular basis for elasticity. *Placenta* 1997;18:301-12.
40. Kanayama N, Terao T, Kawashima Y, Horiuchi K, Fujimoto D. Collagen types in normal and prematurely ruptured amniotic membranes. *American journal of obstetrics and gynecology* 1985;153:899-903.
41. Leppert PC, Yu SY. Three-dimensional structures of uterine elastic fibers: scanning electron microscopic studies. *Connective tissue research* 1991;27:15-31.
42. Schmidt W. The amniotic fluid compartment: the fetal habitat. *Advances in anatomy, embryology, and cell biology* 1992;127:1-100.

43. Sutton L, Mason DY, Redman CW. HLA-DR positive cells in the human placenta. *Immunology* 1983;49:103-12.
44. Bulmer JN, Johnson PM. Macrophage populations in the human placenta and amniochorion. *Clinical and experimental immunology* 1984;57:393-403.
45. Aplin JD, Campbell S, Allen TD. The extracellular matrix of human amniotic epithelium: ultrastructure, composition and deposition. *Journal of cell science* 1985;79:119-36.
46. McParland PC, Taylor DJ, Bell SC. Myofibroblast differentiation in the connective tissues of the amnion and chorion of term human fetal membranes-implications for fetal membrane rupture and labour. *Placenta* 2000;21:44-53.
47. Koo BK, Park IY, Kim J, et al. Isolation and characterization of chorionic mesenchymal stromal cells from human full term placenta. *Journal of Korean medical science* 2012;27:857-63.
48. Malak TM, Sizmur F, Bell SC, Taylor DJ. Fetal fibronectin in cervicovaginal secretions as a predictor of preterm birth. *British journal of obstetrics and gynaecology* 1996;103:648-53.
49. Nehemiah JL, Schnitzer JA, Schulman H, Novikoff AB. Human chorionic trophoblasts, decidual cells, and macrophages: a histochemical and electron microscopic study. *American journal of obstetrics and gynecology* 1981;140:261-8.
50. Yoshida Y, Manabe Y. Different characteristics of amniotic and cervical collagenous tissue during pregnancy and delivery: a morphologic study. *American journal of obstetrics and gynecology* 1990;162:190-3.
51. Malak TM, Ockleford CD, Bell SC, Dagleish R, Bright N, Macvicar J. Confocal immunofluorescence localization of collagen types I, III, IV, V and VI and their ultrastructural organization in term human fetal membranes. *Placenta* 1993;14:385-406.
52. McParland PC, Taylor DJ, Bell SC. Mapping of zones of altered morphology and chorionic connective tissue cellular phenotype in human fetal membranes (amniochorion and decidua) overlying the lower uterine pole and cervix before labor at term. *American journal of obstetrics and gynecology* 2003;189:1481-8.

53. McLaren J, Taylor DJ, Bell SC. Increased concentration of pro-matrix metalloproteinase 9 in term fetal membranes overlying the cervix before labor: implications for membrane remodeling and rupture. *American journal of obstetrics and gynecology* 2000;182:409-16.
54. Fortner KB, Grotegut CA, Ransom CE, et al. Bacteria localization and chorion thinning among preterm premature rupture of membranes. *PloS one* 2014;9:e83338.
55. McLaren J, Taylor DJ, Bell SC. Prostaglandin E(2)-dependent production of latent matrix metalloproteinase-9 in cultures of human fetal membranes. *Molecular human reproduction* 2000;6:1033-40.
56. McLaren J, Taylor DJ, Bell SC. Increased incidence of apoptosis in non-labour-affected cytotrophoblast cells in term fetal membranes overlying the cervix. *Human reproduction (Oxford, England)* 1999;14:2895-900.
57. Lei H, Vadillo-Ortega F, Paavola LG, Strauss JF, 3rd. 92-kDa gelatinase (matrix metalloproteinase-9) is induced in rat amnion immediately prior to parturition. *Biology of reproduction* 1995;53:339-44.
58. Lei H, Furth EE, Kalluri R, et al. A program of cell death and extracellular matrix degradation is activated in the amnion before the onset of labor. *The Journal of clinical investigation* 1996;98:1971-8.
59. Lei H, Kalluri R, Furth EE, Baker AH, Strauss JF, 3rd. Rat amnion type IV collagen composition and metabolism: implications for membrane breakdown. *Biology of reproduction* 1999;60:176-82.
60. Meinert M, Malmstrom A, Tufvesson E, et al. Labour induces increased concentrations of biglycan and hyaluronan in human fetal membranes. *Placenta* 2007;28:482-6.
61. Reti NG, Lappas M, Riley C, et al. Why do membranes rupture at term? Evidence of increased cellular apoptosis in the supracervical fetal membranes. *American journal of obstetrics and gynecology* 2007;196:484.e1-10.

62. Lappas M, Permezel M, Georgiou HM, Rice GE. Nuclear factor kappa B regulation of proinflammatory cytokines in human gestational tissues in vitro. *Biology of reproduction* 2002;67:668-73.
63. Lappas M, Odumetse TL, Riley C, et al. Pre-labour fetal membranes overlying the cervix display alterations in inflammation and NF-kappaB signalling pathways. *Placenta* 2008;29:995-1002.
64. Lappas M, Riley C, Lim R, et al. MAPK and AP-1 proteins are increased in term pre-labour fetal membranes overlying the cervix: regulation of enzymes involved in the degradation of fetal membranes. *Placenta* 2011;32:1016-25.
65. Ekoff M, Kaufmann T, Engstrom M, et al. The BH3-only protein Puma plays an essential role in cytokine deprivation induced apoptosis of mast cells. *Blood* 2007;110:3209-17.
66. Skurk C, Maatz H, Kim HS, et al. The Akt-regulated forkhead transcription factor FOXO3a controls endothelial cell viability through modulation of the caspase-8 inhibitor FLIP. *The Journal of biological chemistry* 2004;279:1513-25.
67. Lappas M, Riley C, Rice GE, Permezel M. Increased expression of ac-FoxO1 protein in prelabor fetal membranes overlying the cervix: possible role in human fetal membrane rupture. *Reproductive sciences (Thousand Oaks, Calif)* 2009;16:635-41.
68. Lappas M, Lim R, Riley C, Menon R, Permezel M. Expression and localisation of FoxO3 and FoxO4 in human placenta and fetal membranes. *Placenta* 2010;31:1043-50.
69. Chai M, Barker G, Menon R, Lappas M. Increased oxidative stress in human fetal membranes overlying the cervix from term non-labouring and post labour deliveries. *Placenta* 2012;33:604-10.
70. Oxlund H, Helmig R, Halaburt JT, Uldbjerg N. Biomechanical analysis of human chorioamniotic membranes. *European journal of obstetrics, gynecology, and reproductive biology* 1990;34:247-55.
71. Lavery JP, Miller CE. The viscoelastic nature of chorioamniotic membranes. *Obstetrics and gynecology* 1977;50:467-72.

72. Manabe Y, Himeno N, Fukumoto M. Tensile strength and collagen content of amniotic membrane do not change after the second trimester or during delivery. *Obstetrics and gynecology* 1991;78:24-7.
73. Schober EA, Kusy RP, Savitz DA. Resistance of fetal membranes to concentrated force applications and reconciliation of puncture and burst testing. *Annals of biomedical engineering* 1994;22:540-8.
74. Pressman EK, Cavanaugh JL, Woods JR. Physical properties of the chorioamnion throughout gestation. *American journal of obstetrics and gynecology* 2002;187:672-5.
75. Lavery JP, Miller CE, Knight RD. The effect of labor on the rheologic response of chorioamniotic membranes. *Obstetrics and gynecology* 1982;60:87-92.
76. Klima G, Zerlauth B, Richter J, Schmidt W. [The microtexture of amnion and chorion connective tissue]. *Anatomischer Anzeiger* 1989;168:395-400.
77. Polishuk WZ, Kohane S, Peranio A. The physical properties of fetal membranes. *Obstetrics and gynecology* 1962;20:204-10.
78. Polishuk WZ, Kohane S, Hadar A. FETAL WEIGHT AND MEMBRANE TENSILE STRENGTH. *American journal of obstetrics and gynecology* 1964;88:247-50.
79. Laufer A, Polishuk WZ, Boxer J, Ganzfried R. Studies of amniotic membranes. *Journal of reproduction and fertility* 1966;12:99-105.
80. Maclachlan TB. A METHOD FOR THE INVESTIGATION OF THE STRENGTH OF THE FETAL MEMBRANES. *American journal of obstetrics and gynecology* 1965;91:309-13.
81. Lavery JP, Miller CE, Johns P. Effect of meconium on the strength of chorioamniotic membranes. *Obstetrics and gynecology* 1980;56:711-5.
82. Kumar D, Moore RM, Mercer BM, Mansour JM, Redline RW, Moore JJ. The physiology of fetal membrane weakening and rupture: Insights gained from the determination of physical properties revisited. *Placenta* 2016;42:59-73.
83. Lavery JP, Miller CE. Deformation and creep in the human chorioamniotic sac. *American journal of obstetrics and gynecology* 1979;134:366-75.

84. Oyen ML, Calvin SE, Landers DV. Premature rupture of the fetal membranes: is the amnion the major determinant? *American journal of obstetrics and gynecology* 2006;195:510-5.
85. Chua WK, Oyen ML. Do we know the strength of the chorioamnion? A critical review and analysis. *European journal of obstetrics, gynecology, and reproductive biology* 2009;144 Suppl 1:S128-33.
86. Chowdhury B, David AL, Thrasivoulou C, Becker DL, Bader DL, Chowdhury TT. Tensile strain increased COX-2 expression and PGE release leading to weakening of the human amniotic membrane. *Placenta* 2014;35:1057-64.
87. Blencowe H, Cousens S, Chou D, et al. Born too soon: the global epidemiology of 15 million preterm births. *Reproductive health* 2013;10 Suppl 1:S2.
88. Behrman RE, Butler AS. The National Academies Collection: Reports funded by National Institutes of Health. In: Behrman RE, Butler AS, eds. *Preterm Birth: Causes, Consequences, and Prevention*. Washington (DC): National Academies Press (US) National Academy of Sciences; 2007.
89. Ou CW, Orsino A, Lye SJ. Expression of connexin-43 and connexin-26 in the rat myometrium during pregnancy and labor is differentially regulated by mechanical and hormonal signals. *Endocrinology* 1997;138:5398-407.
90. Parry LJ, Bathgate RA. The role of oxytocin and regulation of uterine oxytocin receptors in pregnant marsupials. *Experimental physiology* 2000;85 Spec No:91s-9s.
91. Kendal-Wright CE. Stretching, mechanotransduction, and proinflammatory cytokines in the fetal membranes. *Reproductive sciences (Thousand Oaks, Calif)* 2007;14:35-41.
92. Loudon JA, Sooranna SR, Bennett PR, Johnson MR. Mechanical stretch of human uterine smooth muscle cells increases IL-8 mRNA expression and peptide synthesis. *Molecular human reproduction* 2004;10:895-9.
93. Jeyasuria P, Subedi K, Suresh A, Condon JC. Elevated levels of uterine anti-apoptotic signaling may activate NFkB and potentially confer resistance to caspase 3-

mediated apoptotic cell death during pregnancy in mice. *Biology of reproduction* 2011;85:417-24.

94. Lye SJ, Mitchell J, Nashman N, et al. Role of mechanical signals in the onset of term and preterm labor. *Frontiers of hormone research* 2001;27:165-78.

95. Mercer BM. Preterm premature rupture of the membranes. *Obstetrics and gynecology* 2003;101:178-93.

96. Goldenberg RL, Culhane JF, Iams JD, Romero R. Epidemiology and causes of preterm birth. *Lancet* 2008;371:75-84.

97. Veleminsky M, Tosner J. Relationship of vaginal microflora to PROM, pPROM and the risk of early-onset neonatal sepsis. *Neuro endocrinology letters* 2008;29:205-21.

98. Akins ML, Luby-Phelps K, Bank RA, Mahendroo M. Cervical Softening During Pregnancy: Regulated Changes in Collagen Cross-Linking and Composition of Matricellular Proteins in the Mouse¹. *Biology of reproduction* 2011;84:1053-62.

99. Yellon SM, Dobyans AE, Beck HL, Kurtzman JT, Garfield RE, Kirby MA. Loss of Progesterone Receptor-Mediated Actions Induce Preterm Cellular and Structural Remodeling of the Cervix and Premature Birth. *PloS one* 2013;8:e81340.

100. Mogami H, Kishore AH, Shi H, Keller PW, Akgul Y, Word RA. Fetal fibronectin signaling induces matrix metalloproteases and cyclooxygenase-2 (COX-2) in amnion cells and preterm birth in mice. *The Journal of biological chemistry* 2013;288:1953-66.

101. Lockwood CJ, Toti P, Arcuri F, et al. Mechanisms of abruption-induced premature rupture of the fetal membranes: thrombin-enhanced interleukin-8 expression in term decidua. *The American journal of pathology* 2005;167:1443-9.

102. Shubert PJ, Diss E, Iams JD. Etiology of preterm premature rupture of membranes. *Obstetrics and gynecology clinics of North America* 1992;19:251-63.

103. Cnattingius S. The epidemiology of smoking during pregnancy: smoking prevalence, maternal characteristics, and pregnancy outcomes. *Nicotine & tobacco research : official journal of the Society for Research on Nicotine and Tobacco* 2004;6 Suppl 2:S125-40.

104. Berkowitz GS, Blackmore-Prince C, Lapinski RH, Savitz DA. Risk factors for preterm birth subtypes. *Epidemiology (Cambridge, Mass)* 1998;9:279-85.
105. Harger JH, Hsing AW, Tuomala RE, et al. Risk factors for preterm premature rupture of fetal membranes: a multicenter case-control study. *American journal of obstetrics and gynecology* 1990;163:130-7.
106. Albertsen K, Hannerz H, Borg V, Burr H. The effect of work environment and heavy smoking on the social inequalities in smoking cessation. *Public health* 2003;117:383-8.
107. Holzman C, Paneth N. Maternal cocaine use during pregnancy and perinatal outcomes. *Epidemiologic reviews* 1994;16:315-34.
108. Amini SB, Catalano PM, Dierker LJ, Mann LI. Births to teenagers: trends and obstetric outcomes. *Obstetrics and gynecology* 1996;87:668-74.
109. Branum AM, Schoendorf KC. The influence of maternal age on very preterm birth of twins: differential effects by parity. *Paediatric and perinatal epidemiology* 2005;19:399-404.
110. Astolfi P, Zonta LA. Delayed maternity and risk at delivery. *Paediatric and perinatal epidemiology* 2002;16:67-72.
111. Adams Waldorf KM, Singh N, Mohan AR, et al. Uterine overdistention induces preterm labor mediated by inflammation: observations in pregnant women and nonhuman primates. *American journal of obstetrics and gynecology* 2015;213:830.e1-.e19.
112. Moutquin JM. Socio-economic and psychosocial factors in the management and prevention of preterm labour. *BJOG : an international journal of obstetrics and gynaecology* 2003;110 Suppl 20:56-60.
113. Al Riyami N, Al-Ruheili I, Al-Shezaw F, Al-Khabori M. Extreme preterm premature rupture of membranes: risk factors and fetomaternal outcomes. *Oman medical journal* 2013;28:108-11.

114. Mohan AR, Sooranna SR, Lindstrom TM, Johnson MR, Bennett PR. The effect of mechanical stretch on cyclooxygenase type 2 expression and activator protein-1 and nuclear factor-kappaB activity in human amnion cells. *Endocrinology* 2007;148:1850-7.
115. Rice GE. Cytokines and the initiation of parturition. *Frontiers of hormone research* 2001;27:113-46.
116. Bowen JM, Chamley L, Keelan JA, Mitchell MD. Cytokines of the placenta and extra-placental membranes: roles and regulation during human pregnancy and parturition. *Placenta* 2002;23:257-73.
117. Skinner KA, Challis JR. Changes in the synthesis and metabolism of prostaglandins by human fetal membranes and decidua at labor. *American journal of obstetrics and gynecology* 1985;151:519-23.
118. Uchide K, Ueno H, Inoue M, Sakai A, Fujimoto N, Okada Y. Matrix metalloproteinase-9 and tensile strength of fetal membranes in uncomplicated labor. *Obstetrics and gynecology* 2000;95:851-5.
119. Kumar D, Fung W, Moore RM, et al. Proinflammatory cytokines found in amniotic fluid induce collagen remodeling, apoptosis, and biophysical weakening of cultured human fetal membranes. *Biology of reproduction* 2006;74:29-34.
120. Bryant-Greenwood GD. The extracellular matrix of the human fetal membranes: structure and function. *Placenta* 1998;19:1-11.
121. Jabareen M, Mallik AS, Bilic G, Zisch AH, Mazza E. Relation between mechanical properties and microstructure of human fetal membranes: an attempt towards a quantitative analysis. *European journal of obstetrics, gynecology, and reproductive biology* 2009;144 Suppl 1:S134-41.
122. Helmig R, Oxlund H, Petersen LK, Uldbjerg N. Different biomechanical properties of human fetal membranes obtained before and after delivery. *European journal of obstetrics, gynecology, and reproductive biology* 1993;48:183-9.
123. Mori R, Power KT, Wang CM, Martin P, Becker DL. Acute downregulation of connexin43 at wound sites leads to a reduced inflammatory response, enhanced

keratinocyte proliferation and wound fibroblast migration. *Journal of cell science* 2006;119:5193-203.

124. Mendoza-Naranjo A, Cormie P, Serrano AE, et al. Overexpression of the gap junction protein Cx43 as found in diabetic foot ulcers can retard fibroblast migration. *Cell biology international* 2012;36:661-7.

125. Balasubramaniyan V, Dhar DK, Warner AE, et al. Importance of Connexin-43 based gap junction in cirrhosis and acute-on-chronic liver failure. *Journal of hepatology* 2013;58:1194-200.

126. Wang CM, Lincoln J, Cook JE, Becker DL. Abnormal connexin expression underlies delayed wound healing in diabetic skin. *Diabetes* 2007;56:2809-17.

127. Wang X, Ma A, Zhu W, et al. The role of connexin 43 and hemichannels correlated with the astrocytic death following ischemia/reperfusion insult. *Cellular and molecular neurobiology* 2013;33:401-10.

128. Mendoza-Naranjo A, Cormie P, Serrano AE, et al. Targeting Cx43 and N-cadherin, which are abnormally upregulated in venous leg ulcers, influences migration, adhesion and activation of Rho GTPases. *PloS one* 2012;7:e37374.

129. Papanna R, Bebbington MW, Moise K, Jr. Novel findings of iatrogenic fetal membrane defect after previous fetoscopy for twin-twin transfusion syndrome. *Ultrasound in obstetrics & gynecology : the official journal of the International Society of Ultrasound in Obstetrics and Gynecology* 2013;42:118-9.

130. Devlieger R, Millar LK, Bryant-Greenwood G, Lewi L, Deprest JA. Fetal membrane healing after spontaneous and iatrogenic membrane rupture: a review of current evidence. *American journal of obstetrics and gynecology* 2006;195:1512-20.

131. Papanna R, Molina S, Moise KY, Moise KJ, Jr., Johnson A. Chorioamnion plugging and the risk of preterm premature rupture of membranes after laser surgery in twin-twin transfusion syndrome. *Ultrasound in obstetrics & gynecology : the official journal of the International Society of Ultrasound in Obstetrics and Gynecology* 2010;35:337-43.

132. Yamamoto M, Ville Y. Twin-to-twin transfusion syndrome: management options and outcomes. *Clinical obstetrics and gynecology* 2005;48:973-80.
133. Jani JC, Nicolaides KH, Gratacos E, et al. Severe diaphragmatic hernia treated by fetal endoscopic tracheal occlusion. *Ultrasound in obstetrics & gynecology : the official journal of the International Society of Ultrasound in Obstetrics and Gynecology* 2009;34:304-10.
134. Lewi L, Gratacos E, Ortibus E, et al. Pregnancy and infant outcome of 80 consecutive cord coagulations in complicated monochorionic multiple pregnancies. *American journal of obstetrics and gynecology* 2006;194:782-9.
135. Quintero RA, Chmait RH, Murakoshi T, et al. Surgical management of twin reversed arterial perfusion sequence. *American journal of obstetrics and gynecology* 2006;194:982-91.
136. Quintero RA, Johnson MP, Romero R, et al. In-utero percutaneous cystoscopy in the management of fetal lower obstructive uropathy. *Lancet* 1995;346:537-40.
137. Welsh A, Agarwal S, Kumar S, Smith RP, Fisk NM. Fetal cystoscopy in the management of fetal obstructive uropathy: experience in a single European centre. *Prenatal diagnosis* 2003;23:1033-41.
138. Oepkes D. Re: Risk factors associated with preterm delivery after fetoscopic laser ablation for twin-twin transfusion syndrome. R. Papanna, D. Block-Abraham, L. K. Mann, I. A. Buhimschi, M. Bebbington, E. Garcia, N. Kahlek, C. Harman, A. Johnson, A. Baschat and K. J. Moise Jr. *Ultrasound Obstet Gynecol* 2014; 43: 48-53. *Ultrasound in obstetrics & gynecology : the official journal of the International Society of Ultrasound in Obstetrics and Gynecology* 2014;43:11-2.
139. Mari G, Roberts A, Detti L, et al. Perinatal morbidity and mortality rates in severe twin-twin transfusion syndrome: results of the International Amnioreduction Registry. *American journal of obstetrics and gynecology* 2001;185:708-15.
140. Ierullo AM, Papageorghiou AT, Bhide A, Fratelli N, Thilaganathan B. Severe twin-twin transfusion syndrome: outcome after fetoscopic laser ablation of the placental

vascular equator. *BJOG : an international journal of obstetrics and gynaecology* 2007;114:689-93.

141. Snowise S, Mann LK, Moise KJ, Jr., Johnson A, Bebbington MW, Papanna R. Preterm prelabor rupture of membranes after fetoscopic laser surgery for twin-twin transfusion syndrome. *Ultrasound in obstetrics & gynecology : the official journal of the International Society of Ultrasound in Obstetrics and Gynecology* 2017;49:607-11.

142. Harrison MR, Albanese CT, Hawgood SB, et al. Fetoscopic temporary tracheal occlusion by means of detachable balloon for congenital diaphragmatic hernia. *American journal of obstetrics and gynecology* 2001;185:730-3.

143. Deprest J, Jani J, Van Schoubroeck D, et al. Current consequences of prenatal diagnosis of congenital diaphragmatic hernia. *Journal of pediatric surgery* 2006;41:423-30.

144. Cabassa P, Fichera A, Prefumo F, et al. The use of radiofrequency in the treatment of twin reversed arterial perfusion sequence: a case series and review of the literature. *European journal of obstetrics, gynecology, and reproductive biology* 2013;166:127-32.

145. Lee H, Bebbington M, Crombleholme TM. The North American Fetal Therapy Network Registry data on outcomes of radiofrequency ablation for twin-reversed arterial perfusion sequence. *Fetal diagnosis and therapy* 2013;33:224-9.

146. Anumba DO, Scott JE, Plant ND, Robson SC. Diagnosis and outcome of fetal lower urinary tract obstruction in the northern region of England. *Prenatal diagnosis* 2005;25:7-13.

147. Holmes N, Harrison MR, Baskin LS. Fetal surgery for posterior urethral valves: long-term postnatal outcomes. *Pediatrics* 2001;108:E7.

148. Morris RK, Khan KS, Kilby MD. Vesicoamniotic shunting for fetal lower urinary tract obstruction: an overview. *Archives of disease in childhood Fetal and neonatal edition* 2007;92:F166-8.

149. Biard JM, Johnson MP, Carr MC, et al. Long-term outcomes in children treated by prenatal vesicoamniotic shunting for lower urinary tract obstruction. *Obstetrics and gynecology* 2005;106:503-8.

150. Debska M, Kretowicz P, Oledzka A, et al. Early vesico-amniotic shunting - does it change the prognosis in fetal lower urinary tract obstruction diagnosed in the first trimester? *Ginekologia polska* 2017;88:486-91.
151. Adzick NS, Harrison MR, Crombleholme TM, Flake AW, Howell LJ. Fetal lung lesions: management and outcome. *American journal of obstetrics and gynecology* 1998;179:884-9.
152. Crombleholme TM, Coleman B, Hedrick H, et al. Cystic adenomatoid malformation volume ratio predicts outcome in prenatally diagnosed cystic adenomatoid malformation of the lung. *Journal of pediatric surgery* 2002;37:331-8.
153. Davenport M, Warne SA, Cacciaguerra S, Patel S, Greenough A, Nicolaides K. Current outcome of antenally diagnosed cystic lung disease. *Journal of pediatric surgery* 2004;39:549-56.
154. Makin EC, Hyett J, Ade-Ajayi N, Patel S, Nicolaides K, Davenport M. Outcome of antenatally diagnosed sacrococcygeal teratomas: single-center experience (1993-2004). *Journal of pediatric surgery* 2006;41:388-93.
155. Swamy R, Embleton N, Hale J. Sacrococcygeal teratoma over two decades: birth prevalence, prenatal diagnosis and clinical outcomes. *Prenatal diagnosis* 2008;28:1048-51.
156. Roberts HE, Moore CA, Cragan JD, Fernhoff PM, Khoury MJ. Impact of prenatal diagnosis on the birth prevalence of neural tube defects, Atlanta, 1990-1991. *Pediatrics* 1995;96:880-3.
157. Velie EM, Shaw GM. Impact of prenatal diagnosis and elective termination on prevalence and risk estimates of neural tube defects in California, 1989-1991. *American journal of epidemiology* 1996;144:473-9.
158. Adzick NS. Fetal surgery for myelomeningocele: trials and tribulations. Isabella Forshall Lecture. *Journal of pediatric surgery* 2012;47:273-81.
159. Oakeshott P, Hunt GM. Long-term outcome in open spina bifida. *The British journal of general practice : the journal of the Royal College of General Practitioners* 2003;53:632-6.

160. Simpson JM. Fetal cardiac interventions: worth it? *Heart (British Cardiac Society)* 2009;95:1653-5.
161. Freud LR, McElhinney DB, Marshall AC, et al. Fetal aortic valvuloplasty for evolving hypoplastic left heart syndrome: postnatal outcomes of the first 100 patients. *Circulation* 2014;130:638-45.
162. Gratacos E, Sanin-Blair J, Lewi L, et al. A histological study of fetoscopic membrane defects to document membrane healing. *Placenta* 2006;27:452-6.
163. Sydorak RM, Hirose S, Sandberg PL, et al. Chorioamniotic membrane separation following fetal surgery. *Journal of perinatology : official journal of the California Perinatal Association* 2002;22:407-10.
164. Papanna R, Mann LK, Moise KJ, Jr., et al. Histologic changes of the fetal membranes after fetoscopic laser surgery for twin-twin transfusion syndrome. *Pediatric research* 2015;78:247-55.
165. Carvalho NS, Moron AF, Menon R, et al. Histological evidence of reparative activity in chorioamniotic membrane following open fetal surgery for myelomeningocele. *Experimental and therapeutic medicine* 2017;14:3732-6.
166. Devlieger R, Riley SC, Verbist L, Leask R, Pijnenborg R, Deprest JA. Matrix metalloproteinases-2 and -9 and their endogenous tissue inhibitors in tissue remodeling after sealing of the fetal membranes in a sheep model of fetoscopic surgery. *Journal of the Society for Gynecologic Investigation* 2002;9:137-45.
167. Devlieger R, Deprest JA, Gratacos E, Pijnenborg R, Leask R, Riley SC. Matrix metalloproteinases -2 and -9 and their endogenous tissue inhibitors in fetal membrane repair following fetoscopy in a rabbit model. *Molecular human reproduction* 2000;6:479-85.
168. Mallik AS, Fichter MA, Rieder S, et al. Fetoscopic closure of punctured fetal membranes with acellular human amnion plugs in a rabbit model. *Obstetrics and gynecology* 2007;110:1121-9.

169. Gratacos E, Deprest J. Current experience with fetoscopy and the Eurofoetus registry for fetoscopic procedures. *European journal of obstetrics, gynecology, and reproductive biology* 2000;92:151-9.
170. Ochsenbein-Kolble N, Jani J, Lewi L, et al. Enhancing sealing of fetal membrane defects using tissue engineered native amniotic scaffolds in the rabbit model. *American journal of obstetrics and gynecology* 2007;196:263.e1-7.
171. Sopher D. The response of rat fetal membranes to injury. *Annals of the Royal College of Surgeons of England* 1972;51:240-9.
172. Papanna R, Mann LK, Tseng SC, et al. Cryopreserved human amniotic membrane and a bioinspired underwater adhesive to seal and promote healing of iatrogenic fetal membrane defect sites. *Placenta* 2015;36:888-94.
173. Mogami H, Hari Kishore A, Akgul Y, Word RA. Healing of Preterm Ruptured Fetal Membranes. *Scientific reports* 2017;7:13139.
174. Pfaffl MW. A new mathematical model for relative quantification in real-time RT-PCR. *Nucleic acids research* 2001;29:e45.
175. Pfaffl MW, Horgan GW, Dempfle L. Relative expression software tool (REST) for group-wise comparison and statistical analysis of relative expression results in real-time PCR. *Nucleic acids research* 2002;30:e36.
176. Lee DA, Brand J, Salter D, Akanji OO, Chowdhury TT. Quantification of mRNA using real-time PCR and Western blot analysis of MAPK events in chondrocyte/agarose constructs. *Methods in molecular biology (Clifton, NJ)* 2011;695:77-97.
177. Bennett MV, Contreras JE, Bukauskas FF, Saez JC. New roles for astrocytes: gap junction hemichannels have something to communicate. *Trends in neurosciences* 2003;26:610-7.
178. Goodenough DA, Paul DL. Beyond the gap: functions of unpaired connexon channels. *Nature reviews Molecular cell biology* 2003;4:285-94.
179. Valiunas V, Polosina YY, Miller H, et al. Connexin-specific cell-to-cell transfer of short interfering RNA by gap junctions. *The Journal of physiology* 2005;568:459-68.

180. Sohl G, Willecke K. Gap junctions and the connexin protein family. *Cardiovascular research* 2004;62:228-32.
181. Herve JC, Bourmeyster N, Sarrouilhe D, Duffy HS. Gap junctional complexes: from partners to functions. *Progress in biophysics and molecular biology* 2007;94:29-65.
182. Batra N, Riquelme MA, Burra S, Kar R, Gu S, Jiang JX. Direct regulation of osteocytic connexin 43 hemichannels through AKT kinase activated by mechanical stimulation. *The Journal of biological chemistry* 2014;289:10582-91.
183. Dbouk HA, Mroue RM, El-Sabban ME, Talhouk RS. Connexins: a myriad of functions extending beyond assembly of gap junction channels. *Cell communication and signaling : CCS* 2009;7:4.
184. Mese G, Richard G, White TW. Gap junctions: basic structure and function. *The Journal of investigative dermatology* 2007;127:2516-24.
185. Musil LS, Goodenough DA. Multisubunit assembly of an integral plasma membrane channel protein, gap junction connexin43, occurs after exit from the ER. *Cell* 1993;74:1065-77.
186. Laird DW, Castillo M, Kasprzak L. Gap junction turnover, intracellular trafficking, and phosphorylation of connexin43 in brefeldin A-treated rat mammary tumor cells. *The Journal of cell biology* 1995;131:1193-203.
187. Wong P, Tan T, Chan C, et al. The Role of Connexins in Wound Healing and Repair: Novel Therapeutic Approaches. *Frontiers in physiology* 2016;7:596.
188. Zhang XF, Cui X. Connexin 43: Key roles in the skin. *Biomedical reports* 2017;6:605-11.
189. Chin KY. Connexins, a new target in wound treatment. *Journal of wound care* 2011;20:386-90.
190. Goliger JA, Paul DL. Wounding alters epidermal connexin expression and gap junction-mediated intercellular communication. *Molecular biology of the cell* 1995;6:1491-501.

191. Cronin M, Anderson PN, Cook JE, Green CR, Becker DL. Blocking connexin43 expression reduces inflammation and improves functional recovery after spinal cord injury. *Molecular and cellular neurosciences* 2008;39:152-60.
192. Coutinho P, Qiu C, Frank S, Tamber K, Becker D. Dynamic changes in connexin expression correlate with key events in the wound healing process. *Cell biology international* 2003;27:525-41.
193. Becker DL, Thrasivoulou C, Phillips AR. Connexins in wound healing; perspectives in diabetic patients. *Biochimica et biophysica acta* 2012;1818:2068-75.
194. Adzick NS, Longaker MT. Scarless fetal healing. Therapeutic implications. *Annals of surgery* 1992;215:3-7.
195. Hopkinson-Woolley J, Hughes D, Gordon S, Martin P. Macrophage recruitment during limb development and wound healing in the embryonic and foetal mouse. *Journal of cell science* 1994;107 (Pt 5):1159-67.
196. Redd MJ, Cooper L, Wood W, Stramer B, Martin P. Wound healing and inflammation: embryos reveal the way to perfect repair. *Philosophical transactions of the Royal Society of London Series B, Biological sciences* 2004;359:777-84.
197. Tarzemany R, Jiang G, Larjava H, Hakkinen L. Expression and function of connexin 43 in human gingival wound healing and fibroblasts. *PloS one* 2015;10:e0115524.
198. Sutcliffe JE, Chin KY, Thrasivoulou C, et al. Abnormal connexin expression in human chronic wounds. *The British journal of dermatology* 2015;173:1205-15.
199. Brandner JM, Houdek P, Husing B, Kaiser C, Moll I. Connexins 26, 30, and 43: differences among spontaneous, chronic, and accelerated human wound healing. *The Journal of investigative dermatology* 2004;122:1310-20.
200. Charles CA, Tomic-Canic M, Vincek V, et al. A gene signature of nonhealing venous ulcers: potential diagnostic markers. *Journal of the American Academy of Dermatology* 2008;59:758-71.

201. Ongstad EL, O'Quinn MP, Ghatnekar GS, Yost MJ, Gourdie RG. A Connexin43 Mimetic Peptide Promotes Regenerative Healing and Improves Mechanical Properties in Skin and Heart. *Advances in wound care* 2013;2:55-62.
202. Pringle AK, Iannotti F, Wilde GJ, Chad JE, Seeley PJ, Sundstrom LE. Neuroprotection by both NMDA and non-NMDA receptor antagonists in in vitro ischemia. *Brain research* 1997;755:36-46.
203. Quintero RA, Carreno CA, Yelian F, Evans MI. Repair kinetics of amnion cells after microsurgical injury. *Fetal diagnosis and therapy* 1996;11:348-56.
204. Bilic G, Ochsenbein-Kolble N, Hall H, Huch R, Zimmermann R. In vitro lesion repair by human amnion epithelial and mesenchymal cells. *American journal of obstetrics and gynecology* 2004;190:87-92.
205. Devlieger R, Gratacos E, Verbist L, Pijnenborg R, Deprest J. Gestational age-dependent repair kinetics of microsurgical defects in monolayers of human amniocytes. *Gynecologic and obstetric investigation* 2010;69:62-6.
206. Theodossiou TA, Thrasivoulou C, Ekwobi C, Becker DL. Second harmonic generation confocal microscopy of collagen type I from rat tendon cryosections. *Biophysical journal* 2006;91:4665-77.
207. Ochsenbein-Kolble N, Bilic G, Hall H, Huch R, Zimmermann R. Inducing proliferation of human amnion epithelial and mesenchymal cells for prospective engineering of membrane repair. *Journal of perinatal medicine* 2003;31:287-94.
208. Parolini O, Alviano F, Bagnara GP, et al. Concise review: isolation and characterization of cells from human term placenta: outcome of the first international Workshop on Placenta Derived Stem Cells. *Stem cells (Dayton, Ohio)* 2008;26:300-11.
209. Miki T, Lehmann T, Cai H, Stolz DB, Strom SC. Stem cell characteristics of amniotic epithelial cells. *Stem cells (Dayton, Ohio)* 2005;23:1549-59.
210. Engels AC, Van Calster B, Richter J, et al. Collagen plug sealing of iatrogenic fetal membrane defects after fetoscopic surgery for congenital diaphragmatic hernia. *Ultrasound in obstetrics & gynecology : the official journal of the International Society of Ultrasound in Obstetrics and Gynecology* 2014;43:54-9.

211. Papanna R, Mann LK, Moise KY, Johnson A, Moise KJ, Jr. Absorbable gelatin plug does not prevent iatrogenic preterm premature rupture of membranes after fetoscopic laser surgery for twin-twin transfusion syndrome. *Ultrasound in obstetrics & gynecology : the official journal of the International Society of Ultrasound in Obstetrics and Gynecology* 2013;42:456-60.
212. Quintero RA, Morales WJ, Allen M, Bornick PW, Arroyo J, LeParc G. Treatment of iatrogenic previable premature rupture of membranes with intra-amniotic injection of platelets and cryoprecipitate (amniopatch): preliminary experience. *American journal of obstetrics and gynecology* 1999;181:744-9.
213. Genz HJ. [Treatment of premature rupture of the fetal membranes by means of fibrin adhesion]. *Die Medizinische Welt* 1979;30:1557-9.
214. Quintero RA. New horizons in the treatment of preterm premature rupture of membranes. *Clinics in perinatology* 2001;28:861-75.
215. Young BK, Roque H, Abdelhak YE, Poiolek D, Demopulos R, Lockwood CJ. Minimally invasive endoscopy in the treatment of preterm premature rupture of membranes by application of fibrin sealant. *Journal of perinatal medicine* 2000;28:326-30.
216. Young BK, Roman AS, MacKenzie AP, et al. The closure of iatrogenic membrane defects after amniocentesis and endoscopic intrauterine procedures. *Fetal diagnosis and therapy* 2004;19:296-300.
217. Sener T, Ozalp S, Hassa H, Yalcin OT, Polay S. Maternal blood clot patch therapy: a model for postamniocentesis amniorrhea. *American journal of obstetrics and gynecology* 1997;177:1535-6.
218. O'Brien JM, Milligan DA, Barton JR. Gelatin sponge embolization. a method for the management of iatrogenic preterm premature rupture of the membranes. *Fetal diagnosis and therapy* 2002;17:8-10.
219. Lewi L, Van Schoubroeck D, Van Ranst M, et al. Successful patching of iatrogenic rupture of the fetal membranes. *Placenta* 2004;25:352-6.

220. Bilic G, Brubaker C, Messersmith PB, et al. Injectable candidate sealants for fetal membrane repair: bonding and toxicity in vitro. *American journal of obstetrics and gynecology* 2010;202:85.e1-9.
221. Haller CM, Buerzle W, Brubaker CE, et al. Mussel-mimetic tissue adhesive for fetal membrane repair: a standardized ex vivo evaluation using elastomeric membranes. *Prenatal diagnosis* 2011;31:654-60.
222. Haller CM, Buerzle W, Kivelio A, et al. Mussel-mimetic tissue adhesive for fetal membrane repair: an ex vivo evaluation. *Acta biomaterialia* 2012;8:4365-70.
223. Mann LK, Papanna R, Moise KJ, Jr., et al. Fetal membrane patch and biomimetic adhesive coacervates as a sealant for fetoscopic defects. *Acta biomaterialia* 2012;8:2160-5.
224. Devlieger R, Ardon H, Verbist L, Gratacos E, Pijnenborg R, Deprest JA. Increased polymorphonuclear infiltration and iatrogenic amniotic band after closure of fetoscopic access sites with a bioactive membrane in the rabbit at midgestation. *American journal of obstetrics and gynecology* 2003;188:844-8.
225. Baumgarten K, Moser S. The technique of fibrin adhesion for premature rupture of the membranes during pregnancy. *Journal of perinatal medicine* 1986;14:43-9.
226. Quintero RA, Romero R, Dzieczkowski J, Mammen E, Evans MI. Sealing of ruptured amniotic membranes with intra-amniotic platelet-cryoprecipitate plug. *Lancet* 1996;347:1117.
227. Louis-Sylvestre C, Rand JH, Gordon RE, Salafia CM, Berkowitz RL. In vitro studies of the interactions between platelets and amniotic membranes: a potential treatment for preterm premature rupture of the membranes. *American journal of obstetrics and gynecology* 1998;178:287-93.
228. Chmait RH, Kontopoulos EV, Chon AH, Korst LM, Llanes A, Quintero RA. Amniopatch treatment of iatrogenic preterm premature rupture of membranes (iPPROM) after fetoscopic laser surgery for twin-twin transfusion syndrome. *The journal of maternal-fetal & neonatal medicine : the official journal of the European Association of*

Perinatal Medicine, the Federation of Asia and Oceania Perinatal Societies, the International Society of Perinatal Obstet 2017;30:1349-54.

229. Reddy UM, Shah SS, Nemiroff RL, et al. In vitro sealing of punctured fetal membranes: potential treatment for midtrimester premature rupture of membranes. American journal of obstetrics and gynecology 2001;185:1090-3.

230. Sciscione AC, Manley JS, Pollock M, et al. Intracervical fibrin sealants: a potential treatment for early preterm premature rupture of the membranes. American journal of obstetrics and gynecology 2001;184:368-73.

231. Quintero RA. Treatment of previable premature ruptured membranes. Clinics in perinatology 2003;30:573-89.

232. Sung JH, Kuk JY, Cha HH, et al. Amniopatch treatment for preterm premature rupture of membranes before 23 weeks' gestation and factors associated with its success. Taiwanese journal of obstetrics & gynecology 2017;56:599-605.

233. Harmanli OH, Wapner RJ, Lontz JF. Efficacy of fibrin glue for in vitro sealing of human chorioamniotic membranes. The Journal of reproductive medicine 1998;43:986-90.

234. Cobo T, Borrell A, Fortuny A, et al. Treatment with amniopatch of premature rupture of membranes after first-trimester chorionic villus sampling. Prenatal diagnosis 2007;27:1024-7.

235. Mandelbrot L, Bourguignat L, Mellouhi IS, Gavard L, Morin F, Bierling P. Treatment by autologous amniopatch of premature rupture of membranes following mid-trimester amniocentesis. Ultrasound in obstetrics & gynecology : the official journal of the International Society of Ultrasound in Obstetrics and Gynecology 2009;33:245-6.

236. Pathak B, Khan A, Assaf SA, Miller DA, Chmait RH. Amniopatch as a treatment for rupture of membranes following laser surgery for twin-twin transfusion syndrome. Fetal diagnosis and therapy 2010;27:134-7.

237. Ferianec V, Krizko M, Jr., Papcun P, et al. Amniopatch - possibility of successful treatment of spontaneous previable rupture of membranes in the second trimester of

pregnancy by transabdominal intraamniotic application of platelets and cryoprecipitate. *Neuro endocrinology letters* 2011;32:449-52.

238. Kwak HM, Choi HJ, Cha HH, et al. Amniopatch treatment for spontaneous previabile, preterm premature rupture of membranes associated or not with incompetent cervix. *Fetal diagnosis and therapy* 2013;33:47-54.

239. Richter J, Henry A, Ryan G, DeKoninck P, Lewi L, Deprest J. Amniopatch procedure after previabile iatrogenic rupture of the membranes: a two-center review. *Prenatal diagnosis* 2013;33:391-6.

240. O'Brien JM, Barton JR, Milligan DA. An aggressive interventional protocol for early midtrimester premature rupture of the membranes using gelatin sponge for cervical plugging. *American journal of obstetrics and gynecology* 2002;187:1143-6.

241. O'Brien JM, Mercer BM, Barton JR, Milligan DA. An in vitro model and case report that used gelatin sponge to restore amniotic fluid volume after spontaneous premature rupture of the membranes. *American journal of obstetrics and gynecology* 2001;185:1094-7.

242. Quintero RA, Morales WJ, Bornick PW, Allen M, Garabelis N. Surgical treatment of spontaneous rupture of membranes: the amniograft--first experience. *American journal of obstetrics and gynecology* 2002;186:155-7.

243. Beck V, Lewi P, Gucciardo L, Devlieger R. Preterm prelabor rupture of membranes and fetal survival after minimally invasive fetal surgery: a systematic review of the literature. *Fetal diagnosis and therapy* 2012;31:1-9.

244. Barrett DW, David AL, Thrasivoulou C, et al. Connexin 43 is overexpressed in human fetal membrane defects after fetoscopic surgery. *Prenatal diagnosis* 2016;36:942-52.

245. Barrett DW, Kethees A, Thrasivoulou C, et al. Trauma induces overexpression of Cx43 in human fetal membrane defects. *Prenatal diagnosis* 2017;37:899-906.

246. Luks FI, Deprest JA, Peers KH, Steegers EA, van Der Wildt B. Gelatin sponge plug to seal fetoscopy port sites: technique in ovine and primate models. *American journal of obstetrics and gynecology* 1999;181:995-6.

247. Deprest JA, Papadopulos NA, Decaluw H, Yamamoto H, Lerut TE, Gratacos E. Closure techniques for fetoscopic access sites in the rabbit at mid-gestation. *Human reproduction (Oxford, England)* 1999;14:1730-4.
248. Papadopulos NA, Klotz S, Raith A, et al. Amnion cells engineering: a new perspective in fetal membrane healing after intrauterine surgery? *Fetal diagnosis and therapy* 2006;21:494-500.
249. Liekens D, Lewi L, Jani J, et al. Enrichment of collagen plugs with platelets and amniotic fluid cells increases cell proliferation in sealed iatrogenic membrane defects in the foetal rabbit model. *Prenatal diagnosis* 2008;28:503-7.
250. Engels AC, Hoylaerts MF, Endo M, et al. In vitro sealing of iatrogenic fetal membrane defects by a collagen plug imbued with fibrinogen and plasma. *Prenatal diagnosis* 2013;33:162-7.
251. Mendoza GA, Acuna E, Allen M, Arroyo J, Quintero RA. In vitro laser welding of amniotic membranes. *Lasers in surgery and medicine* 1999;24:315-8.
252. Mendez-Figueroa H, Papanna R, Berry DL, Moise KJ, Jr. Precipitated egg white as a sealant for iatrogenic preterm premature rupture of the membranes. *American journal of obstetrics and gynecology* 2010;202:191.e1-6.
253. Kivelio A, Dekoninck P, Perrini M, et al. Mussel mimetic tissue adhesive for fetal membrane repair: initial in vivo investigation in rabbits. *European journal of obstetrics, gynecology, and reproductive biology* 2013;171:240-5.
254. Lee BP, Dalsin JL, Messersmith PB. Synthesis and gelation of DOPA-modified poly(ethylene glycol) hydrogels. *Biomacromolecules* 2002;3:1038-47.
255. Jones Richard G, Ober Christopher K, Hodge P, Kratochvíl P, Moad G, Vert M. Terminology for aggregation and self-assembly in polymer science (IUPAC Recommendations 2013). *Pure and Applied Chemistry* 2012:463.
256. Cui H, Cheetham AG, Pashuck ET, Stupp SI. Amino acid sequence in constitutionally isomeric tetrapeptide amphiphiles dictates architecture of one-dimensional nanostructures. *Journal of the American Chemical Society* 2014;136:12461-8.

257. Blodgett KB. Films Built by Depositing Successive Monomolecular Layers on a Solid Surface. *Journal of the American Chemical Society* 1935;57:1007-22.
258. Bain CD, Troughton EB, Tao YT, Evall J, Whitesides GM, Nuzzo RG. Formation of monolayer films by the spontaneous assembly of organic thiols from solution onto gold. *Journal of the American Chemical Society* 1989;111:321-35.
259. Whitesides GM, Laibinis PE. Wet chemical approaches to the characterization of organic surfaces: self-assembled monolayers, wetting, and the physical-organic chemistry of the solid-liquid interface. *Langmuir* 1990;6:87-96.
260. Decher G. Fuzzy Nanoassemblies: Toward Layered Polymeric Multicomposites. *Science (New York, NY)* 1997;277:1232-7.
261. Carvajal D, Bitton R, Mantei JR, Velichko YS, Stupp SI, Shull KR. Physical properties of hierarchically ordered self-assembled planar and spherical membranes. *Soft Matter* 2010;6:1816-23.
262. Tisi DK, Emard JJ, Koski KG. Total protein concentration in human amniotic fluid is negatively associated with infant birth weight. *The Journal of nutrition* 2004;134:1754-8.
263. Deprest J, Emonds MP, Richter J, et al. Amniopatch for iatrogenic rupture of the fetal membranes. *Prenatal diagnosis* 2011;31:661-6.
264. Caughey AB, Robinson JN, Norwitz ER. Contemporary diagnosis and management of preterm premature rupture of membranes. *Reviews in obstetrics & gynecology* 2008;1:11-22.
265. So T. [The role of matrix metalloproteinases for premature rupture of the membranes]. *Nihon Sanka Fujinka Gakkai zasshi* 1993;45:227-33.
266. Woods JR, Jr. Reactive oxygen species and preterm premature rupture of membranes-a review. *Placenta* 2001;22 Suppl A:S38-44.
267. Dutta EH, Behnia F, Boldogh I, et al. Oxidative stress damage-associated molecular signaling pathways differentiate spontaneous preterm birth and preterm premature rupture of the membranes. *Molecular human reproduction* 2016;22:143-57.

268. Lee SY, Buhimschi IA, Dulay AT, et al. IL-6 trans-signaling system in intra-amniotic inflammation, preterm birth, and preterm premature rupture of the membranes. *Journal of immunology (Baltimore, Md : 1950)* 2011;186:3226-36.
269. Goldenberg RL, Iams JD, Miodovnik M, et al. The preterm prediction study: risk factors in twin gestations. National Institute of Child Health and Human Development Maternal-Fetal Medicine Units Network. *American journal of obstetrics and gynecology* 1996;175:1047-53.
270. Kirkinen P, Jouppila P. Polyhydramnion. A clinical study. *Annales chirurgiae et gynaecologiae* 1978;67:117-22.
271. Heinonen PK. Unicornuate uterus and rudimentary horn. *Fertility and sterility* 1997;68:224-30.
272. Joyce EM, Diaz P, Tamarkin S, et al. In-vivo stretch of term human fetal membranes. *Placenta* 2016;38:57-66.
273. Artal R, Burgeson RE, Hobel CJ, Hollister D. An in vitro model for the study of enzymatically mediated biomechanical changes in the chorioamniotic membranes. *American journal of obstetrics and gynecology* 1979;133:656-9.
274. Mauri A, Perrini M, Ehret AE, De Focatiis DS, Mazza E. Time-dependent mechanical behavior of human amnion: macroscopic and microscopic characterization. *Acta biomaterialia* 2015;11:314-23.
275. Sooranna SR, Lee Y, Kim LU, Mohan AR, Bennett PR, Johnson MR. Mechanical stretch activates type 2 cyclooxygenase via activator protein-1 transcription factor in human myometrial cells. *Molecular human reproduction* 2004;10:109-13.
276. Liu S, Nigam C, Koh EY, Stains JP. Connexin43 Mediated Delivery of ADAMTS5 Targeting siRNAs from Mesenchymal Stem Cells to Synovial Fibroblasts. *PloS one* 2015;10:e0129999.
277. Nasrallah R, Laneuville O, Ferguson S, Hebert RL. Effect of COX-2 inhibitor NS-398 on expression of PGE2 receptor subtypes in M-1 mouse CCD cells. *American journal of physiology Renal physiology* 2001;281:F123-32.

278. Chakraborty S, Mitra S, Falk MM, et al. E-cadherin differentially regulates the assembly of Connexin43 and Connexin32 into gap junctions in human squamous carcinoma cells. *The Journal of biological chemistry* 2010;285:10761-76.
279. Legerlotz K, Jones GC, Screen HR, Riley GP. Cyclic loading of tendon fascicles using a novel fatigue loading system increases interleukin-6 expression by tenocytes. *Scandinavian journal of medicine & science in sports* 2013;23:31-7.
280. Uldbjerg N, Ulmsten U. The physiology of cervical ripening and cervical dilatation and the effect of abortifacient drugs. *Bailliere's clinical obstetrics and gynaecology* 1990;4:263-82.
281. Norman M, Ekman G, Malmstrom A. Prostaglandin E2-induced ripening of the human cervix involves changes in proteoglycan metabolism. *Obstetrics and gynecology* 1993;82:1013-20.
282. Norman M, Ekman G, Malmstrom A. Changed proteoglycan metabolism in human cervix immediately after spontaneous vaginal delivery. *Obstetrics and gynecology* 1993;81:217-23.
283. Wu WX, Ma XH, Yoshizato T, Shinozuka N, Nathanielsz PW. Differential expression of myometrial oxytocin receptor and prostaglandin H synthase 2, but not estrogen receptor alpha and heat shock protein 90 messenger ribonucleic acid in the gravid horn and nongravid horn in sheep during betamethasone-induced labor. *Endocrinology* 1999;140:5712-8.
284. Chowdhury B, David AL, Thrasivoulou C, Becker DL, Bader DL, Chowdhury TT. Tensile strain increased COX-2 expression and PGE2 release leading to weakening of the human amniotic membrane. *Placenta* 2014;35:1057-64.
285. Dunn CA, Su V, Lau AF, Lampe PD. Activation of Akt, not connexin 43 protein ubiquitination, regulates gap junction stability. *The Journal of biological chemistry* 2012;287:2600-7.
286. Kumar D, Springel E, Moore RM, et al. Progesterone inhibits in vitro fetal membrane weakening. *American journal of obstetrics and gynecology* 2015;213:520.e1-9.

287. Kumar D, Moore RM, Mercer BM, et al. In an in-vitro model using human fetal membranes, 17-alpha hydroxyprogesterone caproate is not an optimal progestogen for inhibition of fetal membrane weakening. *American journal of obstetrics and gynecology* 2017;217:695.e1-.e14.
288. Romero R, Dey SK, Fisher SJ. Preterm labor: one syndrome, many causes. *Science (New York, NY)* 2014;345:760-5.
289. Dunn CA, Lampe PD. Injury-triggered Akt phosphorylation of Cx43: a ZO-1-driven molecular switch that regulates gap junction size. *Journal of cell science* 2014;127:455-64.
290. Gilmartin DJ, Soon A, Thrasivoulou C, Phillips AR, Jayasinghe SN, Becker DL. Sustained Release of Cx43 Antisense Oligodeoxynucleotides from Coated Collagen Scaffolds Promotes Wound Healing. *Advanced healthcare materials* 2016;5:1786-99.
291. Moron A, Athanasiou AV, Barbosa MM, et al. 87: Biomarkers in amniotic fluid at the time of fetal myelomeningocele surgery predict premature rupture of membranes. *American Journal of Obstetrics & Gynecology*;218:S64.